A combined Kalman Filter and Error in Constitutive Relation approach for system identification in structural dynamics.

Albert Alarcon Cot

Une approche de l'identification en dynamique des structures combinant l'erreur en relation de comportement et le filtrage de Kalman

Thèse présentée pour l'obtention du titre de

DOCTEUR DE L'ÉCOLE POLYTECHNIQUE
Spécialité : Mécanique

par

Albert Alarcón Cot

Soutenue le 4 *juin 2012 devant le jury composé de*

Président :	**Claude Blanzé**	Professeur, CNAM, France
Rapporteurs :	**Laurent Champaney**	Professeur, ENS-Cachan, France
	Geert Lombaert	Professeur, KU Leuven, Belgique
Examinateur :	**Andrew W. Smyth**	Professeur, Columbia University, USA
Directeur :	**Marc Bonnet**	Directeur de recherche, CNRS, France
Encadrant :	**Charles Bodel**	Ingénieur de recherche, EDF, France

Laboratoire de Mécanique des Solides
École Polytechnique, France

LaMSID
UMR EDF - CNRS 2832, France

b

à Carole

a la meva família

d

Acknowledgments

I would like to express my most sincere gratitude to my advisors, Marc Bonnet and Charles Bodel, not only for the quality of their guidance but also for the confidence they offered me from the very beginning and the patience and help they showed all along this period.

I also owe all my gratitude to all the members of my defense committee: Claude Blanzé for accepting being the committee chairman, Geert Lombaert and Laurent Champaney for their effort in reviewing this dissertation, their questions, comments, and useful feedback on this work. And obviously, a very special thanks to Andrew W. Smyth for having accepted to be part of my defense committee, which honors me, but also for warmly hosting me at Columbia University during a summer internship, where I had the chance to share rich and inspiring interactions with him.

During this work, I spent most of my time at the Mechanics and Acoustics research department of EDF, where I always felt pleased to work. I would therefore like to sincerely thank Laurent Billet, Sebastien Caillaud and François Weackel, not only for having accepted me as a Ph.D student, but also for their permanent trust that made possible new, challenging, projects such as giving me the possibility work at Columbia University or establishing a cooperation with the LMT laboratory of ENS-Cachan.

In the cooperation with the LMT, I had he chance to work with Frederic Ragueneau and the LMT laboratory fellows in the construction of a nontrivial test setup, and I would like to acknowledge them for their invaluable contribution.

Of course, this research wouldn't had been possible without Mathieu Corus and Jean-Philippe Argaud from EDF R&D, with whom I had discussion of priceless help from both technical and scientific point of view. I cannot forget either the nice experience I had supervising Maïlys Pache during her final-year undergraduate internship. Her commitment and diligence considerably helped me to both improve this work and acquire a deeper insight of the involved techniques.

And, most importantly, I want to thank, warmly, all those who have have been there for all what is not written hereafter: colleagues, new and old friends, and all the people I love. The list will be too long, but let me at least mention a few, starting from the guys from the Laboratoire de Mécanique des Solides of the École Polytechnique, with a special big up to Eva and Nico, whose ability to unconditionally make me laugh goes far beyond expectations. I also truly want to thank all the colleagues from T61 without exception, for their permanent good vibes. And specially "la bande de joyaux connards" with Laurent, Thibaud, Charles, Lise, John 'Blue Eyes',Nicolas, JC and Emeric, for having shared so many "romantiK" moments together and inspired me day after day. The moments I spent in NYC will also last

as an unforgettable experience and I wish to specially thank Mike, Adrian, and particularly Aude for her contagious energy. I won't forget to broadly thank all my friends who have continuously been by my side, for their continuous encouragement and interest that helped me carry on, and all those little moments that makes a strong whole. Special thoughts go to Laura, Esteban and Paola without whom anything would be as it is today, so many "calle treces, haches intercaladas, loquitos-por-ti, peches, penestines, guayavez, vueltas imposibles, vinitos y trasnochadas" to regret.

For sure, I would also wish to express all my gratitude to my beloved family, from Barcelona to Caen, from the youngest (2!) to the elder (99!) whose unconditional love made this thesis possible.

Finally, and above all, my deepest gratitude and love goes to Carole for her never ending encouragement, support, patience and love during all these years.

Abstract

Throughout its industrial activity, and particularly in the field of structural vibrations, French electricity producer EDF faces dimensioning, monitoring and diagnosis problems. Experimental information is often combined with numerical simulations to complete the *a priori* knowledge of structural behavior needed to address industrial issues. Vibration expertise is thus required in a broad range of fields such as health monitoring, structural modification assessment and boundary conditions identification.

This work aims to find a method to combine experimental and numerical information for model-updating purposes and thus improve their predictive power. More specifically, the problem of structures with evolutionary mechanical properties is addressed. To this end, this thesis proposes a combined use of the Error in Constitutive Relation (ECR) and Kalman filtering (KF) techniques.

In structural dynamics, the ECR is an energy-based approach to solve inverse problems. ECR functionals measure the model error by evaluating the difference between kinematically and dynamically admissible fields using an energy norm. This technique presents interesting features such as good ability to spatially localize erroneously modeled regions, strong robustness in presence of noisy data, and good regularity properties of cost functions. On the other hand, the Kalman filtering techniques are prediction-correction algorithms for recursive system estimation. The Kalman filtering is particularly suitable for studying evolutionary systems embedding noisy data from both model and observation.

The main part of this work is devoted to establish and evaluate a general-purpose identification approach using ECR and KF. In order to achieve this goal, the ECR is initially used to improve the a priori knowledge of model errors. Furthermore, ECR functionals are introduced in a state-space description of the identification problem. Its resolution is performed by means of the Unscented Kalman Filter (UKF), a second-order, reduced-cost, Kalman filter.

The adequacy of the ECR-UKF approach to address problems of industrial relevance is shown through different numerical examples, such as structural time-varying damage assessment of a complex structures, boundary conditions identification of in-operation structures and field reconstruction problems. Moreover, these examples are used to improve the performance of the ECR-UKF algorithm, particularly the introduction of algebraic constraints in the ECR-UKF algorithm and the influence of error covariance matrix design.

Finally, this approach is evaluated in more complex problems such as the identification of boundary impedances from an experimental campaign and the damage assessment in a complex civil structure subjected to seismic loads.

h

Contents

List of Figures

Notations

This section summarizes the conventions and notations used in the sequel. Possible alternate uses of the ensuing definitions are explicitly stated where applicable.

$\mathbb{N}$	Euclidean space of natural numbers
$\mathbb{R}^d$	Euclidean d-space of real numbers
$\mathbb{C}^d$	Euclidean d-space of complex numbers
$\mathbf{M}(\mathbb{K})_{m,n}$	Space of $(m \times n)$ matrices whose entries are in $\mathbb{K}$
Ω	Background elastic or viscoelastic solid
E	Sub-structure of the elastic or viscoelastic solid
δ_{ij}	Kronecker symbol
$\mathbf{I}_n$	Identity matrix of size $n \times n$
$\mathbf{0}_n$	Square zeros matrix of size $n \times n$
$\mathbb{E}[\cdot]$	Expectation operator
E	Young modulus
ν	Poisson's ratio
d	Structural damage
ϱ	Mass density
σ	Stress tensor
ε	Deformation tensor
$\mathcal{C}$	Constitutive law
t	Time variable
ω	Angular frequency
$\tilde{u}$	Vector of measured displacements
$\tilde{f}$	Vector of measured efforts
$[M]$	Finite Element mass matrix
$[C]$	Finite Element damping matrix
$[K]$	Finite Element stiffness matrix
$\{F\}$	Finite Element external forces vector
$\{q\}$	Finite Element nodal displacement vector
Π	Projection operator from the semi-discretized FE space to the observation space
$\bigsqcup$	Global Finite Element matrix assembly operator
X^b	*A priori* or background system state vector

X^a	Analyzed system state vector
$M(\cdot)$	Generic state-transition operator
$H(\cdot)$	Generic observation operator
Q	Covariance matrix of model errors
R	Covariance matrix of observation errors
P^b	Background state error covariance matrix
P^a	Analyzed state error covariance matrix
K	Kalman gain matrix
W	Unscented sigma weighting factor
γ	Unscented sigma point scaling factor
α	Spread controlling parameter in sigma point construction for the Unscented transformation
κ	Secondary parameter in sigma point construction for the Unscented transformation
$[X^b]$	Unscented transformation sigma points around background state vector X^b
$[y^b]$	Observable transformed sigma points through the observation function $H(\cdot)$
$\mathcal{U}$	Space of admissible displacements
$\mathcal{S}$	Space of admissible stresses
u	Kinematically admissible field
v	Dynamically admissible field associated to internal efforts
w	Dynamically admissible field associated to inertial efforts
$\hat{u}$	Optimal kinematically admissible field
$\hat{v}$	Optimal dynamically admissible field associated to internal efforts
$\hat{w}$	Optimal dynamically admissible field associated to inertial efforts
$\xi^2_\omega(\cdot)$	Drucker inequality function at angular frequency ω
$\xi^2_{\omega r}(\cdot)$	Relative Drucker inequality function at angular frequency ω
$[G]_R$	Observation weighting positive-definite matrix of ECR functionals
e^2_ω	Drucker inequality function at angular frequency ω
$\xi^2_{Tr}(\cdot)$	Weighted relative Drucker inequality function for a frequency range of interest
$\eta(\omega)$	Weighting function defined over a frequency range of interest
$\mathcal{T}_\omega$	Triple of best admissible fields
r	Weighting scalar of the ECR functional
$\overline{\xi^2}_{Tr}$	Modified $\xi^2_{Tr}(\cdot)$ function including algebraic constraints
$\mathfrak{E}$	Set of potential incorrectly-modeled regions selected for model updating
θ	Vector of model-updating parameters
$\hat{\theta}$	Optimal vector of model parameters
$\mathcal{Q}$	Stationarity error covariance matrix in the state-space description using ECR functionals
$\mathcal{R}$	Observation error covariance matrix in the state-space description using ECR functionals
ζ	Target value of the state-space description using ECR functionals
ϑ	Scaling factor of state estimation error covariance matrices
Σ	Standard deviations diagonal matrix for the construction of P^b in a decomposotion design
C	Matrix of spatial correlations for the construction of P^b in a decomposotion design
λ_{spatial}	Characteristic spatial correlation length

Introduction and general overview

EDF group is the first European producer of electric energy with a power capacity of 96 GW installed in France in 2010. Electricity production uses thermal combustion (14%), renewable energies (21%) and nuclear fission (65%). Within the framework of its industrial activity, EDF takes a major place not only in the energy generation field but also in all the main activities related to the electrical industry, namely the transmission, distribution and commercial areas.

One of the priorities of the group is to guarantee the safety of the generation plants, without forgetting the industrial need of maintaining high efficiency. In this context, the EDF research division (R&D) plays a major role in the decision-making of the group, acting as a guarantor for the suitability of the long-term strategies but also taking part in the resolution of in-operation issues during exploitation. As a component of EDF R&D, the Mechanics and Acoustics Analysis department (AMA) provides the expertise in the field of structural mechanics through a wide-scope of research activity (rupture, fluid-structure interaction, vibrations, seismic, rotor-dynamic machines, etc.) from both the computational and experimental viewpoints.

This work arises from AMA department's need to improve solution methodologies for inverse problems in structural dynamics.

EDF's industrial need

The AMA department frequently faces dimensioning, monitoring and diagnosis problems, particularly in the field of structural vibrations. In many cases, experimental information is combined with numerical simulations to complete the *a priori* knowledge of structural behavior in an effort to address industrial issues. Expertise in vibrations is required for a broad range of needs such as health monitoring, structural modification assessment or boundary conditions identification.

Consequently, numerical models must be of good quality in order to accurately predict the behavior of analyzed structures. To this end, experimental data is generally used for model-updating or field reconstruction purposes. Up to now, the AMA department has generally relied on least-square's type methods to solve identification problems. Moreover, due to the industrial context when studying in-operation structures, linear Finite Element (FE) models are often employed for the sake of reactivity.

In the present work, we investigate alternative solution methods for the above-mentioned problems

in the particular industrial context of EDF. More specifically, we aim at studying the dynamic behavior of a generic structure whose available linear FE model $\mathcal{M}$ has the well-known form:

$$[M]\{\ddot{q}\}(t) + [C]\{\dot{q}\}(t) + [K]\{q\}(t) = \{F\}(t) \tag{1}$$

where $[M]$, $[C]$ and $[K]$ represent the mass, damping and stiffness matrices respectively, $\{q\}$ is the vector of nodal displacements and $\{F\}$ the vector of external loads. Besides, the FE model is supposed not to be inconsistent with a set of available experimental data $\tilde{u}$ for the same structure, and consequently to embed modeling inaccuracies which are *a priori* unknown.

Hence, the goal of this work is to provide a general method to improve the *a priori* knowledge of the dynamic behavior of a structure from both an inaccurate FE model $\mathcal{M}$ and a set of available experimental data $\tilde{u}$. This general goal is formulated in terms of the following three main objectives:

1. **Identify model inaccuracies and improve the knowledge of the structure's dynamical behavior.**
   The *a priori* model $\mathcal{M}$ is supposed to inaccurately predict the real structure's dynamics and therefore contains model bias. In the present work, we will postulate that such an uncharacterized bias is of a parametrized form $\mathcal{M}(\theta)$ where θ represents a vector of model parameters (e.g. material parameters, boundary conditions, etc.). In other words, the model inaccuracy is assumed to be attributable to incorrectly-known values of a set of model parameters. Thus, with the help of a set of available experimental data $\tilde{u}$, we will seek to both identify the nature of the parameter bias (in terms of spatial location and magnitude) and provide a response field estimation.

2. **Take into account the case of evolutionary mechanical properties.**
   In some industrial cases, mechanical properties may evolve during in-operation conditions. Indeed, in some cases EDF has to deal with situations when, for example, investigating whether power plant structures suffer from structural damage during operation (seismic activity, extreme loads, etc.), or evaluate time-varying parameters of rotor-dynamic machines which are usually a function of the rotational speed. In other cases, structures may suffer from structural modifications (boundaries, etc.) as a consequence of maintenance periods. In this work, we will aim at taking into account the possibility of evolutionary structures in two different configurations:

   Case A The structure evolves between two or more events well-separated in time and we aim to identify and quantify the total change undergone between these two events. Thus, the evolution law is not necessary sought and parameters will be treated as invariant when modeling each event (e.g. case of changing properties due to maintenance operations).

   Case B Structural parameters evolve during the studied event. Consequently, we aim not only to identify parameter overall changes but also to estimate its evolution, which is supposed *a priori* unknown (e.g. case of damage evolution during in-operation conditions).

3. **Investigate and develop methods applicable to industrial analyses.**
   Aside from the industrial relevance of the studied problems, the investigations carried out in this work aim at being capitalized for further use in engineering situations. Thus, all the techniques must be applicable to complex structures within moderate computational cost. For this reason, numerical simulations are carried out within the environment of the public FE software *Code_Aster* (www.code-aster.org) developed by EDF R&D.

Considered methods

The choice of the considered methods directly stands from the three main targets defined above. From a general point of view, one can see that we seek to give the best state and parameter estimation in structural dynamics problems from both a (FEM-based) mathematical model and a set of available experimental data. Moreover, since model $\mathcal{M}(\theta)$ is supposed to contain bias error, its *a priori* predictions are improved and corrected by taking advantage of experimental (noisy) data.

Consequently, this work aims at solving a category of inverse problems where the existence of both model and observation errors need to be taken into account. Inverse problems have been largely studied within the last decades in a wide range of applications. The reader may find a general overview describing general theory and inversion techniques in [80]. More specifically in structural mechanics, a general description of inversion methods can be found in [16, 13] or [91]. Depending on the nature of the inversion problem, specific theories have come to light, for instance the Bayesian approach described in [65] extending the inversion theory to a probabilistic framework.

In this work, Data Assimilation (DA) techniques have been investigated as a way to address inverse problems related to the three above-described main objectives. DA aims at providing optimal state and parameter estimation from the conjunction of uncertain experimental and numerical information. In that sense, model and measurement errors are naturally taken into account, conveniently addressing the first of our targets. Initially introduced in control theory as a method to track model changes in dynamical systems, DA techniques have been widely and successfully used in the past two decades in problems with strong time-varying systems, particularly in the area of geophysics (atmosphere, ocean). DA thus opportunely suits our need of studying evolutionary mechanical properties.

Data Assimilation techniques, however, require good characterization of model and measurement errors (*a priori* error knowledge) to provide proper system estimations. In the problems we want to address, the *a priori* knowledge of modeling errors can be quite poor. We therefore enrich it by means of the Error in the Constitutive Relation (ECR). The ECR belong to the category of inverse problems based on energy functionals and represents an alternative to the classical least-square or reciprocity methods in structural mechanics. In particular, the ECR presents interesting features that we propose to exploit such as the ability to spatially localize model errors or the good (empirically observed) convexity properties of cost functions near local minima.

Overview of the thesis

In light of the above topics and issues, this dissertation is divided into three parts. Part I gives an introduction to Error in Constitutive Relation (ECR) and Data Assimilation (DA) techniques where the formulation details and the interesting features of each approach are developed.

In the second, central, part of this dissertation, a general strategy combining DA and ECR methods is proposed. While the first chapter of part II is devoted to building the proposed method, a second chapter puts the strategy at work on problems of industrial relevance, such as structural damage assessment, boundary conditions mis-modeling or field reconstruction. Finally, a third chapter proposes various improvements of this approach, in particular studying the possibility of introducing constraints in the Unscented Kalman filter framework and the influence of the covariance matrices design.

The third and last part of this thesis is devoted to assessing the capabilities and robustness of the combined approach when applied to industrial complex problems. Two different applications are examined. The first one investigates the use of the ECR as a method to localize and characterize structural damage. It is based in the so-called SMART international research benchmark started in 2007 by EDF and CEA (the French Atomic Energy Commission) aimed at assessing the resistance of civil engineering structures to seismic activity. The second application is devoted to an experimental campaign where a reinforced concrete beam is placed in a testing bench that strongly modifies its dynamic behavior. The combined approach is used to identify initially mis-modeled boundary conditions and improve the FE model representativity.

Part I

Introduction to Error in Constitutive Relation and Data Assimilation methods

Chapter 1

Identification methods and Error in Constitutive Relation

Contents

1.1 Reference Problem

In the general framework of nature's physics, and in particular in solid mechanics, it is often necessary to evaluate or identify physical quantiti es governing a system of interest. In many cases, the sought-after quantities (Young's modulus, damping coefficients, etc.) may not be directly measurable and one has to exploit other, measurable, quantities (accelerations, deformations, etc.) for the purposes of gaining information. The principle of identification methods consists in establishing a mathematical relation based on physical laws, also known as the model, linking both measurable and non-measurable quantities in a way that the sought-after quantities (in some cases referred to as parameters) can be found from the available measurements. Thus, from a mathematical point of view, the solution of such a problem may encounter problems of existence, uniqueness and continuity of the solutions [13]. Hence, identification methods may be considered in the category of inverse problems where, in contrast with the resolution of a direct problem as illustrated in Figure 1.1, the problem of ill-posedness has to be overcome.

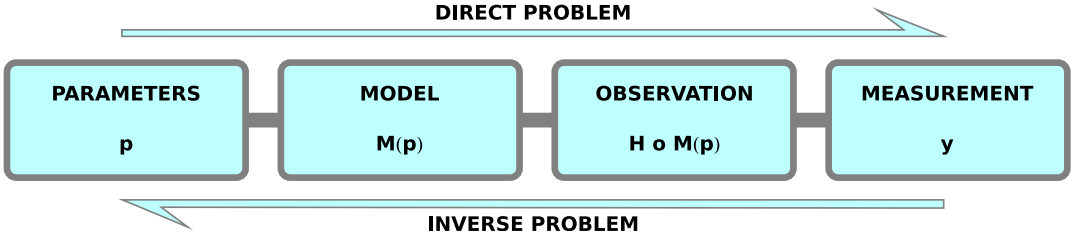

Figure 1.1: *Illustration of a direct problem and its related inverse problem.*

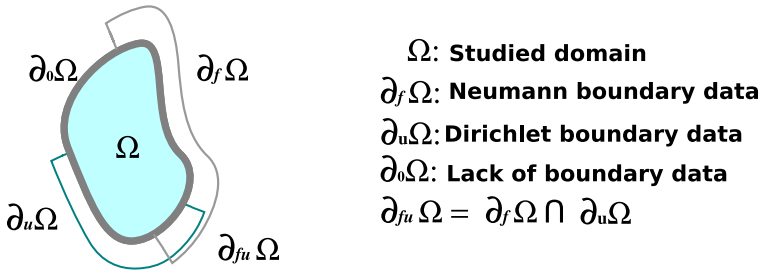

Figure 1.2: *Definition of the studied domain and its boundaries from available data.*

From the mechanical point of view, the reference problem we aim to solve consists of studying the evolution of a structure occupying a volume Ω represented in Figure 1.2 in a time interval $t \in [0, T]$.

The structural behavior is given by the solution of the reference problem defined by:

Find the displacements $u(z,t) \in \mathcal{U}(\bar{u})$ and stresses $\sigma(z,t) \in \mathcal{S}(\bar{f})$ $\forall t \in [0,T], \forall z \in \Omega$ verifying the following relations:

- Equilibrium

$$-\rho\ddot{u}(z,t) + div(\sigma(z,t)) = 0 \tag{1.1}$$

- Constitutive relation

$$\sigma(z,t) = \mathcal{C}(\varepsilon(u(z,t)), \theta) \tag{1.2}$$

where ε is the strain tensor and θ represents a given set of model parameters defining the structural properties (material, geometry, etc.). Moreover, the space of admissible displacements $\mathcal{U}(\bar{u})$ and admissible stresses $\mathcal{S}(\bar{f})$ are defined by:

$$\begin{cases} \mathcal{U}(\bar{u}) = \{u(z,t) \text{ s.r. } |u(z,t) = \bar{u} \quad \text{for} \quad z \in \partial_u\Omega \quad \text{and} \quad u(z,0) = u_0, \dot{u}(z,0) = \dot{u}_0\} \\ \mathcal{S}(\bar{f}) = \{\sigma(z,t) \text{ s.r. } |\sigma(z,t) \cdot n = \bar{f} \text{ for } z \in \partial_f\Omega\} \end{cases} \tag{1.3}$$

where "s.r." denote sufficiently regular functions defined on Ω of bounded strain and kinetic energy for $u(z,t)$ and square-integrable for $\sigma(z,t)$, and n is the normal vector to the surface $\partial\Omega_f$.

The problem is said to be well-posed in the sense of Hadamard [16] if, and only if, the three following conditions are verified:

1. A solution $u(z,t)$ exists $\forall z \in \Omega, \forall t \in [0,T]$ for given $\bar{u}$ and $\bar{f}$.
2. The solution $u(z,t)$ is unique.
3. The solution depends continuously on $\bar{u}$ and $\bar{f}$.

Well-posedness requires in particular $\partial\Omega = \partial_u\Omega \bigcup \partial_f\Omega$ and $\partial_u\Omega \bigcap \partial_f\Omega = \emptyset$ (with reference to Figure 1.2). In this description, the direct problem will be generally ill-posed for at least two reasons:

1. The presence of overdetermined data $\bar{u}$ and $\bar{f}$ in $\partial_{fu}\Omega$ generally leads to the non-existence of the solution, except for the case where $\bar{u}$ and $\bar{f}$ are compatible with the constitutive relation (1.2).

2. The lack of data in a certain region of the boundary $\partial_0\Omega$ can lead to non-uniqueness. This will be particularly the case when $\partial_{fu}\Omega = \emptyset$. In this case, prescribing either force or displacement boundary data on $\partial_0\Omega$ restores well-posedness.

In our case, we will seek to find the set of model parameters θ and the solution field u satisfying the above model equations (1.1) and (1.2) that better represents the available data. Since the available data $\bar{u}$ and $\bar{f}$ might be noisy and overdetermined, and the model equations inaccurate with respect to real physics (domain discretization, material,etc.), the solution of this inverse problem might be in many cases ill-posed in the sense of Hadamard as it may not respect one or more of the above-listed conditions. In the field of solid mechanics, many authors have investigated the identification of model properties from observed data. To give an example, it has been shown in [20, 14] that, in the elastic case, the problem of finding a field of distributed properties $\mathrm{E}(z)$ in the whole space Ω is an ill-posed problem in the sense of Hadamard and the introduction of an *a priori* knowledge that approximates the solution is mandatory.

Several methods exist for solving problems of model properties identification, depending on the nature of the problem (statics, dynamics, available data, etc.). The identification problem generally ends up being formulated as an optimization problem, namely seeking the minimum of a cost function that quantifies in a certain metrics the difference between a model prediction and the available data.

Among the different existing approaches for building suitable cost function, the following families can be distinguished:

- The least-squares approaches [81] where the difference between data and the direct model solution projected onto the observation space is measured with a L^2 norm.
- An approach based on auxiliary fields. In linear mechanics, these approaches exploit the Maxwell-Betti reciprocity theorem and generally cost functions are built upon the overdetermined data over the boundary domain. An interesting example using this approach can be found in [3] for crack detection inside an elastic body.
- An approach consisting on energy-based functionals, and particularly those based in the Error in Constitutive Relation (ECR) for which a detailed description is given later.

On the other hand, the ill-posedness of the identification problem will generally lead to sensitivity or instability of the solutions with respect to noisy data. To overcome this issue, we will distinguish between two classical approaches:

- The widely used Tikhonov regularization techniques ([84], [13]) where an additional term is introduced in the aforementioned cost functions. This term represents an *a priori* knowledge about the sought-after solution and has the property to stabilize the results with respect to noise in data.
- The probabilistic approaches [80, 24, 6] where data and model uncertainties are quantified using a stochastic framework, and a probability density function for the unknown parameters is usually sought.

In the next section, a more in-depth description of ECR-based identification methods is provided. For more information on inverse problems, the reader can find a general overview in [13, 81, 80] and in particular for structural mechanics in [14, 16].

1.2 Energy-based functionals. Introduction to the Error in Constitutive Relation

In the case of the least-squares or the auxiliary fields approaches, the quality of a model is measured by either the distance between the measured data to the solution of the direct problem or the reciprocity gap. On the contrary, the energy-based functionals propose to measure the model error by evaluating the difference between kinematically and statically admissible fields using an energy norm. Finding the best admissible fields itself leads to the resolution of a secondary problem, leading to a two-step inverse solution procedure for the general identification process.

This technique has first been introduced by P. Ladevèze in 1975 as a method to evaluate the quality of the solution of a FE model [55], where the concept of Error in constitutive Relation (ECR) first appeared. Since then, several versions and many applications have been proposed, see for example [57, 60, 70] for model quality assessment or [19, 37, 42, 2, 67, 26] for model updating and identification problems.

The background idea of Error in Constitutive Relation can be introduced from two different points of view:

- A first approach valid for Generalized Standard Materials (GSM) [43]. For such materials, the constitutive equations are described from the expressions of the energy potential and the dissipation potential. The difference between two admissible states associated with both force and displacement boundary conditions are characterized by the residual:

$$e(\varepsilon, \sigma) = \phi(\sigma) + \phi^*(\varepsilon) - \sigma : \varepsilon \tag{1.4}$$

  where ϕ^* is the potential defined by the Legendre-Fenchel transformation of ϕ. In the case of elasticity, those potentials are defined by:

$$\phi(\sigma) = \frac{1}{2}\sigma^T K^{-1}\sigma, \quad \phi^*(\varepsilon) = \frac{1}{2}\varepsilon^T K\varepsilon \tag{1.5}$$

  where K is the Hooke tensor. This error is positive-definite and vanishes when the admissible states are compatible with the constitutive relation. Thus, it can be used as a measure to build ECR functionals.
- The second point of view comes from the principle of stability in the sense of Drucker which, for a given structure, stipulates that for any couple of evolution states (considering the same initial state) the following inequality stands:

$$\int_0^T \int_\Omega (\sigma_2 - \sigma_1) : (\varepsilon_2 - \varepsilon_1) dz dt \geq 0 \qquad \forall t \in [0, T], \quad \forall z \in \Omega \tag{1.6}$$

  It can be shown that the Drucker error vanishes for the case where the two couples (σ_1, ϵ_1) and (σ_2, ϵ_2) are compatible with both the history of boundary conditions and the constitutive relation, the Drucker error being positive otherwise. Within the small perturbations principle, the response

of a given structure is unique for all evolution coming from the same boundary condition history. This uniqueness property is verified in most of the constitutive relations such as elasticity, plasticity, viscoelasticity, etc. except from some singular cases (damage laws). Indeed, the integration of the virtual work equations for a given structure gives:

$$\int_0^T \int_\Omega (\sigma_2 - \sigma_1) : (\varepsilon_2 - \varepsilon_1) dz dt + \int_0^T \int_\Omega \frac{1}{2} \rho (\dot{u}_1 - \dot{u}_2)^2 dz dt = 0 \tag{1.7}$$

and considering the Drucker inequality (1.6) one can easily obtain:

$$\int_\Omega \frac{1}{2} \rho (\dot{u}_1 - \dot{u}_2)^2 dz dt \leq 0 \qquad \forall t \in [0, T], \quad \forall z \in \Omega \tag{1.8}$$

Hence, it is clear that for a given structure $\dot{u}_1$ and $\dot{u}_2$ are necessarily the same for all $t \in [0, T]$ as the two evolutions have the same initial condition. Thus, deriving this expression, the history of deformations must be identical and so has to be the history of constrains from the constitutive relation law. This hypothesis has therefore been exploited to define a residual indicator based in the Drucker inequality as a measure of the compatibility of the constitutive relation of a structure with respect to the boundary conditions.

Since the introduction of such a concept, several studies have successfully applied this principle to different applications such as model verification [58] and model updating problems [56, 59], under linear or nonlinear conditions [10, 19], either in the frequency domain [27] or the time domain [36, 37]. Consequently, the constitutive relation appears to be an appropriate indicator of the quality of a model with respect to measured data history and some particularly good properties deserve to be highlighted:

- Excellent ability to locate erroneously modeled regions in space. Indeed, in [10] it is demonstrated that regions where the ECR density is high correspond to those which contain the most erroneous constitutive relations.
- Strong robustness in presence of noisy data [37].
- Good convexity properties of cost functions [42].

In the following, classical formulations of the ECR are reviewed for the static and the dynamic cases. Moreover, a frequency domain formulation is presented with a special interest for the case of a FE framework.

Classic formulation. The static case.

In the field of static elasticity, the ECR can be formulated in one of its most classical forms. Consider the case where $\partial_0 \Omega = \emptyset$ and $\partial_{uf} \Omega \neq \emptyset$. Thus, the elasticity tensor $\mathcal{C}$ that better represents the available data $\bar{u}$ and $\bar{f}$ is sought by solving the following minimization problem:

Find the kinematic admissible field $u_{KA} \in \mathcal{U}(\bar{u})$, the static admissible field $\sigma_{SA} \in \mathcal{S}(\bar{f})$, and the constitutive relation $\mathcal{C}$ that minimize:

$$J(u_{KA}, \sigma_{SA}, \mathcal{C}) = \int_\Omega (\sigma_{SA} - \mathcal{C} : \varepsilon(u_{KA})) : \mathcal{C}^{-1} : (\sigma_{SA} - \mathcal{C} : \varepsilon(u_{KA}))d\Omega \tag{1.9}$$

where the admissible spaces are defined by:
$\begin{cases} \mathcal{U}(\bar{u}) = \{u(z) \text{ s.r. } |u(z) = \bar{u} \quad \text{for} \quad z \in \partial_u\Omega\} \\ \mathcal{S}(\bar{f}) = \{\sigma(z) \text{ s.r. } |\sigma(z) \cdot n = \bar{f} \text{ for } z \in \partial_f\Omega, div(\sigma(z)) = 0 \text{ for } z \in \Omega\} \end{cases}$

In this static case, it can be shown that the solution fields u_{KA} and σ_{SA} are uncoupled. In practice, this means that both fields can be computed separately as a Neumann and a Dirichlet problem respectively.

Modified formulation. The dynamic case.

In the case of elastodynamics, nevertheless, it has been proved in [36, 2] that the resolution of an ECR introduces an additional issue since the kinematic and dynamically admissible fields are coupled not only by the constitutive relation (1.2) but also by the equilibrium equation (1.1). In addition, a regularization technique is introduced to deal with the presence of noisy measurements. In this context, a modified approach has been proposed by Feissel and Allix in [36]. In their investigations, they considered the case with $\partial_0\Omega = \emptyset$ and $\partial_f\Omega = \partial_u\Omega = \partial_{fu}\Omega$. Their formulation of the ECR problem is summarized below:

Find the kinematic admissible field $u_{KA} \in \mathcal{U}(u_b)$, the dynamic admissible field $\sigma_{DA} \in \mathcal{S}(f_b, u)$, and the constitutive relation $\mathcal{C}$ that minimize:

$$\begin{aligned} J(u_{KA}, \sigma_{DA}, \mathcal{C}) = &\int_0^T \int_\Omega (\sigma_{DA} - \mathcal{C} : \varepsilon(u_{KA})) : \mathcal{C}^{-1} : (\sigma_{DA} - \mathcal{C} : \varepsilon(u_{KA}))d\Omega dt \\ &+ \int_0^T \left(\int_{\partial_u\Omega} d_u(u_b, \bar{u})dS + \int_{\partial_f\Omega} d_f(f_b, \bar{f})dS \right) dt \end{aligned} \tag{1.10}$$

where the admissible spaces are defined by:
$\begin{cases} \mathcal{U}(u_b) = \{u(z,t) \text{ s.r. } |u(z,t) = u_b \quad \text{for} \quad z \in \partial_u\Omega, \quad u(z,0) = u_0, \dot{u}(z,0) = \dot{u}_0\} \\ \mathcal{S}(f_b, u) = \{\sigma(z,t) \text{ s.r. } |\sigma(z,t) \cdot n = f_b \text{ for } z \in \partial_f\Omega, \quad -\rho\ddot{u}(z,t) + div(\sigma(z,t)) = 0 \text{ for } z \in \Omega\} \end{cases}$

where the terms d_u and d_f represent a discrepancy measure to be defined (usually based on the L^2 norm, e.g. $d_u(v, w) = \|v - w\|^2$)).

In all the cases, the ECR approach relies upon distinguishing between two sets of relations: reliable and unreliable. The latter will therefore be relaxed by simply introducing them in the ECR functional and finding a solution that best fulfills them. In the case of elastodynamics defined in (1.10) the following sets of relations can be introduced:

- Reliable relations:

$$\begin{cases} -\rho\ddot{u} + div(\sigma) = 0 \\ u(z,0) = u_0 \\ \dot{u}(z,0) = \dot{u}_0 \end{cases} \tag{1.11}$$

- Unreliable relations and quantities:

$$\begin{cases} \sigma = C\varepsilon \\ \bar{u} \\ \bar{f} \end{cases} \tag{1.12}$$

An interesting work by Feissel, Allix and Nguyen in [37, 67] has recently shown that in the identification process by means of ECR functionals, the obtainment of admissible fields u_{KA} and σ_{DA} and the correction of the constitutive relation $\mathcal{C}$ are two well-separated steps and therefore one can use different functionals to solve each problem. In particular in one of the examples the identification problem is defined as follows:

Given a constitutive relation $\mathcal{C}$, find the fields $\sigma_{DA} \in \mathcal{S}(f_b, u)$, $u_{KA} \in \mathcal{U}(u_b)$ minimizing

$$\begin{aligned} J(u_{KA}, \sigma_{DA}, \mathcal{C}) = &\int_0^T \int_\Omega (\sigma_{DA} - \mathcal{C} : \varepsilon(u_{KA})) : \mathcal{C}^{-1} : (\sigma_{DA} - \mathcal{C} : \varepsilon(u_{KA})) d\Omega dt \\ &+ \int_0^T \left(\int_{\partial_u \Omega} d_u(u_b, \bar{u}) dS + \int_{\partial_f \Omega} d_f(f_b, \bar{f}) dS \right) dt \end{aligned} \tag{1.13}$$

where $\mathcal{S}(f_b, u)$ and $\mathcal{U}(u_b)$ are defined in (1.10) and the functional used to measure the discrepancy on the constitutive relation is

$$G(u_{KA}, \sigma_{DA}, \mathcal{C}) = \int_0^T \int_\Omega (\sigma_{DA} - \mathcal{C} : \varepsilon(u_{KA})) : \mathcal{C}^{-1} : (\sigma_{DA} - \mathcal{C} : \varepsilon(u_{KA})) d\Omega dt \tag{1.14}$$

This approach has been tested with satisfying results in a 1-D case where the Young's modulus is sought and the measurement noise reached 60%. Experiments were realized for both homogeneous and heterogeneous moduli. In all the cases, the ECR approach presented excellent properties of robustness against noisy data as well as good convexity properties of cost functions. However, the research performed in [36] and [67] clearly pinpointed one of the major limitations of this method: its computational cost when solving the minimization problem. As a matter of fact, the resolution of the ECR problem in elastodynamics leads to a large system of space-time equations where the admissible fields are coupled to the solution of a time-backwards adjoint problem. Hence the application of such a formulation for an industrial size problem is still an area of open research. In the following we will use the frequency domain formulation which is presented below.

Frequency-domain formulation. Application to a FE formulation.

In the scope of the present work and with the aim to avoid prohibitive computational costs that would prevent the use of the ECR in industrial cases, a frequency-domain formulation will be adopted from now

on. This derivation of the ECR was studied by [19] in a FE framework and further adopted by [26, 27] to a high DOF case. Thus, this version of the ECR is the most suitable when dealing with linear FE models of industrial size.

To fix the ideas, consider the above equations (1.1) and (1.2) and assume that the sought-after solutions are of the form:

$$\Re(u_\omega(z)e^{i\omega t}), \quad \Re(\sigma_\omega(z)e^{i\omega t}) \tag{1.15}$$

where $\Re(\cdot)$ represents the real part of a complex number and ω is the angular frequency. Then, equation (1.1) can be rewritten as:

$$-\rho\omega^2 u_\omega(z) + div(\sigma_\omega(z)) = 0 \tag{1.16}$$

When it comes to the constitutive relation, the following expressions are considered:

$$\begin{cases} \sigma_\omega(z) = (K + i\omega C)\epsilon(u_\omega(z)) \\ \Gamma_\omega(z) = -\rho\omega^2 u_\omega(z) \end{cases} \tag{1.17}$$

where Γ_ω represents the inertial forces, and K and C are respectively the Hooke and damping tensors. From the above equations (1.17), the following spaces are defined:

$$\begin{cases} \mathcal{U}(\bar{u}) = \{u_\omega(z) \text{ s.r. } |u_\omega(z) = \bar{u} \quad \text{for} \quad z \in \partial_u\Omega\} \\ \mathcal{S}(\bar{f}) = \{\sigma_\omega(z) \text{ s.r. } |\sigma_\omega(z) = (K + i\omega C)\epsilon(v_\omega(z)), \quad \sigma(z)\cdot n = \bar{f} \quad \text{for} \quad z \in \partial_f\Omega\} \\ \mathcal{D}(\sigma) = \{\Gamma_\omega(z) \text{ s.r. } |\Gamma_\omega(z) = -\rho\omega^2 w_\omega(z), \quad \Gamma_\omega(z) + div(\sigma_\omega(z)) = 0 \quad \text{for} \quad z \in \Omega\} \end{cases} \tag{1.18}$$

where $u_\omega(z)$, $v_\omega(z)$ and $w_\omega(z)$ are displacement fields and in the sequel will be denoted u, v and w respectively for the sake of clarity. Thus, the Drucker inequality (1.6) can be rewritten, for a given angular frequency ω, by considering a triple of displacement fields only, as:

$$\begin{aligned} \xi_\omega^2(u,v,w) = \int_\Omega \{ & \frac{\gamma}{2}\text{Trace}[(K + T\omega^2 C)(\epsilon(v) - \epsilon(u))^*(\epsilon(v) - \epsilon(u))] \\ & + \frac{1-\gamma}{2}\rho\omega^2(u-w)^*(u-w)\}\text{d}\Omega \end{aligned} \tag{1.19}$$

where $\gamma \in [0,1]$ is a weighting scalar indicating the relative quality of the constitutive relations (1.17) and the superscript "*" represents the complex conjugate. Hence, from the above definition (1.18) of admissible spaces we will refer to u as a kinematically admissible field, v as a dynamically admissible field related to the K and C tensors and w as a dynamically admissible field related to inertial forces.

Since the expression of the Drucker error has been defined for the frequency domain, the following expressions can be developed in order to be applied for the study of real structures.

A relative structural error can be defined as:

$$\xi_{\omega r}^2 = \frac{\xi_\omega^2}{D_\omega^2} \tag{1.20}$$

where D_ω^2 represents the reference structural energy defined by:

$$D_\omega^2 = \int_\Omega (\frac{\gamma}{2}\text{Trace}[(K + T\omega^2 C)\epsilon(u)^*\epsilon(u)] + \frac{1-\gamma}{2}\rho\omega^2 u^* u)\text{d}\Omega \tag{1.21}$$

Besides, if we are interested in studying the influence of different regions of Ω to the global error, we might consider a subdivision of sub-domains $E \in \mathbf{E}$ of Ω in a way that $\Omega = \bigcup_{i=1}^{n_E} E_i$. Thus, the global error can be interpreted as the contribution of all the local errors and we obtain:

$$\xi_{\omega r}^2 = \sum_{E \in \Omega} \xi_{\omega E r}^2 \tag{1.22}$$

Moreover, when studying the behavior of a structure in the frequency domain, it is natural to be interested in its behavior in a bandwidth of interest $[\omega_{min}, \omega_{max}]$ of angular frequencies. Thus, we can define the bandwidth relative error as:

$$\xi_{Tr}^2 = \int_{\omega_{min}}^{\omega_{max}} \eta(\omega) \xi_{\omega r}^2 \mathrm{d}\omega \tag{1.23}$$

where $\eta(\omega)$ is a weighting function defined over $[\omega_{min}, \omega_{max}]$ satisfying the following condition:

$$\int_{\omega_{min}}^{\omega_{max}} \eta(\omega) \mathrm{d}\omega = 1 \qquad \eta(\omega) \geq 0 \tag{1.24}$$

In most of the industrial and application cases, and in the particular scope of interest of this work, the study of structural dynamic behavior is performed by means of Finite Element models. In order to adopt the above error expressions in a FE framework, the discretization of equation (1.16) leads to the following matrix equation:

$$[-\omega^2[M] + j\omega[C] + [K]]\{q\} = \{F\} \tag{1.25}$$

where $[M], [C]$ and $[K]$ are the so-called mass, damping and stiffness matrices respectively. Moreover, $\{F\}$ and $\{q\}$ are the vectors of nodal forces and displacements. Within this framework, the following considerations will be made with regard to the inverse problem we aim to solve:

- $\partial_0 \Omega = \emptyset$
- The prescribed loading $\bar{f}$ over $\partial_f \Omega$ is considered as a reliable information (e.g. external loadings, free surfaces, etc.) and directly embedded in $\{F\}$.
- A set of unreliable displacement data $\tilde{u}$ (e.g. sensor measurement on a free surface) is available over $\partial_{fu} \Omega$.
- Displacement data $\bar{u}$ are restricted to the boundary $\partial_{u \setminus f} \Omega = \partial_u \Omega - \partial_{fu} \Omega$ and considered as a reliable information (e.g. clampings). This reliable kinematic information is generally enforced in the construction of model matrices by either introducing Lagrange multipliers or by considering matrices with active DOFs only, which is the solution adopted in the sequel.

Hence, the above FE matrix equation (1.25) and the Drucker inequality (1.19) leads to the following expression of the modified Error in Constitutive Relation in a FE framework:

Find the kinematic admissible field $u \in \mathcal{U}(\Pi, \bar{u})$, and the dynamic admissible fields $(v, w) \in \mathcal{D}(\{F\}, \bar{u})$ minimizing:

$$e_\omega^2(\{u\},\{v\},\{w\}) = \frac{\gamma}{2}\{u-v\}^*[K+T\omega^2 C]\{u-v\} + \frac{1-\gamma}{2}\{u-w\}^*\omega^2[M]\{u-w\} + \frac{r}{1-r}\{\Pi u - \tilde{u}\}^*[G_R]\{\Pi u - \tilde{u}\} \tag{1.26}$$

where the admissible spaces are defined by:

$$\begin{cases} \mathcal{U}(\Pi,\bar{u}) = \{\ \{u\} \text{ s.r. } | \sum_{i=1}^N u_i\varphi_i(z) = \bar{u} \text{ for } z \in \partial_{u\setminus f}\Omega,\ u(z) = \Pi\{u\} \text{ for } z \in \partial_{fu}\Omega\} \\ \mathcal{D}(\{F\},\bar{u}) = \{\ \{w\},\{v\} \text{ s.r. } | \sum_{i=1}^N v_i\varphi_i(z) = \sum_{i=1}^N w_i\varphi_i(z) = \bar{u} \quad \text{for} \quad z \in \partial_{u\setminus f}\Omega, \\ \qquad [K+i\omega C]\{v\} - \omega^2[M]\{w\} = \{F\}\ \} \end{cases}$$

where $(\varphi_1, \ldots, \varphi_N)$ are the basis functions, r is a weighting scalar, Π a projection operator from the space of structural nodal displacements to the observation space and $[G_R]$ represents a symmetric positive-definite matrix. Notice that, in this formulation, unreliable displacements $\tilde{u}$ are introduced as an additional term in the ECR functional (1.26). As described for the dynamic formulation in time domain, this consists of the modified formulation and corresponds to the regularization term stabilizing the solutions in case of noisy data (e.g. experimental measurements). Moreover, although the choice of matrix $[G_R]$ is not *a priori* defined it is usually chosen to be dimensionally consistent with the induced energy norm as proposed in [26, 27]. In our case the following choice is made:

$$[G_R] = \frac{\gamma}{2}[[K_R] + T\omega^2[C_R]] + \frac{1-\gamma}{2}\omega^2[M_R] \tag{1.27}$$

where the index "R" represents the Guyan reduction on the observation space.

Hence, in order to evaluate the discrepancy of a FE model with respect to a set of measurements, a two step method is adopted:

1. Given a set of model parameters θ that parametrize $[M] = [M(\theta)], [C] = [C(\theta)], [K] = [K(\theta)]$, obtain the triple of admissible fields $\mathcal{T}_\omega = (\hat{u}, \hat{v}, \hat{w})$ that minimizes (1.26). This minimization problem leads to the resolution of linear equations as developed in Appendix B.
2. Evaluate the model error by computing $e_\omega^2(\mathcal{T}_\omega, \theta)$, or its relative form $\frac{e_\omega^2(\mathcal{T}_\omega,\theta)}{D_\omega^2(\hat{u},\theta)}$

In the present work, we aim not only at studying model errors in a bandwidth of frequencies, but also at monitoring their spatial distribution over Ω. For these reasons, from now on, the following expression is adopted to evaluate the total model error:

$$\xi_{Tr}^2 = \int_{\omega_{min}}^{\omega_{max}} \eta(\omega) \left(\sum_{E\in\Omega} \frac{e_{E\omega}^2(\mathcal{T}_\omega,\theta)}{D_\omega^2(\hat{u},\theta)} \right) \mathrm{d}\omega \tag{1.28}$$

Thus, since the triple of admissible fields solution of (1.26) depends on θ ($\mathcal{T}_\omega = \mathcal{T}_\omega(\theta)$), the problem of finding the best set of model parameters θ that better represents the noisy data $\bar{u}$ can be written as:

$$\hat{\theta} = \arg\min_{\theta\in\Theta} \xi_{Tr}^2(\theta) \tag{1.29}$$

where Θ is the space of admissible parameters.

The well-behaved nature of functional (1.28) with respect to θ is one of the main features that we aim to take advantage of in this work. A visual example is presented in Figure 1.3, where a ξ^2_{Tr} functional is evaluated in a 4-DOF dynamic system for different values of stiffness (k) and mass (m) as described in Figure 1.3(a), where all displacements are supposed to be observed and the external load is supposed to contain a single frequency. This surface is compared to the one obtained with a least square functional of the form $\|\tilde{u} - \Pi q_{\text{direct}}\|^2$, where q_{direct} represents the solution of the associated direct problem. As it can be seen in Figure 1.3(b) and Figure 1.3(c), the ECR functional exhibits a clear minimum while the least square surface presents several local minima and peaks.

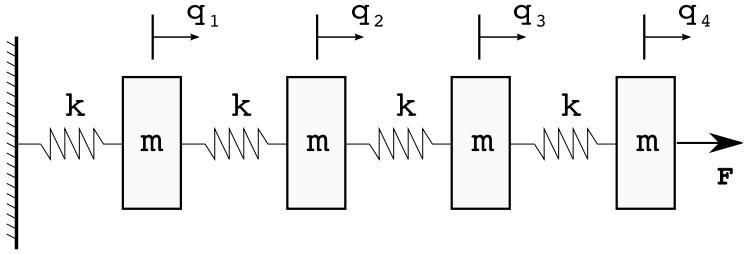

(a) 4-DOF system definition

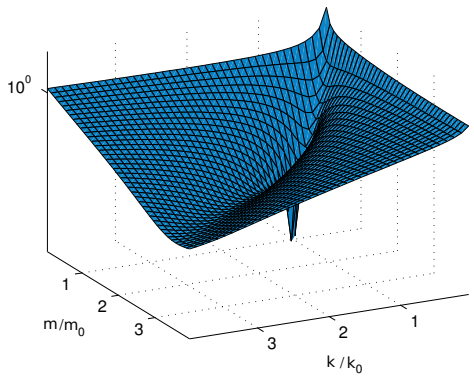

(b) ERC functional (ξ^2_{Tr})

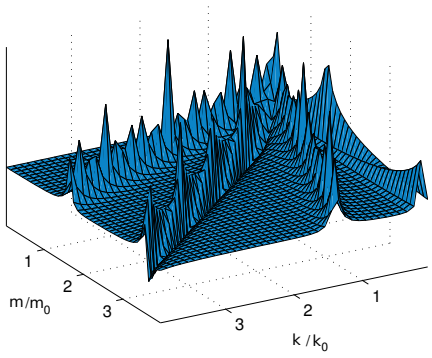

(c) Least squares functional $\|\tilde{u} - \Pi q_{\text{direct}}\|$

Figure 1.3: *Comparison between ECR and least squares functionals convexity for a 4-DOF dynamic system varying stiffness (k) and mass (m) parameters.*

To conclude with the frequency-domain FE formulation of the ECR, it is important to point out some of its main features that make them particularly interesting for our usage:

- Model data is introduced in this ECR version on the basis of $[M], [C]$ and $[K]$ matrices. Those objects are classically used in FE software, which facilitates the manipulation of ECR concepts.
- The adopted ECR formulation is based on displacement fields only. Again, this feature facilitates

its integration in FE software. The computation of $e^2_{E\omega}$ and D^2_ω is a straightforward calculation of elementary and/or global energies.

- Large-DOF models can be studied either by using convenient sparse matrix operators or by implementing model reduction techniques as proposed in [27].
- Obtaining the triple of admissible fields $\mathcal{T}_\omega$ does not require the computation of the adjoint solution (as required in the time-domain formulation) which in some cases can be a difficult task to perform within the classical FE software functions.

1.3 Conclusions

In this chapter, the general concepts of the Error in Constitutive Relation have been introduced as a suitable basis for identification problems in structural mechanics. The ECR approach is a measure of the discrepancy of admissible fields which can be derived from either the Drucker error or the Legendre-Fenchel error. Here, classical and modified formalisms are presented and, in particular, the adequacy of the FE frequency-domain formulation to industrial contexts is highlighted.

As a matter of fact, ECR-based approaches present specific features that make them particularly attractive when dealing with an identification problem in structural mechanics: good convexity of cost functionals, ability to localize model errors in space, and robustness in the presence of of noisy data. For these reasons, they are adopted in this work as a tool to both enhance the *a priori* model error knowledge and alleviate the stability problems when performing parameter identification with Kalman filtering (KF), which are presented in the next chapter. Combining Kalman filtering and ECR make up the core of this work and is further developed and studied in part II.

Chapter 2

Data Assimilation

Contents

2.1 Introduction

The main purpose of data assimilation (DA) techniques consists of providing a system state estimation from all the available information obtained from both numerical simulation and physical observations of all kinds. Thus, the final aim of all DA techniques is to provide optimal past, present and, most importantly, future state estimations. To do so , many different techniques exist to enrich the system's theoretical knowledge (also referred to as the *a priori* knowledge) with the help of available observations.

The origins of data assimilation go back to the 1940 decade when Norbert Wiener showed a growing interest to build optimal predictors for stationary time series [89], proposing a first application in the ballistics domain during the Second World War. The Wiener predictors were somehow reviewed during the 1960's by Rudolph E. Kálmán to extend the formalism to non-stationary time series, giving birth to the celebrated Kalman Filter (KF) [53].

Since its origins, data assimilation techniques have seen a vast and still growing number of applications, providing a theoretical framework for addressing problems of very diverse nature, such as avionics and spaceship control, medical imaging, neutron transport, optimal interpolation, system identification, etc. Data assimilation can therefore be considered as an approach for solving inverse problems.

Nowadays, DA is widely employed in the domain of external geophysics (weather forecast, oceanography, etc.) for the purpose of reconstructing the initial state of chaotic systems (Lorenz, atmosphere,

etc.) for whom the quality of the initial state guess crucially affects the reliability of future predictions. The reader can refer to [66, 68, 69] for some illustrative examples.

In addition to the aforementioned usage of data assimilation techniques, numerous research has been done towards solving various parameter identification problems. In the field of structural mechanics, one of the first works (Hoshiya et al. [47, 48]) employed a Kalman filter approach for structural identification purposes in a FE framework. More recently, many other works have proposed a sequential approach based on Kalman filtering to perform parameter identification, see for example a cohesive crack model identification proposed by Bolzon et al. in [12], or a Kalman filter based strategy for linear structural system identification in [85]. In parallel, despite the increasing success of Kalman filter methods in structural mechanics, many other studies began to highlight some of its limitations, as studied by Corigliano et al. in [23, 22, 21] concerning problems of divergence of the method in a nonlinear identification framework. Besides, other contributions like [64] and [61] point to some other difficulties related to the stabilization of the estimates or the problem of dealing with high DOF models, with different strategies adopted to improve their performances.

In this chapter, an introduction to data assimilation concepts is presented. We will first introduce the basic ideas of the two main families of data assimilation techniques, i.e. the variational and the sequential approaches. Furthermore, an application example will illustrate the adequacy of the sequential approach to the problem of time variant structural identification. For more details, the reader may refer to [11] for a general overview on data assimilation techniques, and [40, 44, 75, 41, 76] for deeper and specific considerations on the use of Kalman filter.

2.2 Concepts and classic notation in data assimilation

In this section we introduce the essential concepts of DA techniques and the notations that are generally used. For this, a causal system governed by a finite number of state variables is considered. The evolution of such a system is studied within a time interval $t \in [0, T]$, where a finite number N of observations are available at a discrete time instants $t_k = [t_0, t_1, ..., t_{N-1}]$. Thus, the purpose of data assimilation is to provide a best estimator of system states over time.

Moreover, the system is represented by the following discrete stochastic equations:

$$\begin{cases} X_{k+1} = M_k(X_k, w_k) \\ \tilde{u}_k = H_k(X_k, v_k) \end{cases} \tag{2.1}$$

where at time $t = t_k$, $X_k \in \mathbb{R}^n$ and $\tilde{u}_k \in \mathbb{R}^m$ represent the vector of states and the vector of observations respectively. Also, $M_k(\cdot)$ is the so-called transition operator while $H_k(\cdot)$ represents an observation function establishing the relationship between the internal state and observable variables. Finally, w_k and v_k are stochastic process modeling the error noise in state and observation equations.

Both noises are assumed to be unbiased and therefore satisfy the following conditions:

$$\begin{cases} \mathbb{E}[w_k] = 0 \\ \mathbb{E}[w_k w_l^T] = Q_k \delta_{kl} \end{cases} \tag{2.2}$$

$$\begin{cases} \mathbb{E}[v_k] = 0 \\ \mathbb{E}[v_k v_l^T] = R_k \delta_{kl} \end{cases} \tag{2.3}$$

where Q_k and R_k are the so-called model and observation error covariance matrices respectively. In general, for the sake of simplicity, errors are assumed to be additive and, what is more, the hypothesis of Gaussian stochastic process is made. Notice that although the unbiased character of w_k and v_k might seem restrictive, an *a priori* unknown system bias can be introduced in $M_k(\cdot)$ and $H_k(\cdot)$ without any loss of generality.

All data assimilation methods aim at finding the best estimation of the true state X_k^{true} at each time instant $t_k = [t_0, t_1, ..., t_{N-1}]$. The result of such an estimation is a vector X_k^a of the same dimension as X_k^{true}, generally referred to as the analyzed state. In some cases, the vector X_k^a is referred to as the best estimate and can also be written as $\hat{X}_k$. In many cases, the estimated state X_k^a is used to predict the system state at time $t = t_{k+1}$ by means of $M_k(\cdot)$. Thus, the obtained state is referred to as the *a priori* state estimation and is generally denoted X_{k+1}^b, where the superscript b stands for "background". Since the vector of states is assumed to obey a stochastic process, each quantity is consequently associated with an error covariance matrix:

$$X_k^b \quad \longmapsto \quad P_k^b, \qquad X_k^a \quad \longmapsto \quad P_k^a \tag{2.4}$$

generally referred to as the background and analysis error covariance matrices.

2.3 Sequential and variational formalisms: Kalman filter and 4D-Var

In this section the two main families of data assimilation techniques are presented. All of them can be interpreted as a natural extension of the well-known Best Linear Unbiased Estimator (BLUE) which is described in detail in Appendix A. However, for the sake of clarity the background ideas are summarized herein.

Consider a time-independent linear problem where both an *a priori* state estimation $\{X^b, P^b\}$ and a vector of observations $\tilde{u}$ with its associated measurement error covariance matrix R are available. Thus, the best linear unbiased estimation is given by the expressions:

$$\begin{cases} X^a = X^b + K(\tilde{u} - HX^b) \\ P^a = (I - KH)P^b \end{cases} \tag{2.5}$$

where H is the related linear observation operator and K, the so-called gain matrix, is given by the expression:

$$K = P^b H^T (R + HP^b H^T)^{-1} \tag{2.6}$$

The above equations are obtained by seeking an unbiased estimator that minimizes the committed scalar error measure (Trace(P^a)).

Within the BLUE formalism, one can traditionally distinguish two main families in data assimilation techniques: the sequential methods, based on the stochastic estimation theory where the most widely used approach is the Kalman filter ([44], [40], [75]) and, on the other hand, the variational methods based on control theory, whose most representative form is the 4D-Var ([11]).

For the sake of clarity, it is important to point out that the main difference between both the 4D-Var and the Kalman filter with respect to the BLUE is that the former incorporate the possibility of a time-variant system, evolving in a period of time $t \in [0, T]$ for which a state estimation is sought for a finite sequence of instants $t_k = [t_0, t_1, ..., t_{N-1}]$. For this, a so-called Markov model $M_k(\cdot)$ is required as defined in equation (2.1).

2.3.1 Variational formalism: 4D-Var

In the interest of extending the stochastic interpolation principle to a general nonlinear time-dependent case, the BLUE formalism has been adapted into a variational approach whose most accomplished form is the 4D-Var. This formalism, broadly used in the field of Numerical Weather Prediction (NWP), proposes to find the sequence of optimal states estimations as the solution of a global error optimization problem, resulting in an incremental four-dimensional variational problem.

To introduce this formalism, let's consider a state vector $X = [X_0, X_1, X_2, ..., X_{N-1}]$ being the assembly of N state vectors at instants $t_k = [t_0, t_1, t_2, ..., t_{N-1}]$. Thus, the 4D-Var seeks to solve the following optimization problem:

Find the optimal state $\hat{X} = [\hat{X}_0, \dots, \hat{X}_{N-1}]$ that minimizes:

$$J(X) = (X_0 - X_0^b)^T (P_0^b)^{-1} (X_0 - X_0^b) + \sum_{k=0}^{N-1} (\tilde{u}_k - H_k X_k)^T (R_k)^{-1} (\tilde{u}_k - H_k X_k) \tag{2.7}$$

subjected to:
$X_{k+1} = M_k(X_k), \quad \forall k \in [0, N-1], \quad k \in \mathbb{N}$

The first approach to solve the above constrained optimization problem simply consists of introducing Lagrange multipliers Λ_k^T and formulating the optimality conditions verified by the Lagrangian:

$$L(X, \Lambda) = J(X) + \sum_{k=0}^{N-1} \Lambda_k^T (X_{k+1} - M_k(X_k)) \tag{2.8}$$

However, in the very frequent case of discrete models, a reasoning consisting in expressing the functional $J(X)$ of N variables in terms of the initial state X_0 only, which transforms the original problem (2.7) into the unconstrained optimization of $\tilde{J}(X_0) := J(X)$. This can be done by simply writing the dependence of all state variables X_k on X_0 as:

$$X_k = M_{k-1}(\dots(M_1(M_0(X_0))) \tag{2.9}$$

or, for the linear case:

$$X_k = \left(\prod_{i=0}^{k-1} M_i \right) X_0 \tag{2.10}$$

Without getting into the details, the solution of such a problem is obtained by solving for X_0 the optimality condition:

$$\nabla \tilde{J} = 0 \tag{2.11}$$

Therefore, the solution can be obtained by:

$$X_0^a = X_0^b - \mathcal{H}_{0,N}^{-1} \nabla \tilde{J}(X_0^b) \tag{2.12}$$

where $\mathcal{H}_{0,N}^{-1}$ represents the inverse Hessian of $J(\cdot)$ for a data assimilation window $[t_0, \ldots, t_N]$. Hence, the data assimilation problem under the 4D-Var formalism consists in finding the initial state estimation X_0 that best fits a set of measurements within a time window.

Independent of the chosen method for solving the initial constrained optimization problem (i.e. using the Lagrange multipliers Λ_k^T or calculating $\mathcal{H}_{0,N}^{-1}$ and $\nabla \tilde{J}$), the solution of such a problem requires the introduction of adjoint variables and, consequently, the construction of adjoint operators $M_k^T(\cdot)$. Although numerically well defined, the *adjointization* might lead to technical problems, in particular for high DOF complex systems solved with public or commercial simulation software. However, although alternative techniques such as "Nudging" [8] exist to avoid the construction of adjoint operators, they are still an area of open research.

In Figure 2.1, a representation of a 4D-Var data assimilation process is presented for a small sequence of time intervals.

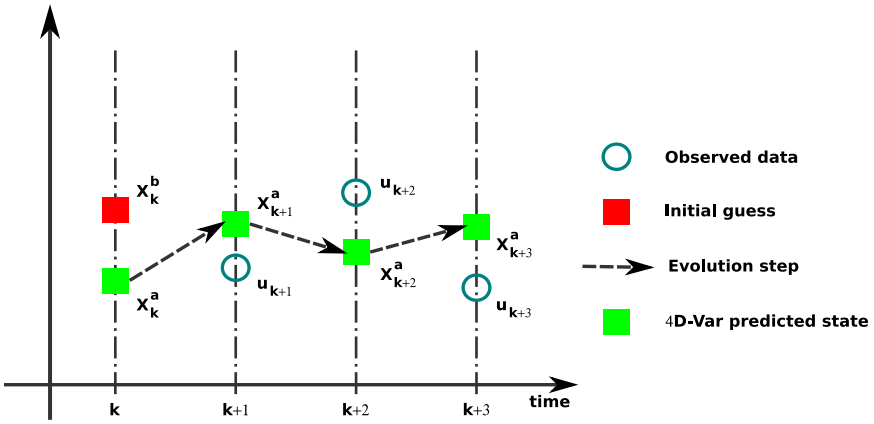

Figure 2.1: *Principle of data assimilation by means of the 4D-Var approach.*

One will remark that, when using a 4D-Var formalism, the sequence of state estimates $[X_0^a, X_1^a, \cdots, X_{N-1}^a]$ is an admissible solution of $M_k(\cdot)$ in the sense of a Markov chain with respect to the initial state since this condition is strongly introduced as a constraint in the optimization problem. That means,

in other words, that the only adjustment variable is the initial state guess and, moreover, that model equations are considered as reliably predicting the state estimation at all other instants. Consequently, the 4D-Var is not well suited to the use of inaccurate models since the only assumed error concerns the initial state guess X_0^b. In addition, in the case of large time windows with a high number of time instants, the sensitivity of functional $\tilde{J}(\cdot)$ with respect to the initial condition X_0 might be very poor, leading to an ill-conditioned inverse problem with potential numerical issues.

Taking the extreme case of subdividing the time interval $t_k = [t_0, t_1, ..., t_{N-1}]$ into N-1 segments $[t_k, t_{k+1}]$ and searching a best state estimation at each time step leads to the solution given by the Kalman filter. The Kalman filter is a prediction-correction recursive algorithm which, at each time step, uses the transition model $M_k(\cdot)$ to propagate optimal states and obtain a future state prediction X_{k+1}^b. This state is then used as an *a priori* information to be corrected with observations and obtain a final state estimation X_{k+1}^a. Thus, the sequence of state estimates $[X_0^a, X_1^a, ..., X_{N-1}^a]$ is not necessarily admissible in the sense of Markov with respect to X_0^a. However, this particularity allows us to obtain state estimations that might be "unreachable" with the sole use of an inaccurate mathematical model. Considered in the present work as a major asset when using inaccurate FE models, the Kalman filter algorithm is presented and described next.

2.3.2 Sequential formalism: The Kalman filter.

As mentioned in the beginning of this section, the sequential approach consists in performing a statistical interpolation (or maximum likelihood estimation) between the *a priori* system information and the observed data at each time step t_k as the process goes on. To do so, for each instant t_k, only immediate past data is used. This approach is also referred to as either recursive or an on-line algorithm. In the linear case, the Kalman filter [53] gives the optimal recursive algorithm for sequential state estimation.

To introduce this algorithm without giving all of its details, suppose that the studied system can be described in a similar way to (2.1) where now the transition and observation functions are linear with additive noises. The state-space description becomes:

$$\begin{cases} X_{k+1} = M_k X_k + w_k \\ \tilde{u}_k = H_k X_k + v_k \end{cases} \tag{2.13}$$

where equations (2.2) and (2.3) are still valid. The Kalman filter equations then proceed, at each time instant $t_k \in [t_0, t_1, ..., t_{N-1}]$, in two different steps:

1. A correction step where a best state estimate X_k^a and P_k^a is obtained by optimally combining observed data and *a priori* state knowledge.
2. A prediction step where the estimates X_k^a and P_k^a are used to obtain the next *a priori* state estimates X_{k+1}^b and P_{k+1}^b with the help of model equations.

The Kalman filter principle is schematically depicted in Figure 2.2 and the sequential equations of Kalman filter are summarized in Figure 2.3.

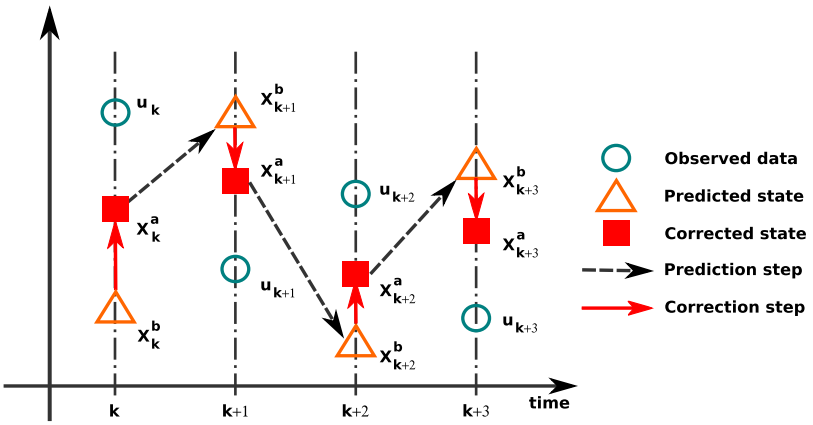

Figure 2.2: *Principle of data assimilation by means of the Kalman filter approach.*

Linear Kalman filter

1. Filter initialization

$$X_0^b \quad \text{and} \quad P_0^b$$

2. At each time step $t_k = [t_1, ..., t_N]$

A CORRECTION

Compute Kalman gain

$$K_k = P_k^b H_k^T (R_k + H_k P_k^b H_k^T)^{-1} \tag{2.14}$$

Correct state best estimate

$$X_k^a = X_k^b + K_k(\tilde{u}_k - H_k X_k^b) \tag{2.15}$$

Correct state covariance estimate

$$P_k^a = (I - K_k H_k) P_k^b \tag{2.16}$$

B PREDICTION

Predict next step *a priori* state

$$X_{k+1}^b = M_{k+1} X_k^a \tag{2.17}$$

Predict next step *a priori* state covariance

$$P_{k+1}^b = M_{k+1} P_k^a M_{k+1}^T + Q_k \tag{2.18}$$

Figure 2.3: *Sequential linear Kalman filter equations.*

Hence, the Kalman filter gives a sequential formalism for optimal state estimation in stochastic linear systems. To summarize, it is interesting to highlight the following points:

- Kalman filter performs at each time step t_k a BLUE optimal interpolation with the only need of state information at t_{k-1}.
- Model equations M_k are used to propagate means and covariances of the states based upon the corrected states.
- The sequence of state estimates $[X_0^a, X_1^a, ..., X_{N-1}^a]$ is not necessarily a Markov process of model M_k.
- The Kalman filter does not provide a general framework applicable to nonlinear systems.
- Propagating covariance matrices in large-DOF systems can entail high computational cost.

The last two listed items represent the major issues of Kalman filtering and since its beginnings, abundant research has been done to overcome them. In the present work, although a Kalman filter approach will be adopted, the problem of reducing the vector state dimension won't be directly addressed from the filtering point of view. Instead, an alternative approach will be adopted based in the Error in Constitutive Relation as described in chapter 1. However, it is interesting to point out that, when dealing with large-DOF systems, evolved filtering methods exist aiming to reduce the computational cost related to covariance matrix operations. In most of the cases, a particular technique to perform Karhunen-Loëve decomposition is sought. The most significant reduced cost algorithms are recalled hereafter (see [11] for more details):

- The RRSQRT filter (Reduced Rank SQuare RooT). This filter is a natural evolution of the KF where only a reduced number of covariance eigenvectors are considered. Covariances are hence written as $P_k = S_k(S_k)^T$ where S_k is of size $n \times m$ and $m \ll n$. Thus, the computational cost is considerably reduced by expressing covariance matrix operations depending in S_k only.
- The SEEK filter(Single Evolutive Extended Kalman). This formulation stands upon the existence of a covariance steady state which solves a discrete matrix Riccati equation.
- The SEIK filter (Single Evolutive Interpolated Kalman). This filter takes the same principle as the SEEK but uses an ensemble technique to deal with nonlinear systems.

Concerning the extension of Kalman filtering to nonlinear systems, the most representative approaches, namely the Extended Kalman filter and the Unscented Kalman filter, are now summarily described.

Extending the Kalman filter to nonlinear systems

As a consequence of its usefulness and ease of implementation, Kalman filtering has widespread applications to engineering, e.g. robotics, aircraft tracking, chemical plant control [22, 47, 76, 72, 61, 64]. From its inception, researchers have investigate ways to extend Kalman filtering to nonlinear systems. In the following, two of the most widely used nonlinear Kalman filters are presented: the Extended Kalman filter and the Unscented Kalman filter.

The Extended Kalman filter (EKF)

The Extended Kalman filter is the most "natural" extension of the linear KF formalism to nonlinear systems. As a matter of fact, the EKF proposes to adopt the original KF formulation where the tangent model and observation operators are used as first order approximation of the corresponding nonlinear relations. Here, we consider the nonlinear system with additive noise:

$$\begin{cases} X_{k+1} = M_k(X_k) + w_k \\ \tilde{u}_k = H_k(X_k) + v_k \end{cases} \tag{2.19}$$

where the w_k and v_k process are still characterized by (2.2) and (2.3). Furthermore, we define:

- $M'_k \equiv \left.\frac{\partial M_k(X)}{\partial X^T}\right|_{X=X_k}$ as the linear tangent model operator.
- $H'_k \equiv \left.\frac{\partial H_k(X)}{\partial X^T}\right|_{X=X_k}$ as the linear tangent observation operator.

The resulting Extended Kalman filter algorithm is given in Figure 2.4.

By virtue of its origins and its simplicity, the Extended Kalman filter has probably been, and still is, the most used Kalman filter formalism, including in structural mechanics (see for example [61] and [12]), as it presents a simple and often efficient approach for dealing with nonlinearities. Nevertheless, this approach can suffer from high inaccuracies and stability problems as demonstrated in [22] where it has been shown that the filter diverges for the cases where the filtering time step $\Delta t = t_k - t_{k-1}$ is not small enough to correctly capture nonlinearities.

For these reasons, alternative approaches have been developed to improve the accuracy and efficiency of the Extended Kalman filter. These include the so-called ensemble methods, and in particular the Unscented Kalman filter (UKF), which embeds many interesting features.

The Unscented Kalman filter (UKF)

As discussed above, the Extended Kalman filter is based on a first-order Taylor expansion of nonlinear functions $M_k(\cdot)$ and $H_k(\cdot)$ as a strategy to approximate nonlinearities. However, depending on the nature and strength of the nonlinearity, a first-order approximation can introduce sufficiently high inaccuracies to make the filter diverge or become unstable [22].

To overcome this issue, the ensemble methods were developed during the 1990's. Inspired by Monte-Carlo sampling, the ensemble methods propose to avoid approximating nonlinear functions and, instead, propagate a sufficiently high number of state samples through the true nonlinear equations to further approach the transformed mean and covariance by computing *a posteriori* sample statistics. The reader can find a general overview on particle filters in [7, 17].

The first filter that implemented the idea of propagating sample states was the Ensemble Kalman Filter (EnsKF) proposed by Evensen in [33], a general overview of which being given in [34]. However, a rigorous mathematical background developed during the early 90's allowed Julier and Ulhmann to introduce in 1996 the so-called Unscented Kalman filter in [50]. The particularity of this approach

Extended Kalman filter

1. Filter initialization

$$X_0^b \quad \text{and} \quad P_0^b$$

2. At each time step $t_k = [t_0, ..., t_{N-1}]$

A CORRECTION

Compute Kalman gain

$$K_k = P_k^b (H_k')^T (R_k + H_k' P_k^b (H_k')^T)^{-1} \tag{2.20}$$

Correct state best estimate

$$X_k^a = X_k^b + K_k(\tilde{u}_k - H_k(X_k^b)) \tag{2.21}$$

Correct state covariance estimate

$$P_k^a = (I - K_k H_k') P_k^b \tag{2.22}$$

B PREDICTION

Predict next step *a priori* state

$$X_{k+1}^b = M_{k+1}(X_k^a) \tag{2.23}$$

Predict next state *a priori* state covariance

$$P_{k+1}^b = M_{k+1}' P_k^a (M_{k+1}')^T + Q_k \tag{2.24}$$

Figure 2.4: *Sequential Extended Kalman filter equations.*

resides in the choice of the propagated sample points, called the sigma points. Based on the mathematical properties of the Unscented Transformation [51], sigma points are chosen in a way that guarantee second-order accuracy of the transformed random variables with a minimal number of sample points. This results into a second-order, reduced-cost, Kalman filter where means and covariances are computed accurately. Hence, this approach differs from the EKF in that the approximation is made on posterior probability functions rather than on the nonlinear system functions.

To illustrate this purpose, Figure 2.5 shows the principle of the Unscented transformation compared to the linearization approach.

As most of variants of Kalman filters, the Unscented version is also divided into a sequence of correction-prediction steps where the nonlinearity issues are overcome with the help of the mathematical Unscented transformation. In addition to the equations of the UKF presented below, the details on the

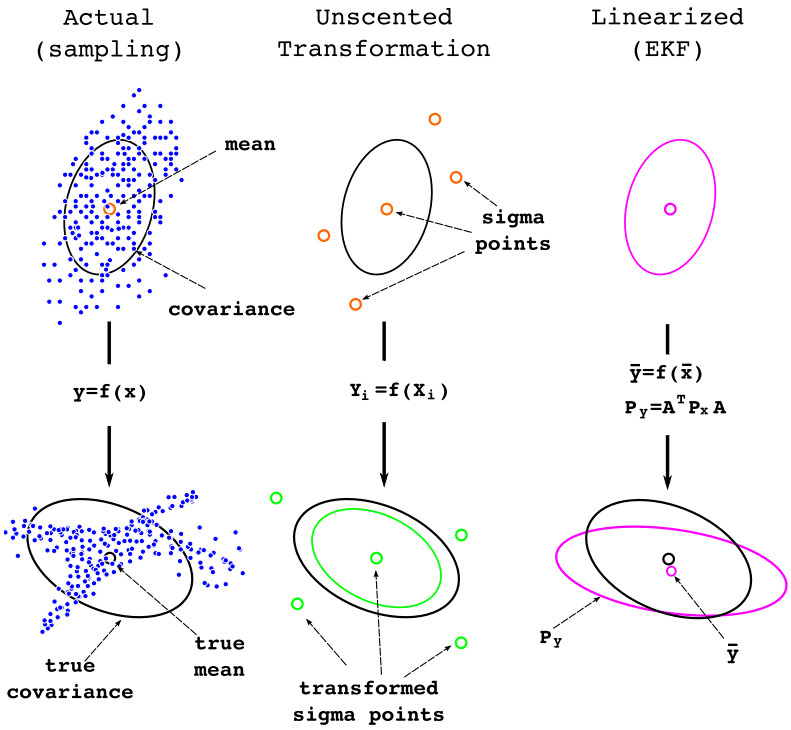

Figure 2.5: *Illustrative comparison between the Unscented and linearization methods for nonlinear stochastic transformations.*

Unscented transformation are given in Appendix C. The reader may refer to [49, 50, 51, 52] for all justifications on accuracy and construction of the Unscented transformation.

For the sake of clarity, before presenting the UKF equations, recall that the Unscented transformation stands on the following three main steps:

1. Build a proper set of sigma points of the *a priori* stochastic process.
2. Propagate all the sigma points through the true nonlinear functions.
3. Evaluate *a posteriori* statistics on the transformed sigma points to approach mean and covariances.

The UKF algorithm is summarized in Figure 2.7, with the formulation details given in Appendix C.

The list below presents some of the advantages of the UKF compared to other filtering paradigms, which constitute the reasons for its adoption in the present work:

- The Unscented transformation ensures a second-order accuracy algorithm, improving on precision and stability with respect to the EKF first-order algorithm.
- The UKF does not require the explicit evaluation of Jacobian and Hessian operators. Those are computed similarly to the finite differences technique making the UKF particularly well adapted to a use within a FE software.
- The UKF computational cost is of same order as the EKF: $O(n^3)$ for state estimation version and $O(n^2)$ for parameter identification where n is the size of the state or parameter vector respectively (see [52, 45] for more details).

2.4 Example of nonlinear identification by means of the Unscented KF

In nuclear power plants, a controlled fission reaction takes place in a core reactor resulting into the production of heat. This energy is used to propel a multi-stage steam turbine assembled to an alternator device allowing the production of electricity. One of the numerous safety barriers consists in isolating a primary irradiated fluid circuit that passes across the core from a secondary turbine propeller circuit. Heat transfer between both circuits is performed by a steam generator that actually acts as a safety component and is composed of hundreds of U-shaped tubes vertically held by support plates as shown in Figure 2.6(a). During in-operation conditions, steam generator tubes vibrate as a consequence of the external fluid excitation and usually hit the support plates at their basis. Sometimes, the presence of a sludge deposit between tubes and support plates not only modifies the secondary fluid flow but also triggers a fluid-elastic instability, potentially leading to rapid tube destruction. Hence, the survey of the gap between the U-shaped tubes and the support plates becomes a major safety issue.

A highly simplified 3-DOF model shown in Figure 2.6(b) is used to study the ability of the UKF algorithm to perform gap identification in this nonlinear structural dynamic framework. The considered governing matrix equation is:

$$[M]\{\ddot{q}\} + [C]\{\dot{q}\} + [K]\{q\} = \{F_{\text{fluid}}(t)\} + \{F_{\text{contact}}(t, q_1)\} \tag{2.25}$$

where $[M]$, $[C]$ and $[K]$ are the associated mass, damping and stiffness matrices while $\{q\} = \{q_1 \quad q_2 \quad q_3\}^T$ is the vector of nodal displacements. On the other hand $\{F_{\text{fluid}}(t)\}$ represents the external fluid forces and is modeled as the following centered Gaussian stochastic process:

$$\{F_{\text{fluid}}(t)\} \sim \{0 \quad 0 \quad \mathcal{N}(0, 30)\}^T \tag{2.26}$$

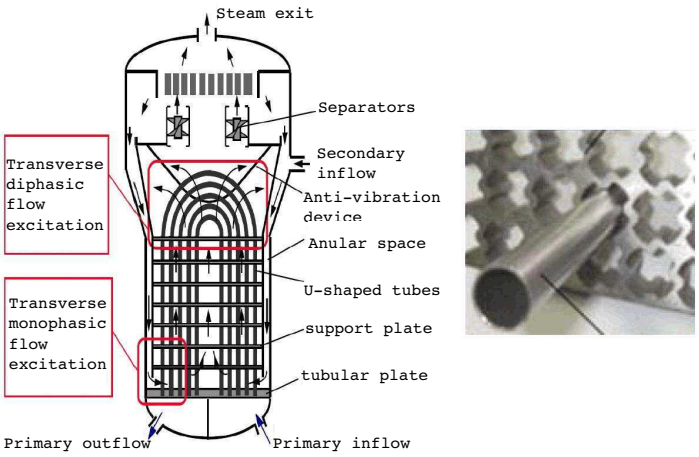

(a) Steam generator scheme and tube-support plate contact zone.

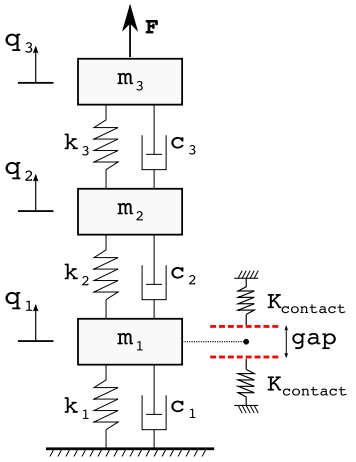

(b) 3-DOF model with contact in node N1

Figure 2.6: *Tube to support plates gap identification problem in steam generators.*

Unscented Kalman filter

1. Filter initialization

$$X_0^b \quad \text{et} \quad P_0^b$$

2. At each time step $t_k = [t_0, ..., t_{N-1}]$

A CORRECTION

Compute sigma points around the state estimate X_k^b

$$[X_k^b] = \{X_k^b .. X_k^b + \gamma\sqrt{P_k^b} .. X_k^b - \gamma\sqrt{P_k^b}\} \tag{2.27}$$

Propagate sigma points through the nonlinear observation function

$$[y_k^b] = H([X_k^b]) \tag{2.28}$$

Compute the expectation of y_k^b through the weighting factors W_j^m

$$\hat{y}_k^b = \sum_{j=0}^{2L} W_j^m [y_k^b]_j \tag{2.29}$$

Compute Kalman gain $$K_k = P_k^{XY}(P_k^{YY})^{-1} \tag{2.30}$$

$$P_k^{YY} = \sum_{j=0}^{2L} W_j^c (([y_k^b]_j - \hat{y}_k^b)([y_k^b]_j - \hat{y}_k^b)^T) + R_k \tag{2.31}$$

$$P_k^{XY} = \sum_{j=0}^{2L} W_j^c (([X_k^b]_j - X_k^b)([y_k^b]_j - \hat{y}_k^b)^T) \tag{2.32}$$

Correct state estimate

$$X_k^a = X_k^b + K_k(\tilde{u}_k - \hat{y}_k^b) \tag{2.33}$$

Correct state covariance estimate

$$P_k^a = P_k^b - K_k(P_k^{XY})^T \tag{2.34}$$

B PREDICTION

compute sigma points around X_k^a

$$[X_k^a] = \{X_k^a .. X_k^a + \gamma\sqrt{P_k^a} .. X_k^a - \gamma\sqrt{P_k^a}\} \tag{2.35}$$

Propagate sigma points through the nonlinear model function

$$[X_{k+1}^b] = M_{k+1}([X_k^a]) \tag{2.36}$$

Predict best state estimate

$$\hat{X}_{k+1}^b = \sum_{j=0}^{2L} W_j^m [X_{k+1}^b]_j \tag{2.37}$$

Predict best state covariance estimate

$$P_{k+1}^b = \sum_{j=0}^{2L} W_j^c (([X_{k+1}^b]_j - \hat{X}_{k+1}^b)([X_{k+1}^b]_j - \hat{X}_{k+1}^b)^T) + Q_k \tag{2.38}$$

Figure 2.7: *Sequential Unscented Kalman filter equations for nonlinear system estimation.*

Moreover, $\{F_{\text{contact}}(t, q_1)\}$ is a nonlinear contact force applied to node N1 and is modeled as:

$$\begin{cases} \{F_{\text{contact}}(t, \{q\})\} = \{0 \quad 0 \quad 0\}^T & \text{if} \quad |q_1| \leq d_{\text{gap}} \\ \{F_{\text{contact}}(t, \{q\})\} = -K_{\text{contact}} \cdot \{q_1 \quad 0 \quad 0\}^T & \text{if} \quad |q_1| > d_{\text{gap}} \end{cases} \tag{2.39}$$

where K_{contact} and d_{gap} are scalars representing respectively the contact stiffness and the gap between the tubes and the support plates.

In this example, a reference model is run in order to obtain synthetic measurements with the following system properties:

- $m_1 = 1\text{kg}$, $m_2 = 0.75\text{kg}$, $m_3 = 2\text{kg}$
- $k_1 = 10\text{N/m}$, $k_2 = 10\text{N/m}$, $k_3 = 10\text{N/m}$
- $c_i = 0.05m_i + 0.001k_i$
- $K_{\text{contact}} = 1000\text{N/m}$
- time-varying gap with initial value $d_{\text{gap}} = 8\text{mm}$

In order to solve the dynamic equation of motion (2.25), the following explicit Euler integration scheme is used:

$$\begin{cases} \{\dot{q}\}_{k+1} = \{\dot{q}\}_k + [M]^{-1}(\{F_{\text{fluid}}\}_k + \{F_{\text{contact}}\}_k - [K]\{q\}_k - [C]\{\dot{q}\}_k) \\ \{q\}_{k+1} = \{q\}_k + \Delta t\{\dot{q}\}_{k+1} \end{cases} \tag{2.40}$$

Figure 2.8 shows both the obtained external fluid effort and contact force for one realization in the time interval $t = [0, 45]\text{s}$ with $\Delta t = 0.001\text{s}$.

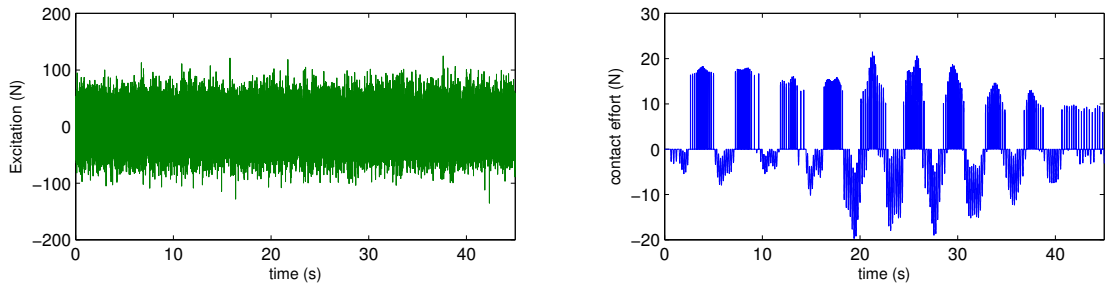

(a) External Gaussian force $F_{\text{fluid}}(t)$.

(b) Contact force F_{contact}.

Figure 2.8: *Evolution of $F_{\text{fluid}}(t)$ and $F_{\text{contact}}(t, q_1)$ in a simulation used to obtain synthetic measurements.*

To illustrate the identification process by means of the Unscented Kalman filter a state-space representation as described in (2.19) has to be built. First of all, the following augmented state vector of unknowns is adopted:

$$X_k = \{\dot{q}_1 \quad \dot{q}_2 \quad \dot{q}_3 \quad q_1 \quad q_2 \quad q_3 \quad d_{\text{gap}} \quad F_{\text{fluid}}\}_k^T \tag{2.41}$$

Indeed, the state vector is referred to as "augmented" since it includes not only the system states $\{\dot{q}\}_k$ and $\{q\}_k$ but also the unknown parameters d_{gap} and F_{fluid} therefore resulting in a joint state and parameter

estimation. Notice that the fluid forces F_{fluid} are considered as states variables since their deterministic value is unknown. Thus, a transition operator $\mathbf{M}_k$ associated with X_k can be built upon the Euler scheme (2.40) for the six first components of X_k. On the other hand, while no evolution equations are known for parameters, a stationarity hypothesis is *a priori* assumed:

$$\left\{ \begin{array}{l} \dfrac{\partial d_{\text{gap}}}{\partial t} = 0 \\ \dfrac{F_{\text{fluid}}}{\partial t} = 0 \end{array} \right. \quad \Rightarrow \quad \left\{ \begin{array}{l} d_{\text{gap }k+1} = d_{\text{gap }k} \\ F_{\text{fluid }k+1} = F_{\text{fluid }k} \end{array} \right. \tag{2.42}$$

This results into the following expression for the transition operator:

$$\mathbf{M}_k(X_k) = \left\{ \begin{array}{c} \{\dot{q}\}_k + [M]^{-1}(\{F_{\text{fluid}}\}_k + \{F_{\text{contact}}\}_k - [K]\{q\}_k - [C]\{\dot{q}\}_k) \\ \{q\}_k + \Delta t\{\dot{q}\}_{k+1} \\ d_{\text{gap }k} \\ F_{\text{fluid }k} \end{array} \right\} \tag{2.43}$$

Concerning the observation equation, in this example, displacement and accelerations are supposed to be measured for the non-contact nodes (N2 and N3) leading to the measurement vector:

$$\tilde{u}_k = \{q_2 \quad q_3 \quad \ddot{q}_2 \quad \ddot{q}_3\}^T \tag{2.44}$$

Thus the consequent linear observation operator $\mathbf{H}_k$ can be obtained from both the equilibrium equation (2.25) and the state vector (2.41). It is defined by:

$$\mathbf{H}_k = \begin{bmatrix} 0 & 0 & 0 & 0 & 1 & 0 & 0 & 0 \\ 0 & 0 & 0 & 0 & 0 & 1 & 0 & 0 \\ c_2/m_2 & -(c_2+c_3)/m_2 & c_3/m_2 & k_2/m_2 & -(k_2+k_3)/m_2 & k_3/m_2 & 0 & 0 \\ 0 & c_3/m_3 & -c_3/m_3 & 0 & -k_3/m_3 & k_3/m_3 & 0 & 1/m_3 \end{bmatrix} \tag{2.45}$$

Hence, the following state-space formulation is considered:

$$\left\{ \begin{array}{l} X_{k+1} = \mathbf{M}_k(X_k) + \mathbf{w}_k \\ \tilde{u}_k = \mathbf{H}_k X_k + \mathbf{v}_k \end{array} \right. \tag{2.46}$$

where the noise processes are characterized by:

$$\left\{ \begin{array}{l} \mathbb{E}[\mathbf{w}_k] = 0 \\ \\ \mathbb{E}[\mathbf{w}_k \mathbf{w}_l^T] = Q_k \delta_{kl} = \begin{bmatrix} Q_k^{\dot{q}} & & \ddots & \mathbf{0} \\ & Q_k^q & & \ddots \\ \ddots & & Q_k^d & \\ \mathbf{0} & \ddots & & Q_k^F \end{bmatrix} \delta_{kl} \end{array} \right. ; \quad \left\{ \begin{array}{l} \mathbb{E}[\mathbf{v}_k] = 0 \\ \mathbb{E}[\mathbf{v}_k \mathbf{v}_l^T] = R_k \delta_{kl} \end{array} \right. \tag{2.47}$$

where, in this case, the following values have been considered:

$$R_k = 10^{-4}\mathbf{I}_4 \qquad Q_k^{\dot{q}} = 10^{-5}\mathbf{I}_3 \qquad Q_k^q = 10^{-5}\mathbf{I}_3 \qquad Q_k^d = 10^{-3} \qquad Q_k^F = 10^{-3} \tag{2.48}$$

The application of the above described Unscented algorithm provides a state and parameter estimation of the dynamic system. In Figure 2.9 we provide the results for the UKF gap estimate in front of the actual time-varying value despite an *a priori* unknown evolution law. As it can be seen, during the initial phase, the algorithm searches a wide range of values of d_{gap} . However, the UKF prediction rapidly stabilizes around the actual value and satisfactorily tracks its evolution over time (see a closer zoom in Figure 2.9(b)). Notice that, although rapid changes are globally captured, the quality of the estimation is not constant, and this is basically due to the fact that in some cases (at $t = 10s$ for example), while the gap value evolves the system oscillates in a region of low and changing contact, so the gap information is hard to capture. In other cases ($t = 20s$) contacts are sufficiently strong to faster capture the system's contact gap information.

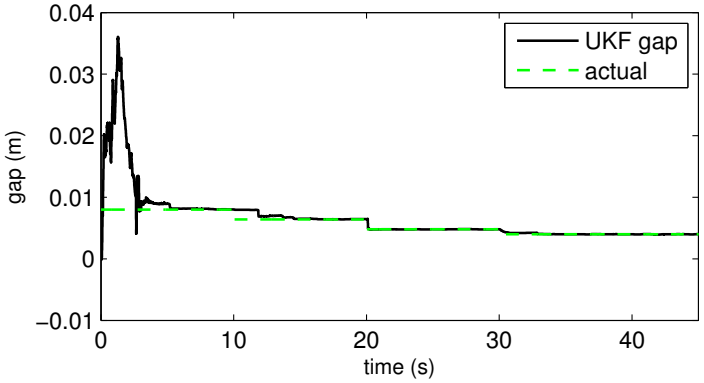

(a) Complete identification process

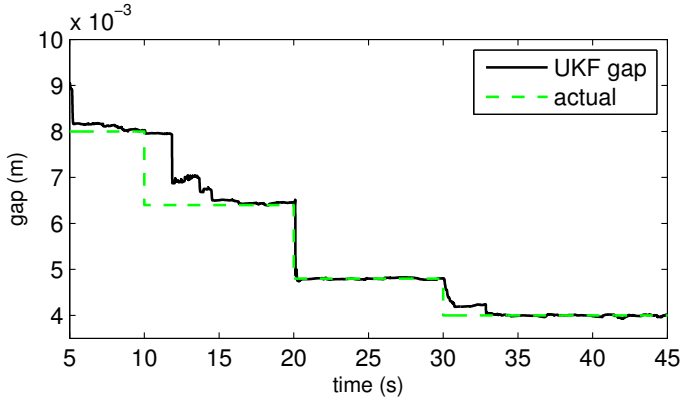

(b) Zoom on time window from $t = 5 - 45$s

Figure 2.9: *Contact gap parameter identification using the Unscented Kalman filter.*

In Figure 2.10 we show the identified unobserved displacement q_1 where after some initial misfitting the estimated displacement satisfactorily reproduces the actual values.

In this example, the UKF has been successfully used to identify the contact gap parameter in a nonlinear dynamic system excited by an unmeasured random external force. The implementation leads

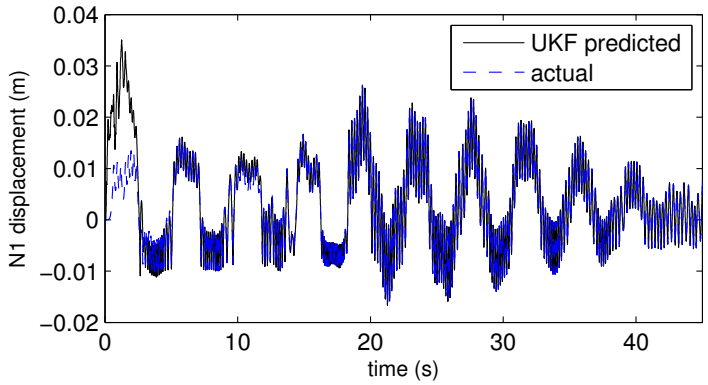

Figure 2.10: *Unobserved N1 displacement identification using the Unscented Kalman filter.*

to a joint state and parameter identification problem which has the ability to track the parameter evolution over time. Moreover, the use of the UKF does not require the calculation of Hessian or Jacobian operators making it particularly suitable to implement in FE codes with black-box functions.

2.5 Conclusions

In this chapter the principles of data assimilation techniques have been introduced and classified into two main families: the variational formalism where the 4D-Var is its most accomplished approach, and the sequential formalism where the Kalman filter is the most representative algorithm.

Although the 4D-Var presents the important advantage of being a general approach for all dynamic systems, it presents two major disadvantages within the scope of this work: firstly, it requires the computation of an adjoint operator, which is generally difficult to implement in FE codes, and secondly the result of the optimization problem is necessarily an admissible solution of the mathematical model, which impedes the identification of *a priori* unknown time-varying parameter laws. However, the latter goal is achievable with the Kalman filter formalism since exact admissibility need not be enforced. Despite the ease of implementation of the Kalman filter, this formalism presents two main issues: the extension to nonlinear problems and the use of high DOFs systems. In this chapter, two approaches applicable to nonlinear problems have been presented: a linearization approach (EKF) and the ensemble approach (UKF). The UKF is retained in this work for both its higher accuracy and its ease implementation.

In the general case of studying complex structures with a large number of DOFs, model errors are generally *a priori* poorly known. Thus, the problem of identifying distributed model parameters (variation of Young's modulus for damage detection, structural modification detection, identifying mass density distributions, etc.) will become an ill-conditioned problem [20]. Hence, applying Kalman filtering to such a problem may lead not only to divergence or unstable solutions but also to extremely expensive identification algorithms since a high number of parameters is sought.

To overcome this issue, we propose in part II to use the Error in Constitutive Relation technique as a strategy to improve the *a priori* model error knowledge and, by this, both reduce the computational cost and reduce the ill-poseness of the inverse problem.

Part II

Towards a combined use of Kalman filtering and Error in Constitutive Relation

Introduction

This part is dedicated to studying the combined application of the Error in Constitutive Relation and Kalman filtering techniques in an effort to improve FE model representativity. It aims at establishing a general-purpose identification approach for industrial use. Accordingly, special attention is devoted to both the relevance of the addressed problems and the viability of their numerical implementation.

In this context, this second part is structured into three main chapters. The first chapter describes the main features of interest of each of the ECR and KF techniques, in preparation for building a general strategy combining both. The second chapter is devoted to a study of the adequacy of the proposed ECR-UKF approach for addressing issues of industrial interest. To this end, the problems of structural damage identification, boundary condition mis-modeling identification and field reconstruction are investigated with the help of numerical examples. Finally, the third chapter aims at improving the numerical ECR-UKF algorithm in two different axes: the introduction of algebraic constraints on the sought-after parameters and the influence of the parameter error covariance design in the quality of the results. Both of them are based on the above-studied case of boundary condition mis-modeling identification.

All of the numerical simulations presented herein have been performed within the environment of the public FE software *Code_Aster* (`www.code-aster.org`) developed by the research division (R&D) of EDF. In most of the investigations carried out herein, specific routines associated with the particular needs of the ECR and UKF algorithms were required. They are implemented combining both Python language and *Code_Aster* operators. The reader will find further details on such implementation as well as user-oriented advices in Appendix D.

Chapter 3

A Kalman filter and ECR strategy for structural dynamics model identification

Contents

3.1 Purpose

In this chapter we propose a general strategy for system identification in structural dynamics based on coupling Kalman filtering and Error in Constitutive Relation techniques. The reason for doing so is to take advantage and combine their interesting individual features (as described in chapters 1 and 2) resulting in a general strategy that contains all of them.

Recall that it is assumed to have at our disposal both a set of measurements $\tilde{u}$ over the studied structure and a FE mechanical model of the form:

$$[-\omega^2[M(\theta)] + i\omega[C(\theta)] + [K(\theta)]]\{q\} = \{F\} \tag{3.1}$$

where the existence of model and measurement errors is assumed. Moreover, the available *a priori* information on model errors can be quite scarce and we thus seek within this approach to:

- Improve the *a priori* knowledge of model errors by a preliminary analysis exploiting the measurements in order to build proper data assimilation operators.
- Perform system identification considering evolutionary mechanical properties.

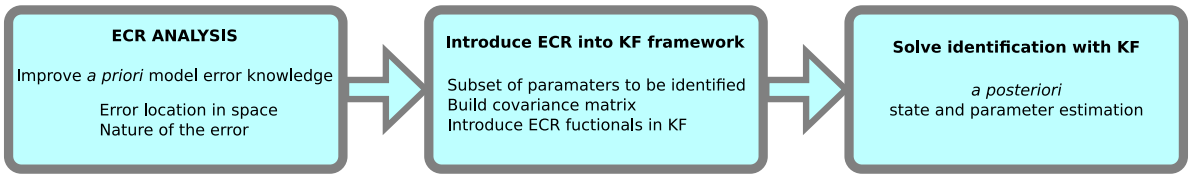

Figure 3.1: *General scheme for the combined use of Error in Constitutive Relation (ECR) and Kalman Filtering (KF).*

In this context, the proposed strategy is based in three main background ideas. The first is to improve the *a priori* model errors knowledge by using the ECR ability to localize model errors in space and determine their nature. Once this information is available, the second step consists of building a new state-space formulation for data assimilation purposes. This mainly consists of choosing a reduced subset of parameters to be identified and take advantage of the well-conditioned character of the ECR cost functionals by introducing them into the Kalman Filter framework. Finally, the third step incorporates these elements and consists in solving the identification problem by applying a Kalman Filter algorithm in order to obtain an *a posteriori* estimation of the structure evolution.

For the sake of clarity, Figure 3.1 gives a general overview of the main steps of the Error in Constitutive Relation and Kalman Filter combined strategy.

In light of the above-mentioned topics and issues, this chapter presents the details for each of the main steps presented in Figure 3.1, each of which is addressed in one of the following three sections. The last section of the chapter presents an illustrative example giving the details of the main steps of this approach.

3.2 Improving *a priori* knowledge with the ECR

In this section we present an approach whose goal is to improve the *a priori* knowledge of model errors based on a preliminary frequency-domain ECR analysis. The choice of using the ECR method to do so is motivated by some of its interesting properties described in chapter 1 that might be exploited further.

In particular, a useful property of the ECR that one wants to exploit is its ability to spatially localize modelling errors. Indeed, as presented in chapter 1, given a set of model parameters θ the ECR functionals are used to first obtain a triple of "best" admissible fields $\mathcal{T}_\omega = (\hat{u}, \hat{v}, \hat{w})$ that minimize an energy-based cost functional, which in our FE framework is chosen to be:

$$\begin{aligned} e_\omega^2(\{u\},\{v\},\{w\}) =& \frac{\gamma}{2}\{u-v\}^*[K+T\omega^2 C]\{u-v\} + \frac{1-\gamma}{2}\{u-w\}^*\omega^2[M]\{u-w\} \\ &+ \frac{r}{1-r}\{\Pi u-\tilde{u}\}^*[G_R]\{\Pi u-\tilde{u}\} \end{aligned} \tag{3.2}$$

whose minimization is discussed in Appendix B.

Qualitatively speaking, the triple $\mathcal{T}_\omega$ contains the information of the model quality with respect to a set of measurements $\tilde{u}$ for an angular frequency ω. As a matter of fact, notice that if the model is perfect,

the field $\hat{u}$ coincides with $\tilde{u}$ at sensor locations leading to $\hat{u} = \hat{v} = \hat{w}$. On the other hand, if the assumed model is unable to exactly reproduce the information contained in $\tilde{u}$, then differences between $\hat{u}$, $\hat{v}$ and $\hat{w}$ may appear and the model is thus deemed erroneous in the sense of the constitutive relation error.

In order to quantify the quality or the agreement of the model with respect to $\tilde{u}$, the evaluation of the triple $\mathcal{T}_\omega$ through an ECR indicator is required. This can be done evaluating:

$$\xi^2_{\omega r}(\hat{u}, \hat{v}, \hat{w}, \theta) = \frac{e^2_\omega(\hat{u}, \hat{v}, \hat{w}, \theta)}{D^2_\omega(\hat{u}, \theta)} \tag{3.3}$$

Moreover, notice that since the admissible fields $(\hat{u}, \hat{v}, \hat{w})$ are defined over the whole structure Ω, the evaluation of (3.3) can be performed either over the whole structure Ω or any other sub-structure $E \in \Omega$. Since the global model error is additive with respect to Ω, it can be recast as a sum of local errors of each sub-structure:

$$\xi^2_{\omega r}(\hat{u}, \hat{v}, \hat{w}, \theta) = \sum_{E \in \Omega} \frac{e^2_{\omega E}(\hat{u}, \hat{v}, \hat{w}, \theta)}{D^2_\omega(\hat{u}, \theta)} + d_u(\hat{u}, \tilde{u}, \theta) \tag{3.4}$$

where

$$d_u(\hat{u}, \tilde{u}, \theta) = \frac{\frac{r}{1-r}\{\Pi\hat{u} - \tilde{u}\}^*[G_R]\{\Pi\hat{u} - \tilde{u}\}}{D^2_\omega(\hat{u}, \theta)} = \frac{\|\Pi\hat{u} - \tilde{u}\|_{G_R}}{D^2_\omega(\hat{u}, \theta)} \tag{3.5}$$

In the case of the FE formulation, taking each finite element as a sub-structure yields the distribution of the model error indicator over the structure. It is known [10] that parts of the sub-structure affected by modeling errors are highlighted by the distribution provided by $e^2_{\omega E}(\hat{u}, \hat{v}, \hat{w}, \theta)$. This is precisely one of the main properties that we are exploiting in the present strategy in order to improve *a priori* knowledge of model errors.

Hence, by performing this preliminary ECR analysis we can distinguish the parts of Ω that need to be updated from those for which the model shows better agreement (in the sense of the constitutive relation error) with respect the measurements. This is rich and useful information that can considerably reduce the number of model parameters to be identified and importantly improve the conditioning of the inversion.

In a second time, one can obtain a more accurate knowledge of the nature of the model error by studying the different contributions of $\xi^2_{\omega r}$. Recall that in the right-hand side of (3.4) the error distribution is given by:

$$\frac{e^2_{\omega E}(\hat{u}, \hat{v}, \hat{w}, \theta)}{D^2_\omega(\hat{u}, \theta)} = \text{Ind}_{K_E} + \text{Ind}_{M_E} \tag{3.6}$$

where

$$\text{Ind}_{K_E} = \frac{\frac{\gamma}{2}\{\hat{u} - \hat{v}\}^*[K + T\omega^2 C]_E\{\hat{u} - \hat{v}\}}{D^2_\omega(\hat{u}, \theta)} = \frac{\|\hat{u} - \hat{v}\|_{K_E, C_E}}{D^2_\omega(\hat{u}, \theta)} \tag{3.7}$$

$$\text{Ind}_{M_E} = \frac{\dfrac{1-\gamma}{2}\{\hat{u} - \hat{w}\}^*\omega^2[M]_E\{\hat{u} - \hat{w}\}}{D^2_\omega(\hat{u}, \theta)} = \frac{\|\hat{u} - \hat{w}\|_{M_E}}{D^2_\omega(\hat{u}, \theta)} \tag{3.8}$$

Aside from the normalizing term $D^2_\omega(\hat{u},\theta)$, the expression (3.6) reveals that the error indicator is the sum of two main contributions. While the first can be associated with the strain energy of the discrepancy between $\tilde{u}$ and $\tilde{v}$, the second term corresponds to a kinetic energy of the discrepancy between $\tilde{u}$ and $\tilde{w}$.

For low damping models, it can be shown (see [10]) that contribution Ind_{K_E} is mainly related to a stiffness error while contribution Ind_{M_E} are typically related to mass errors. In the following, we will use Ind_{K_E} and Ind_{M_E} to detect stiffness and mass errors of the mechanical model, respectively.

Consequently, from a preliminary ECR analysis, one can identify regions from the structure that need to be updated and also distinguish the nature of the parameters involved in the error. Figure 3.2 summarizes the different steps needed to perform the preliminary ECR analysis.

I Preliminary ECR analysis.

(a) Define a frequency range of interest $[\omega_{min},\omega_{max}]$.

(b) For $\omega \in [\omega_{min},\omega_{max}]$ and given θ obtain the triple of admissible fields $\mathcal{T}_\omega = (\hat{u},\hat{v},\hat{w})$ by solving optimality equations associated with the ECR cost functional $e^2_{\omega E}(\{u\},\{v\},\{w\})$ defined in (1.26) .

(c) Obtain the distribution over Ω of the ECR indicator by evaluating for each substrucure $E \in \Omega$:

$$\xi^2_{Er} = \int_{\omega_{min}}^{\omega_{max}} \eta(\omega) \left(\frac{e^2_{\omega E}(\mathcal{T}_\omega,\theta)}{D^2_\omega(\{\hat{u}\},\theta)} \right) \mathrm{d}\omega$$

(d) Select potential incorrectly regions $\mathfrak{E} \in \Omega$ based on the previous error distribution using the selection criterion:

$$\xi^2_{Er} \geq \delta . \max_{E\in\Omega} \xi^2_{Er} \quad \Rightarrow \quad E \in \mathfrak{E}$$

with δ a user-defined value, for example $\delta = 0.8$

(e) Distinguish from the nature of the error by evaluating the contributions Ind_{K_E} and Ind_{M_E} of ξ^2_{Er} as defined in (3.7) and (3.8) for $E \in \mathfrak{E}$.

Figure 3.2: *Overview of the preliminary ECR analysis to improve a priori model error knowledge.*

Besides the interests of the above-mentioned ECR properties, namely localize incorrectly modeled regions of the structure and distinguish their nature, the chosen formulation adopted in the present work is also particularly adapted to represent error fields over Ω. As a matter of fact, since the adopted formulation describes all the error fields in terms of nodal displacements, valuable information can be extracted from the admissible fields $(\hat{u},\hat{v},\hat{w})$ and can be used to build structural response field estimators. In an effort to propose a state estimation within the framework of the combined use of ECR and Kalman filtering, the last section 4.3 of the next chapter is devoted to studying the performances of using $\mathcal{T}_\omega$ for

field reconstruction purposes.

3.3 Introducing the ECR functionals into Kalman Filtering

As presented above, we discuss herein how the Kalman filter can be used as a technique to deal with a general optimization problem without losing the generality of time-varying systems.

The essence of this method is to understand the Kalman Filter algorithm as a quasi-Newton descent method that encodes second-order information about the identification problem by means of the covariance matrices.

In the following, we present the analogies between the Kalman filter and the recursive optimization problem in a linear framework and also its natural extension to the non-linear case. An explanatory formulation of the Extended Kalman filter as a quasi-Newton descent method is proposed for a better understanding of the reasons for the introduction of the proposed state-space formulation embedding ECR cost functionals.

To illustrate this idea, assume that we deal with a linear system where we have at our disposal a number N of measurements $\tilde{u}_k \in \mathbb{R}^m$ related to a linear matrix model $H_k \in \mathbf{M}_{m,n}(\mathbb{R})$ in a way that:

$$\tilde{u}_k = H_k X + \eta_k \qquad \text{for } k \in [0, 1, \dots, N-1] \tag{3.9}$$

where $X \in \mathbb{R}^n$ represents a vector of states and η_k denotes a (measurement or model) error. Furthermore, assume that we want to tackle with the problem of minimizing the least squares cost functional given by:

$$\hat{X} = \underset{X}{\text{Argmin}} \quad J(X) = \frac{1}{2} \sum_{k=0}^{N-1} (\tilde{u}_k - H_k X)^T R_k^{-1} (\tilde{u}_k - H_k X) + \frac{\lambda}{2} X^T L X \tag{3.10}$$

where R_k is a symmetric positive-definite weighting matrix and $\frac{\lambda}{2} X^T L X$ represents a regularization term since matrix L is chosen to be positive-definite too. The solution of such a problem can be found in a recursive manner by the algorithm presented in Figure 3.3 (see [79] for more details on this algorithm).

Besides, in the context of parameter identification through Kalman filtering, a mathematical model concerning parameter evolution laws is needed. Generally, in the absence of *a priori* knowledge about evolution laws for the parameters, stationarity is assumed. In that particular case, this comes to consider an identity matrix as the parameter evolution model and the Kalman filter equations can be rewritten as presented in Figure 3.4.

Comparing Figure 3.3 and Figure 3.4 one can observe that performing parameter estimation by means of the Kalman Filter only differs from the linear recursive algorithm by the introduction of matrix Q_k in the covariance update step (Hessian inverse update step for the case of the recursive algorithm). The origin of this difference comes from the fact that, in Kalman Filter state-space formulation, one assumes the presence of model errors. In fact, the stationarity equation is in this case written of the form:

$$X_{k+1} = X_k + \epsilon_k \tag{3.11}$$

Recursive algorithm for a linear optimization problem

I Initialization

$$\hat{X}_0 = (H_0^T R_0^{-1} H_0 + \lambda L)^{-1} H_0^T R_0^{-1} \tilde{u}_0$$

$$P_0 = (H_0^T R_0^{-1} H_0 + \lambda L)^{-1}$$

II For $k \in [1 \dots N-1]$

1 Evaluate gain K_k for step k

$$K_k = P_{k-1} H_k^T (H_k P_{k-1} H_k^T + R_k)^{-1}$$

2 Optimum update at step k as a result of the introduction of the new measurement $\tilde{u}_k$

$$\hat{X}_k = \hat{X}_{k-1} + K_k(\tilde{u}_k - H_k \hat{X}_{k-1})$$

3 Hessian inverse update at step k

$$P_k = (I - K_k H_k) P_{k-1}$$

Figure 3.3: *Recursive algorithm solving a least square optimization problem for linear systems.*

where ϵ_k represents a term of error in the stationarity assumption.

From a variational point of view, assuming the existence of such a "stationarity" error naturally modifies the cost function (3.10) that we are seeking to minimize by the introduction of an additional term. This term takes into account the existence of ε_k and the goal to minimize its variance. Hence, one can say that the Kalman filter is an algorithm that aims at finding the sequence of estimates $\{\hat{X}_0, \hat{X}_1, \cdots, \hat{X}_{N-1}\}$ that minimizes J:

$$J(X_0, X_1, \cdots, X_{N-1}) = \frac{1}{2} \sum_{k=0}^{N-1} [(\tilde{u}_k - H_k X_k)^T R_k^{-1} (\tilde{u}_k - H_k X_k) + (X_k - X_{k-1})^T Q_k^{-1} (X_k - X_{k-1})] \tag{3.12}$$

where the symmetric positive-definite matrix Q_k weights the condition of stationarity of X, which is treated as a penalty term (and is thus allowed to be satisfied approximately, rather than exactly).

From this particular point of view, it is interesting to highlight the following remarks concerning the role of Q_k:

1. Similar to the $\frac{\lambda}{2}L$ term in (3.10), the covariance matrix Q_k introduces a regularization term in the cost function (3.12) at each iteration k, which is similar to Tikhonov regularization.
2. From a sequential point of view, the covariance matrix Q_k plays a role of "memory" in the esti-

Parameter identification using linear Kalman Filter

I Initialization

$$\hat{X}_0 = E[X_0] \text{ and } P_0 = E[(X_0 - \hat{X}_0)(X_0 - \hat{X}_0)^T]$$

II For $k \in [1 \dots N-1]$

1 Compute Kalman gain K_k at step k

$$K_k = P_{k-1} H_k^T (H_k P_{k-1} H_k^T + R_k)^{-1}$$

2 Parameter update at step k

$$\hat{X}_k = \hat{X}_{k-1} + K_k(\tilde{u}_k - H_k \hat{X}_{k-1})$$

3 Covariance update at step k

$$P_k = (I - K_k H_k) P_{k-1} + Q_k$$

Figure 3.4: *Linear Kalman Filter algorithm for parameter identication.*

mation procedure. Indeed, the stationarity condition of X is weakened by the presence of process noise ε_k (characterized by Q_k). Thus, when looking at the expression (3.12), one can observe that the larger the eigenvalues of Q_k, the smaller the penalty of $(X_k - X_{k-1})$. In the same way, one can make the analogous remark for $(X_k - X_j)$ with $k - j > 1$. Consequently, the larger the eigenvalues of Q_k, the faster the algorithm "forgets" past values of X_k.

3. As a direct consequence of the above-mentioned properties, the introduction of Q_k allows the Kalman filter algorithm to handle time-variant systems since the parameter stationarity becomes a weak condition. This is one of the main features sought in this work.
4. From the identification point of view, the estimation $\hat{X}_k$ for sufficiently large k has a small sensitivity to the initial conditions X_0 and P_0 since the covariance matrix Q_k behaves as a "forgetting factor". This is particularly interesting for systems where the *a priori* knowledge of the initial estimates is poor.

All the identification methods presented above are optimal estimators since the mathematical model H_k is linear. When addressing the estimation problem for nonlinear systems, a large number of extensions of the recursive linear algorithm exist and are known as sub-optimal procedures. Under the Kalman filter formalism, one of the most widely used approach to tackle with nonlinear systems is the so-called Extended Kalman filter (EKF) which is presented in more details in section 2.3.2. As previously mentioned, the EKF extends the standard Kalman filter algorithm by simply linearize the state-space nonlinear models at each instant around the most recent state estimate. Hence, the EKF uses the information

contained in the Jacobian operator to approach nonlinearities.

In the sequel, the EKF parameter identification formalism is compared to a quasi-Newton descent method for the sake of clarity. However, the Unscented Kalman filter will be adopted, which can be simply seen as a more accurate variant of the EKF that behaves similarly.

To fix the ideas, assume now that $h(X)$ is our nonlinear mathematical model and h'_k represents the linear tangent operator of $h(\cdot)$ at X_k. Thus, the EKF equations applied to $h(X)$ are shown in Figure 3.5.

Parameter identification using the Extended Kalman Filter.

I Initialization

$$\hat{X}_0 = \mathbb{E}[X_0] \text{ and } P_0 = \mathbb{E}[(X_0 - \hat{X}_0)(X_0 - \hat{X}_0)^T]$$

II For $i \in [1 \dots k]$

1 Compute Kalman gain K_k at step k

$$K_k = P_{k-1} h_k'^T (h'_k P_{k-1} h_k'^T + R_k)^{-1}$$

2 Parameter update at step k

$$\hat{X}_k = \hat{X}_{k-1} + K_k(\tilde{u}_k - h(\hat{X}_{k-1}))$$

3 Covariance update at step k

$$P_k = (I - K_k h'_k) P_{k-1} + Q_k$$

Figure 3.5: *Extended Kalman Filter algorithm for parameter identification.*

Suppose now that the nonlinear function that we used as a model is a cost functional of the type (3.10) that includes both a physical model and a set of measurements. In other words, our mathematical model $h(\cdot)$ is now supposed to be a function $J : \mathbb{R}^n \to \mathbb{R}$, J' being its Jacobian. In this particular configuration of the Kalman filter, it is important to point out some important features that will help to better understand the interest of this approach:

- The observation space in this particular configuration of the Kalman filter is no longer the space of physical observations $\tilde{u}_k$. As a matter of fact, the new observation space measures, through $J(X)$ the discrepancy between our physical model and measurements $\tilde{u}$.
- Physical measurements $\tilde{u}_k$ are implicitly embedded in the cost functional $J(X)$ and don't appear directly in the new observation space. We therefore define a new observation variable z_j that will play the role of a "target value" for the discrepancy measure $J(X)$.
- Since times steps k are implicitly included in $J(X)$, the recursive framework in this particular configuration is related to the iterative optimization process and is materialized using the subscript

j in order to better distinguish it from discrete time steps k.

Taking into account the above considerations and rearranging terms of the EKF description given in Figure 3.5, on can observe that the EKF performs a quasi-Newton descent method to evaluate the descent steps and the Hessian update. In Figure 3.6 we describe the EKF algorithm in a Newton method fashion and one can easily observe this similarity.

quasi-Newton method description of the Extended Kalman filter

I Initialization

$$\hat{X}_0 = \mathbb{E}[X] \text{ and } P_0 = \mathbb{E}[(X - X_0)(X - X_0)^T]$$

II For $j \in [1 \dots N-1]$

1 Compute descent direction d_j for step j

$$d_j = P_j J'(X_j)^T$$

2 Compute descent coefficient η_j for step j

$$\eta_j = \frac{z_j - J(X_j)}{J'(X_j)^T P_j J'(X_j) + R_j}$$

3 Parameter update at step j

$$X_{j+1} = \hat{X}_j + \eta_j d_j$$

4 Hessian inverse update at step j

$$P_{j+1} = [I + \eta_j d_j \frac{J'(X_j)}{J(X_j)}]P_j + Q_k$$

Figure 3.6: *Description of the EKF for parameter identification as a quasi-Newton method.*

In most of the cases, since the problem of minimizing the functional $J(\cdot)$ is addressed, it is natural to fix the value of the target z_j to the desired goal, which for minimization purposes is set to $z_j = 0 \, \forall j$. When doing this, the EKF seeks to minimize the cost function $J(X)$ in a particular quasi-Newton method where the Hessian inverse update and the descent coefficient are given in Figure 3.6.

It is convenient, though, to state some remarks about this particular algorithm:

- R_j influences the value of the descent coefficient η_j and controls convergence speed. In fact, one can consider the R_j parameter as a damping factor of the algorithm: η_j is a decreasing function of R_j, hence large values of R_j slow down the convergence avoiding fast variations of the estimates (stability).
- Matrix Q_j modifies the information contained in the Hessian inverse, changing the descent direc-

tion d_j throughout the iterative procedure. In addition to its regularization effect at each iteration j, Q_j also affects the convergence and stability of the algorithm.

- By making the analogy with the classic descent and quasi-Newton methods, it is important to point out that parameter identification within a Kalman filter framework doesn't guarantee reaching globally optimal estimators if the cost functional presents local minima. Hence, it is important to pay special attention to the convexity of J and the initial estimates X_0.

Choice of ECR functionals as a measure of the observation space

In the previous section, we have discussed the analogy between the recursive least squares optimization problem and Kalman filtering. We have seen how, in the linear case, the Kalman filter is an optimal estimator of a modified least square problem where the functional has the ability to handle time-variant systems. This is specifically done by postulating the presence of an error ε_k in the stationarity equation (3.11). Furthermore, we have shown how the EKF, which is a natural extension of the Kalman filter to deal with nonlinear problems, can be seen as a particular quasi-Newton method from a minimization point of view.

Considering the case where a cost function is introduced as a mathematical model in the observation space with a new observation variable z, we know that any of the Kalman filter derivations will aim to minimize (up to a regularization term), the residual $\sum_j (z_j - \hat{z})_j^T (z_j - \hat{z})_j$ where z_j is a target value and $\hat{z}_j$ is the best estimate at iteration j. Therefore, Kalman filtering can be used as a general algorithm to tackle a minimization problem.

Hence, since the Error in Constitutive Relation functionals are very well suited to parameter identification problems in structural mechanics, we propose to introduce them in the observation space as the chosen measure of the discrepancy between a mechanical model and physical measurements. Thus, the proposed state-space formulation for parameter identification takes the form:

$$\begin{cases} \theta_{j+1} = \theta_j + w_j^\theta \\ \zeta_j = \xi_{Tr}^2(\theta_j) + e_j \end{cases} \tag{3.13}$$

where vector θ_j parametrizes the mechanical FE operators $[M]$, $[C]$ and $[K]$ at step j as defined in (3.1). Besides, w_j^θ and e_j represent zero-mean Gaussian additive errors for the stationarity and the observation equations through the ECR cost function respectively with:

$$\begin{cases} \mathbb{E}[w_j^\theta] = 0 \\ \mathbb{E}[w_j^\theta w_l^{\theta T}] = \mathcal{Q}_j \delta_{jl} \\ \mathbb{E}[e_j] = 0 \\ \mathbb{E}[e_j e_l^T] = \mathcal{R}_j \delta_{jl} \end{cases} \tag{3.14}$$

Moreover, while $\xi_{Tr}^2(\theta_j)$ gives a measure of the quality of the mechanical model through the ECR cost function (1.28), the term ζ_j represents a target value for $\xi_{Tr}^2(\theta_j)$.

3.4 Solving the identification problem by using ECR - UKF coupled method

In the foregoing sections, we have seen how the Error in Constitutive Relation can be used to improve the *a priori* lack of knowledge of FE model errors. Moreover, we have presented the Kalman filter as an algorithm to solve a general optimization problem, allowing ECR cost functions to be introduced into a suitable state-space formulation. Based on the previous developments, this section now gives the details of the algorithm used to solve the parameter identification problem combining both Error in Constitutive Relation and Unscented Kalman filter.

For this, assume that a preliminary ECR analysis as described in Figure 3.2 has been performed. From this improved *a priori* model error information, it is possible to select a reduced size model vector θ of parameters for model updating. Furthermore, since an unknown evolution of model parameters is sought, a stationarity law weakened by a random error is assumed:

$$\dot{\theta} = 0 + \mathcal{W}(t) \tag{3.15}$$

where $\mathcal{W}(t)$ is a random process. The presence of $\mathcal{W}(t)$ in the evolution law of θ relaxes the stationarity condition and as a consequence can be exploited to approach the parameter evolution law. At this point, time-discretizing (3.15) and introducing ECR functionals as a measure of the observation space leads to a state-space description of the problem as described in (3.13) and (3.14).

Since Kalman filter algorithms attempt to minimize the residual $\sum_j \|e_j\|_{\mathcal{R}_j}$ where $e_j = \zeta_j - \xi^2_{Tr}(\theta_j)$, the minimization of $\xi^2_{Tr}(\cdot)$ can be obtained by simply postulating:

$$\zeta_j = 0 \quad \forall j \tag{3.16}$$

It is easy to observe that the aforementioned state-space description requires a nonlinear Kalman filter approach, since the observation operator $\xi^2_{Tr}(\cdot)$ is a nonlinear function of θ. In the present work, the use of the UKF is proposed and is motivated by the following reasons:

- The UKF achieves second order accuracy of model functions for any (sufficiently smooth) nonlinearity improving the performances of the Extended Kalman filter.
- The UKF is particularly well suited for implementation in a FEM environment, as it does not require actual explicit evaluation of the Jacobian and Hessian of the nonlinear equations. This information is instead obtained by a minimal set of carefully chosen sample points.
- The same order of complexity $\mathcal{O}(n^2)$ as EKF can be achieved for parameter estimation [45].

The details of the Unscented Kalman filter applied to the ECR minimization problem are given in Figure 3.7.

3.5 Numerical example of structural parameter identification

In this section, we describe the application of the combined ECR-UKF strategy with a numerical example. It aims at highlighting the main steps involved when putting the strategy to use and demonstrating its validity.

ECR based Unscented Kalman filter for parameter estimation

I Filter initialization

$$\theta_0 = \mathbb{E}[\theta] \quad \text{and} \quad P_0^\theta = \mathbb{E}[(\theta - \theta_0)(\theta - \theta_0)^T]$$

II For $j \in [1 \dots \infty]$

1 Build matrix of sigma points around θ_j

$$[\theta_j] = \{\theta_j \qquad \theta_j + \sqrt{(m+\lambda)P_j^\theta} \qquad \theta_j - \sqrt{(m+\lambda)P_j^\theta}\}$$

2 Propagate sigma points through the ECR cost function $\xi_{Tr}^2(\cdot)$

$$[\zeta_j] = \xi_{Tr}^2([\theta_j])$$

3 Best estimate $\hat{\zeta}_j$ through Unscented weighting factors W_k^m

$$\hat{\zeta}_j = \sum_{k=0}^{2L} W_k^m [\zeta_j]_k$$

4 Compute Kalman gain

$$K_j^\theta = P_j^{\theta\zeta}(P_j^{\zeta\zeta})^{-1}$$

$$P_j^{\zeta\zeta} = \sum_{k=0}^{2L} W_k^c (([\zeta_j]_k - \hat{\zeta}_j)([\zeta_j]_k - \hat{\zeta}_j)^T) + \mathcal{R}_j$$

$$P_j^{\theta\zeta} = \sum_{k=0}^{2L} W_k^c (([\theta_j]_k - \theta_j)([\zeta_j]_k - \hat{\zeta}_j)^T)$$

5 Parameter update

$$\theta_{j+1} = \theta_j - K_j^\theta \hat{\zeta}_j$$

6 Covariance update

$$P_{j+1}^\theta = P_j^\theta - K_j^\theta (P_j^{\theta\zeta})^T + \mathcal{Q}_j$$

Figure 3.7: *Description of the Unscented Kalman filter with ECR cost functions in observation space for minimization purpose.*

For this, we propose to study the dynamical behavior of a simplified concrete beam subjected to an external time-harmonic load. The structure is supposed to have free-clamped extremities and the presence of a damaged region is assumed.

Figure 3.8(a) shows a Finite Element model used to generate synthetic data. The structure is supposed to have elastic properties and the presence of damage d is modeled as:

$$d = \frac{\mathrm{E_{ref}} - \mathrm{E_{true}}}{\mathrm{E_{ref}}} \tag{3.17}$$

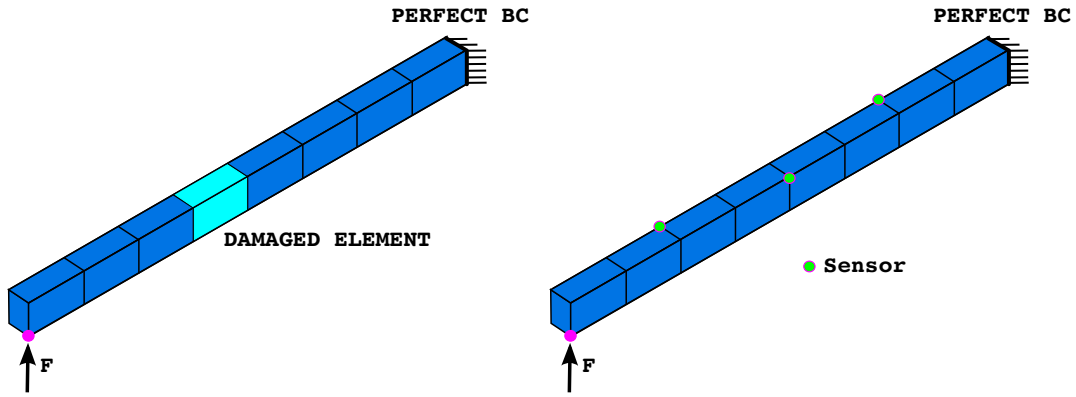

(a) Free-clamped concrete beam with structural damage.

(b) Set of sensors over the concrete beam

Figure 3.8: *FE model used to generate synthetic measurement data.*

where E_{ref} represents a reference structural Young modulus and E_{true} the actual Young modulus of the damaged region. Thus, the damage parameter d represents a relative loss of stiffness and has to verify $0 \leq d \leq 1$.

The structure has a length of $3,75$m and a constant rectangular section (height=$0,22$m, width=$0,15$m), and the Young modulus, mass density and Poisson's ratio are respectively set to $E = 2 \times 10^{10}$N/m^2, $\varrho = 2400$kg/m^3 and $\nu = 0,2$.

In this first example, we consider the case where the external load amplitude of $F = 100$N containing a single fundamental frequency of 20Hz. Moreover, since structural damage is assumed to be localized in a unique element, vector d is set to be:

$$d = (d_1 \quad d_2 \quad d_3 \quad d_4 \quad d_5 \quad d_6 \quad d_7 \quad d_8)^T = (0 \quad 0 \quad 0 \quad 0.9 \quad 0 \quad 0 \quad 0 \quad 0)^T \tag{3.18}$$

where d_i is the structural damage corresponding to the ith finite element.

The above described FE model is thus used to generate a set of synthetic measurements $\tilde{u}_\omega \in \mathbb{R}^m$ obtained by projecting the nodal displacement solution $q_\omega \in \mathbb{R}^n$ using the observation operator Π built from the sensor locations described in Figure 3.8(b). Moreover, the synthetic measurements are perturbed with 5% of Gaussian error and therefore obtained in the following way:

$$\tilde{u}_\omega = [\Delta]\Pi q_\omega \tag{3.19}$$

where $[\Delta] \in \mathrm{M}(\mathbb{R})_{m,m}$ and $\Delta_{ij} \sim \mathcal{N}(1, 0.05) \cdot \delta_{ij}$.

Note a reference FE model used for model updating is assumed to be the same as the one described in Figure 3.8(a) endowed with the previously-given (homogeneous) reference material properties.

In this context, the goal of the specific strategy we want to apply here is to improve the knowledge on model errors where no prior assumptions are available. For doing so, we want to first evaluate the

presence of model errors, then locate them in space and, if possible, identify its nature and intensity (i.e. get as close as possible to (3.18)).

Preliminary ECR analysis

The first step of the procedure consists of performing an ECR analysis of the structure. Given a set of measurements over the reference FE model, the triple of admissible fields $\mathcal{T}_\omega = (\hat{u}, \hat{v}, \hat{w})$ is calculated for $\omega = 40\pi$ rad/s by minimizing the ECR cost functional (1.28). For the sake of illustration, Figure 3.9 presents the computed $\{\hat{u} - \hat{v}\}$ and $\{\hat{u} - \hat{w}\}$ fields.

Moreover, the beam is divided into 8 substructures, each corresponding to an element of the mesh, so that $\Omega = \bigcup_{i=1}^{8} E_i$ in order to evaluate Ind_{K_E}, Ind_{M_E} indicators (3.6) with the use of $\mathcal{T}_\omega$.

In Figure 3.10, the Ind_{K_E}, Ind_{M_E} indicators are presented over the beam giving an estimation of the parametric error field. One can easily observe how the error related to Ind_{K_E} is more relevant than Ind_{M_E}. This emphasizes the fact that the nature of the error is probably associated to the stiffness matrix $[K]$. Besides, one can also remark that the error seems to be concentrated in elements 4 and 5, and specially in the former. Indeed, applying a selection criterion as proposed in Figure 3.2 results into the potential incorrectly-modeled regions $\mathfrak{E} = \{E_4, E_5\}$.

As we can see, a first ECR analysis introduces valuable *a priori* information about model error: it accurately estimates the location of the error over the beam and, moreover, indicates that the error is mainly related to stiffness.

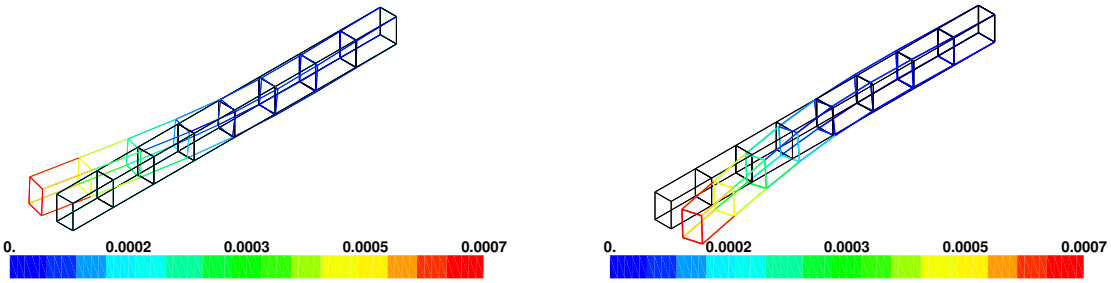

Figure 3.9: *Admissible fields $\{u - v\}$ (left) and $\{u - w\}$ (right) minimizing the ECR cost function for the reference FE model.*

Model parameter estimation

As a result of the preliminary ECR analysis, the obtained information about the FEM error can be introduced by selecting a new reduced parameter vector θ containing a set of model parameters to be identified. Hence, from the previous information, one can consider here that the vector of model parameters selected for updating is:

$$\theta = \{d_4 \quad d_5\}^T \tag{3.20}$$

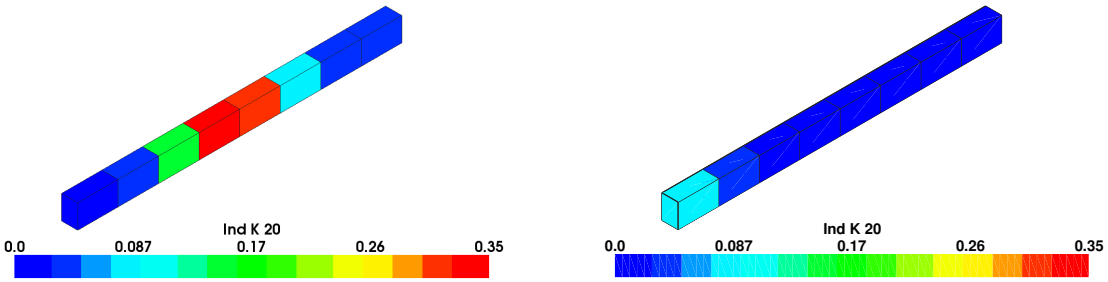

Figure 3.10: *Distribution of Ind_{K_E} (right) and Ind_{M_E} (left) error indicators over the structure for the reference FE model.*

and a convenient parametrization of the FEM would be:

$$\begin{aligned} [M] &= \bigsqcup_{i=1}^{8} [M]_{E_i} \\ [K] = [K(\theta)] &= \bigsqcup_{i=1}^{8} [K]_{E_i} \quad ; \qquad \mathrm{E}_k = (1 - d_k) \cdot \mathrm{E}_0 \quad \text{for} \quad k = 4, 5 \end{aligned} \tag{3.21}$$

Notice that the reduced size of model parameters to be updated is one of the key reasons for using the ECR analysis as a method to improve the *a priori* knowledge of model errors. At this point, the correction step will only be performed for d_4 and d_5 since the rest of parameters remain constant. To do so, a state-space formulation as (3.13) is needed. In this first example, we tackle the case of time-invariant parameters since measurements $\tilde{u}_\omega$ represent a steady-state situation of the structure. Therefore, we can write

$$\zeta_j = 0 \quad \forall j, \qquad \tilde{u}_{\omega j} = \tilde{u}_\omega \quad \forall j \tag{3.22}$$

In this particular case, Figure 3.11 shows the result of the identification process for the afore-described system where the Unscented Kalman filter has been used as an algorithm to obtain parameter estimates as described in Figure 3.7. It can be seen that the identification converges towards the actual values of θ showing how both, ECR cost functions can be introduced as a measure in the observation space and the UKF can be used for optimization purposes in this specific framework.

As a visual example, Figure 3.12 illustrates, for 2 different intial guesses of θ_0, the sequence of UKF estimates over ECR cost function isolines. From this example, it is easy to observe that the UKF algorithm behaves as a descent method seeking the minimum of the ECR. In this example, we can also remark that, for the cases where the UKF estimates live in a low gradient region of the ECR cost function, the algorithm presents slow convergence towards the true values. In the next examples of this chapter, we will see how the covariance matrix $\mathcal{Q}_j$ plays a very important role in this issue.

This example is also used to solve the case where, from the analysis of Figure 3.10, the vector of model parameters is increased with a certain lack of knowledge of the global stiffness. Within this

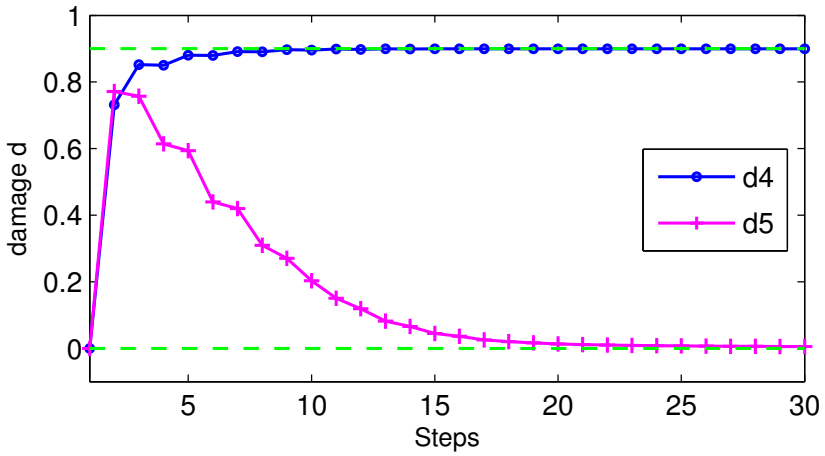

Figure 3.11: *Identification of damage parameters with the ECR-UKF algorithm.*

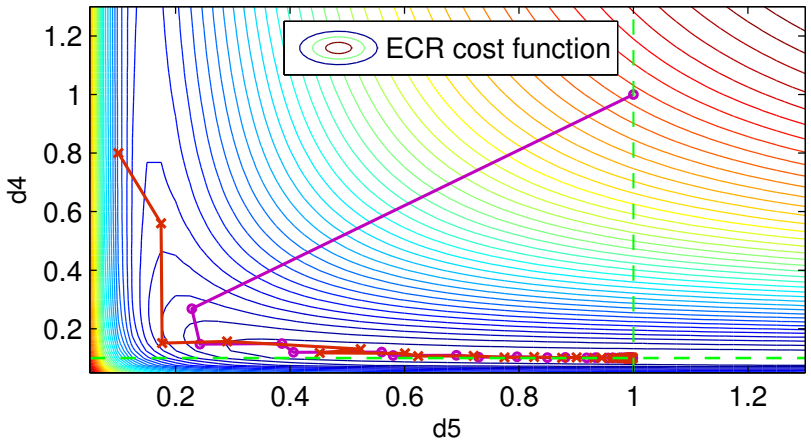

Figure 3.12: *Identification paths over ECR cost function using UKF algorithm for two different initial guesses of θ_0 .*

assumption the new vector of model parameters is defined by:

$$\theta = \{d_4 \quad d_5 \quad d_{\bar{4}\bar{5}}\}^T \tag{3.23}$$

where $d_{\bar{4}\bar{5}}$ is the stiffness reduction of all the elements of the beam except E_4 and E_5. Thus, the parametrization of the FEM becomes:

$$\begin{aligned} [M] &= \bigsqcup_{i=1}^{8} [M]_{E_i} \\ [K] = [K(\theta)] &= \bigsqcup_{i=1}^{8} [K]_{E_i} \quad ; \qquad \mathrm{E}_k = (1 - d_k) \cdot \mathrm{E}_0 \quad \text{for} \quad k = 4, 5, \bar{4}\bar{5} \end{aligned} \tag{3.24}$$

Figure 3.13 shows that, despite a less precise *a priori* information of model errors, the procedure leads to a satisfying estimation of the stiffness bias for the whole structure. Nevertheless, the identification requires more steps to achieve convergence and, once again, one can observe that the optimal estimation of d_5 slows down the convergence. In section 5.2, where the influence of the covariance matrix in the estimation procedure is studied and we will show how the algorithm parameters can be tuned to obtain faster convergence.

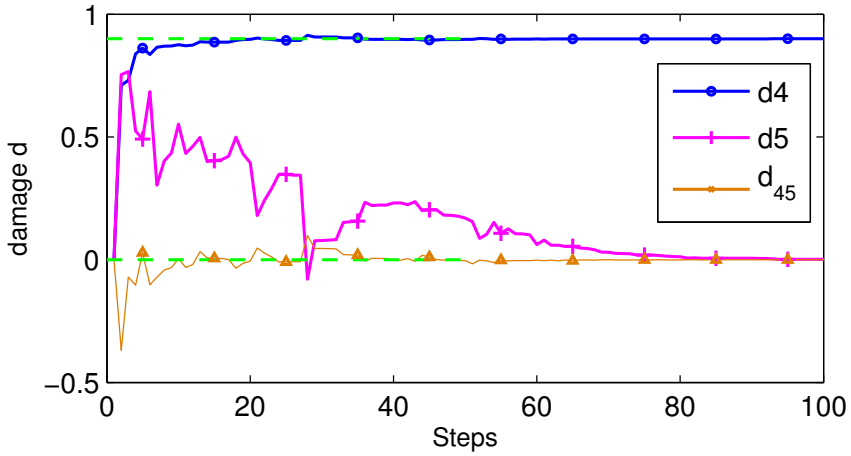

Figure 3.13: *Identification of model parametres θ defined in* (3.23) *by means of the ECR and UKF coupled strategy.*

Moreover, in order to evaluate the performances of the coupled ECR and UKF strategy, the parametrization defined in (3.23) and (3.24) has been used to both compare UKF and EKF algorithms and evaluate the effectiveness of changing the observation space from measurement spaces to a measure given by the ECR functional.

Figure 3.14 illustrates the evolution of $\xi^2_{Tr}(\theta_j)$ throughout the identification process when solving the identification problem with either the EKF or the UKF. It can be seen that the UKF presents general better performance than EKF and, in particular, a faster convergence and a better final parameter estimaton. This can be explained by the fact that UKF achieves second-order accuracy when evaluating covariance matrices while EKF carries out first order approximation of the estimates only by linearizing system nonlinear functions, and in our particular case, the observation operator $\xi^2_{Tr}(\cdot)$.

For comparison purposes, an identification of vector (3.23) has been performed considering the use of the Boolean projection operator Π in the observation space. In this case, the corresponding state-space description for parameter identification is:

$$\begin{cases} \theta_{j+1} = \theta_j + w_j^\theta \\ \tilde{u}_j = \Pi q_\omega(\theta_j) + e_j \end{cases} \tag{3.25}$$

The UKF is therefore used to identify θ. The results shown in Figure 3.15 and Figure 3.16 illustrate the poor ability of this approach to achieve convergence towards actual values. This seems to be natural

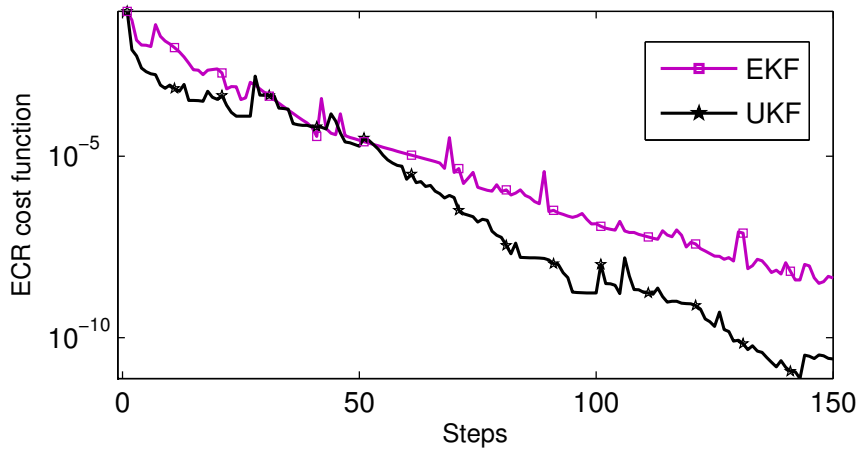

Figure 3.14: *Comparison of $\xi^2_{Tr}(\theta_j)$ residual along the identification process for Extended Kalman filter and Unscented Kalman filter.*

since the convexity properties of the cost function built upon a Boolean operator is poor with respect to the ECR cost function.

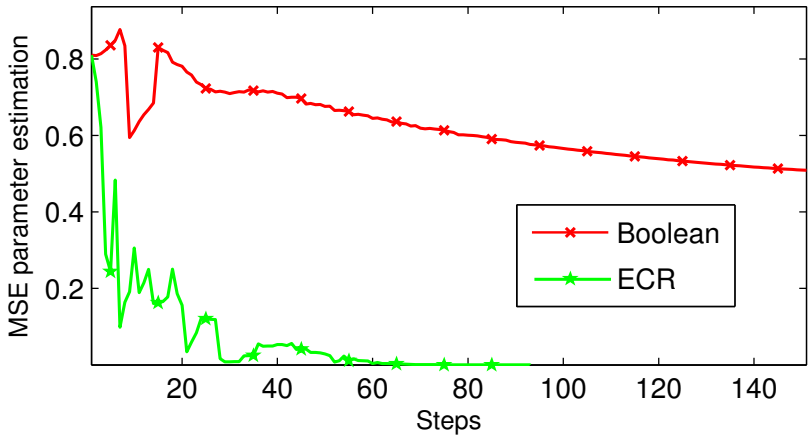

Figure 3.15: *Comparison of the parameter θ Mean Square Error (MSE) when applying UKF with ECR or Boolean observation operators.*

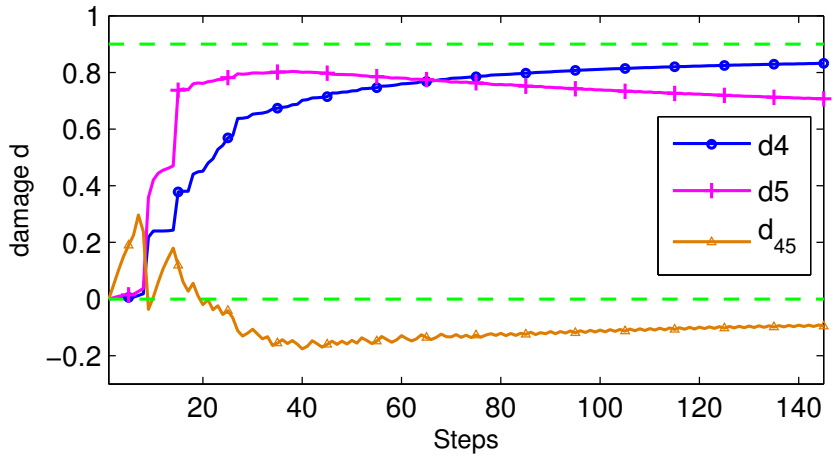

Figure 3.16: *Identification of model parameters θ defined in* (3.23) *with UKF with the Boolean observation operator* Π.

3.6 Conclusions

In this chapter, the principles of the combined ECR-UKF approach have been developed. For this, the first section 3.2 proposes to exploit the ECR to spatially localize model errors and identify their nature. Furthermore, sections 3.3 and 3.4 show how the preliminary ECR information can be introduced into a state-space description and solved with the UKF. The general approach is summarized in Figure 3.17 below and illustrated throughout a numerical example in the last section. In this example, the ECR presents a good ability to localize errors in space and the ECR-UKF conveniently solves the parameter identification problem.

The next two chapters are devoted to further investigate the adequacy of this approach to answer the main objectives of this work as defined in the introduction and general overview of the thesis. In that sense, chapter 4 puts in use the ECR-UKF in cases of industrial relevance. Thus, the problems of structural damage assessment and boundary condition mis-modeling identification are addressed. Moreover, in an effort to propose a state estimation strategy within the framework of the ECR-UKF, section 4.3 studies a field reconstruction problem based on ECR information.

The last chapter of this part aims at improving the performances of the ECR-UKF in order to propose a robust algorithm for a future use. For this, the introduction of algebraic constraints and a parametric study of error covariance matrix are addressed.

I Preliminary ECR analysis

(a) Define a frequency range of interest $[\omega_{min}, \omega_{max}]$.

(b) For $\omega \in [\omega_{min}, \omega_{max}]$ and given θ obtain the triple of admissible fields $\mathcal{T}_\omega = (\hat{u}, \hat{v}, \hat{w})$ by solving the inverse problem associated to the ECR cost functional $e^2_\omega(\{u\}, \{v\}, \{w\})$ defined in (1.26).

(c) Obtain a topology over Ω of the ECR indicator by evaluating for each substrucure $E \in \Omega$:

$$\xi^2_{Er} = \int_{\omega_{min}}^{\omega_{max}} \eta(\omega) \left(\frac{e^2_{\omega E}(\mathcal{T}_\omega, \theta)}{D^2_\omega(\{\hat{u}\}, \theta)} \right) \mathrm{d}\omega$$

(d) Localize potentially mis-modeled regions $\mathfrak{E} \in \Omega$ based on the previous error topology by using a selection criterion:

$$\xi^2_{Er} \geq \delta . \max_{E \in \Omega} \xi^2_{Er} \quad \Rightarrow \quad E \in \mathfrak{E}$$

with δ a user defined value, for example $\delta = 0.8$

(e) Distinguish from the nature of the error by evaluating the different contributors Ind_{K_E} and Ind_{M_E} of ξ^2_{Er} as defined in (3.7) and (3.8) for $E \in \mathfrak{E}$.

II Model parameter estimation

(a) Parametrize model matrix $[M(\theta)], [C(\theta)]$ and $[K(\theta)]$ with $\theta = \{\theta_1 \dots \theta_n\}^T$ according to Ind_{K_E} and Ind_{M_E} indicators of the preliminary ECR analysis.

(b) Introduce discrete stationarity equation of θ and ECR cost function in a state-space description as defined in (3.13):

$$\begin{cases} \theta_{j+1} = \theta_j + w^\theta_j \\ \zeta_j = \xi^2_{Tr}(\theta_j) + e_j \end{cases}$$

(c) Perform model parameter identification by applying Unscented Kalman filter equations to the previous state-space description as detailed in Figure 3.7.

Figure 3.17: *General overview for model state and parameter estimation combining ECR and Unscented Kalman filter.*

Chapter 4

ECR and UKF for model enhancement in problems of industrial relevance

Contents

4.1 Damage identification through the ECR-UKF strategy for high DOF models

Structural damage or health monitoring has received considerable attention during the last few decades, and is still an area of active research. The reader can find an interesting overview on this topic in [35] or a literature review in [30]. Broadly speaking, in structural dynamics, damage detection is generally based in the basic idea that modal properties (eigenfrequencies, modes shapes or modal damping) are functions of the physical properties of the structure and therefore changes in the physical properties will cause changes in the modal properties. This assumption has been widely applied in the field of civil structures (see for example the work of Teughels and De Roeck in [83, 73]) and applied within specific techniques depending on the problem's nature, as for instance in concrete structures [87, 63], for on-line identification with the the help of neural networks [74] or Kalman filtering [61], and using fuzzy logic for uncertainty quantification in [25].

This section is dedicated to evaluate the ability of the ECR-UKF approach to tackle the problem of structural damage identification as an alternative to the above-mentioned research contributions. Hence, it wishes to accomplish two of the main purposes of this discipline, namely localize damage in space and provide an estimation of the severity of the damage.

For this, we have chosen to study the dynamical behavior of a damaged power plant cooling tower subjected to wind loads. In this case, an additional challenge is to tackle high degrees of freedom (DOF) complex models, which is generally required in industrial contexts.

The geometry of the chosen FE model is presented in Figure 4.1 where its main characteristics are:

- Number of DOF: 6624
- Material: concrete with elastic properties $\mathrm{E} = 20 \cdot 10^9 \mathrm{N/m}^2$, $\varrho = 2400 \mathrm{kg/m}^3$ and $\nu = 0,2$. Low Rayleigh damping with $\alpha_{Ray} = 1.2425$ and $\beta_{Ray} = 6.3649 \cdot 10^{-6}$
- External load: white noise of $1000N$ over the frequency range $[0\mathrm{Hz}, 5\mathrm{Hz}]$ on x direction. Force is uniformly applied to all nodes with coordinates verifying $x < 0$.
- Damaged region $\mathcal{D}$ presented in Figure 4.1(a) with stiffness reduction corresponding to $d_{\mathcal{D}} = 0.6$ where $\mathrm{E}_{\mathcal{D}} = (1 - d_{\mathcal{D}})\mathrm{E}_0$.
- Number of sensors: 30 measuring in x, y and z direction. Spatial distribution is shown in Figure 4.1(b).
- 5% of sensor noise

In this example, the above-described FEM is used to generate synthetic measurements whereas an equivalent FE model with no structural damage is used as a reference model for identification purposes.

One of the main issues when dealing with large DOF problems is to manipulate model matrices. In particular, for a $\mathcal{N}$-DOF FE model, the corresponding ECR problem is of size $3\mathcal{N}$. Besides, it is widely known that one of the main difficulties of Kalman filtering is to deal with large DOF problems. To overcome those obstacles, we propose to reduce the model size by projecting matrices onto a reduced space as proposed in [27]. Hence, in structural dynamics, the physical displacements $\{q\}$ can be described by

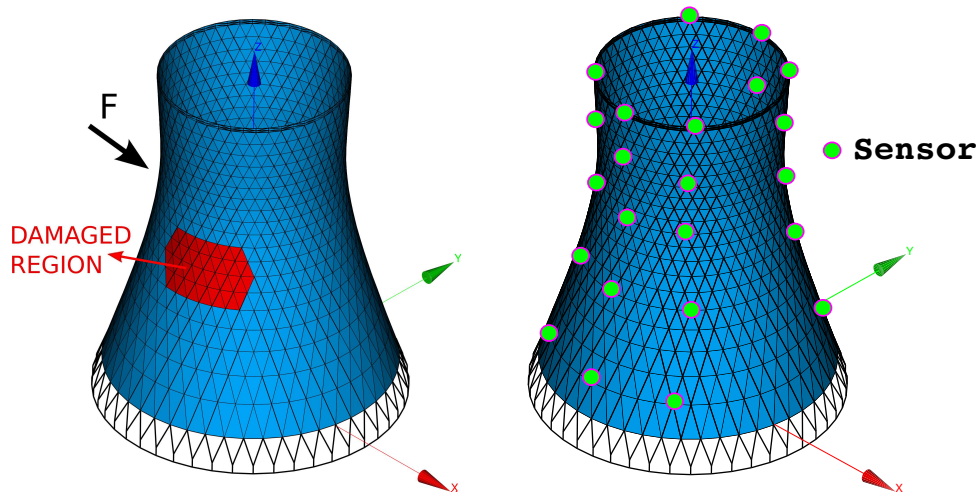

(a) Cooling tower with structural damage subjected to wind loads.

(b) Set of sensors over the cooling tower

Figure 4.1: *Power plant cooling tower FE model used to generate synthetic measurement data.*

the following substitution:

$$\{q\} = \Phi\{p\} \tag{4.1}$$

where $\{p\}$ are the so-called generalized displacements since $\Phi = [\varphi_1, \varphi_2, ..., \varphi_{\mathcal{N}}]$ is a projection matrix built from the normalized eigenvectors φ_i such that:

$$\begin{cases} \Phi^T[M]\Phi = [Id] \\ \Phi^T[K]\Phi = [\Lambda] \end{cases} \tag{4.2}$$

where $[\Lambda] = \text{diag}(\omega_1^2, \omega_2^2, ..., \omega_{\mathcal{N}}^2)$. For low-damping structures, modal damping can be assumed and the hypothesis that equations are fully decoupled holds:

$$[\Gamma] = \Phi^T[C]\Phi = 2\text{diag}(\zeta_1\omega_1, \zeta_2\omega_2, ..., \zeta_n\omega_{\mathcal{N}}) \tag{4.3}$$

In order to significantly decrease the size of the model matrices, a reduced basis of size $r < \mathcal{N}$ built upon a Ritz reduction method is applied. In this case, the following approximation is used:

$$\{u\} \simeq \Phi^{\text{red}}\{p^{\text{red}}\} \tag{4.4}$$

where $\Phi^{\text{red}} = [\varphi_1, \varphi_2, ..., \varphi_r]$ and $\{p^{\text{red}}\} = \{p_1, p_2, ..., p_r\}^T$. Moreover, the reduced basis Φ^{red} will be enriched with a Schur complement φ^S associated to a static correction. Thus, the proposed reduced projection basis is set to be $\Phi_R = [\Phi^{\text{red}}, \varphi^S]$ and the corresponding model matrices become:

$$\begin{cases} [\bar{M}] = \Phi_R^T[M]\Phi_R \\ [\bar{\Lambda}] = \Phi_R^T[K]\Phi_R \\ [\bar{\Gamma}] = \Phi_R^T[C]\Phi_R \\ \bar{F} = \Phi_R^T F \end{cases} \tag{4.5}$$

The projected reduced model (4.5) is therefore used to evaluate the model error through the ECR indicator $\xi_{Tr}^2(\cdot)$, drastically reducing the computational cost of this calculation. Notice that, when evaluating the ECR cost functional using a reduced model, the observation operator Π needs to consequently be transformed by $\bar{\Pi} = \Phi_R^T\Pi$. In the present example, a reduced basis of 70 eigenvectors completed with a static response has been used to evaluate the ECR spectrum of the reference model. The results shown in Figure 4.2 reveal the model error content over the bandwidth of interest. In our case, the reference model response seems to be significantly erroneous around 0.9Hz, 1.1Hz, 1.35Hz and 2.47Hz, where the ECR spectrum presents its higher values.

The information contained in the ECR spectrum can usefully be introduced in the construction of the weighting function $\eta(\omega)$ needed in the evaluation of $\xi_{Tr}^2(\cdot)$. In this example the choice of the weighting function is illustrated in Figure 4.2 where the above-mentioned frequencies are chosen as a reference bandwidth for model error evaluation.

Based on the previous choice of $\eta(\omega)$ and considering every element of the FE mesh as a substructure, the study of the $\xi_{Er}^2(\cdot)$ over the whole structure leads to a model error distribution. Considering that Ind_{M_E} is negligible compared to Ind_{K_E} indicator, only the result of the Ind_{K_E} over the cooling tower is

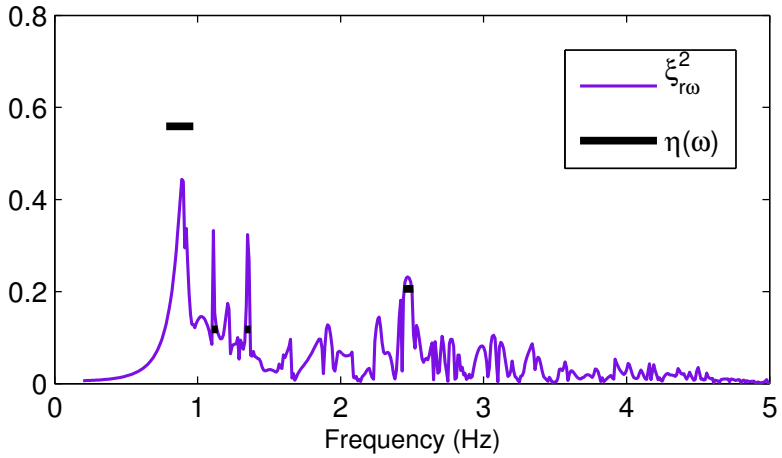

Figure 4.2: *ECR spectrum for reference cooling tower FE model and consequent choice of weighting function $\eta(\omega)$.*

shown in Figure 4.3(a). As it can be observed, a satisfying agreement between the true damaged region and the identified with the ECR analysis is obtained. Hence, it can be stated that the results qualitatively improves the *a priori* knowledge of regions presenting a stiffness bias.

Considering the preliminary ECR analysis, a choice of reduced model parameters to be updated is therefore possible. In our example, Figure 4.3(b) shows a possible division of the mis-modeled regions of the cooling tower based in a ECR selection criterion. Notice that, since global dynamic behavior is

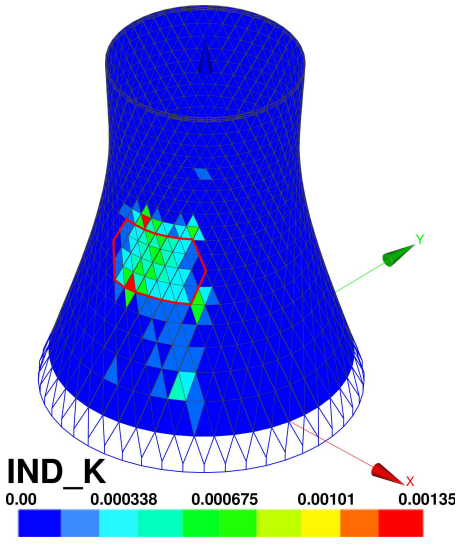

(a) Distribution of Ind_{K_E} indicator for the reference model.

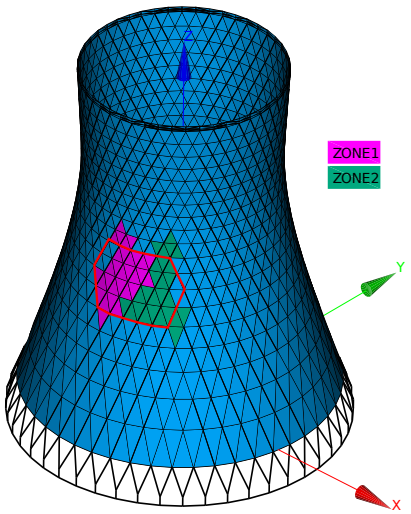

(b) Updating selected regions based in ECR analysis

Figure 4.3: *Results of the preliminary ECR analysis over the power plant cooling tower FE model.*

sought, the size of the regions to be updated are larger than the size of a mesh element. In the proposed decomposition, "zone1" and "zone2" correspond to global continuous regions of "higher" and "lower" Ind_{K_E} indicator respectively. Hence, a FE model parametrization can be done in a similar way to (3.21) where the sub-structures k that parametrize the global stiffness matrix $[K]$ can either be $zone1$ and $zone2$. Three different parametrization cases are summarized in Figure 4.4 where the UKF algorithm is applied to a state-space description of the form (3.13). Figure 4.4(a) shows the results for two cases where the choice of a single region is introduced in the updating algorithm (the union of $zone1 + zone2$ and $zone1$ only). On the other hand, the case where $zone1$ and $zone2$ are considered as potentially different damaged zones is treated in Figure 4.4(b).

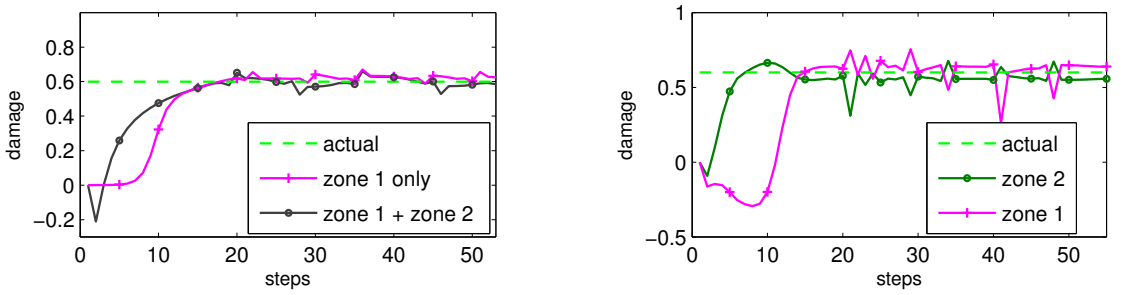

(a) Distribution of Ind_{K_E} indicator for the reference model.

(b) Identification of $zone1$ and $zone2$ separately.

Figure 4.4: *ECR-UKF approach for damage identification of a power plant cooling tower based in a ECR preliminary analysis.*

In all the cases, despite the fact that the damage location is not exact, the identified loss of stiffness parameters is close to the actual damage value. One will remark a certain lack of stability of the solution, in particular for the case in Figure 4.4(b). This can be explained by the fact that both the selected regions to be updated are inaccurate and the introduction of a constant covariance of the parameters error $\mathcal{Q}_j$ makes the algorithm search in the neighboring regions of the optimum set of parameters. In section 5.2 we will try to improve this point by analyzing the role of $\mathcal{Q}_j$ throughout the identification process. Nevertheless, it is clear that the *a priori* knowledge of the initial FE model is improved since the location of a damaged zone and its intensity are identified satisfactorily. Indeed, Figure 4.5 shows how the proposed strategy enhances the quality of the FE model from perspective of the modal response.

4.1.1 Case of evolving parameters

Based in the previous power plant cooling tower example, this investigation deals with the case of evolving parameters. In particular, we consider the case where the damage evolution law is *a priori* unknown and the aim of this study is to demonstrate how the Kalman filter framework is particularly suited to treat such a situation.

Firstly, since the ECR is formulated in the frequency-domain, a time-frequency equivalence is re-

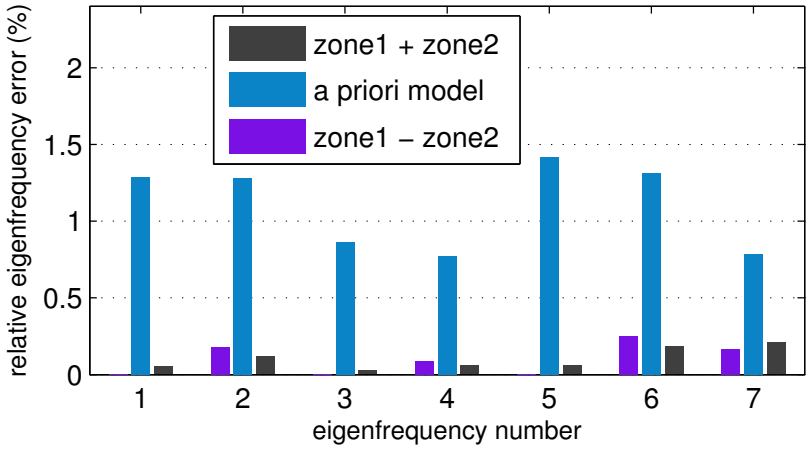

Figure 4.5: *Comparison of the eigenfrequencies relative error of the a priori FE model, the identified* $zone1 + zone2$ *and the separately identified* $zone1$-$zone2$ *models with respect to real eigenfrequencies.*

quired. Suppose that we dispose of time-domain measurements $\tilde{u}(t)$ defined in $t \in [0 : T]$. It is assumed, on the other hand, that the sought-after evolution is slow enough to be captured from a windowing partition of $\tilde{u}(t)$ in a sequence of m shorter samples $\tilde{u}_j(t)$ for $j = [1, \ldots, m]$ given by:

$$\begin{cases} \tilde{u}_j(t) = \tilde{u}(t) \quad \text{for} \quad t \in [t_j : t_j + \overline{T}] \\ t_j = (j-1)(1-\mathbf{o})\overline{T} \end{cases} \tag{4.6}$$

where $\overline{T}$ is the sample window duration such that $\overline{T} < T$ and $\mathbf{o} \in [0 : 1)$ represents the samples overlap. As a matter of fact, samples are built with a certain overlap to prevent information loss and generally different filters (Hanning, Hamming, rectangular, flat-top, etc.) are applied to each sample to avoid the leakage effect. Thus, a Fourier transformation of each sample $\tilde{u}_j(t)$ can be performed leading to a sequence of frequency-domain measurements $\{\tilde{u}\}_j$ for $j = [1, \ldots, m]$.

In order to capture the dynamics of the lower eigenfrequency modes, in this work we have systematically chosen a sample window duration verifying $\overline{T} > 1/f^1_{\text{eig}}$, where f^1_{eig} is the lowest structural eigenfrequency in the studied frequency range. On the other hand, the choice of the overlap $\mathbf{o}$ determines the time step sampling allowing to capture structural changes corresponding to $(1-\mathbf{o})\overline{T}$. This is a user-dependent choice built upon the *a priori* knowledge of sought changes. In this work we have chosen $\mathbf{o}$ so that the time step $(1-\mathbf{o})\overline{T}$ is of the order of magnitude of the highest eigenperiods $(1-\mathbf{o})\overline{T} \approx 1/f^1_{\text{eig}}$.

Hence, the iterations steps j from (3.13) can now be considered as time-steps since they correspond to each window sample. Consequently, measurements $\{\tilde{u}\}_j$ are recursively introduced in $\xi^2_{Tr}(\cdot)$ as the identification process goes on. Thus, we can rewrite the state-space formulation in (3.13) for the evolution problem as:

$$\begin{cases} \theta_{j+1} = \theta_j + w^\theta_j \\ \zeta_j = \xi^2_{Tr}(\theta_j, \{\tilde{u}\}_j) + e_j \end{cases} \tag{4.7}$$

where the condition $\zeta_j = 0 \quad \forall j$ is maintained since the the minimum of $\xi^2_{Tr}(\cdot)$ is tracked.

In this example, we have used a sequence of $m = 60$ samples of a time duration $\overline{T} = 2.5s$ with an overlap $\mathbf{o} = 0.6$. Moreover, the final damage state has been chosen to be identical to that of the stationary case of section 4.1 and, therefore, the preliminary ECR analysis is fully described in Figure 4.2 and Figure 4.3. Hence, we consider that the final state contains all the information about the presence of damage and the spatial localization step is based in that assumption. In this case, the model parametrization is chosen to be the Young's modulus of the union of $zone1$ and $zone2$.

Figure 4.6 illustrates how the ECR-UKF coupled method has the ability to track damage evolution over time. Qualitatively speaking, the damage evolution law identified by the ECR-UKF algorithm agrees quite well with the actual damage evolution and, in consequence, the knowledge of structural changes is improved. Note that the estimated evolution law presents a delay when sudden damage occurs. This is a well known Kalman filter phenomenon that can be easily explained by the modeling of error covariance matrix $\mathcal{Q}_j$, as illustrated in Figure 4.7. Indeed, introducing "high" values of $\mathcal{Q}_j$ implicitly reflects a low confidence on the parameter stationarity equation. Accordingly, Kalman filter allows bigger variations in the sequence of parameter estimations and faster variations can be captured at the expense of solution stability. On the contrary, "small" values of $\mathcal{Q}_j$ guarantee a better stability of the solution while rapid changes are difficult to detect. In that sense, modeling covariance matrices $\mathcal{Q}_j$ becomes an important issue, deserving of a separate study (see section 5.2).

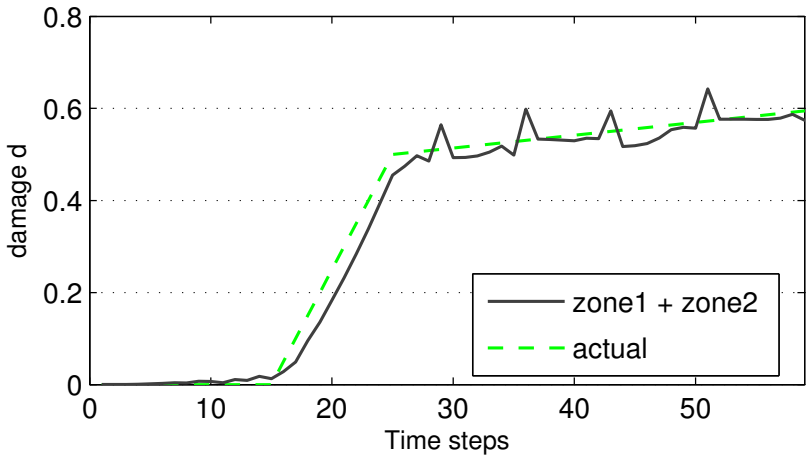

Figure 4.6: *ECR-UKF approach for time-varying damage identification of a power plant cooling tower. Damage region is based on the ECR preliminary analysis of Figure 4.3.*

In this section we have studied the ability of the ECR-UKF for damage assessment in complex structures. The preliminary ECR analysis, showed a good ability to spatially localize erroneously modeled regions without any *a priori* knowledge of their location. As a matter of fact, after performing model reduction aiming at reducing computational cost, an ECR spectrum revealed the most erroneously frequencies which were further used to evaluate the space distribution of model errors. Furthermore,

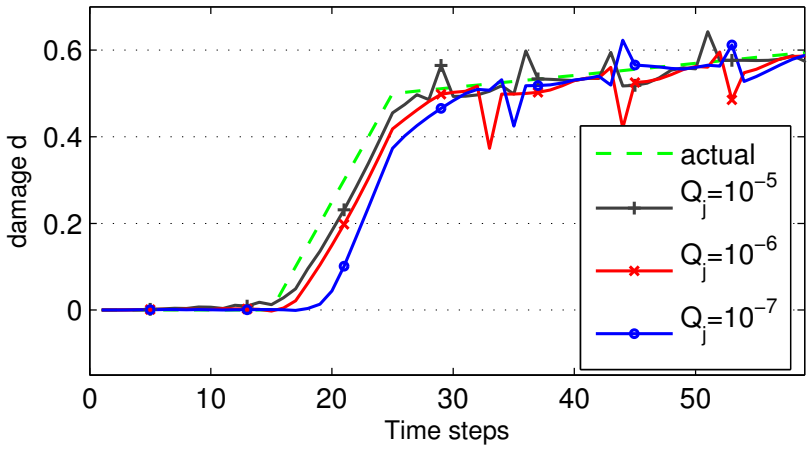

Figure 4.7: *Influence of the covariance matrix $\mathcal{Q}_j$ in time-varying damage identification using the ECR-UKF approach for a power plant cooling tower.*

model-updating was performed by means of a reduced-size model parametrization and solved by the ECR-UKF. This approach was tested for both invariant and time-evolving damage with convergence to the actual magnitude of damage. The study of identifying structural flaws in complex structures is further completed in chapter 6 where the use of ECR methods are applied to a FE model of nuclear power plant auxiliaries building subjected to seismic loads.

4.2 Identifying incorrect modelling of boundary conditions

In many industrial cases the accuracy of boundary condition modeling directly determines the quality of model predictions. As a matter of fact, in-operation structures are often subjected to environment coupling that significantly affects its global dynamic behavior. Moreover, since the information about the boundary coupling is difficult to obtain, structures are often studied as isolated bodies and in many cases perfect boundary condition modeling is considered (perfect clamping, free edges, etc.). In many cases, the knowledge of erroneous boundary modeling is supposed to be *a priori* known, and in these circumstances, one can find specific approaches in the literature as [1] for Euler-Bernoulli beam formulation, or a more general approach for frequency-domain formulation in the work of Frikha et al. in [38, 39].

In the numerical example treated herein, the problem of boundary conditions mis-modeling is addressed with the assumption that the location of boundary errors is *a priori* unknown. To do so, a simplified FE model of a double-clamped concrete beam is considered where one of the clampings is supposed to be imperfect. The geometry presented in Figure 4.8 corresponds to the FE model used to generate synthetic measurements.

In order to represent an imperfect clamping that introduces dynamical coupling with the concrete beam, a frequency domain boundary impedance has been modeled of the form:

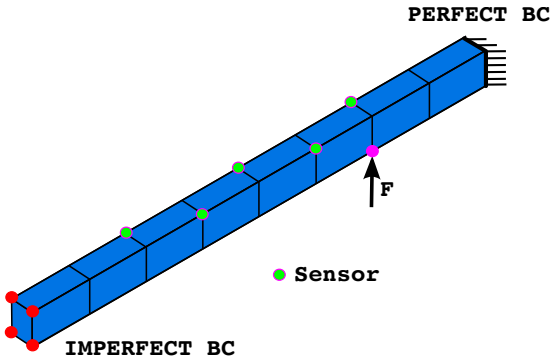

Figure 4.8: *FE model of a concrete beam containing imperfect clamping used to generate synthetic data.*

$$z(\omega) = (-\omega^2 m + k)^{-1} \tag{4.8}$$

In the present example, an identical impedance of the form (4.8) is applied at each of the four nodes highlighted in red in Figure 4.8.

Moreover, the main characteristics of the FE model are given in the following description:

- Number of DOF: 96
- Material: concrete with elastic properties E $= 20 \cdot 10^9$N/m^2, $\varrho = 2400$kg/m^3 and $\nu = 0,2$. Low Rayleigh damping with $\alpha_{Ray} = 1.2425$ and $\beta_{Ray} = 6.3649 \cdot 10^{-6}$
- Impedance $z(\omega)$ parameters: $k = 10^7$N/mm, $m = 33.057$kg
- External force: white noise with $445N$ mean over the bandwidth $[0Hz, 600Hz]$
- Number of sensors: 5 in z direction only.
- 5% of sensor noise

We consider the case where a reference model is assumed to have perfect clamped boundary conditions. The goal of the proposed approach is to first locate (in frequency and space) the presence of imperfectly-modeled boundary conditions. Secondly, the identification of impedance parameters is sought in order to improve the knowledge of neighboring coupling and the predictive quality of the structure model.

In this context, given a set of measurements $\tilde{u}$ generated by the above-described FEM, a first ECR analysis introduces valuable *a priori* information about the agreement of the reference model to $\tilde{u}$. In our example, the ECR spectrum shown in Figure 4.9 indicates that the double-clamped beam gives particularly bad predictions in the bandwidth $[0\text{Hz}, 150\text{Hz}]$. Nevertheless, we can observe that for a very particular set of frequencies, the ECR spectrum presents important drops. This is can be easily explained by the fact that, for those f requencies, model responses are mainly orthogonal to both sensor direction and model error, which are basically in the z direction.

Going into the details of the model error in the bandwidth $[0Hz, 150Hz]$, a distribution of model error is evaluated with the help of Ind_K and Ind_M indicators. The results of this preliminary ECR

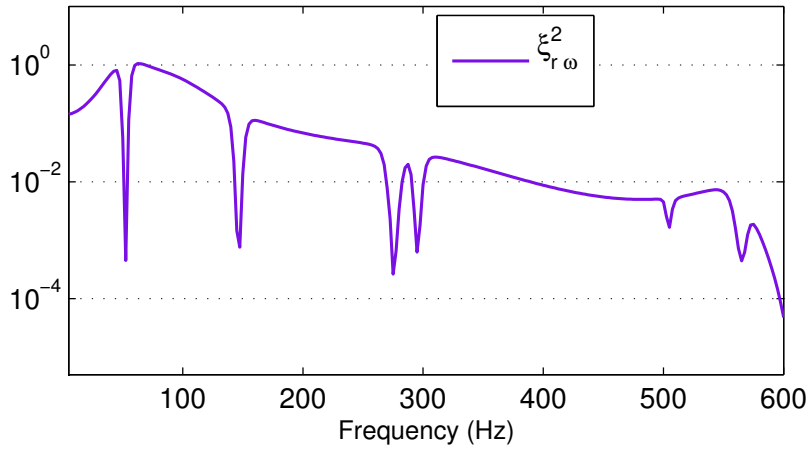

Figure 4.9: *ECR spectrum for perfect double-clamped FE model.*

analysis are given in Figure 4.10. As it can be seen, model error seems to be fully concentrated in the element containing mis-modeled DOF. It is important to remark that only Ind_K indicator reveals the presence of error in this region. Indeed, when looking at Figure 4.10(b) we observe that the mass error indicator does not suggest the potential presence of mass errors on the boundary.

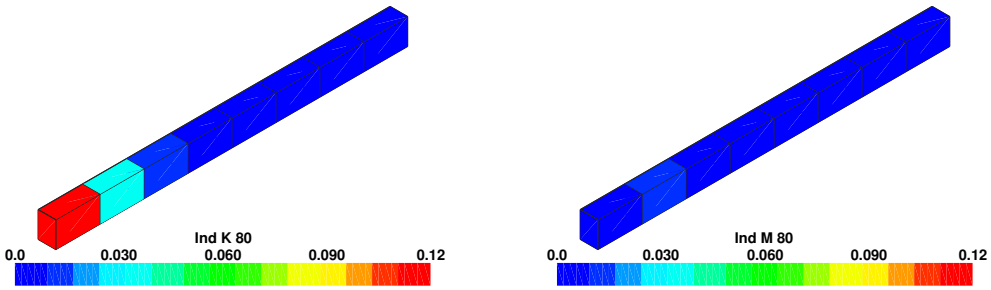

(a) Distribution of Ind_{K_E} (b) Distribution of Ind_{M_E}

Figure 4.10: *Preliminary ECR analysis for a perfect double-clamped concrete beam FE model. Distribution of $IndK$ and $IndM$ estimators over the structure at 80Hz.*

What happens if we liberate the potentially erroneous DOF initially representing a perfect clamping? The answer can be seen in Figure 4.11 where now the Ind_M indicator is the main witness of the presence of boundary error. Comparing both extreme cases, when perfect clamping is assumed the adjacent element to the boundary condition seems to embed high stiffness error. Besides, when a free edge condition is supposed instead, the stiffness error vanishes while a high mass error appears. This particular behavior suggests the presence of model errors directly attributable to the boundary condition modeling.

The preliminary ECR analysis helps us to localize model error in space and, at this point, the suspicion of a boundary condition modeling error stands. To further investigate the error of the perfect

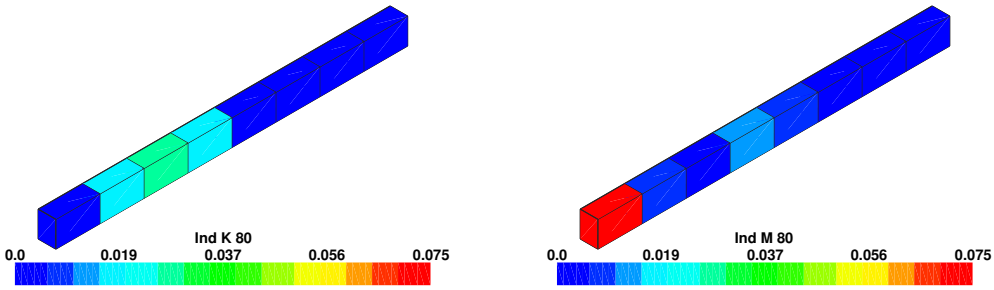

(a) Distribution of Ind_{K_E} (b) Distribution of Ind_{M_E}

Figure 4.11: *Preliminary ECR analysis for a perfect simple-clamped concrete beam FE model. Distribution of $IndK$ and $IndM$ estimators over the structure at 80Hz.*

clamping condition, we propose to adopt the methodology developed in [38] and [39] that aims to characterize the unknown boundary behavior based in a condensation and inversion technique. To fix the ideas, suppose that our frequency-domain FE model is described by:

$$[K + i\omega C - \omega^2 M]\{q\} = \{F\} \quad \Rightarrow \quad [Z_\omega]\{q\} = \{F\} \tag{4.9}$$

where $\{q\}$ and $\{F\}$ are the vectors of nodal displacements and external forces respectively. Moreover, $[Z_\omega]$ represents the dynamic stiffness of the studied structure. In a preliminary stage, equation (4.9) can be rearranged by separating internal and boundary DOF, leading to the following expression:

$$\begin{bmatrix} Z_{ii} & Z_{ib} \\ Z_{bi} & Z_{bb} \end{bmatrix} \begin{Bmatrix} q_i \\ q_b \end{Bmatrix} = \begin{Bmatrix} F_i \\ F_b \end{Bmatrix} \tag{4.10}$$

By simply using the first row of equations in (4.10), it is possible to condensate the internal displacements q_i as a function of the boundary q_b DOF by:

$$q_i = Z_{ii}^{-1}(F_i - Z_{ib}q_b) \tag{4.11}$$

Besides, given a linear observation operator Π projecting the internal displacements q_i into the measurement space, the problem of finding the better boundary displacements q_b that better represents a set of measurements $\tilde{u}$ can be written as:

$$\hat{q}_b = \underset{q_b}{\text{Arg min}} \quad \|\tilde{u} - \Pi q_i\|^2 = \|\tilde{u} - \Pi Z_{ii}^{-1}(F_i - Z_{ib}q_b)\|^2 \tag{4.12}$$

The problem (4.12) can be solved by a least square method involving a pseudo-inverse operator to obtain:

$$\begin{aligned} \hat{q}_b &= Z^+(\Pi Z_{ii}^{-1} F_i - \tilde{u}) \\ Z^+ &= ([\Pi Z_{ii}^{-1} Z_{ib}]^T W [\Pi Z_{ii}^{-1} Z_{ib}])^{-1} [\Pi Z_{ii}^{-1} Z_{ib}]^T W \end{aligned} \tag{4.13}$$

where Z^+ represents the Moore-Penrose pseudo-inverse [13] of model equations in (4.12). In the expression given by (4.13), a weighting matrix W is introduced in order to improve the conditioning of

Z^+. Once the estimation of boundary displacements is obtained by applying the expression in (4.13), the second row of equations (4.10) can be exploited to evaluate the corresponding nodal forces:

$$\hat{F}_b = Z_{bi}[Z_{ii}^{-1}(F_i - Z_{ib}\hat{q}_b)] + Z_{bb}\hat{q}_b \tag{4.14}$$

In the present example, equations (4.13) are used to obtain a preliminary estimation of boundary displacements for the suspected DOF revealed by the preliminary ECR analysis, the results of which are given in Figure 4.12. This estimate confirms that a significant displacement in boundary DOF exist and, consequently, a perfect clamped modeling is erroneous.

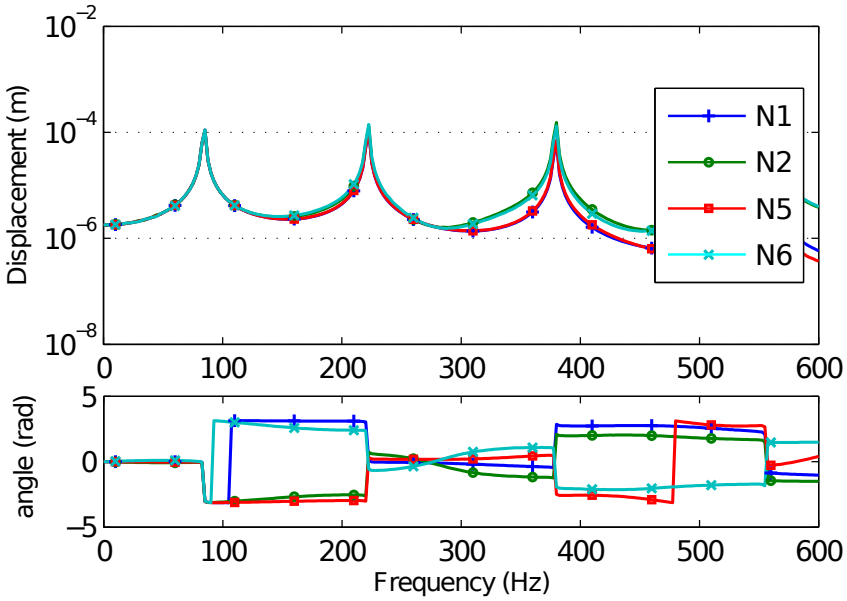

Figure 4.12: *Identified boundary displacements in z direction for the erroneous clamping DOF.*

Furthermore, the assumption that all the incriminated DOFs have a similar boundary impedance stands since the four estimated displacements $\hat{q}_b$ are very similar. Estimating boundary efforts by means of equation (4.14) allows an estimation of the boundary impedance $\hat{q}_b/\hat{F}_b$.

In Figure 4.13, the estimated impedances for each boundary DOF are shown as functions of the frequency. As it can be seen, the existence of a common boundary impedance is suggested with a main resonance around $87.5Hz$ for the four DOFs. Indeed, the four estimated $\hat{q}_b/\hat{F}_b$ not only present a very close resonance in the frequency bandwidth, but a very similar static and high frequency response. Thus, these informations are used to consider a parametrization of a boundary impedance leading to a vector of model parameters θ to be identified that takes the form:

$$\theta = \{k \quad m\}^T \tag{4.15}$$

where k and m are the parameters of a boundary impedance of the form (4.8). In addition, the vector of initial guesses θ_0 is built from the available information of the $\hat{q}_b/\hat{F}_b$ functions. Hence, in our case we

have chosen to set k_0 as the mean value of $\hat{q}_b/\hat{F}_b$ at $0Hz$ for all the DOF. Besides, since the impedance presents a single resonance around $\hat{f} = 87.5Hz$, the initial guess for m_0 is set to $m_0 = k_0/(2\pi\hat{f})^2$. In the present example, we obtain:

$$\theta_0 = \{1.1 \cdot 10^7 \text{N/mm} \quad 36.39\text{kg}\}^T \tag{4.16}$$

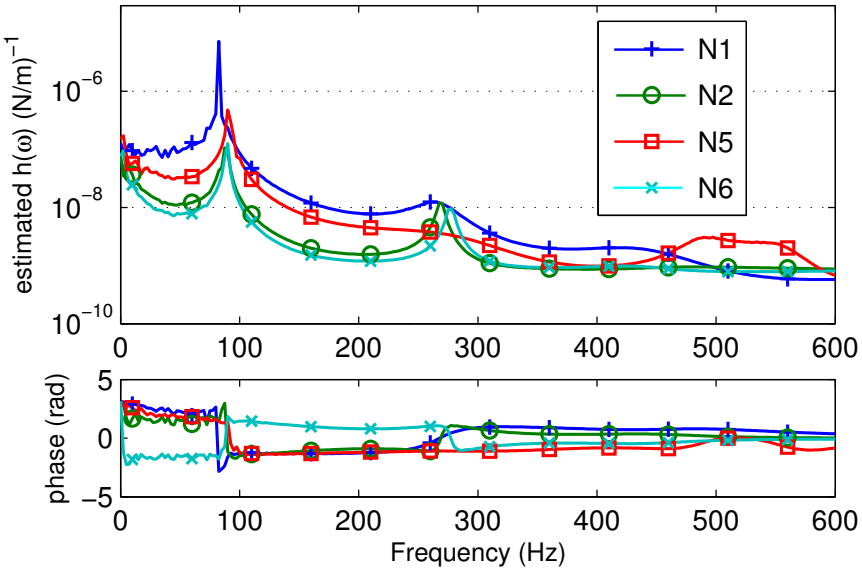

Figure 4.13: *Identified impedance in z direction for the erroneous clamping degrees of freedom.*

When optimal impedance is sought, a parametrization of FE model matrices is considered depending on boundary impedance k and m parameters. Moreover, as in the previous examples, a state-space formulation with ECR functionals in observation space is adopted and solved by applying Unscented Kalman filter algorithm as described in Figure 3.7.

The results of such an identification are presented in Figure 4.14 where one can see that convergence is achieved at actual values for both k and m parameters. As a complement, Figure 4.15 illustrates the evolution of θ_j estimation throughout the identification process over the ECR cost function. As it can be seen, the UKF tracks the optimum value of the ECR cost function and behaves as a gradient descent method.

Notice that, in the example of figures 4.14 and 4.15, the values of θ_0 are more noisy with respect to the ones proposed in (4.16). This is deliberately done in order to evaluate the robustness of the proposed experience to "further" initial guess of θ, since we consider that closer values of θ_0 will also lead to convergence. In this particular example we have taken $\theta_0 = \{10^8 \text{ N/mm} \quad 10 \text{ kg}\}^T$.

Next, boundary mis-modeling in presence of structural damage is addressed. This example introduces a new complexity since the distinction of boundary error and damage error becomes blurred due

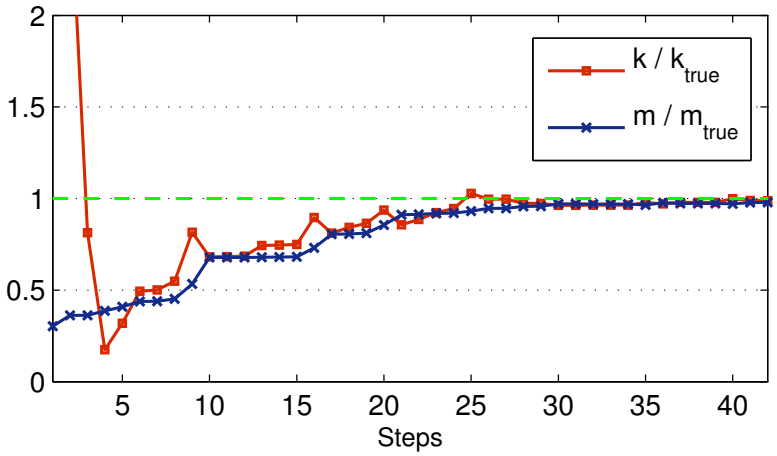

Figure 4.14: *Identification of boundary impedance parameters through the ECR-UKF method.*

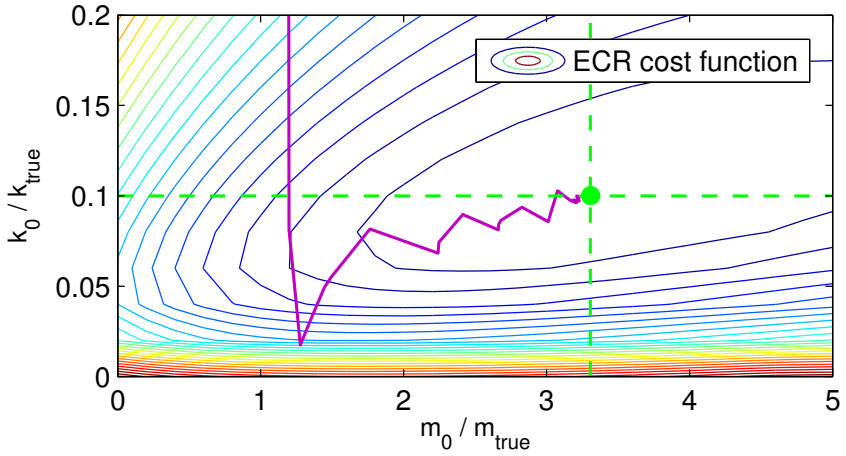

Figure 4.15: *Identification path of impedance parameters over the ECR cost function.*

to their simultaneous presence.

The numerical FE model used to generate synthetic data is presented in Figure 4.16. This FE model only differs from the above-described by the presence of structural damage represented with a highlighted element in Figure 4.16. In this way, a boundary impedance of the form (4.8) and structural damage following (3.17) are considered. While the main characteristics of the FE model as previously described, the presence of damage in element 3 is considered and the global damage vector takes the form:

$$d = (d_1 \quad d_2 \quad d_3 \quad d_4 \quad d_5 \quad d_6 \quad d_7 \quad d_8)^T = (0 \quad 0 \quad 0.6 \quad 0 \quad 0 \quad 0 \quad 0 \quad 0)^T \tag{4.17}$$

Again, the first step consists in performing a preliminary ECR analysis. The spectrum shown in Figure 4.17 compares the previously obtained spectrum with the actual one.

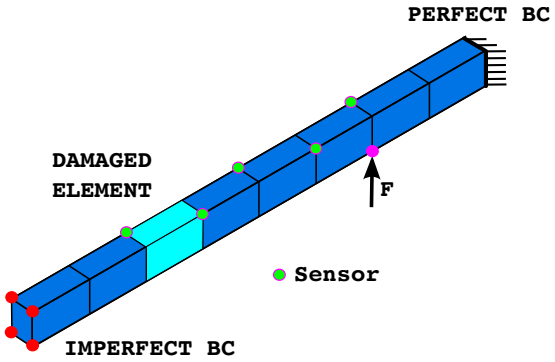

Figure 4.16: *FE model of a concrete beam containing imperfect clamping and structural damage used to generate synthetic data.*

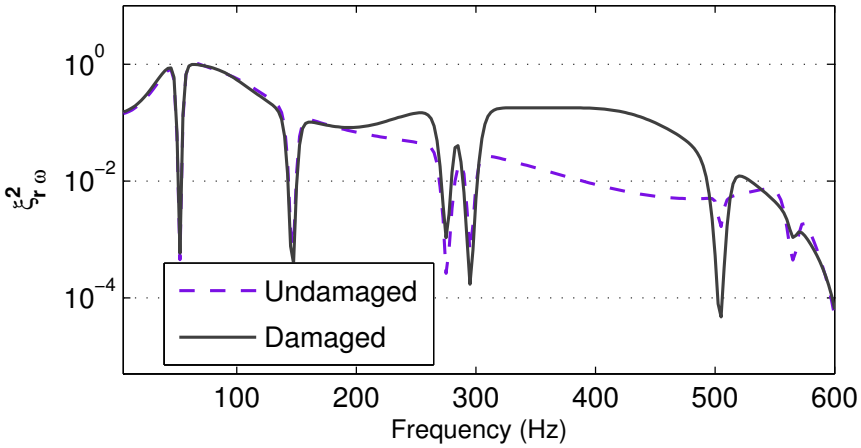

Figure 4.17: *ECR spectrum for perfect clamped FE model.*

As can be seen, the presence of structural damage in this particular configuration contributes to global error in the frequency range $[200Hz, 500Hz]$ while low frequency error is still mainly dominated by the boundary mis-modeling error. Analyzing the elementwise distribution of ECR error over the beam highlights the presence of modelling error concentrated basically in the boundary and the damaged element. Figure 4.18 illustrates the distribution of Ind_K and Ind_M for frequencies 80Hz and 400Hz corresponding to the highest ECR values. Similarly to the previous example, Ind_K appears to be a good indicator to locate boundary mis-modeling and damage since Ind_M is negligible compared to stiffness errors.

Again, since a bad clamping is therefore suspected, removing the kinematic constraint globally suggests a mass error in the erroneous boundary through the Ind_{M_E} indicator. Nevertheless, differently to the previous example, a stiffness error is also highlighted by Ind_{K_E} in the damaged element revealing the presence of a stiffness bias in element number 3. The most relevant results of Ind_{M_E} and Ind_{K_E}

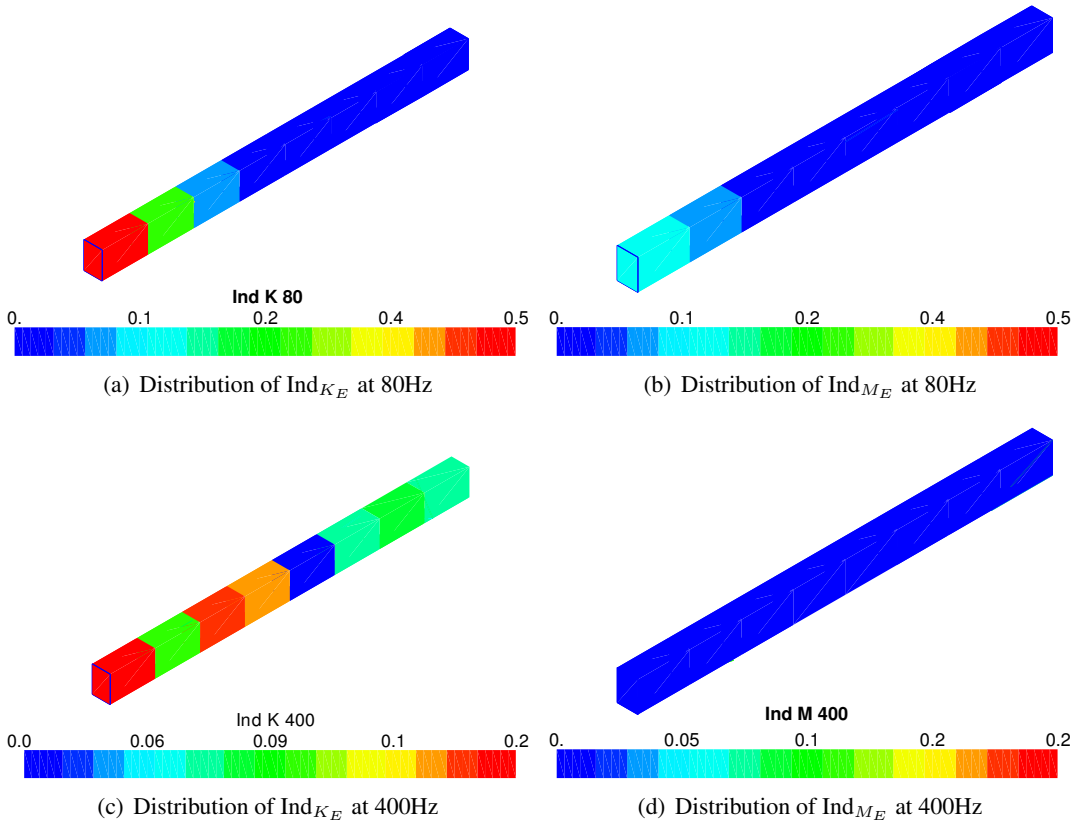

(a) Distribution of Ind_{K_E} at 80Hz

(b) Distribution of Ind_{M_E} at 80Hz

(c) Distribution of Ind_{K_E} at 400Hz

(d) Distribution of Ind_{M_E} at 400Hz

Figure 4.18: *Preliminary ECR analysis for a perfect double-clamped concrete beam FE model. Distribution of $IndK$ and $IndM$ estimators over the structure for different frequencies.*

distribution in free-clamped conditions are shown in Figure 4.19.

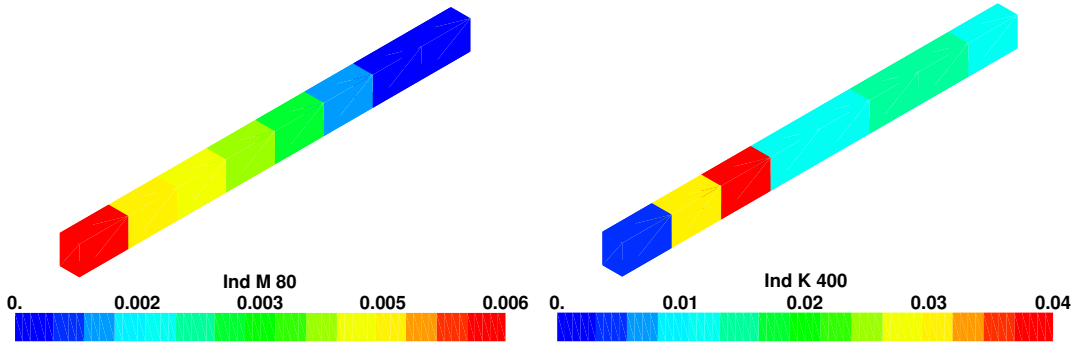

(a) Distribution of Ind_{M_E} at 80Hz

(b) Distribution of Ind_{K_E} at 400Hz

Figure 4.19: *ECR analysis for a perfect simple-clamped concrete beam FE model. Distribution of most relevant ECR error indicators.*

At this point, it seems clear that the reference model embeds a stiffness error on element number

3, which is effectively the true element containing damage. In addition, the perfect clamping boundary condition is also suspected, and a further analysis is needed in order to determine the nature of the boundary error.

In a similar way to the previous example, condensation and inversion formulas in (4.13) and (4.14) are used to investigate about suspected boundary DOF behavior. It is important to remark that the correctness of the boundary DOF identification is directly related to the quality of the model as explained in [39]. In our case, we know that the structure potentially contains significant stiffness error in element number 3 and we can therefore expect the results from this approach to be consequently polluted. In addition, in this example the stiffness error is located close to the incorrectly-modeled boundary constraint, making the distinction between structural damage and boundary error more difficult.

Figures 4.20 and 4.21 illustrate the results of the boundary DOF identification approach. It can be seen that, in particular in Figure 4.20, all the suspected boundary DOF present significant displacements and a perfect clamping condition can be questioned.

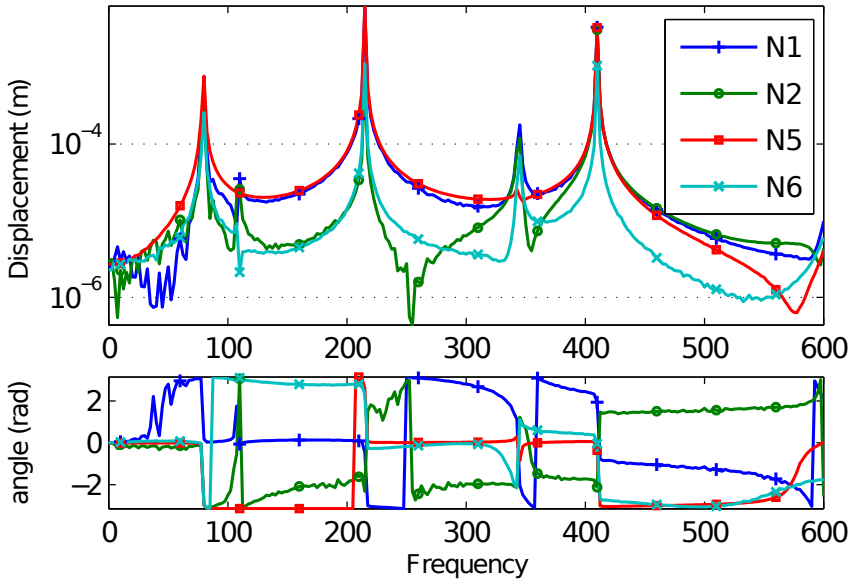

Figure 4.20: *Identified boundary displacements in Z direction for the erroneous clamping DOF in presence of structural damage.*

Besides, we remark that all DOFs show a similar behavior with resonances at the same frequencies. Therefore, since the presence of structural error modeling is known and all the DOFs belong to the same section of the beam, we can roughly assume the presence of a global impedance for the whole boundary DOF.

This hypothesis contrasts with the analysis of the function $\hat{q}_b/\hat{F}_b$ shown in Figure 4.21. When looking at the identified functions, it can be observed that the sensitivity of the results to an inaccurate

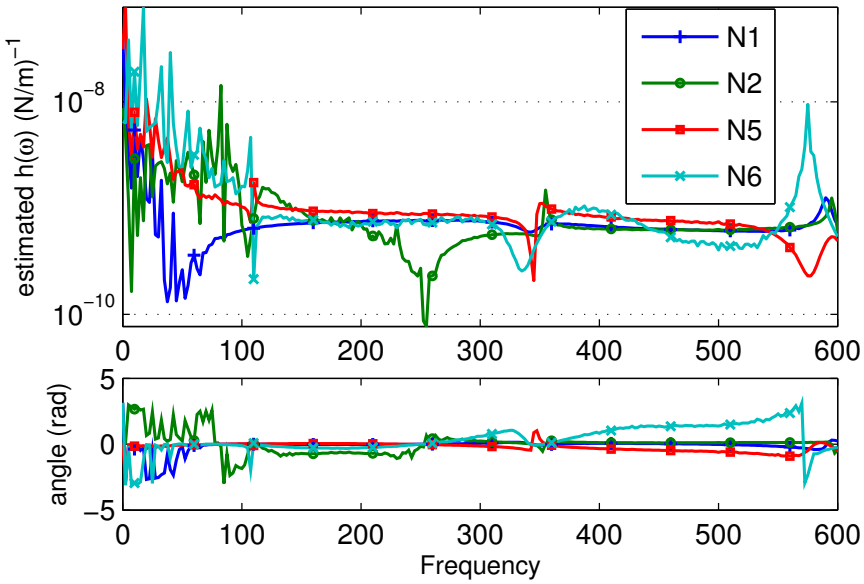

Figure 4.21: *Identified $\hat{q}_b/\hat{F}_b$ in Z direction for the erroneous clamping DOF in presence of structural damage.*

modeling of the structure is higher than that of the estimated $\hat{q}_b$. In particular, while the results seem relatively stable for frequencies higher than $150Hz$, the identification becomes of poor quality in the range $[0Hz, 150Hz]$ and the inversion becomes ill-conditioned. This can be probably explained by the lack of sensors between the damaged region and the erroneous boundary, making it harder to distinguish between both errors. Thus, the results of such an estimation must be carefully interpreted in this case.

The choice of model parameters introduced in the vector θ to be updated is based in the previous analysis. From the preliminary ECR results, the presence of a potential stiffness bias in element number 3 leads to a natural choice a stiffness reduction parameter d_3. When it comes to boundary conditions, the ECR error distribution suggests a boundary mis-modeling confirmed by the presence of resonances in the estimation of $\hat{q}_b$ as shown in Figure 4.20. Nevertheless, the number of poles of a potential boundary impedance is hard to define from Figure 4.21 since the identification becomes noisy for the frequency range $[0\text{Hz}, 150\text{Hz}]$. The choice of a single pole impedance stands from both the ECR spectrum in Figure 4.17 where a significant boundary error clearly reaches a peak around $80Hz$ and from the analysis of the model response based on the identified $\hat{q}_b$.

Hence, two different θ vectors are studied. The simplest is obtained by assuming a common parametrization of the boundary impedance for the whole boundary DOF. Consequently, the vector of model parameters θ is defined by

$$\theta^A = \{d_3 \quad k \quad m\}^T \tag{4.18}$$

where d_3 is a damage parameter of element 3 and k and m the boundary impedance parameters as defined

by (4.8). In the case where the interpretation of the results given by Figure 4.20 and Figure 4.21 lead to suspicion of a different impedance for N1-N5 and N2-N6 DOF, the following parametrization can be assumed

$$\theta^B = \{d_3 \quad k1 \quad m1 \quad k2 \quad m2\}^T \tag{4.19}$$

where in this case $k1$ and $m1$ represent the impedance parameters of N1-N5 DOFs and $k2$ and $m2$ the corresponding parameters for the N2-N6 DOFs.

The initial guess for both θ_0 are obtained in the same way as the precedent example and result into $\theta_0 = \{0 \quad 1.656{\cdot}10^6\text{N/mm} \quad 9.93\text{kg}\}^T$ for the first case and $\theta_0 = \{0 \quad 1.656{\cdot}10^6\text{N/mm} \quad 9.93\text{kg} \quad 1.656{\cdot}10^6\text{N/mm} \quad 9.93\text{kg}\}^T$ for the latter.

Introducing such a parametrization into a state-space formulation of the form (3.13) and solving the problem by applying the UKF algorithm leads to the results presented in Figure 4.22.

As can be seen, the estimates in both cases are converging towards the true values simultaneously for all damage and impedance parameters. In particular, results appear to be stable for the parametrization proposed in (4.19) which is supposed to be *a priori* a worst-posed problem since the boundary impedance parameters are duplicated and the concerned DOF are relatively close in space. In these conditions, the use of ECR measure ensures a good convexity of the cost function and helps the algorithm to reach optimal parameter estimation.

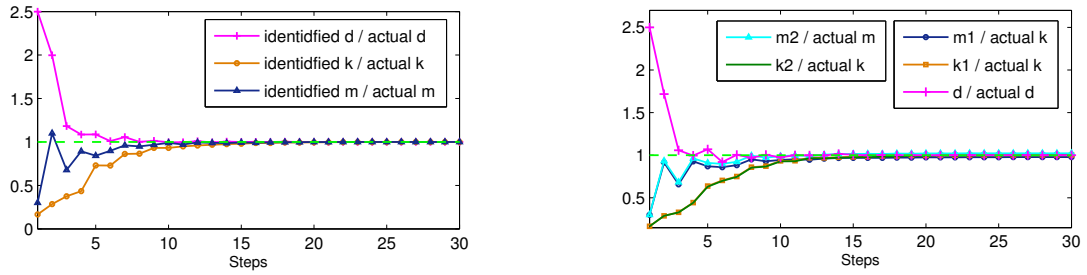

(a) Case with $\theta = \theta^A$ (b) Case with $\theta = \theta^B$

Figure 4.22: *Identification of damage and boundary impedance parameters with the ERC-UKF approach for different parametrization of updating vector θ.*

The example of boundary error in presence of structural damage is finally used to address the problem of evolving parameters in a similar fashion to the case of the power plant cooling tower discussed in section 4.1.1. To do so, the previous example gives the key ideas of the preliminary ECR analysis, the study of the boundary error and the choice of a model parametrization in a vector θ to be updated. Thus, the parametrization proposed in (4.19) is introduced in a state-space formulation of the form (4.7) and solved by application of the UKF algorithm. Furthermore, whereas the impedance parameters are considered to be time-invariant, structural damage evolves over time. In this example, the structure is supposed to be initially undamaged when sudden and rapid damage appears followed by more stabilized slow damage evolution. Thus, a windowing partition of time-domain measurements is performed as

defined in equation (4.6). Here, a sequence of $m = 60$ samples of a time duration $\overline{T} = 0.05s$ with an overlap $\mathbf{o} = 0.77$ are used.

The results of the identification are shown in Figure 4.23. It can be observed that, despite the initial guess for the impedance parameters is inaccurate, the algorithm reaches a consistent guess of θ rapidly enough so that the damage evolution law is correctly tracked. In addition, both a good stability of the impedance estimates while damage is evolving and a satisfying stability of the tracked damage when changes occurs (step 15 and 25) can be observed.

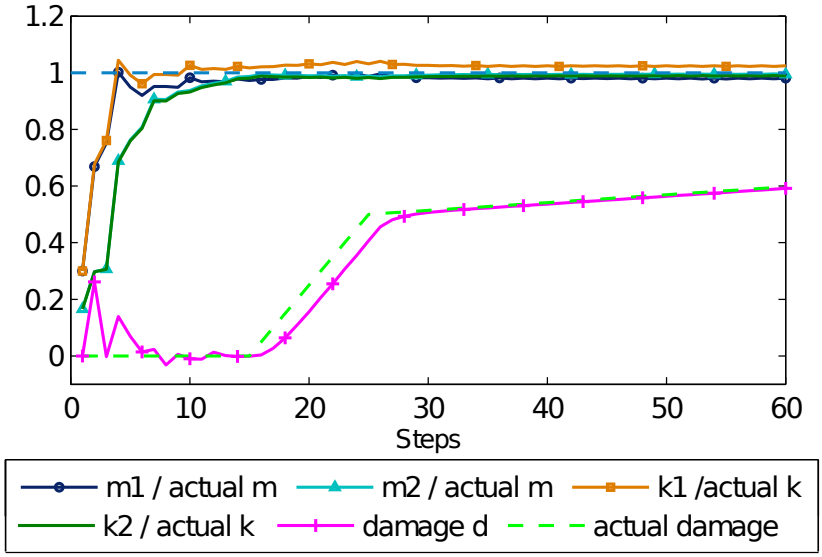

Figure 4.23: *Identification of damage and boudanry impedance parameters with the ERC-UKF approach for the case of evolving damage and a model parametrization described in* (4.19).

In this example, we have studied the ability of the ECR-UKF approach to identify mis-modeled boundary conditions. To this aim, he have analyzed a structure where one of the initially-assumed clamped boundaries is actually subjected to an interaction with a neighboring structure, modeled with a simplified impedance. The preliminary ECR analysis showed, again, a good ability to highlight regions with potentially mis-modeled boundary conditions. However, although the ECR spectrum indicates high model errors for frequencies close to the actual impedance resonance, a deeper study is proposed to enrich this information and build a proper impedance parametrization. For this, an existing technique based in a condensation and matrix inversion approach is used. This technique provides a good estimation of boundary forces and displacements consequently leading to a satisfactory identification of impedance parameters with the ECR-UKF. However, the quality of this boundary displacements and forces is directly related to quality of the FE model. Thus, a study with a structure embedding unknown damage is also performed. Here, the initial information concerning the boundary impedance is less accurate, although sufficient to satisfactorily identify both impedance parameters and structural damage. Alike the

precedent example of the power plant cooling tower, the case of invariant and evolving parameters are proposed.

To conclude, the study of mis-modeled boundary conditions is completed in chapter 7 which is devoted to an experimental campaign. Moreover, a time-domain approach for boundary identification is also studied and is proposed next.

4.2.1 A time-domain approach for the identification of mis-modeled boundaries

In the previous example, the problem of boundary conditions mis-modeling is addressed in the frequency domain where the presence of a boundary coupling is introduced as a parametrized impedance (cf. (4.8)). The advantage of the obtained information is that it condensates the global dynamic behavior of the neighboring structures and can be used to predict the system response under different operating conditions. However, the proposed modeling assumes a linear response of the boundary interaction between the structure and the surrounding elements.

In many real cases, structures can be enclosed in a complex non-linear environment making this kind of impedance modeling unsuitable. To deal with this issue, we propose in this section to address the problem of boundary conditions mis-modeling in the time-domain where the poorly known boundary conditions are introduced as unknown variables of the mechanical model. Specifically, unknown boundary displacements and its derivatives are estimated without introducing any assumption on the nature of the surrounding elements and thus estimated as a model parameter. In that sense, the approach can be used with all kind of boundary mis-modeling since no assumptions are done with respect to the neighboring phenomena. However, the estimation of the boundary response is valid only under the operating conditions and cannot be used to predict model response under different operating conditions.

Consider the well-known structural dynamics equilibrium equation in its FE semi-discretization form given by:

$$[M]\{\ddot{q}\} + [C]\{\dot{q}\} + [K]\{q\} = \{F(t)\} \tag{4.20}$$

where commonly $[M]$, $[C]$ and $[K]$ are respectively the mass, damping and stiffness matrices while $\{F(t)\}$ and $\{q\}$ represent external loadings and nodal displacement vectors.

In a very similar way to the transformation used in (4.10) initially proposed in [39], $\{q\}$ can be partitioned into internal DOF $\{q_i\}$ and boundary DOF $\{q_b\}$, leading to a rearranged equilibrium equation that can be expressed in the following form:

$$\begin{bmatrix} M_{ii} & M_{ib} \\ M_{bi} & M_{bb} \end{bmatrix} \begin{Bmatrix} \ddot{q}_i \\ \ddot{q}_b \end{Bmatrix} + \begin{bmatrix} C_{ii} & C_{ib} \\ C_{bi} & C_{bb} \end{bmatrix} \begin{Bmatrix} \dot{q}_i \\ \dot{q}_b \end{Bmatrix} + \begin{bmatrix} K_{ii} & K_{ib} \\ K_{bi} & K_{bb} \end{bmatrix} \begin{Bmatrix} q_i \\ q_b \end{Bmatrix} = \begin{Bmatrix} F_i(t) \\ F_b(t) \end{Bmatrix} \tag{4.21}$$

When dealing with the problem of unknown boundary conditions, equation (4.21) offers the possibility to separate well-known model operators to those embedding the lack of knowledge of the surrounding phenomena. As a matter of fact, the *a priori* unknown coupling of the studied structure through the boundary is condensed in the $[M_{bb}]$, $[C_{bb}]$, $[K_{bb}]$ and $F_b(t)$ operators. To avoid the use of such an information when solving this equation, the proposed approach consists of using the first row of equations in

(4.21) only what leads to the following expression:

$$[M_{ii}]\{\ddot{q}_i\} + [C_{ii}]\{\dot{q}_i\} + [K_{ii}]\{q_i\} = \{F_i(t)\} - [M_{ib}]\{\ddot{q}_b\} - [C_{ib}]\{\dot{q}_b\} - [K_{ib}]\{q_b\} \tag{4.22}$$

The influence of the surrounding phenomena can be therefore interpreted as an external loading that modifies t he response of a perfectly clamped structure through the well-known operators $[M_{ib}]$, $[C_{ib}]$, $[K_{ib}]$ and the boundary response $\{\ddot{q}_b\}$, $\{\dot{q}_b\}$ and $\{q_b\}$, which in our approach are considered as model unknowns to be identified.

In order to obtain a formulation of the problem suitable for a Kalman filter identification approach, a central difference time discretization is adopted to build the evolution model of the governing equation (4.22). Thus, considering a time interval $[t_0 : t_N]$ in a sequence of time steps, the following approximations are introduced for the velocity and acceleration vectors at time t_j:

$$\dot{q}^j \cong \frac{q^{j+1} - q^{j-1}}{2\Delta t}, \qquad \ddot{q}^j \cong \frac{q^{j+1} - 2q^j + q^{j-1}}{\Delta t^2} \tag{4.23}$$

where Δt corresponds to the time step in the time interval $[t_j : t_{j+1}]$. It is known that the central difference scheme is conditionally stable with a critical time step given by $\Delta t_{\text{critical}} = \frac{2}{\omega_{\text{max}}}$, where ω_{max} is the highest angular eigenfrequency of the FE model (4.22). In the following a time step $\Delta t = 0.9\Delta t_{\text{critical}}$ is adopted to ensure stability. Applying these approximations to (4.22) leads to the following expression:

$$\left[\frac{M_{ii}}{\Delta t^2} - \frac{C_{ii}}{2\Delta t}\right]\{q_i^{j+1}\} + \left[K_{ii} - \frac{2M_{ii}}{\Delta t^2}\right]\{q_i^j\} + \left[\frac{M_{ii}}{\Delta t^2} + \frac{C_{ii}}{2\Delta t}\right]\{q_i^{j-1}\} = \mathcal{F}^j \tag{4.24}$$

where

$$\mathcal{F}^j = \{F_i^j\} - \left[\frac{M_{ib}}{\Delta t^2} - \frac{C_{ib}}{2\Delta t}\right]\{q_b^{j+1}\} - \left[K_{ib} - \frac{2M_{ib}}{\Delta t^2}\right]\{q_b^j\} - \left[\frac{M_{ib}}{\Delta t^2} + \frac{C_{ib}}{2\Delta t}\right]\{q_i^{j-1}\} \tag{4.25}$$

Finally , in order to obtain a step-forward algorithm of the mechanical model requested in a Kalman filter state-space formulation, equation (4.24) can be rearranged as:

$$\{q_i^{j+1}\} = \left[\frac{M_{ii}}{\Delta t^2} - \frac{C_{ii}}{2\Delta t}\right]^{-1}\left(\mathcal{F}^j - \left[K_{ii} - \frac{2M_{ii}}{\Delta t^2}\right]\{q_i^j\} - \left[\frac{M_{ii}}{\Delta t^2} + \frac{C_{ii}}{2\Delta t}\right]\{q_i^{j-1}\}\right) \tag{4.26}$$

To illustrate this time-domain approach, we propose to study the case of the structure with structural damage in presence of boundary condition mis-modeling presented in Figure 4.16. For the sake of simplicity, we assume that a preliminary ECR analysis is already performed and the *a priori* information about boundary error as well as stiffness bias location is available. Hence, the aim of this study is to show how a state and parameter estimation can be performed taking into account a boundary condition lack of knowledge that substantially modifies the *a priori* structural response.

In this example, we propose to tackle the state and parameter estimation problem by means of two different algorithms. The first approach consists in applying the widely known Extended Kalman filter in its joint state and parameter formulation. Thus, an augmented state vector is considered containing

both model states and unknown parameters. In our case, the augmented vector of states $X \in \mathbb{R}^{2n+5}$ can be written as:

$$X^j \equiv \{q_i^j \quad q_i^{j-1} \quad d_3^j \quad q_b^{j+1} \quad q_b^j \quad q_b^{j-1} \quad F_i^j\}^T \tag{4.27}$$

where the two first terms correspond to the structure nodal displacements and the latter 5 terms are the unknown parameters, namely the structural damage, the future, present and past boundary displacements and finally the external force. Notice that the external force is considered as stochastic model unknown since the structure is excited with a zero-mean white noise and its deterministic value is unknown. Moreover, while the introduction of the boundary DOF q_b^{j+1}, q_b^j and q_b^{j-1} alleviate the perfect clamping condition, the introduction of d_3^j in the state vector stands since structural damage is sought. Hence, a discrete state-space formulation of the evolution problem can be written in the following form:

$$\begin{cases} X_{j+1} = f(X_j) + w_j^X \\ \tilde{u}_j = H(X_j) + v_j \end{cases} \tag{4.28}$$

where, as in the precedent cases, w_j^X and v_j are independent zero-mean white Gaussian noise processes with covariance matrices $\mathcal{Q}_j$ and $\mathcal{R}_j$ respectively. Besides, while $\tilde{u}_j \in \mathbb{R}^m$ represents a set of measurements at time t_j, the $H(\cdot)$ operator corresponds to a function allowing to extract the corresponding displacements of vector X_j at sensor positions. In our case, the observation function $H(\cdot)$ is a linear matrix operator $H \in \mathrm{M}(\mathbb{R})_{m,2n+5}$ given by:

$$H = [\Pi \quad \mathbf{0}] \tag{4.29}$$

Finally, function $f(\cdot)$ is the associated discrete non-linear state mapping defined by:

$$X^{j+1} = f^j(X^j) = \begin{Bmatrix} \left[\frac{M_{ii}}{\Delta t^2} - \frac{C_{ii}}{2\Delta t}\right]^{-1} \left(\mathcal{F}^j - \left[K_{ii} - \frac{2M_{ii}}{\Delta t^2}\right]\{q_i^j\} + \left[\frac{M_{ii}}{\Delta t^2} + \frac{C_{ii}}{2\Delta t}\right]\{q_i^{j-1}\}\right) \\ q_i^j \\ d_3^j \\ q_b^{j+1} \\ q_b^{j+1} \\ q_b^j \\ F_i^j \end{Bmatrix} \tag{4.30}$$

whose Jacobian in the state variable space is given by:

$$\mathbf{f}^j(x^j) \equiv \left.\frac{\partial f^j(x)}{\partial x^T}\right|_{x=x^j} = \begin{bmatrix} \frac{\partial f_I^j(x)}{\partial q_i^j} & \frac{\partial f_I^j(x)}{\partial q_i^{j-1}} & \frac{\partial f_I^j(x)}{\partial d_3^j} & \frac{\partial f_I^j(x)}{\partial q_b^{j+1}} & \frac{\partial f_I^j(x)}{\partial q_b^j} & \frac{\partial f_I^j(x)}{\partial q_b^{j-1}} & \frac{\partial f_I^j(x)}{\partial F_i^j} \\ \mathbf{I} & \mathbf{0}^T & \mathbf{0}^T & \mathbf{0}^T & \mathbf{0}^T & \mathbf{0}^T & \mathbf{0}^T \\ 0 & 0 & 1 & 0 & 0 & 0 & 0 \\ 0 & 0 & 0 & 1 & 0 & 0 & 0 \\ 0 & 0 & 0 & 1 & 0 & 0 & 0 \\ 0 & 0 & 0 & 0 & 1 & 0 & 0 \\ 0 & 0 & 0 & 0 & 0 & 0 & 1 \end{bmatrix}_{X=X^j} \tag{4.31}$$

where $\mathbf{I}$ represents the identity matrix and

$$\begin{aligned}
\frac{\partial f_I^j(x)}{\partial q_i^j} &= \left[\frac{M_{ii}}{\Delta t^2} - \frac{C_{ii}}{2\Delta t}\right]^{-1}\left[K_{ii} - \frac{2M_{ii}}{\Delta t^2}\right] \\
\frac{\partial f_I^j(x)}{\partial q_i^{j-1}} &= \left[\frac{M_{ii}}{\Delta t^2} - \frac{C_{ii}}{2\Delta t}\right]^{-1}\left[\frac{M_{ii}}{\Delta t^2} + \frac{C_{ii}}{2\Delta t}\right] \\
\frac{\partial f_I^j(x)}{\partial d_3^j} &= \left[\frac{M_{ii}}{\Delta t^2} - \frac{C_{ii}}{2\Delta t}\right]^{-1}\frac{\partial K_{ii}}{\partial d_3^j}\{q_i^j\} \\
\frac{\partial f_I^j(x)}{\partial q_b^{j+1}} &= -\left[\frac{M_{ii}}{\Delta t^2} - \frac{C_{ii}}{2\Delta t}\right]^{-1}\left[\frac{M_{ib}}{\Delta t^2} - \frac{C_{ib}}{2\Delta t}\right] \\
\frac{\partial f_I^j(x)}{\partial q_b^j} &= -\left[\frac{M_{ii}}{\Delta t^2} - \frac{C_{ii}}{2\Delta t}\right]^{-1}\left[K_{ib} - \frac{2M_{ib}}{\Delta t^2}\right] \\
\frac{\partial f_I^j(x)}{\partial q_b^{j-1}} &= -\left[\frac{M_{ii}}{\Delta t^2} - \frac{C_{ii}}{2\Delta t}\right]^{-1}\left[\frac{M_{ib}}{\Delta t^2} + \frac{C_{ib}}{2\Delta t}\right] \\
\frac{\partial f_I^j(x)}{\partial F_i^j} &= \left[\frac{M_{ii}}{\Delta t^2} - \frac{C_{ii}}{2\Delta t}\right]^{-1}\{\mathbf{1}\}_n
\end{aligned} \tag{4.32}$$

where $\{\mathbf{1}\}_n$ is a vector of size n whose entries are 1. Thus, the Extended Kalman filter equations developed in Figure 2.4 are applied to obtain a joint state and parameter estimation.

On the other hand, we aim to apply the Unscented Kalman filter equations to the studied example in order to compare the performances of these two different non-linear filtering approaches. However, since the computational cost of the UKF in its joint state and parameter version is of $\mathcal{O}(N^3)$ (compared to a $\mathcal{O}(N^2)$ for the EKF) and the size of vector (4.27) is relatively high ($N = 2n + 5 = 197$), a different strategy is adopted to apply the Unscented transformation equations. For this, a dual KF-UKF approach is proposed herein considerably reducing the computational cost of the joint state and parameter UKF version and taking benefit of the Unscented accuracy notwithstanding.

For this, the dual approach consists in making two different filters run in parallel, a first one for state estimation and a second one for parameter estimation. In our approach, a first linear Kalman filter is used to perform state estimation while an Unscented Kalman filter is adopted to obtain optimal estimation of the parameters. Obviously, both filters feed one another at each time step in order to maintain updated the global state and parameter information of the studied system. To better illustrate our purpose, a block diagram is proposed in Figure 4.24 showing the dual KF-UKF proposed algorithm.

Notice that the computational cost of this algorithm is considerably improved compared to the joint UKF by simply applying the linear Kalman filter to the states q absorbing 192 of the estimated DOFs and reducing to a 5 DOF the vector introduced in the UKF algorithm. Furthermore, a computational cost of $\mathcal{O}(n^2)$ can be achieved in UKF in its parameter estimation version (see [45]).

In this context, the two following vectors are considered for the dual KF-UKF approach:

$$q^j \equiv \{q_i^j \quad q_i^{j-1}\}^T, \qquad \theta^j \equiv \{d_3^j \quad q_b^{j+1} \quad q_b^j \quad q_b^{j-1} \quad F_i^j\}^T \tag{4.33}$$

and their consequent coupled state-space formulation is:

$$\begin{cases} q^{j+1} = \overline{f}(q^j, \hat{\theta}^j) + w_j^q \\ \tilde{u}_j = \Pi q_i^j + v_j \end{cases} \qquad \begin{cases} \theta^{j+1} = \theta^j + w_j^\theta \\ \tilde{u}_j = G(\hat{q}^{j-1}, \theta^j) + v_j \end{cases} \tag{4.34}$$

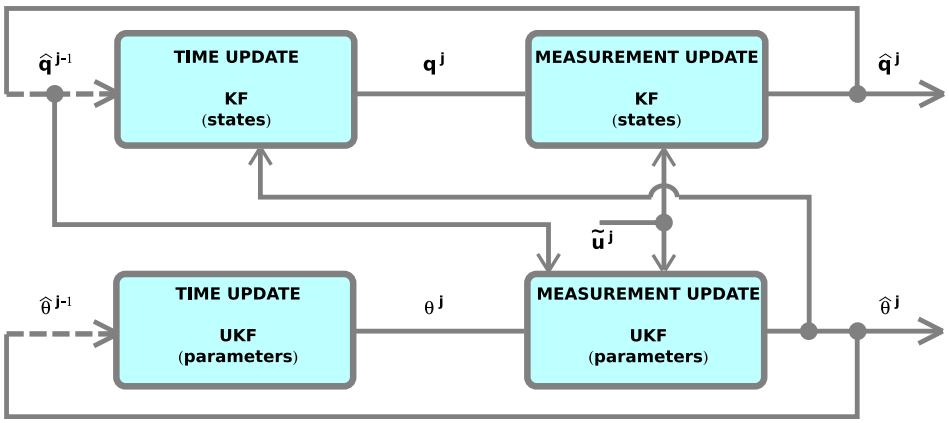

Figure 4.24: *Block diagram of dual Linear and Unscented Kalman filtering (KF-UKF) for respectively state and parameter estimation.*

where, in this description, w_j^q and w_j^θ are the consequent zero-mean white noise Gaussian processes with covariance matrices $\mathcal{Q}_j^{qq}$ and $\mathcal{Q}_j^{\theta\theta}$ respectively. Remark that these matrices are the related state and parameter covariance matrices embedded in $\mathcal{Q}_j$ in the EKF algorithm. Moreover, $\overline{f}$ correspond to the two first row equations of (4.30) and $G(\cdot)$ is a nonlinear function that propagates the states and makes a projection into the observation space.

The two proposed algorithms are applied to the problem of identifying structural damage in presence of boundary condition mis-modeling. Figure 4.25 shows the identified damage parameter for both approaches.

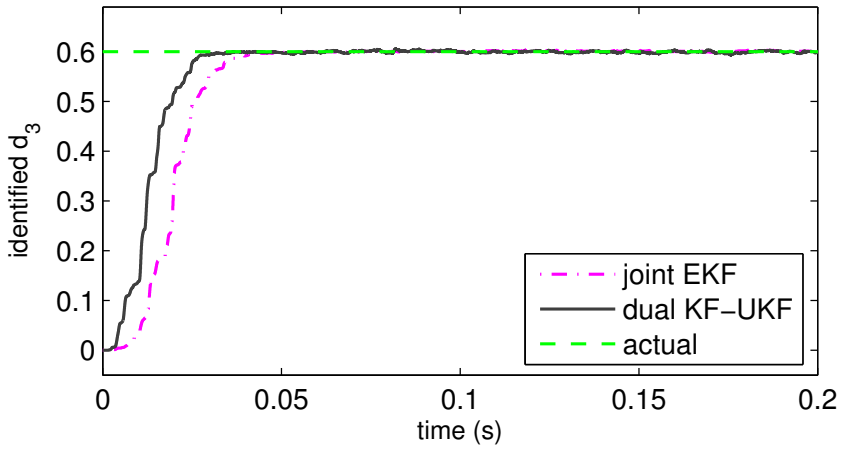

Figure 4.25: *Comparison of identified d_3 damage parameter using dual KF-UKF and joint EKF filtering.*

As it can be seen, in both cases the algorithms reach the sought damage value of 0.6. Nevertheless,

the dual KF-UKF approach presents a better convergence ratio towards the actual damage value than the one provided by the EKF.

When it comes to boundary condition displacements, a comparison of the identified q_b^j for the KF-UKF and EKF methods is shown in Figure 4.26. Similarly to the damage parameter case, the KF-UKF dual estimation presents a better ability to identify the unknown boundary displacement. As a matter of

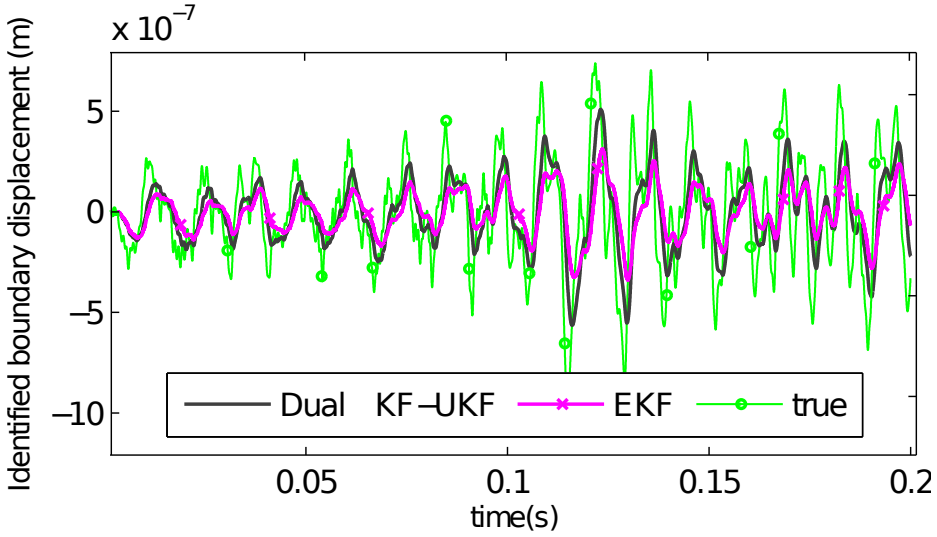

Figure 4.26: *Comparison of identified q_b^j unknown boundary displacement using dual KF-UKF and joint EKF filtering.*

fact, the dual KF-UKF method has the ability to capture faster variations of q_b^j than the one provided by the joint EKF estimator. In that respect, the boundary displacements are better represented with the dual estimator and peak amplitudes (faster changes) are better represented with this algorithm.

Finally, the estimaton of the external load F_i^j is shown in Figure 4.27, where the KF-UKF algorithm is used. The results of the EKF case are omitted since they are fully comparable with those provided in Figure 4.27. It can be observed that, while the actual load is a zero-mean Gaussian process, the identified effort truly corresponds to its mean value.

In this example the case of time-domain structural damage identification in the presence of boundary mis-modeling is addressed. We have proposed a formulation to deal with the boundary mis-modeling that can be used for cases with complex non-linear boundary behavior. In this example we show how the Kalman filter can deal with such a problem by means of the EKF and satisfactorily identify structural damage. Besides, a dual KF-UKF is proposed to enhance the performance of the EKF by using the Unscented transformation for parameter estimation and avoiding high computational cost of this algorithm by simply applying a linear Kalman filter for the case of state estimation.

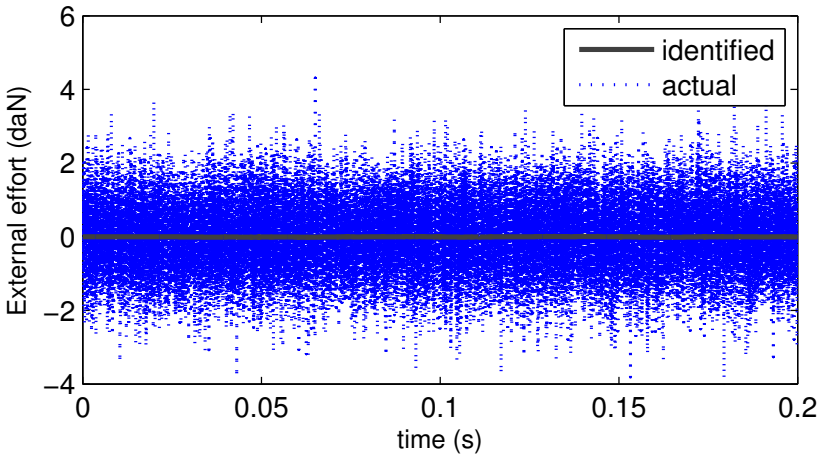

Figure 4.27: *Identified unknown external effort F_i^j with the dual KF-UKF approach.*

4.3 Comparison of ECR and BLUE methods for structural field reconstruction

In this section the problem of state estimation or field reconstruction in structural dynamics is addressed in an effort to propose a complete state and parameter estimation strategy based on ECR analysis and Kalman filtering. Hence, two different approaches directly related to these techniques are studied and compared.

Broadly speaking, the problem of field reconstruction itself arises from the category of an inverse problem since the estimation of the full state (i.e. displacement, velocity and acceleration history of all DOFs) is sought from a mathematical model and a set of partial and noisy measurements (e.g. sensor displacements, external efforts, overabundant data, etc.). In the framework of structural dynamics, the mathematical model giving the *a priori* harmonic displacements q_ω estimation is recalled below:

$$(-\omega^2[M(\hat{\theta})] + i\omega[C(\hat{\theta})] + [K(\hat{\theta})])q_\omega = F(\omega) \quad \text{for} \quad \omega \in [\omega_{min}, \omega_{max}] \tag{4.35}$$

where $\hat{\theta}$ is a vector parameterizing the mass $[M]$, damping $[C]$ and stiffness $[K]$ matrices in a FE formulation and $F(\omega)$ is the vector of external efforts. Thus, the problem we are tackling consists in finding an optimal state estimation $\hat{q}_\omega$ from the available *a priori* information given by (4.35) and a set of available measurements $\tilde{u}$ over the structure.

To tackle this data expansion problem, many different approaches exist depending on the nature of the problem and the available *a priori* information (see an interesting overview in [9]). Within the family of the well known least squares approach, we will cite the so-called kriging technique [78, 5] which is a method to interpolate the value of a random field at an unobserved location from observations of its value at nearby locations. In a linear framework, kriging can be directly related to the Best Linear Unbiased Estimator (BLUE), which is presented in detail in Appendix A. The BLUE technique has been

widely used in the domain of geosciences as a satisfying method for spatial interpolation and is actually the theoretical background of the variational formalisms 3D-Var and 4D-Var [11] in use for e.g. weather forecasting. Moreover, the linear Kalman filter can be understood as extending the BLUE to a sequential framework. Indeed, in the BLUE formalism the optimal state estimation $\hat{q}_\omega$ is given by the expression:

$$\hat{q}_\omega = q_\omega + K(\tilde{u} - \Pi q_\omega) \tag{4.36}$$

where Π is a linear observation operator and K is the so-called gain matrix, obtained by:

$$K = \Pi^T P^b (\Pi^T P^b \Pi + R)^{-1} \tag{4.37}$$

where P^b and R are the covariance matrices of model and observation errors respectively. One can easily observe that these expressions precisely correspond to the state update equations in the linear Kalman filter at each iteration step and, once again, the quality of the estimation is directly affected by the *a priori* knowledge of model and observation errors introduced under the form of covariance matrices. However, while in the Kalman algorithm the P^b matrices are recursively built and enriched by their propagation through the model equations, in the BLUE algorithm they need to be built based on the only assumption of *a priori* available error information. In our proposal to use BLUE estimation for state estimation in structural dynamics, a description of an ECR-based design of P^b matrices will be discussed further.

As an alternative way to perform data expansion, the BLUE approach will be compared to the information directly obtained from the solution of the ECR problem. As a matter of fact, when regarding the ECR optimization problem, the first step consists in obtaining the best triple of admissible fields $\mathcal{T}_\omega = (\hat{u}, \hat{v}, \hat{w})$. Thus, the kinematic admissible field $\hat{u}$ can be seen as the optimal state estimation in the sense of the ECR cost function (1.26), where $\hat{u}$ is the "best compromise" field between the measurements $\tilde{u}$ and the dynamically admissible fields $\hat{v}$ and $\hat{w}$ that actually play a role of regularization functions.

Whilst the method based on the ECR admissible field $\hat{u}$ doesn't need any additional assumptions to obtain the sought state estimation, the BLUE approach requires the construction of error covariance matrices P^b and R. Obviously, the quality of the results is directly related to the accuracy of the information introduced in this operators. Since the sensor error information is usually available and well known, the construction of matrix R is not a major issue and, in many cases, the assumption of uncorrelated measurement noise stands. On the other hand, however, the construction of matrix P^b becomes a major problem since the nature of model errors is in general poorly known and the assumption of uncorrelated errors is too restrictive.

Although the design of P^b is problem-dependent and there's no general approach to build such an operator, four general approaches are discussed in [4, 5] for a general data assimilation problem consisting in:

- Diagonal design
- Decomposition design
- Kriging design
- Kalman filtering design

In the case of a BLUE estimation, and in the very common case of a Boolean observation matrix Π and a diagonal covariance matrix R, the diagonal design approach is not appropriate since the state estimation will differ from the *a priori* state at sensor locations only. On the other hand, whereas the Kalman filtering approach is adapted to a recursive framework only, the kriging and the decomposition techniques propose a design based on spatial considerations of model errors. In the case treated herein the only available information on model errors is given by the (deterministic) ECR error fields. In that sense, the decomposition method seems to be the more appropriate approach to design P^b matrices and will be described and analyzed in the following.

The decomposition design technique proposes to build the error covariance matrix as the following product:

$$P^b = \Sigma^T C \Sigma \tag{4.38}$$

where Σ is a diagonal positive-definite matrix containing the standard deviation of the errors σ taking the form:

$$\Sigma = \text{diag}(\sigma_1, \sigma_2, \cdots, \sigma_i, \cdots, \sigma_N) \tag{4.39}$$

and C is a symmetric positive-definite matrix containing the correlations as:

$$C = \begin{bmatrix} 1 & & c_{ij} \\ & \ddots & \\ c_{ji} & & 1 \end{bmatrix} \tag{4.40}$$

Hence, the problem of designing matrix P^b is therefore translated into the definition of the more meaningful matrices Σ and C. In this approach we propose to build matrix Σ from the available error information given by the ECR analysis. Thus, it seems natural to build this matrix, at a given frequency ω, upon the available error field being the difference between the *a priori* model response q_ω and the ECR estimation response $\hat{u}_\omega$ solving equation (4.35) as follows:

$$\mathrm{e}_\omega = \hat{u}_\omega - q_\omega \tag{4.41}$$

leading to the following design for Σ:

$$\Sigma = \text{diag}(|\mathrm{e}_\omega|) \tag{4.42}$$

When it comes to the matrix of spatial correlations C we propose a design based on the following two considerations:

1. Spatial correlations exponentially decrease as a function of the Euclidean distance between DOFs.
2. At a given frequency ω, spatial correlations are a function of the structure's deformation shape $\hat{u}_\omega$.

Considering the previous hypothesis, the following design is proposed:

$$c_{ij} = \text{sign}(\hat{u}_i \hat{u}_j) \cdot \exp\left(-\frac{2||\hat{u}_i| - |\hat{u}_j||}{|\hat{u}_i| + |\hat{u}_j|}\right) \cdot \exp\left(-\frac{\tilde{\mathbf{d}}(\text{DOF}_i, \text{DOF}_j)}{\lambda_{\text{spatial}}}\right) \tag{4.43}$$

where $\tilde{\mathbf{d}}(\text{DOF}_i, \text{DOF}_j)$ represents the Euclidean distance between the i^{th} and j^{th} DOFs, and λ_{spatial} represents a correlation length.

For the sake of clarity, a 1D example is given to illustrate the above-defined correlation function c_{ij}. For this, consider a 1D structure of unit length whose corresponding deformation shape $\hat{u}_\omega$ is given in Figure 4.28. Suppose that the structure is discretized in 70 DOF distributed uniformly along its length. Thus, Figure 4.29 visualizes the matrix C "shape" built upon the proposed correlation function.

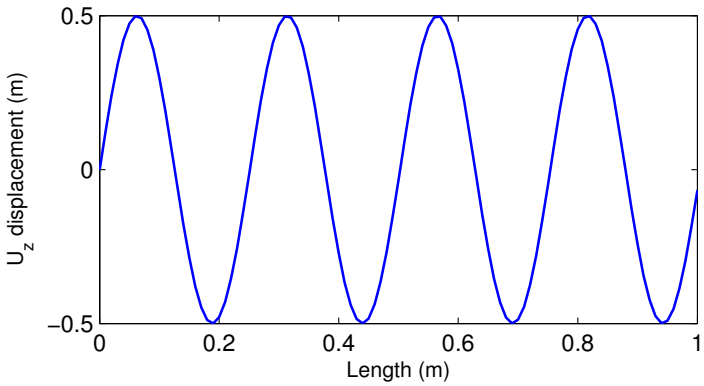

Figure 4.28: *Illustrative example of a 1D structure deflection $\hat{u}_\omega$ over the structure length.*

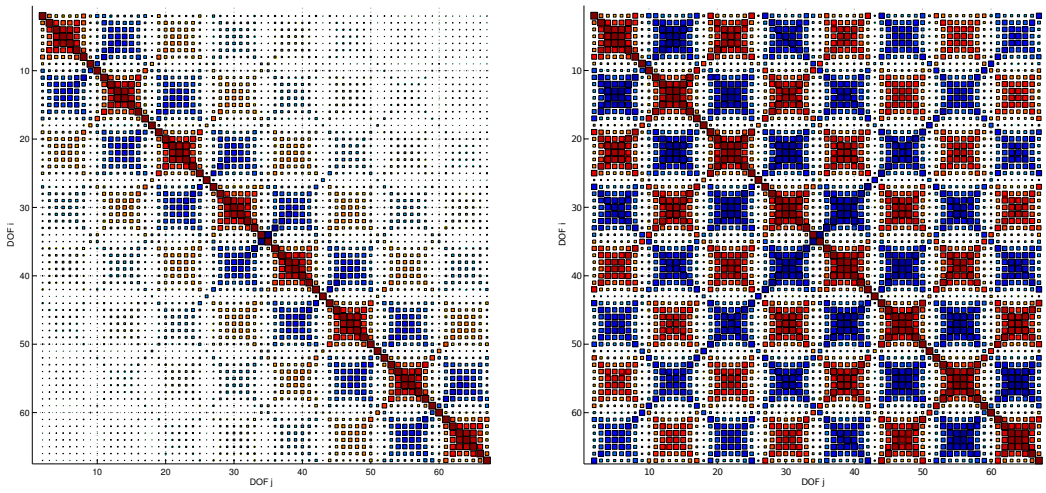

(a) Low spatial correlation ($\lambda_{spatial} = 25m$) (b) High spatial correlation ($\lambda_{spatial} = 250m$)

Figure 4.29: *Illustration of the correlation matrix C shape for a 1D example.*

As it can be seen, the example shows how C matrices respect both of the above-mentioned hypothesis

for c_{ij} function: exponential decorrelation as a function of the distance between DOFs and a correlation shape related to the deformation shape $\hat{u}_\omega$.

Hence, with the help of functions (4.42) and (4.43) the main shape of error covariance matrix P^b is designed in a decomposition fashion as described in (4.38). Besides, in the next examples, $\lambda_{spatial}$ is chosen so that correlation decreases of 90% for a distance corresponding to the sensors separation:

$$\lambda_{spatial} = \frac{\tilde{\mathbf{d}}(\text{sensor}_i, \text{sensor}_j)}{\ln(0.1)} \tag{4.44}$$

Obviously, this is a user defined assumption and, in the case studied herein, it is motivated by the fact that since sensors are regularly distributed in space, the subsequent correlation function C fully covers the studied structure. In addition, the influence of a sensor information with regards to the adjoining ones is supposed to be low (10% or less) for the sake of field reconstruction smoothness.

At this point, in order to adapt the design of P^b to the actual problem, Desroziers et al. proposed in [29, 28] to perform the following homothety:

$$\hat{P}^b = \vartheta P^b \tag{4.45}$$

where ϑ is a scalar. By doing so, Desroziers et al. show how the data assimilation process will remain consistent with posterior statistics in the observation space and therefore optimality can be achieved. Among the different possibilities of posterior statistics to choose ϑ and achieve optimality proposed in [28] the expression below is adopted here

$$\mathbb{E}[d_a^o (d_b^o)^T] = R \tag{4.46}$$

where the quantities d_a^o and d_b^o are defined by

$$\begin{cases} d_b^o = \Pi q_\omega - \tilde{u} \\ d_a^o = \Pi \hat{q}_\omega - \tilde{u} \end{cases} \tag{4.47}$$

In practice, matrix R is chosen to be diagonal and for the sake of simplicity in the following examples we will choose parameter ϑ in a way that $\text{Trace}(d_a^o (d_b^o)^T) = \text{Trace}(R)$.

In the following examples, a comparison of field reconstruction between the proposed BLUE approach which is summarized in Figure 4.30 and the state estimation given by ECR minimization is presented. The quality of a field reconstruction $q_{estimate}$ will be compared to the actual state q_{actual} by means of the indicator:

$$\kappa(q_{estimate}, q_{actual}) := \frac{\langle q_{estimate}, q_{actual} \rangle}{\sqrt{\langle q_{estimate}, q_{estimate} \rangle \langle q_{actual}, q_{actual} \rangle}} \tag{4.48}$$

which is basically a Modal Assurance Criterion (MAC) which can takes values in $[-1 : 1]$ and measures the collinearity of both $q_{estimate}$ and q_{actual} vectors.

The first example is based on the parameter identification problem of a concrete beam in presence of structural damage and boundary mis-modelling of section 4.2. In order to both compare the performances of each method for many different cases and integrate the field reconstruction in a full state-and-parameter estimation approach, the BLUE and ECR techniques are examined at each UKF iteration of the sequence obtained in the identification process of Figure 4.22(a).

The results of this exercise are shown in Figure 4.31 where after obtaining the estimated states at each iteration the pseudo-MAC criterion κ is compared. Figures show the results for 10 frequencies corresponding to the first most excited eigenfrequencies of the actual structure.

It can be seen that in most of the cases both ECR and BLUE estimations improve the quality of model *a priori* estimation. However, this is not systematic and generally appears to be the case for the first parameters iterations. This is probably due to the fact that, not only measurements are noisy, but also model parametrization is inaccurate enough to build unsatisfactory *a priori* states. However, it has to be said that the ECR approach globally presents better performances compared to the BLUE ones. As

ECR-based BLUE state estimation.

For $\omega \in [\omega_{min}, \omega_{max}]$

1. Obtain the *a priori* model response q_ω and the ECR kinematically admissible field $\hat{u}_\omega$.
2. Compute the *a priori* error field $\mathrm{e}_\omega = \hat{u}_\omega - q_\omega$.
3. Compute the error covariance matrix as $P^b = \Sigma^T C \Sigma$ where
   (a) $\Sigma = \mathrm{diag}(|\mathrm{e}_\omega|)$
   (b) $C_{ij} = \mathrm{sign}(\hat{u}_i \hat{u}_j) \cdot \exp\left(-\frac{2||\hat{u}_i| - |\hat{u}_j||}{|\hat{u}_i| + |\hat{u}_j|}\right) \cdot \exp\left(-\frac{\tilde{\mathbf{d}}(\mathrm{DOF}_i, \mathrm{DOF}_j)}{\lambda_{\mathrm{spatial}}}\right)$; where $\tilde{\mathbf{d}}(\mathrm{DOF}_i, \mathrm{DOF}_j)$ represents the Euclidean distance between the i^{th} and j^{th} DOFs, and $\lambda_{\mathrm{spatial}}$ represents a spatial correlation length.
4. Set $\hat{P}^b = \vartheta P^b$
5. Build the gain matrix $K(\vartheta) = \Pi^T \hat{P}^b (\Pi^T \hat{P}^b \Pi + R)^{-1}$
6. Set the state estimation as $\hat{q}_\omega(\vartheta) = q_\omega + K(\vartheta)(\tilde{u} - \Pi q_\omega)$
7. Evaluate posterior statistics
$$\begin{cases} d_b^o = \Pi q_\omega - \tilde{u} \\ d_a^o = \Pi \hat{q}_\omega - \tilde{u} \end{cases}$$
8. Choose parameter ϑ so that $\mathrm{Trace}(d_a^o (d_b^o)^T) = \mathrm{Trace}(R)$.
9. Obtain the final state estimation as $\hat{q}_\omega = q_\omega + K(\tilde{u} - \Pi q_\omega)$.

Figure 4.30: *Overview of the ECR-based BLUE state estimation procedure.*

a matter of fact, this can be observed not only for the cases where the *a priori* guess is "close" to the actual values (see figures 4.31(a) and 4.31(c)) but also when initial guesses give a poor estimation of the structure state as can be seen in Figure 4.31(g).

A second example is considered, involving a larger number of DOFs, namely that of the power plant cooling tower previously studied in section 4.1. In this case, both BLUE and ECR approaches are compared through the identification process shown in Figure 4.4(b). The state estimation is performed at frequencies 0.9Hz, 1.1Hz, 1.35Hz and 2,47Hz for which the ECR spectrum (see ECR in Figure 4.2) is highest. In this case the ECR approach clearly gives the best state estimation with excellent results although, again, in both cases ECR and BLUE improve the *a priori* state knowledge.

Figure 4.33 shows the state error fields (difference between estimated field and actual field) for the initial set of parameters at frequency 2.47Hz. It can be seen how the *a priori* error presents an axisymmetric distribution around z axis and how the BLUE estimator maintains this structure slightly corrected in the damaged region. Besides, in the ECR state estimation, error is not only reduced in terms of magnitude (scale factor is reduced by one order of magnitude in Figure 4.33(c)) but also remains mainly concentrated in the constitutive relation erroneous region (damaged region).

In real cases, the initial FE model may give an inaccurate *a priori* estimation of the structure state where MAC values can fall to very low values. In an effort to evaluate the performances of both techniques in a case where the initial guess is particularly inaccurate, an *a priori* FE model is built where the Young's modulus is set to $E = 5E_0$ for the whole structure leading to a particularly erroneous initial state guess. The results of the error fields are presented in Figure 4.34 for the frequency of 2.47Hz. As it can be seen, the initial *a priori* state presents a very poor correlation ($\kappa = 0.361$) with respect to the actual state. Nevertheless, after performing a BLUE state estimation the representativity of the estimated field increases up to a $\kappa = 0.541$. However, despite a bad guess of the whole structure's Young's modulus, the ECR represents the best state estimator considerably raising the state representativity up to a $\kappa = 0.909$, which can be considered as an excellent result.

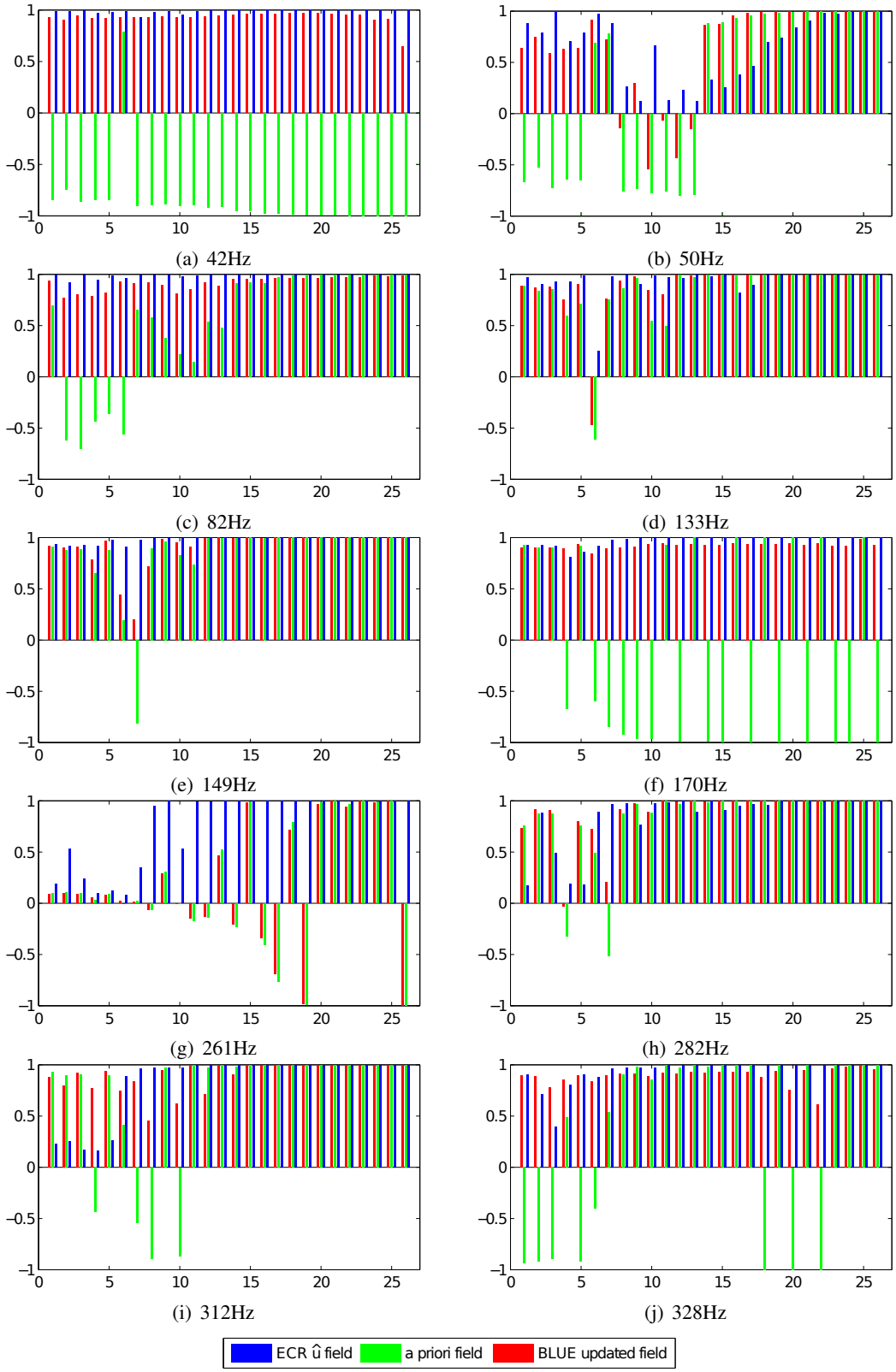

Figure 4.31: *Sequence of state estimation quality during the damage and boundary impedance parameter identification process of the concrete beam example. Comparison of κ criterion between initial guess, ECR and BLUE estimators.*

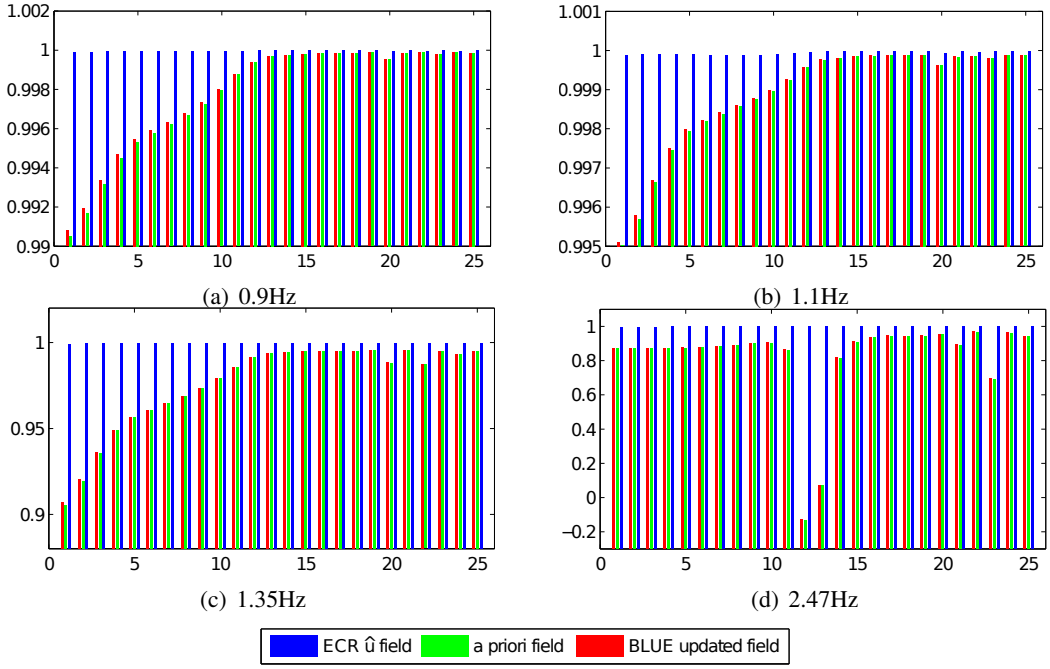

Figure 4.32: *Sequence of state estimation quality during the damage parameter identification process of a cooling tower example. Comparison of κ criterion between initial guess, ECR and BLUE estimators.*

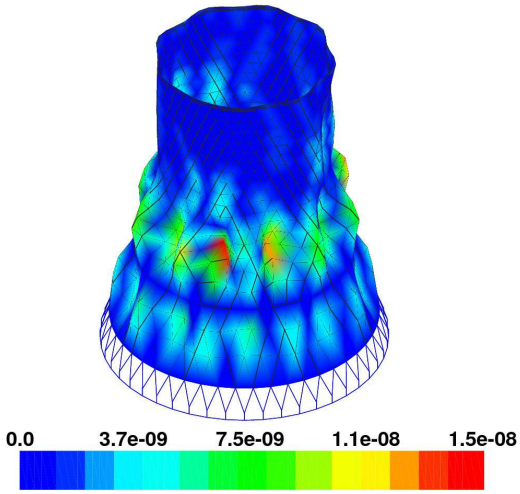

(a) *a priori* state error.

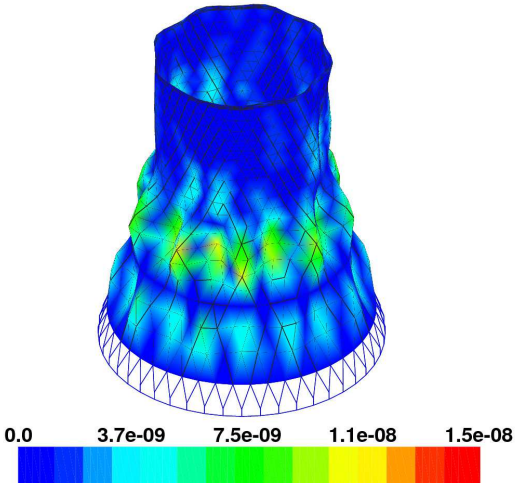

(b) BLUE estimation state error.

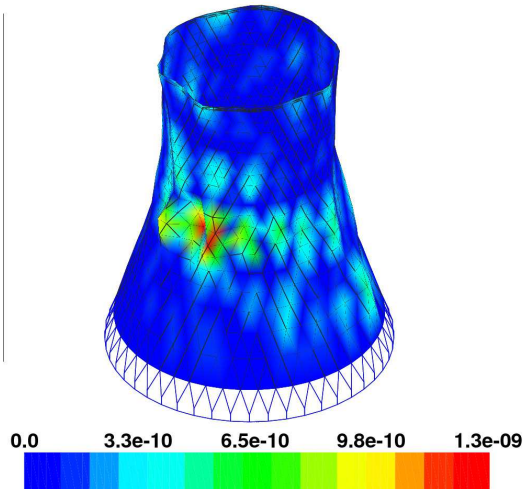

(c) ECR estimation state error.

Figure 4.33: *Cooling tower state estimation error fields at 2.47Hz at first parameter iteration of the ECR-UKF identification process*

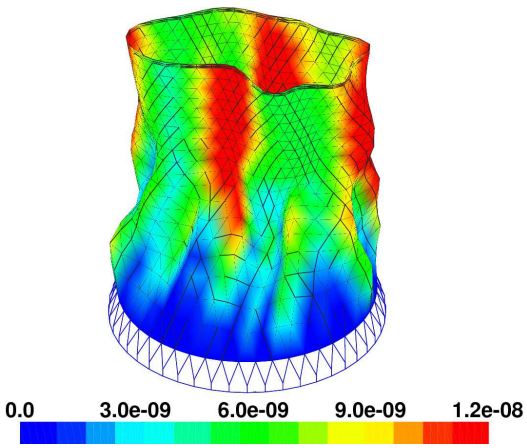

(a) *a priori* state error. $\kappa = 0.361$

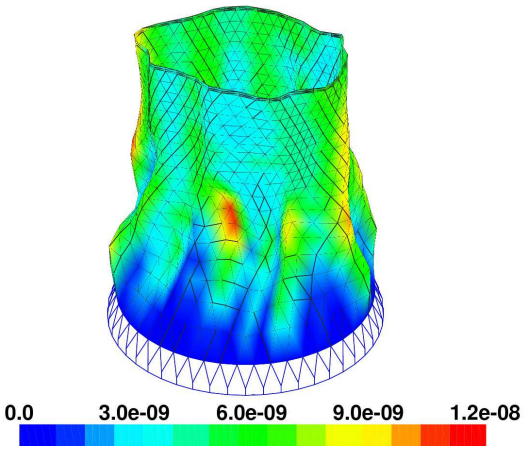

(b) BLUE estimation state error. $\kappa = 0.541$

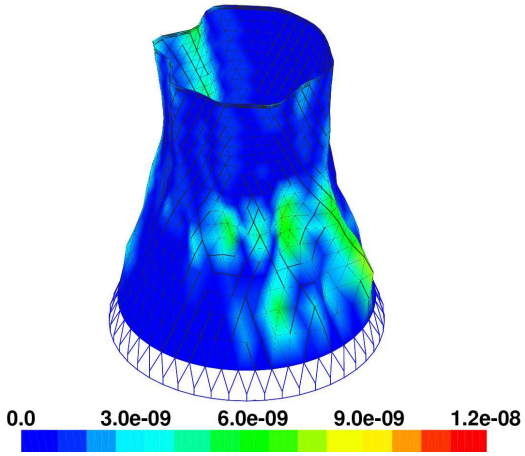

(c) ECR estimation state error. $\kappa = 0.909$

Figure 4.34: *Cooling tower state estimation error fields at 2.47Hz for FEM with a global Young's modulus of* $E = 5E_0$.

In this section, two different strategies based on ECR information (i.e. ECR optimal admissible fields and ECR-based BLUE) have been applied to perform optimal state estimation. The above-described methods have been evaluated in the afore studied cases of a concrete beam and a power plant cooling tower. In most of the cases both techniques seem to improve the quality of the state estimation with respect to its *a priori* knowledge. However, the ECR optimal admissible field $\hat{u}$ seems to give better performances with respect to the BLUE approach in most of the cases. Taking into account these consideration, it is proposed to adopt the ECR optimal admissible field $\hat{u}$ for field reconstruction purposes in structural dynamics. This approach not only presents the advantage to improve the quality of the results obtained by the BLUE approach but also demands no additional computational effort since $\hat{u}$ is naturally obtained when solving the ECR problem for parameter identification.

4.4 Conclusions

This chapter is devoted to the study of the adequacy of the ECR-UKF as an approach to improve FE model representativity in cases of industrial relevance. For this, three main problems are addressed, namely structural flaws assessment, identification of mis-specified boundary conditions and field reconstruction.

An example of structural damage identification is firstly addressed in a high-DOF complex model. In this context, while the ECR showed a good ability to spatially localize model errors, the ECR-UKF conveniently converges to actual values of damage, either for the case of invariant or evolutionary damage. In that sense, the ECR-UKF fulfills the three main targets defined in the introduction of this thesis and it will be further investigated in cases of increasing difficulty in part III.

In section 4.2, the problem of mis-modeled boundary conditions is studied from both the frequency-domain and the time-domain. In the first case, while the ECR shows again a good ability to localize boundary mis-modeled regions, an additional technique based on a condensation and inversion approach is required. Once the information about the boundary impedance is available, the ECR-UKF satisfactorily handles the identification of impedance parameters. An example combining boundary errors and evolving structural damaged is also presented and satisfactorily solved.

Moreover, a time-domain formulation is proposed for boundary errors identification based in Kalman filtering. For this, two approaches are investigated: a joint state and parameter estimation based in the EKF and a dual approach using two filters running in parallel (KF for state and UKF for parameter estimation). With the contributions of these numerical examples, a deeper study devoted to an experimental campaign about mis-modeled boundary identification will be further addressed in chapter 7.

In an effort to propose optimal state estimation within the ECR-UKF approach, the last section of this chapter is dedicated to the study of field reconstruction in structural dynamics. For this, two different methods directly related to the ECR and the Kalman filtering techniques are studied and compared. The first one is based in a BLUE formulation where covariance matrices are built upon the available ECR information. An alternative approach based in the information directly obtained from the triple $\mathcal{T}(\hat{u}, \hat{v}, \hat{w})$ is also proposed. Results show how the kinematically admissible field $\hat{u}$ represents a particularly good field reconstruction and is proposed as a technique to solve future shape expansion problems.

Chapter 5

Improvements of the ECR-UKF algorithm

Contents

5.1 Introducing algebraic constraints in the Unscented Kalman Filter

When dealing with physical phenomena, prior information on the states can often be introduced in the form of equality or inequality constraints expressing physical restrictions (mass or density positiveness, etc.). In the application of state estimators by means of Kalman filtering such constraints are not naturally taken into account. However, many researchers have studied the problem of introducing constraints in Kalman filtering as discussed shortly. In this section we discuss different approaches to address this issue with a direct application to the ECR-UKF algorithm. In particular, the discussion will be limited to the case of algebraic constraints of the form:

$$D\theta \leq c \tag{5.1}$$

where θ is the vector of model states (parameters in our case), D is a known matrix and c is known vector defining the admissible space.

In the case of equality constraints, the most natural approach is to reduce the system model parametrization by enforcing the constraints into the model equations as proposed in [88]. By doing so, the initial problem is therefore transformed into an equivalent unconstrained problem. A clear advantage of this approach is to reduce the model size and in consequence its computational cost. Nevertheless, two main disadvantages exist: (i) the physical meaning of the variables may be lost and (ii) the treatment can not be extended to handling inequality constraints. Other authors (see [46] or [71]) treat state equality constraints as perfect measurements by augmenting the measurement equation with an associated zero variance noise. In this case, the new measurement noise covariance will be singular and, although a

singular covariance does not present any theoretical problems it increases the possibility of numerical issues. In other cases the equality constraints are used to derive the Kalman filter equations in a maximum likelihood approach [76].

The aim of this discussion is, however, to propose a technique applicable to the case of the ECR-UKF approach implemented within the framework of a Finite Element software such as *Code_Aster*. In the following, we propose to study the case described in section 4.2 concerning the identification of model parameters of a concrete beam in the presence of both structural damage and a mis-modeled boundary. Recall the vector of sought parameters:

$$\theta = \{d_3 \quad k \quad m\}^T \tag{5.2}$$

In this case, all the physical parameters are subjected to a constraint of positiveness.

When using the Unscented Kalman filter for nonlinear estimation, the presence of state constraints affects not only the estimates but also the sigma points used to evaluate process and observation covariances. The original UKF equations do not guarantee that any of the sigma points satisfy the constraints and whose satisfaction thus introduces an additional issue to the construction of the constrained UKF equations. During the last 5 years the introduction of algebraic inequality constraints in the Unscented formalism has received an increasing attention and remains an area of open research. An interesting overview of different existing approaches is proposed by Teixeira et al. in [82] where the performances are illustrated through an example of a chemical process. It is interesting though to point out some aspect of the studied techniques:

- The URNDDR (Unscented Recursive Nonlinear Dynamic Data Reconciliation) approach developed by Vachhani and Narasimhanin in [86] proposes to select a set of sigma points and corresponding weights satisfying the constraints in a projection approach. Then, the state estimation is performed by solving a nonlinear constrained optimization problem at each time step (in that sense the URNDDR does not require the computation of a Kalman gain to obtain the estimates). In this approach, constraints are strictly respected in the estimation of both mean and covariance of the states. However, an external algorithm is required to solve the nonlinear optimization problem for the estimates and for this reason it has not been implemented in the example treated herein.

- In the work by Kandepu et al. [54], after propagation of the sigma points through the nonlinear state equations, the (unconstrained) transformed sigma points which are outside the "feasible" region are projected onto the boundary of the feasible region and continue the further steps while subsequently adapt their weights. In the application of such a method in the ECR-UKF example, this approach has led to a non-positiveness of the covariance matrices. In a variant proposed by Chatzi in [18], the sigma points and its corresponding weights are corrected symmetrically around the mean while also trying to maintain the reasoning of propagating a Gaussian random variable of specific mean and variance. The method demands to solve a new optimization problem in order to now minimize the deviation of the new state variance from the originally estimated. For the same above-mentioned reasons this approach has not been implemented in our example.

- In the probability density function truncation approach proposed by Simon in [77], the probability density functions (assumed to be Gaussian) are truncated at the constraints edges. Thus, the constrained state estimate becomes equal to the mean and covariance of the truncated function in the admissible space. This pdf truncation technique has been implemented in the ECR-UKF example treated below. Notwithstanding, it led to numerical issues for the relatively common cases where the initial guess of the Kalman filter is "far" from the actual state. In this situation, the unconstrained state estimate strongly violates the constraints and the remaining pdf function is, roughly speaking, the "tail" of the Gaussian pdf function whose area is close to zero. At this point, the pdf truncation approach gives numerical singularities when normalizing the truncated pdf function to obtain the constrained distribution (refer to [77] for the pdf truncation equations).

In the following, we illustrate the results of two different experiments that particularly fit the needs of the ECR-UKF example. Beginning with the most natural approach which consists in applying a transformation to the initial variables in a way that the effective variables respect condition (5.1). To do so, suppose a bijection T of class C^1 defined by:

$$\begin{array}{rccll} T: & \mathbb{R} & \longrightarrow &]c_1, c_2[& \\ & x_i & \longmapsto & m_i = \dfrac{\epsilon^2}{c_1 + 2\epsilon - x_i} + c_1 & \text{if} \quad x_i < c_1 + \epsilon \\ & x_i & \longmapsto & m_i = x_i & \text{if} \quad c_1 + \epsilon \leq x_i \leq c_2 - \epsilon \\ & x_i & \longmapsto & m_i = \dfrac{\epsilon^2}{c_2 - 2\epsilon - x_i} + c_2 & \text{if} \quad x_i > c_2 - \epsilon \end{array} \tag{5.3}$$

where x_i are the effective variables introduced in the UKF algorithm with values in $\mathbb{R}$ without restrictions. The m_i are, on the other hand, the structural parameters used to build the FE model with values in the constrained space $]c_1, c_2[$ and ϵ is a positive scalar which has been set to $\epsilon = 0.5$ in the next experiments. The considered function is illustrated in Figure 5.1.

In the example of structural parameters for which positiveness is required, we have considered $c_1 = 0$ and $c_2 = \infty$. The results of four different experiments are shown in Figure 5.2 for different initial guesses of θ_0. In fact, the initial guess of θ_0 has a major influence since the "further" the initial guess from the actual state, the stronger the UKF first sigma point estimates will tend to penetrate the constrained space. In figures 5.2(a) and 5.2(b), penetrations are sufficiently smooth so that the algorithm achieves convergence towards the sought parameters. In Figure 5.2(b) it can be seen, though, that this technique presents a certain slowness of convergence when one or more parameters remain close to the boundary of the admissible parameter space. However, when the initial guesses are even further from their actual value, the sigma point estimates (unconstrained) tend to strongly violate boundaries and numerical issues may start to appear leading to divergence or stability problems of the transformed estimates. Figures 5.2(c) and 5.2(d) show the two phenomena due to numerical inaccuracies of the estimated means and covariances near the boundaries. Hence, it is clear that the variable transformation approach cannot be applied with confidence.

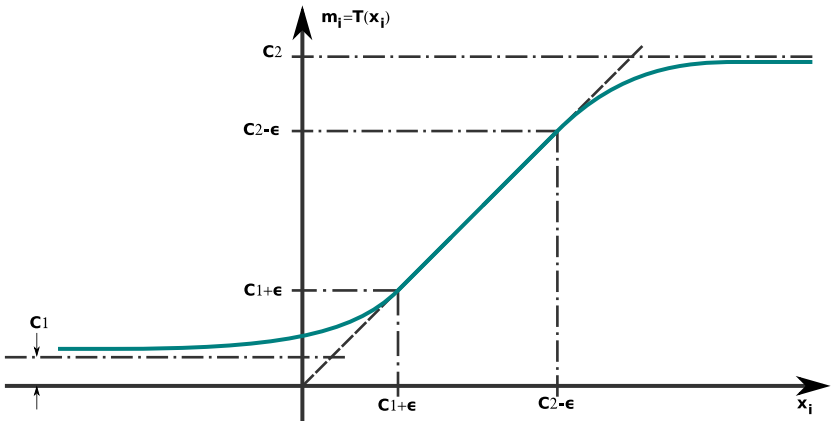

Figure 5.1: *Variable transformation T used to introduce algebraic constraints in the framework of the Unscented Kalman filter for the identification of structural parameters.*

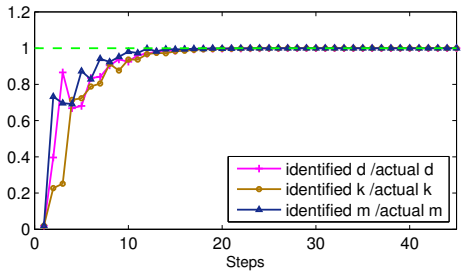

(a) $\theta_0 = \{0.01 \quad 0.01 \quad 0.01\}^T$

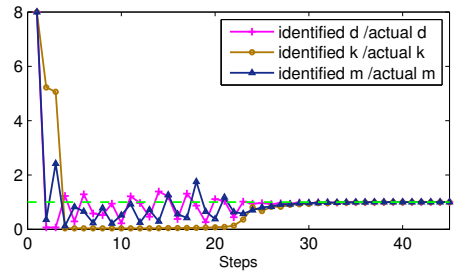

(b) $\theta_0 = \{8.0 \quad 8.0 \quad 8.0\}^T$

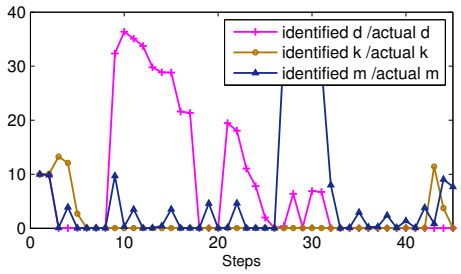

(c) $\theta_0 = \{10.0 \quad 10.0 \quad 10.0\}^T$

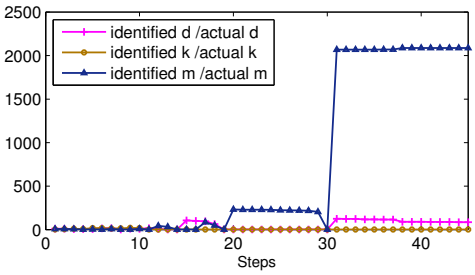

(d) $\theta_0 = \{10.0 \quad 2.0 \quad 6.6\}^T$

Figure 5.2: *Identification of structural damage and impedance parameters incorporating parameter constraints with a variable transformation approach for different initial conditions.*

In order to overcome the aforementioned problems, an adapted technique is proposed below. This approach concerns the particular case we treat here where the observation function is of the form:

$$\xi^2_{Tr}(\theta): \quad \mathbb{R}^m \quad \longrightarrow \quad \mathbb{R}^+$$

Thus, the main idea of this approach consists in completing the observation function in the inadmis-

sible space in a way that penalizes constraint violation and, by doing so, guide the estimates to naturally be repelled away from the constraint boundaries. To do so, the following steps are introduced in the UKF formalism:

1. At each step, project each sigma point $[\theta_j]_i$ into the admissible space so that the observation function can be evaluated. To do so, if the constraints are violated, the following least squares problem can be used to obtain the projected points:

$$[\overline{\theta_j}]_i = \underset{[\overline{\theta_j}]_i}{\arg\min} \quad \|[\theta_j]_i - [\overline{\theta_j}]_i\|_W^2 \quad \text{such that} \quad D[\overline{\theta_j}]_i \leq c \tag{5.4}$$

   where W is a weighting matrix. The solution of such a problem is given by:

$$[\overline{\theta_j}]_i = [\theta_j]_i - W^{-1}\tilde{D}^T(\tilde{D}W^{-1}\tilde{D}^T)^{-1}(\tilde{D}[\theta_j]_i - \tilde{c}) \tag{5.5}$$

   where $\tilde{D}$ and $\tilde{c}$ correspond to the rows of the active constraints of D and c respectively.

   Thus, a projection operator Δ can be defined as:

$$\begin{array}{rccll} \Delta: & \mathbb{R}^m & \longrightarrow & \mathbb{R}^m & \\ & [\theta_j]_i & \longmapsto & [\overline{\theta_j}]_i = [\theta_j]_i & \text{if} \quad D[\theta_j]_i \leq c \\ & [\theta_j]_i & \longmapsto & [\overline{\theta_j}]_i = [\theta_j]_i - W^{-1}\tilde{D}^T(\tilde{D}W^{-1}\tilde{D}^T)^{-1}(\tilde{D}[\theta_j]_i - \tilde{c}) & \text{if} \quad D[\theta_j]_i > c \end{array} \tag{5.6}$$

2. Modify the value of the observation function $\xi_{Tr}^2(\theta)$ with a penalty strategy in order to smoothly repel estimates from the admissible boundaries. The new proposed observation function $\overline{\xi^2}_{Tr}(\cdot)$ is defined as follows:

$$\begin{array}{rccll} \overline{\xi^2}_{Tr}: & \mathbb{R}^m & \longrightarrow & \mathbb{R} & \\ & [\theta_j]_i & \longmapsto & \overline{\xi^2}_{Tr}([\theta_j]_i) = \xi_{Tr}^2([\theta_j]_i) & \text{if} \quad D[\theta_j]_i \leq c \\ & [\theta_j]_i & \longmapsto & \overline{\xi^2}_{Tr}([\theta_j]_i) = \xi_{Tr}^2([\overline{\theta_j}]_i) + K^{pen}\|[\theta_j]_i - [\overline{\theta_j}]_i\| & \text{if} \quad D[\theta_j]_i > c \end{array} \tag{5.7}$$

   where K^{pen} is a positive scalar. In this new function, when the constraints are violated the function is evaluated at the projected sigma point and its value is increased proportionally to the penetration value. This function is illustrated in Figure 5.3 for the sake of clarity.

3. Modify the Kalman gain in order to ensure an admissible estimate as well as positive definiteness of the updated covariances. To do so, a new scaled Kalman gain is sought in order to ensure that all the constraints are respected. Then, the new Kalman gain is reduced by a factor β^{proj} leading to a parameter update equation of the form:

$$\theta_{j+1} = \theta_j - \beta_j^{\text{proj}} K_j^{\theta}\hat{\zeta}_j \quad \text{such that} \quad D\theta_{j+1} \leq c \tag{5.8}$$

where β_j^{proj} is a scalar value such that $0 \leq \beta_j^{\text{proj}} \leq 1$. To obtain such a parameter a first estimation of θ_{j+1} is evaluated with $\beta_j^{proj} = 1$. If constraints are respected the Kalman gain remains unaltered and the algorithm continues on. In the contrary, if constraints are violated, parameter β_j^{proj} is chosen as the scale factor so that the update parameter θ_{j+1} is the projection of θ_j into the constraint boundary $D\theta \leq c$ through the direction given by $K_j^{\theta}\hat{\zeta}_j$. This leads to the following line search:

$$\beta_j^{proj} = \arg\min_{l} \frac{\|\tilde{c}_l - \tilde{D}_l\theta_j\|}{\|K_j^{\theta}\hat{\zeta}_j\|} \tag{5.9}$$

where l is the number of active constraints (number of rows in $\tilde{D}$ and $\tilde{c}$).

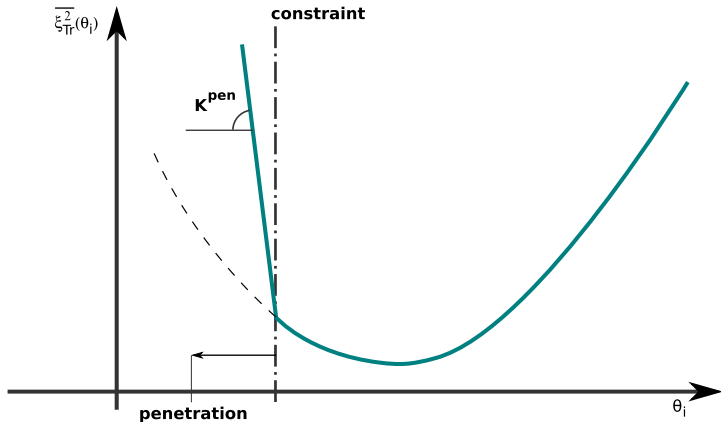

Figure 5.3: *Modification of the ECR observation operator $\xi_{Tr}^2(\cdot)$ with a penalty function depending on the parameter penetration into the inadmissible space.*

The above-mentioned considerations are therefore used to modify the original ECR-UKF algorithm described in Figure 3.7 in order to take into account algebraic inequality constraints. Thus, the proposed constrained ECR-UKF algorithm is detailed in Figure 5.5 where the new and modified steps are colored in red numbers.

This new algorithm has been applied to the case of parameter identification of a concrete beam in presence of structural damage and boundary condition model error. The following assumptions have been made:

$$D = -1 \cdot \mathbf{I}, \quad c = \{0 \quad 0 \quad 0\}^T, \quad W = \mathbf{I}, \quad K^{pen} = 100 \tag{5.10}$$

where $\mathbf{I}$ is the identity matrix. It has to be mentioned that the investigations carried out with this method didn't show a significant sensitivity to the choice of K^{pen} and therefore the assumption $K^{pen} = 100$ is adopted. In Figure 5.4 we show the results of the application of this new algorithm to the identification example. As it can be seen the algorithm converges towards the sought values for the different studied cases and it is important to mention that no numerical issues have been encountered when using this approach. Examples in figures 5.4(b) and 5.4(c) can be compared to those in figures 5.2(c) and 5.2(d)

where the variable transformation (5.3) failed. It can be observed that the positiveness condition is strictly respected by algorithm and the estimates "rebound" in the constraint edge being repelled into the admissible space, as expected. Figure 5.4(d) illustrates the identification results for a severe case with a worse initial guess testing the robustness of the algorithm. Despite this difficulty, the modified ECR-UKF algorithm converges towards the actual values satisfactorily presenting several rebounds in the boundary edge with, notwithstanding, a stable identification process. However, it can be seen that the more often the algorithm bounces off the boundary the more iterations it requires to achieve convergence. This is due to the fact that when projecting estimates and sigma points onto the boundaries the associated covariances are inaccurately estimated and the algorithm needs to recursively enrich this information, spending iterations for doing so.

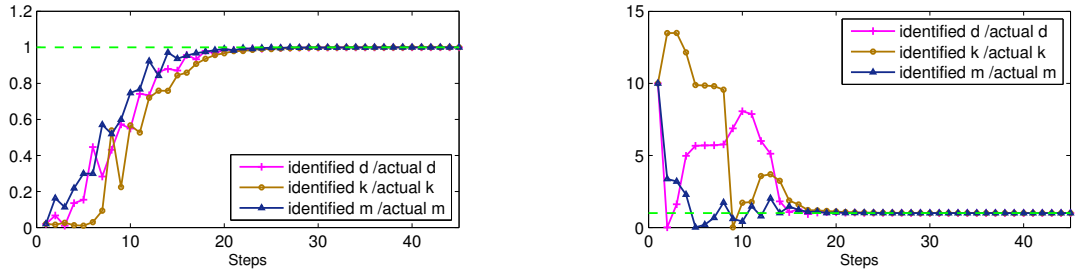

(a) $\theta_0 = \{0.01 \quad 0.01 \quad 0.01\}^T$

(b) $\theta_0 = \{10.0 \quad 10.0 \quad 10.0\}^T$

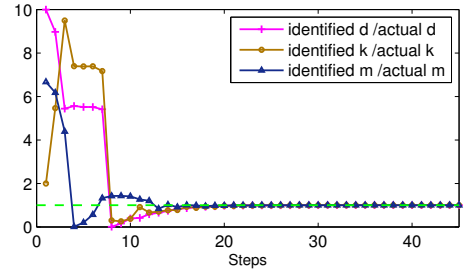

(c) $\theta_0 = \{10.0 \quad 2.0 \quad 6.6\}^T$

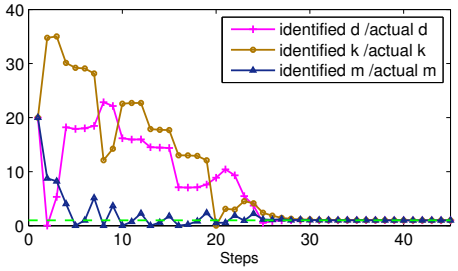

(d) $\theta_0 = \{20.0 \quad 20.0 \quad 20.0\}^T$

Figure 5.4: *Identification of structural damage and impedance parameters incorporating parameter constraints with a sigma points projection approach for different initial conditions.*

To conclude, in this section we have discussed the need and ways to introduce algebraic constraints into Kalman filtering with a particular attention to the case of inequality constraints, which are of main interest in the case of mechanical models. An example of parameter identification using the ECR-UKF algorithm has been analyzed where different approaches have been implemented. While existing methods in the literature presented numerical issues in our case, a solution has been sought for the specific case of the ECR-UKF algorithm. The approach consisting in modifying the ECR based observation function brings the most robust approach in terms of stability even for severe cases. Hence, we propose to use this modified ECR-UKF algorithm when the introduction of algebraic constraints is needed.

ECR based Unscented Kalman filter for parameter estimation

I Initialization

$$\theta_0 = \mathbb{E}[\theta] \quad \text{and} \quad P_0^\theta = \mathbb{E}[(\theta - \theta_0)(\theta - \theta_0)^T]$$

II For $j \in [1 \dots \infty]$

1 Build matrix of sigma points around θ_j

$$[\theta_j] = \{\theta_j \qquad \theta_j + \sqrt{(m+\lambda)P_j^\theta} \qquad \theta_j - \sqrt{(m+\lambda)P_j^\theta}\}$$

2 Project sigma points $[\theta_j]$ onto state intervals

$$[\overline{\theta_j}]_i = \Delta([\theta_j])$$

3 Propagate sigma points through the penalized ECR cost function $\overline{\xi^2}_{Tr}(\cdot)$

$$[\zeta_j] = \overline{\xi^2}_{Tr}([\overline{\theta_j}])$$

4 Best estimate $\hat{\zeta}_j$ through Unscented weighting factors W_i^m

$$\hat{\zeta}_j = \textstyle\sum_{i=0}^{2L} W_i^m [\zeta_j]_i$$

5 Compute Kalman gain

$$K_j^\theta = P_j^{\theta\zeta}(P_j^{\zeta\zeta})^{-1}$$

$$P_j^{\zeta\zeta} = \textstyle\sum_{i=0}^{2L} W_i^c (([\zeta_j]_i - \hat{\zeta}_j)([\zeta_j]_i - \hat{\zeta}_j)^T) + \mathcal{R}_j$$

$$P_j^{\theta\zeta} = \textstyle\sum_{i=0}^{2L} W_i^c (([\theta_j]_i - \theta_j)([\zeta_j]_i - \hat{\zeta}_j)^T)$$

6 Parameter update

$$\theta_{j+1} = \theta_j - \beta_j^{\text{proj}} K_j^\theta \hat{\zeta}_j \quad \text{such that} \quad D\theta_{j+1} \leq c \quad \text{and} \quad 0 \leq \beta_j^{\text{proj}} \leq 1$$

7 Covariance update

$$P_{j+1}^\theta = P_j^\theta - \beta_j^{\text{proj}} K_j^\theta (P_j^{\theta\zeta})^T + \mathcal{Q}_j$$

Figure 5.5: *Modified ECR-UKF algorithm taking into account algebraic state interval constraints. Algorithm steps including a modification of the original UKF are colored in red numbers.*

5.2 Parametric study of ECR-UKF parameter error covariance matrix

In the previous sections, several numerical examples coupling the ECR and UKF techniques are presented in the fashion proposed in chapter 3, showing how these two methods can be combined to obtain both an enriched knowledge of the parametric state of the structure as well as its eventual evolution over time when it occurs. Nevertheless, it is widely known that the quality of the estimation in a sequential Kalman filter approach is directly related to the *a priori* knowledge of model and observation errors. As a matter of fact, this essential *a priori* knowledge is introduced in the Kalman framework in the form of covariance matrices, namely the model error covariance matrix Q_k and the observation error covariance matrix R_k as presented in the linear KF formalism of Figure 2.3. In particular, when referring to the ECR-UKF approach described in Figure 3.7, the subsequent covariance matrices are respectively $\mathcal{Q}_j$ and $\mathcal{R}_j$ as defined in (3.14). In this context, the algorithm can be compared to a quasi-Newton descent method and, as discussed in chapter 3.3, while the role of $\mathcal{R}_j$ only affects the speed, the choice of $\mathcal{Q}_j$ directly affects the convergence rate and the tracking performance.

Hence, in this section the problem of error covariance matrix modeling is addressed within the frame of the proposed ECR-UKF approach. The goal of this parametric study is to investigate the influence of the design of $\mathcal{Q}_j$ in terms of the quality of the estimation. Despite the major importance of covariance matrices in Kalman filtering, its modeling is still an area of open research, currently not often addressed in the literature (cf. [32, 31] in the field of atmospheric research). We will cite, though, the study proposed in [15] where the choice of covariance matrices is performed under the condition of a decreasing Lyapunov function leading to a linear matrix inequality problem which points out the connection of a good convergence between the EKF and the instrumental matrices R_k and Q_k. Moreover, it is interesting to cite the extension of this work to the UKF formalism proposed in [90]. However, in both works the assumption of a linear observation function is made and is therefore not suitable in the ECR-UKF approach.

When it comes to parameter estimation by means of the UKF algorithm, no work has been found in the literature addressing the problem of error covariance design apart from some proposed options in [45]. The present study is therefore based on proposals from [45], as next:

Type A. Set $\mathcal{Q}_j = \upsilon \mathbf{I}$, where $\mathbf{I}$ is the identity matrix. This leads to a simple "fixed" diagonal design of the error covariance matrix.

Type B. Set $\mathcal{Q}_j = \kappa P_j^\theta$. This approximation assumes that covariance matrix $\mathcal{Q}_j$ is consistent with the posterior evaluation of parameter covariance P_j^θ and provides an approximate exponentially decaying weighting on past data.

Type C. Set $\mathcal{Q}_j = (1 - \alpha_{RM}) P_j^\theta + \alpha_{RM} K_j^\theta [\zeta_j - \hat{\zeta}_j][\zeta_j - \hat{\zeta}_j]^T (K_j^\theta)^T$ which is a Robbins-Monro stochastic approximation scheme [62] for estimating the innovations assuming that covariance $\mathcal{Q}_j$ is consistent with both the posterior evaluation of parameter covariance P_j^θ and the covariance of the correction vector $K_j^\theta[\zeta_j - \hat{\zeta}_j]$. Parameter α_{RM} is a weighting factor of both contributors.

In the following, the example of structural damage and impedance parameters presented in section 4.2 is used to compare the different approaches where the model parametrization defined in equation (4.18) is adopted. Hence, only the design of $\mathcal{Q}_j$ matrix is changed in th e next experiments. On the other hand, identical initial conditions are used to initialize the ERC-UKF algorithm where its main characteristics are presented here:

- $\theta_0 = \{d_3 \quad k \quad m\}_0^T = \{0 \quad 1.656 \cdot 10^6 \text{ N/mm} \quad 9.93 \text{ kg}\}^T$
- $P_0^\theta = 10^{-5}\mathbf{I}$
- $\mathcal{R}_j = 0 \quad \forall j$

In Figure 5.6 a type-A error covariance matrix design is examined. The evolution of the ECR cost function $\xi_{Tr}^2(\theta_j)$ residual throughout the identification process is evaluated and compared for different amplitudes υ of $\mathcal{Q}_j = \upsilon 10^{-5}\mathbf{I}$. It can be seen that in all the cases the algorithm presents a very similar convergence ratio and smoothness. Differences start to appear from step 30 where the algorithm starts to reach the steady state solution of the discrete matrix Riccati equation [40]. At this point, we can observe that the ECR residual remains bounded from below in a proportional manner with the amplitude parameter υ. This property allows the most recent data to be emphasized and, in the case of time-varying parameter identification, it maintains the Kalman gain sufficiently large to keep a good tracking. This case will be examined further.

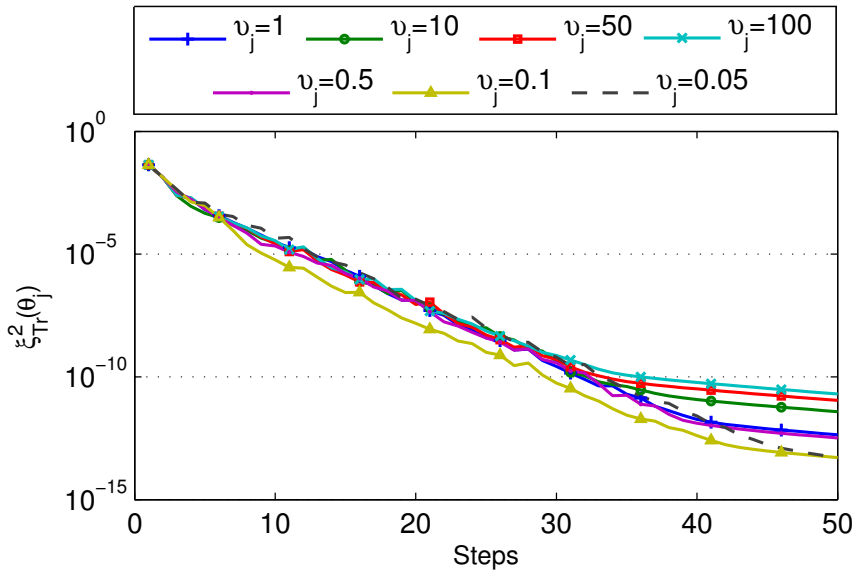

Figure 5.6: *Comparison of $\xi_{Tr}^2(\theta_j)$ residual along the ERC-UKF identification process for different values of υ_j in a $\mathcal{Q}_j = \upsilon_j 10^{-5}\mathbf{I}$ modeling (Type A).*

Figure 5.7 shows the results of a type-B error covariance matrix design where, as in the previous case, the ECR cost function residual is presented for different amplitudes of the κ parameter in $\mathcal{Q}_j =$

$\kappa_j P_j^\theta$. In comparison with the type-A design, a loss of both smoothness in the identification process and convergence speed can clearly be observed. Despite these disadvantages, the algorithm converges towards the actual model parameters. This design has the advantage to introduce a proper order of magnitude of $\mathcal{Q}_j$ without prior assumptions. However, $\mathcal{Q}_j$ anneals towards zero as the identification goes on and might lead to significant inaccuracy for cases where tracking of time-varying parameters is sought.

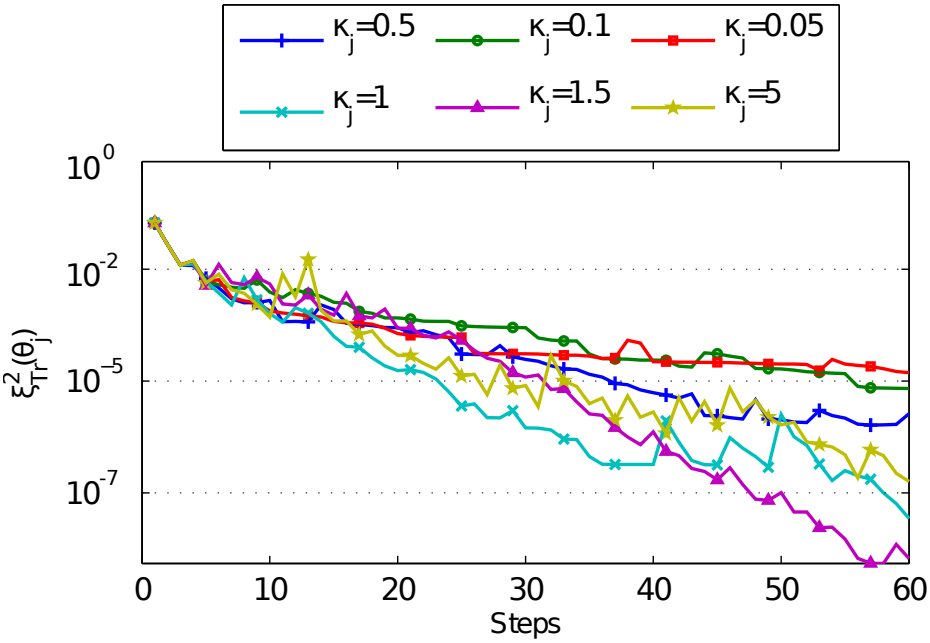

Figure 5.7: *Comparison of $\xi^2_{Tr}(\theta_j)$ residual along the ERC-UKF identification process for different values of κ_j in a $\mathcal{Q}_j = \kappa_j P_j^\theta$ modeling (Type B).*

In that sense, the type-B design can be used to obtain prior order of error covariance matrix $\mathcal{Q}_j$. Hence, we propose to investigate an approach combining type-A and type-B covariance formats, defined as follows:

Type D. Set $\mathcal{Q}_j = \mu\,\mathrm{diag}(P_j^\theta)$. This approximation results into an approximately exponentially decaying weighting on past data with an uncorrelated error through state mapping (diagonal matrix).

Results of the type-D design are presented in Figure 5.8. One can easily observe that this design clearly improves the stability of the solution given by a type-B design due to the fact that matrix $\mathcal{Q}_j$ is forced to be diagonal. In addition, convergence speed is also enhanced and results are comparable to those obtained in Figure 5.6. However, one can remark that for type-D design the quality of the result and in particular speed-rate convergence has a higher sensitivity to the amplitude factor μ than type-A to factor υ. Notice that, for very small values of μ, divergence of the results has been observed. Thereby, the best order of magnitude of μ factor seems to be around $\mu = 1 \pm 0.5$.

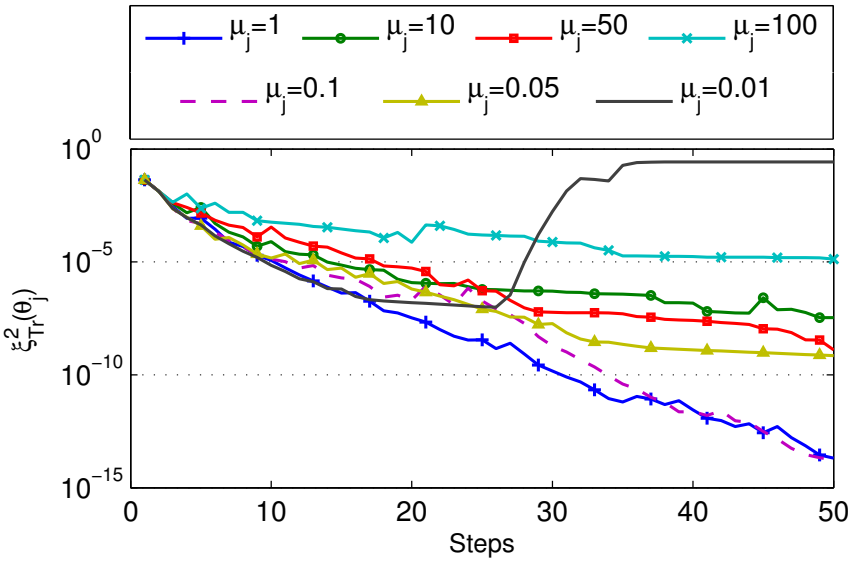

Figure 5.8: *Comparison of $\xi^2_{Tr}(\theta_j)$ residual along the ERC-UKF identification process for different values of μ_j in a $\mathcal{Q}_j = \mu\ \mathrm{diag}(P^{\theta}_j)$ design (Type D).*

The results concerning the type-C design are presented in Figure 5.9. Contrarily to the experience given in [45], the Robbins-Monro approach gives in our case an inappropriate design of the error model covariance matrices $\mathcal{Q}_j$. As a matter of fact, the identification process gets stuck after some iterations depending on the value of the Robbins-Monro parameter α_{RM}. The closer α_{RM} to 1, the sooner the identification gets stuck. This can be seen in the curves presented in Figure 5.9 where one can observe that for $\alpha_{RM} = 0.9$ the identifications fails at the very first iterations while for $\alpha_{RM} = 0.1$ it oscillates (since is a closer design to type B) but finally ends stuck at the same point as the other ones. We can thus conclude that the Robbins-Monro is not a convenient design for the ECR-UKF algorithm.

In order to compare the three "convergent" approaches for the design of $\mathcal{Q}_j$, the best candidates of type-A ($\upsilon = 0.1$), type-B ($\kappa = 0.5$) and type-D ($\mu = 1.0$) are presented in Figure 5.10. While the type-B design presents the worst convergence speed, type-A and type-D designs exhibit very similar performances. Although slight differences exist in the initial steps of the algorithm for type-A and type-D designs, parameter convergence is reached in a very similar way in both cases. This can be appreciated in Figure 5.11 where the parameter estimate evolution throughout the process is shown.

Figure 5.11 shows how the performance differences shown in Figure 5.10 are translated into the parameters space. In particular in figures 5.11(b) and 5.11(c) we see how the type-B design can present both low speed-rate convergence as well as instability of the estimates.

Applying these designs to the time-varying parameters case leads to similar conclusions to the ones obtained for the time-invariant case. To investigate the performances of each design we have used the example of damage evolution in presence of boundary miss-modeling of section 4.2. For this example,

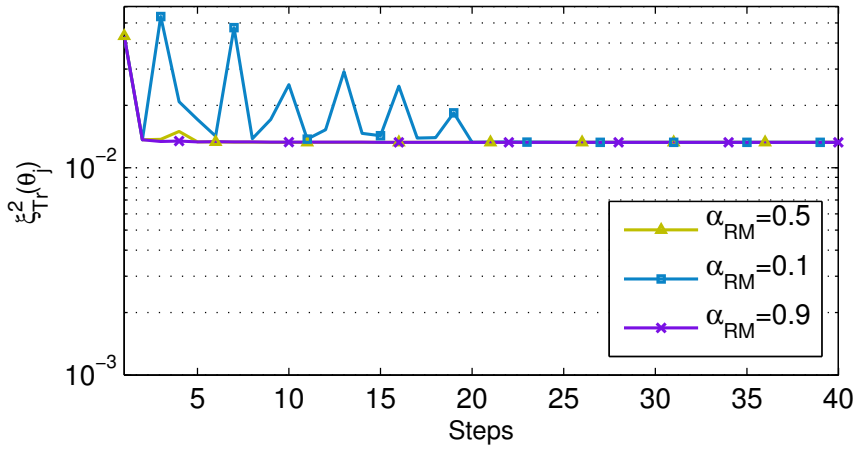

Figure 5.9: *Comparison of $\xi^2_{Tr}(\theta_j)$ residual along the ERC-UKF identification process for different values of α_{RM} in a Robbins-Monro modeling of $\mathcal{Q}_j$ (Type C).*

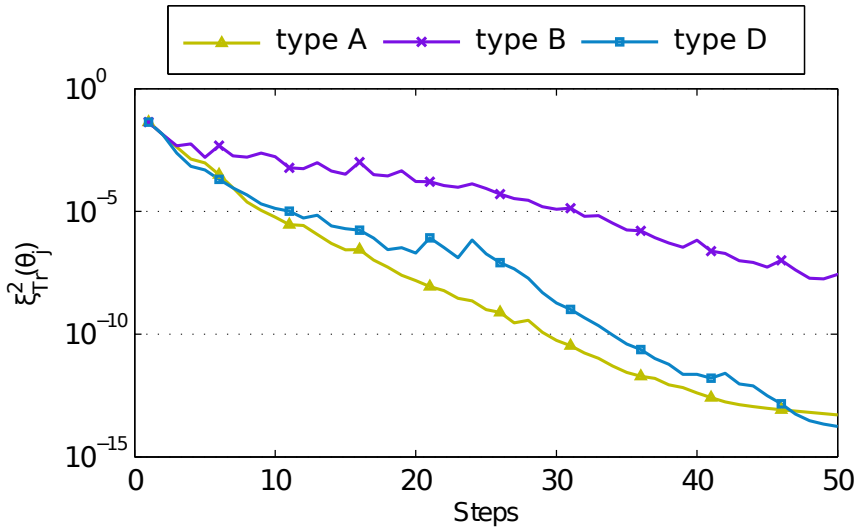

Figure 5.10: *Comparison of $\xi^2_{Tr}(\theta_j)$ residual along the ERC-UKF identification process for different designs of error noise covariance matrix $\mathcal{Q}$: type A ($\upsilon = 0.1$), type B ($\kappa = 0.5$) and type D ($\mu = 1.0$).*

figure 5.12 compares the performances of the algorithm for the three different $\mathcal{Q}_j$ designs.

In Figure 5.12 three different regions can be distinguished: a first region between steps 1 to 15 where the algorithm aims at finding the initial steady state, a second region embedded in between steps 16 and 30 where rapid changes occur and finally, from step 31 till the end, a region where slow changes take place. These three regions explain the "hump-shaped" performance curves where the augmentation of the $\xi^2_{Tr}(\theta_j)$ residual corresponds to the period where the algorithm aims at tracking rapid changes.

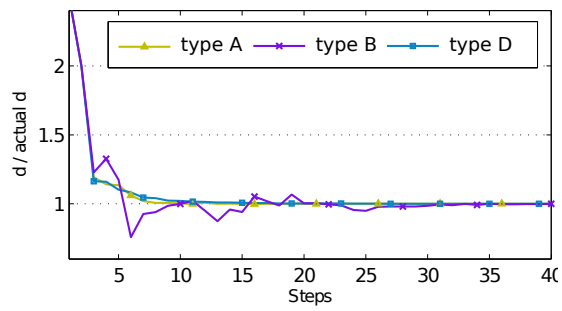

(a) Parameter d_3

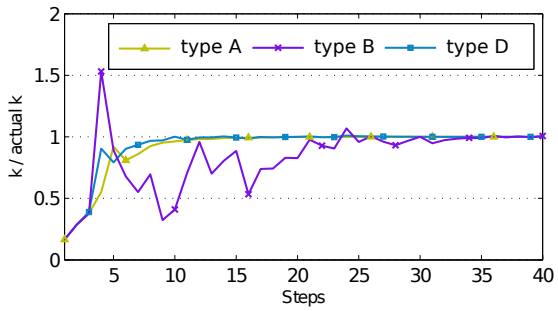

(b) Parameter k

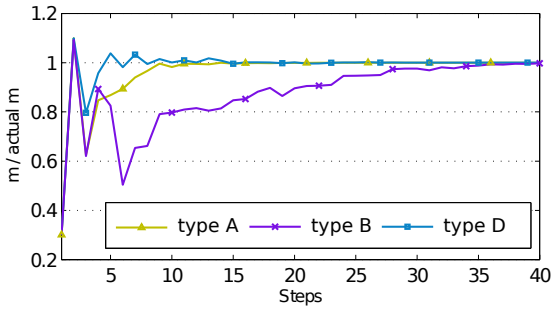

(c) Parameter m

Figure 5.11: *Comparison of the identification results using the ERC-UKF strategy for different modeling of error noise covariance matrix $\mathcal{Q}$.*

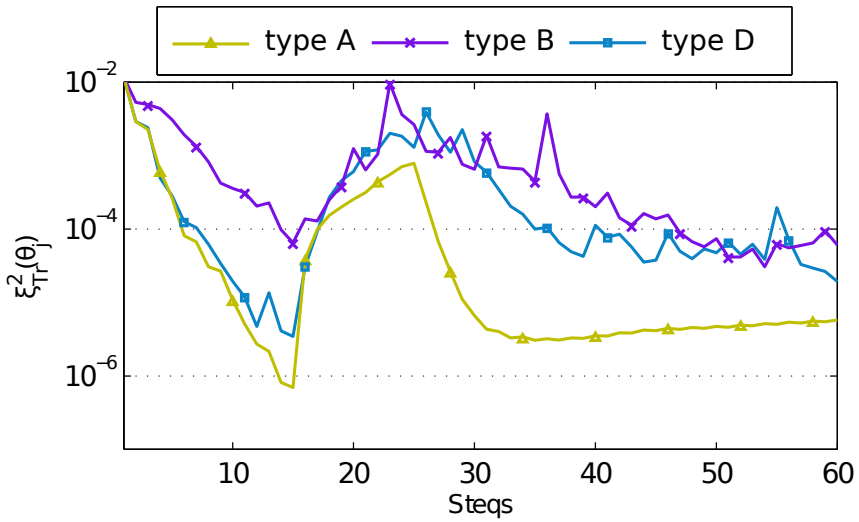

Figure 5.12: *Comparison of $\xi^2_{Tr}(\theta_j)$ residual along the ERC-UKF identification process for different designs of error noise covariance matrix $\mathcal{Q}$ in the case of evolving structural damage: type A ($\upsilon = 0.1$), type B ($\kappa = 0.5$) and type D ($\mu = 1.0$).*

Unlike the conclusions obtained for the time-invariant case, Figure 5.12 shows a better behavior of the type-A design than the other approaches. Indeed, not only the initial state is reached with better accuracy but also rapid changes are better tracked, allowing a more precise estimation during the slow changes period.

Figure 5.13 illustrates the performances of the three approaches when comparing the damage parameter tracking for the evolving-damage case. It can be seen that the performance of type-A error covariance matrix design gives very good results leading to a satisfying posterior knowledge of the structural damage evolution over time. On the other hand, while type-B design globally tracks damage in a correct way, its lack of stability gives an inaccurate idea of the actual damage evolution. Besides, the type-D approach improves the stability of the estimates, at the expense of a somewhat slower convergence. This is due to the fact that, in type-A design, the eigenvalues of P^{θ}_{j+1} stay bounded from below, leaving the Kalman gain K^{θ}_{j} sufficiently "large" to emphasize recent changes of the innovation vector $(\zeta_j - \hat{\zeta}_j)$ and by this better take into account rapid changes. On the contrary, since type-D provides an approximate exponentially decaying factor, all the eigenvalues of P^{θ}_{j+1} vanish and changes are identified with a certain delay and slowness.

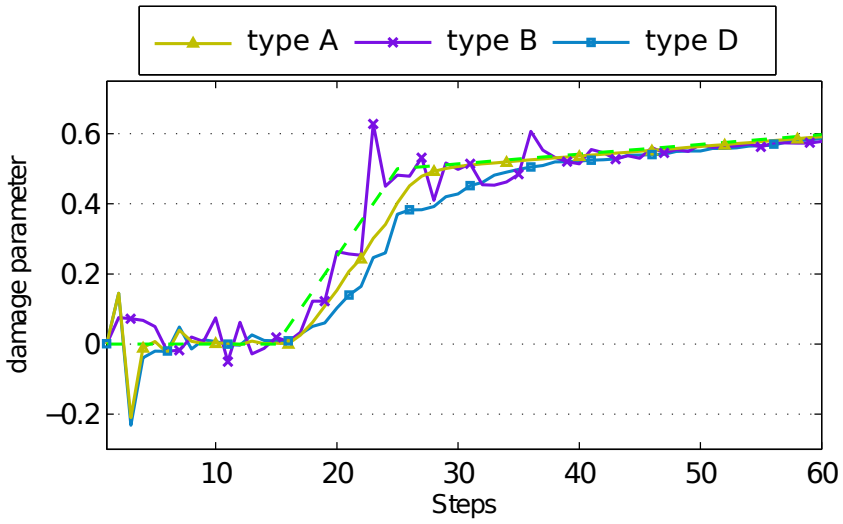

Figure 5.13: *Comparison of the identified damage parameter d_3 along the ERC-UKF identification process for different modeling of error noise covariance matrix $\mathcal{Q}$ in the case of evolving structural damage.*

To conclude, in this section a parametric study of error covariance matrix $\mathcal{Q}_j$ design is addressed with particular attention to the ECR-UKF framework. In particular, four different approaches are investigated using the example of structural damage and boundary impedance parameters identification described in section 4.2. It has been shown that the design of a constant diagonal matrix gives very good results in terms of speed-rate and stability of the solution. In particular, it has the ability to track rapid changes seeming particularly appropriate to the case of time-variant parameters. On the other hand, while the case

of a Robbins-Monro approach makes the algorithm fail in the identification process, two other designs based in the information contained in the posterior parameter covariance P_j^θ are studied. A first approach consisting in $\mathcal{Q}_j = \kappa P_j^\theta$ reaches convergences but lacks of stability. Finally, a modified approach uses $\mathcal{Q}_j = \mu \, \text{diag}(P_j^\theta)$ considerably improving the stability issue and resulting in an approximately exponentially decaying factor where no user defined tuning has to be done concerning the order of magnitude of matrix $\mathcal{Q}_j$. This design seems therefore appropriate for the case of time-invariant parameters identification achieving stability and acceptable speed-rate convergence.

5.3 Conclusions

When using the ECR-UKF algorithm in its original form as proposed in chapter 3, the user may have to upfront some specific issues. This chapter addresses two of the main difficulties encountered when putting in use the ECR-UKF, namely the introduction of algebraic constraints in the estimated vector θ and the design of covariance matrices $\mathcal{Q}_j$.

Concerning the problem of introducing algebraic constraints, two different approaches are studied as an alternative to the methods proposed in the literature. A variable transformation is firstly proposed which, although giving satisfactory results in some cases, it can suffer from numerical issues leading the algorithm to divergence. To overcome this problem a modified ECR-UKF is proposed. It is based on the projection of the UKF sigma points into state intervals and a subsequent modification of the ECR function. This approach proved to be a more robust method to deal with algebraic constraints and is adopted in the further uses of the ECR-UKF.

On the other hand, the design of covariance matrices $\mathcal{Q}_j$ may have a strong influence on the identification process. Since no general guidelines exists for this, the influence of four different designs are studied for the cases invariant and evolving parameters. In both cases, a specific design is proposed and, again, are adopted in the further uses of the ECR-UKF.

Part III

Applications

Introduction

This part is devoted to evaluating the ability and robustness of the ECR-UKF approach when applied to relevant industrial situations. In that sense, it represents a step towards the investigation of two of the main topics studied in chapter 4, namely damage assessment in complex structures and boundary condition mis-modeling identification. Accordingly, this part is divided into two chapters.

Chapter 6 aims at investigate the use of the ECR as a method to localize and characterize structural damage in complex structures subjected to seismic loads. It is based in the so-called SMART international research benchmark started in 2007 by EDF and CEA (the French Atomic Energy Commission) aimed at assessing the resistance of civil engineering structures to seismic activity. It is important to mention that the chapter summarizes the work conducted in the framework of a 6-month undergraduate internship by Maïlys Pache (a final year student of ENSTA-Paristech) and supervised by myself in the course of this thesis. This chapter is completed by Appendix E where the most important chapters of the final internship report written by M. Pache are reproduced.

Chapter 7 is devoted to an experimental campaign where a reinforced concrete beam is placed in a testing bench that strongly modifies its dynamic behavior. Here, a FE model initially assumes perfect clamping boundaries and the problem of mis-modeled boundary conditions is addressed, considering that no *a priori* knowledge of model errors is available. Thus, the use of real, noisy, measurements and the identification of complex boundary impedances represents the main issue of this investigation.

Chapter 6

ECR in civil structures assessment: application to the SMART benchmark

Contents

6.1 Introduction

In the course of this doctoral research, I supervised the work of a final-year undergraduate engineering student (Maïlys Pache, from ENSTA, Paris), who devoted a 6-month internship to both testing the implemented ECR routines with complex FE models and evaluating its robustness on an example of industrial relevance. In particular, we aimed at investigating the use of the ECR as a method to localize and characterize structural damage in complex structures. To this aim, the frequency-domain ECR methods were applied to a FE model of nuclear power plant auxiliaries building made of reinforced concrete and subjected to seismic loads, whose experimental and numerical models are shown in Figure 6.1. Both numerical and experimental models were the object of the so-called SMART international research benchmark started in 2007 by EDF and CEA in order to assess the ability of civil structures to resist seismic activity. The internship was conducted at EDF's research division. This short chapter summarizes this internship work. Further details are given in Appendix E, where the main chapters of M. Pache's final report are reproduced.

6.2 Main results

The contributions of the internship to the goals of this Ph.D were twofold. Firstly, from the methodological point of view, numerical experiments on the SMART model helped to better comprehend and interpret

(a) Experimental specimen placed onto a shaking table at CEA laboratories

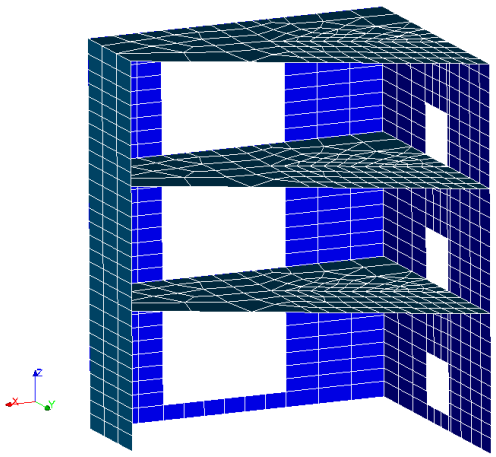

(b) Finite Element model

Figure 6.1: *Nuclear auxiliaries building models subjected to seismic loads used in the SMART benchmark.*

the ECR results as well as its limitations in complex models. Secondly, from the numerical point of view, it helped to adapt the relevant routines written in the course if this work to the *Code_Aster* environment. Cases of increasing difficulty were addressed, from sensitivity studies on linear frequency-domain models to time-domain problems under seismic loadings. The main contributions of this internship work are itemized next.

Methodological contributions

- When evaluating the model error spatial distribution, the importance of the external loading frequency range is shown. When using single-frequency loadings, modeling defects may be only partially detected in complex structures. Usually the quality of ECR indicators is improved when using a large frequency range. This is investigated through information obtained from the ECR spectrum.

- Numerous parametric investigations were carried out concerning the quality of the ECR, with particular emphasis on application to the SMART model. The effect of (i) size, location and intensity of the error, (ii) the chosen set of sensors and (iii) the choice of the regularization parameter r of ECR functionals were considered. Some illustration results are presented in Figure 6.2

- A case where synthetic measurements were obtained from a time-domain nonlinear simulation. Here, the ECR indicators were used to assess the presence of structural damage, inducing deviation from an initially undamaged linear model. Simulations were performed with the DYNA_NON_LINE *Code_Aster* operator and the GLRC_DM constitutive material (global reinforced concrete damage).

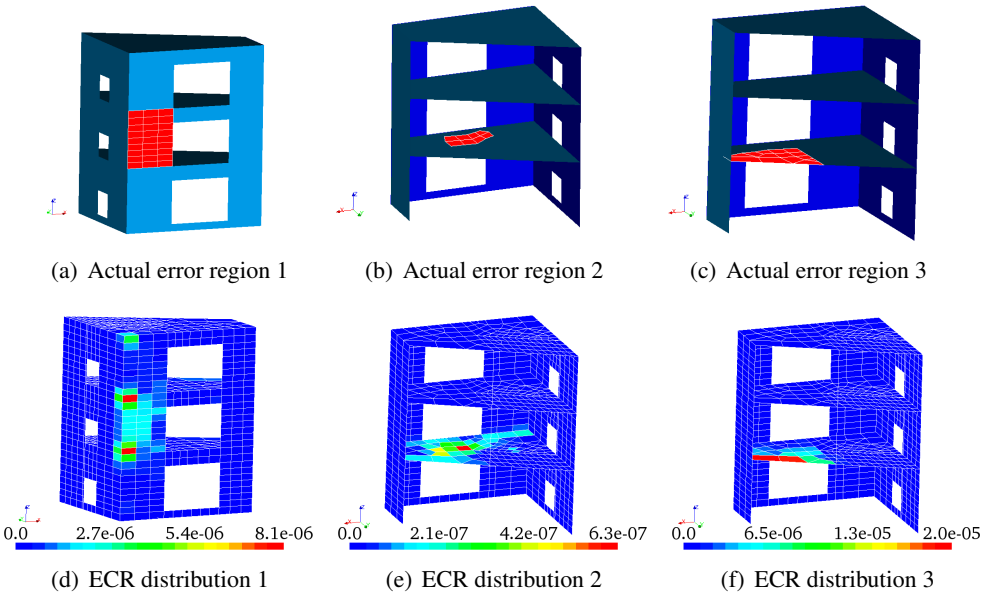

(a) Actual error region 1 (b) Actual error region 2 (c) Actual error region 3

(d) ECR distribution 1 (e) ECR distribution 2 (f) ECR distribution 3

Figure 6.2: *Results of parametric model error localization by means of ECR indicators. Application to different size and location defects.*

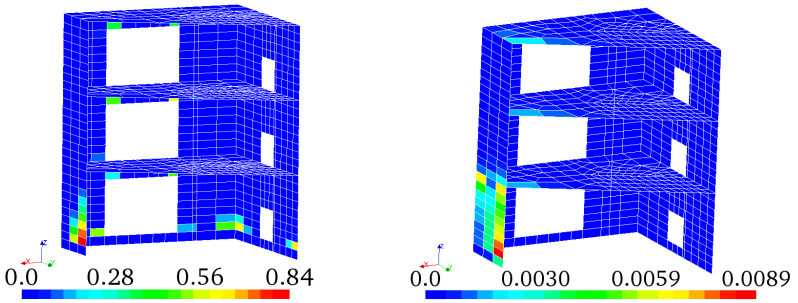

(a) Actual damage from the nonlinear simulation

(b) ECR distribution in an undamaged linear model

Figure 6.3: *Results of an ECR analysis use to spatially localize nonlinear structural behavior (damage law).*

The ECR indicator showed a good ability to spatially localize the presence of nonlinearities, as can be seen in Figure 6.3.

Numerical contributions

- Python routines associated with the resolution of the ECR problem in the *Code_Aster* environment were adapted to the use of large model matrices ($[M]$,$[C]$, $[K]$) with the help of the *sparse.scipy* Python library.

- The evaluation of cumulative (in frequency) ECR indicators

$$\int_{\omega_{\min}}^{\omega_{\max}} \eta(\omega) e_{\omega r}^2 d\omega \tag{6.1}$$

can entail high computational cost when using the CREA_CHAMP *Code_Aster* operator with option ASSE. An optimized method was proposed to avoid the evaluation of error fields $e_{\omega r}^2$ for every quadrature value $\omega_i \in [\omega_{\min}, \omega_{\max}]$.

6.3 Conclusions and further work on the SMART benchmark

In this work the ECR techniques were satisfactorily applied to a case of industrial relevance within the *Code_Aster* environment. In particular, the overall ability of the ECR indicators to spatially detect modeling defects was verified while, notwithstanding, showing some limitations (i.e. defects located at particular regions were hard to capture). One of the most interesting results is the application of the ECR evaluated by exploiting measurements obtained from a nonlinear simulation. In this case, time-frequency equivalences, liable to introduce additional measurement errors, were required. However, the ECR gave qualitatively good results for the spatial localization of modeling errors in complex structures. In the study of the ECR as a method to identify nonlinear structural damage, the damage evolution was, however, difficult to track, due to the non-stationary nature of the external load (earthquake signal) .

The use of experimental measurements will in the near future complete this work. As a longer-term research goal, applying an ECR time-domain formulation will certainly be an interesting approach for structural assessment under seismic loadings.

Chapter 7

Study of a reinforced concrete beam with strong boundary coupling

Contents

7.1 Experimental setup and problem description

This chapter is devoted to an experimental campaign conducted in order to evaluate the ability of the ECR and UKF techniques to both enhance the model representativity and detect model boundary mis-modelings without any *a priori* knowledge of their location or nature. In this experiments, a reinforced concrete beam has been used as a reference structure in a similar way to the study of section 4.2. Here, although supposedly initially double-clamped, the structure is placed in a testing bench introducing strong boundary interaction with the surrounding structures (boundary coupling) which strongly affect the dynamic response. Thus, the use of real measurements as well as the identification of complex boundary impedances represent a step forward in the evaluation of the method's robustness.

The experimental campaign was carried out in cooperation with the LMT laboratory of Ecole Normale Supérieure de Cachan, particularly with the help of Prof. Frédéric Ragueneau. In this project, the design and construction of the test rig as well as the concrete specimens were realized by the LMT. On the other hand, test setup, data acquisition and signal processing were performed by the author.

Two main investigations are presented herein. Firstly, the study of strong boundary mis-modeling is addressed, i.e. locate and identify model errors, to further identify boundary impedances for a better representativity of the coupled beam-environment response. Secondly, the specimen will be damaged at its mid-span with the help of an external quasi-static loading device. The presence of damage will be

sought as a structural modification that also affects the structure's response. Thus, this study embeds the resolution of a sequence of different problems of increasing difficulty since the success of each step depends on the quality of the previous results.

The experimental test setup is presented in Figures 7.1 and 7.2. The concrete beam is placed in a bench composed of steel beams (of type HEB 340 according to the European standard NEN-EN 10025-1/2) and is excited in vertical direction (z) with the help of a test shaker. The input excitation corresponds to a Gaussian noise ($F \sim \mathcal{N}(0, 445)$) having a time duration of 20s. Since the numerical experiments are performed in the frequency domain, a time-frequency equivalence is required. In particular, all the time-domain quantities are sampled in 20 windows and mean values are extracted. In addition, samples are built using Hanning windows that overlap of 50%. In that way, the external loading power-spectrum density is shown in Figure 7.3. It can be observed that the input signal is of good quality in the bandwidth of interest $[5Hz, 350Hz]$ and degenerates for low frequencies $[0Hz, 5Hz]$ which are not studied in this work since they are considered as irrelevant for the structure's response.

On the other hand, a FE model, presented in Figure 7.4, has been created to study the structure's behavior. The main model properties are the following:

- Number of DOF: 276 (138 nodes and 44 hexahedral elements).
- Initial assumption on boundary conditions: double perfect clamping.
- Material: concrete with elastic properties E $= 20 \cdot 10^9$ N/m^2, $\varrho = 2400$ kg/m^3 and $\vartheta = 0,2$. Low Rayleigh damping with $\alpha_{Ray} = 1.2425$ and $\beta_{Ray} = 6.3649 \cdot 10^{-6}$

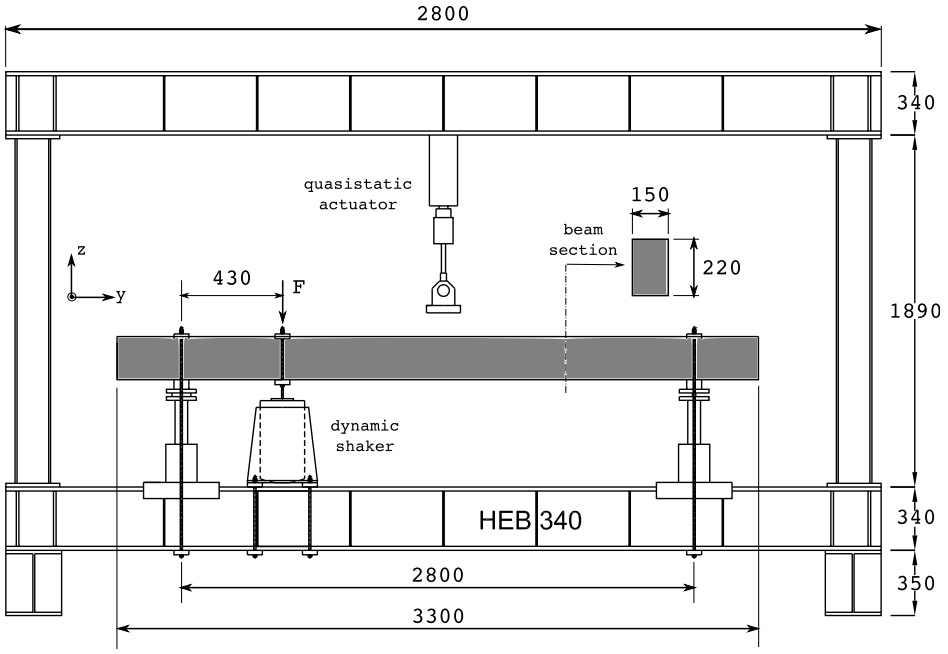

Figure 7.1: *Sketching of the reinforced concrete beam test setup.*

Figure 7.2: *Test setup of the reinforced concrete beam with boundary coupling.*

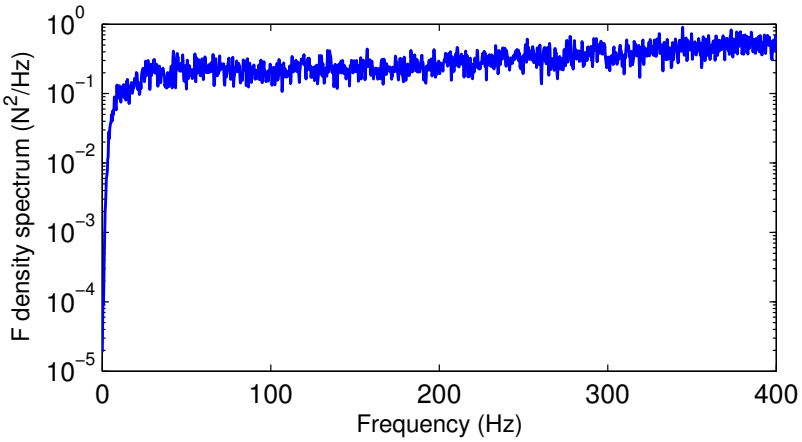

Figure 7.3: *Vertical excitation power-spectrum*

- External loading: $F \sim \mathcal{N}(0, 445)$ in the bandwidth $[5Hz, 350Hz]$.
- Number of sensors: 16 in z direction only.

Notice that the surrounding structure and the consequent coupling with the studied specimen is assumed to be totally unavailable to the hypothetical user.

As represented in Figure 7.4 the density of sensors is relatively high considering that a symmetric distribution of sensors is also set in the lower face of the beam. However, in this study, only 8 upper

sensors and 8 lower sensors are used. The blind or unobserved sensors will be used to compare the model response and the actual response at those locations. As a convention, sensor locations will be denoted as S1, S2,...,S30. Here, S1 to S15 sensors are located on the upper beam face (highest z coordinate) while the lower face sensors are numbered from S16 to S30. Moreover, the numbering increases with the y coordinate. In this description, S14 and S29 correspond, respectively, to the upper and lower sensors located at the same y coordinate as the external load.

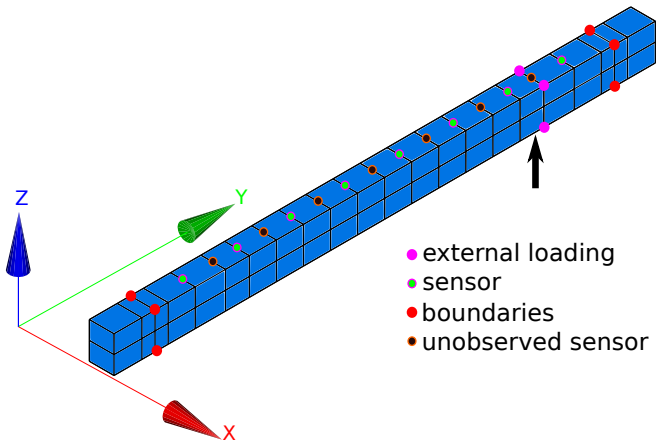

Figure 7.4: *Concrete beam FE mesh description and sensor locations.*

7.2 Boundary impedances identification

As expected, results from a preliminary run of the FEM strongly disagree with the measurements, as illustrated by a comparison of the frequency response functions (FRF) at the mid-span of the beam (S9 location) shown in Figure 7.5. The model gives erroneous information not only about structure's eigenfrequencies and response amplitudes, but also on the modal density, making it totally unexploitable as is. Thus, in an effort to enhance the FE model representativity, an initial ECR analysis is performed.

An ECR spectrum of the global structure with its double-clamped boundary assumption is presented in Figure 7.6. Relative errors are clearly extremely high (from 50% to 300% of relative error) confirming what was already known from simply comparing the response spectrum (Figure 7.5).

In addition, although the model seems to be particularly erroneous at frequencies around 48Hz, important error peaks also appear around 97Hz, 111Hz, 153Hz and 261Hz. To go further on the analysis of the error's nature, the ECR distribution ξ^2_{Er} is studied at those frequencies. In particular, the evaluation of Ind_{K_E} and Ind_{M_E} are computed in order to investigate whether the error comes from a stiffness or mass bias. Figure 7.7 shows the distributions of Ind_{K_E} at peak error frequencies while Ind_{M_E} are omitted since they are smaller by at least one order of magnitude.

As it can be seen in Figure 7.7, model errors seem to be totally concentrated in boundaries. This first analysis indicates the presence of strong boundary coupling and confirming, on the other hand, that the

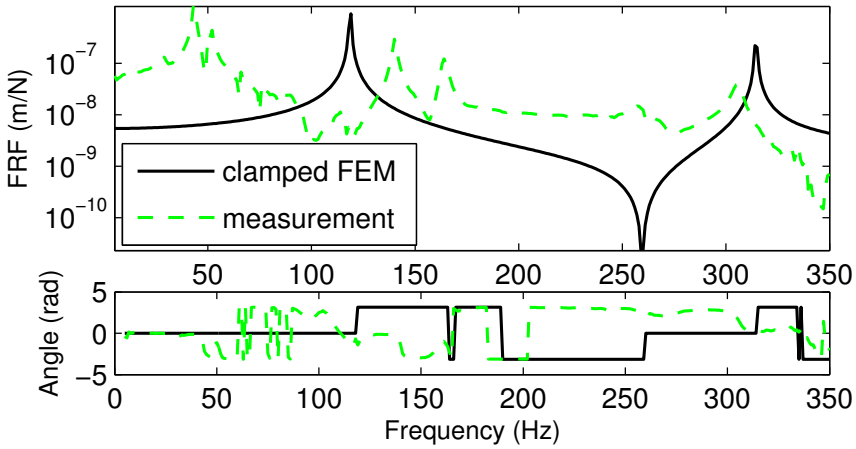

Figure 7.5: *Comparison between measured and initial perfect clamped FEM FRFs at sensor S9.*

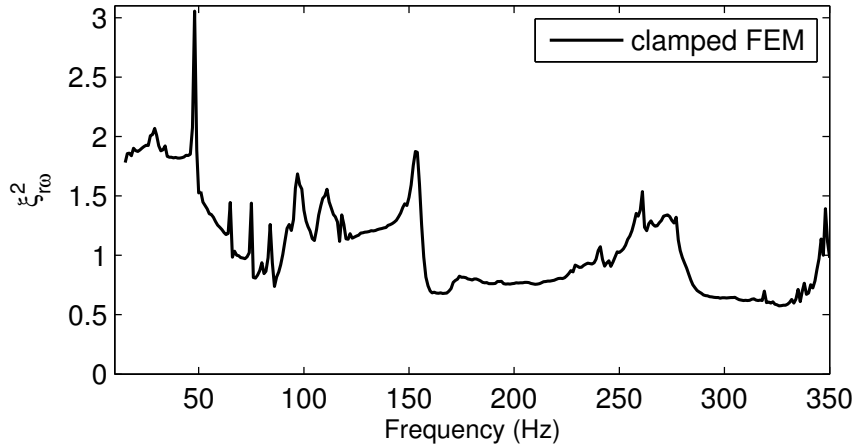

Figure 7.6: *Initial ECR spectrum for a perfect double-clamped FEM.*

ECR preliminary analysis gives a valuable information to improve the model *a priori* knowledge.

In order to improve the accuracy of the FE model, the perfect-clamping boundary conditions are released and, as in the numerical examples treated in previous chapters, the presence of significant boundary displacements is investigated. Hence, equations (4.10) to (4.14) are used to evaluate the boundary DOFs behavior and eventually obtain boundary impedances that would model the influence of the neighboring structures.

To do so, the initial FE model is modified with the introduction of new boundary DOFs supposed to embed the interaction of the beam with the other adjacent structures. A first choice to model this interaction consists in, for each clamping, condensate the DOFs of the 4 nodes into a single one in a

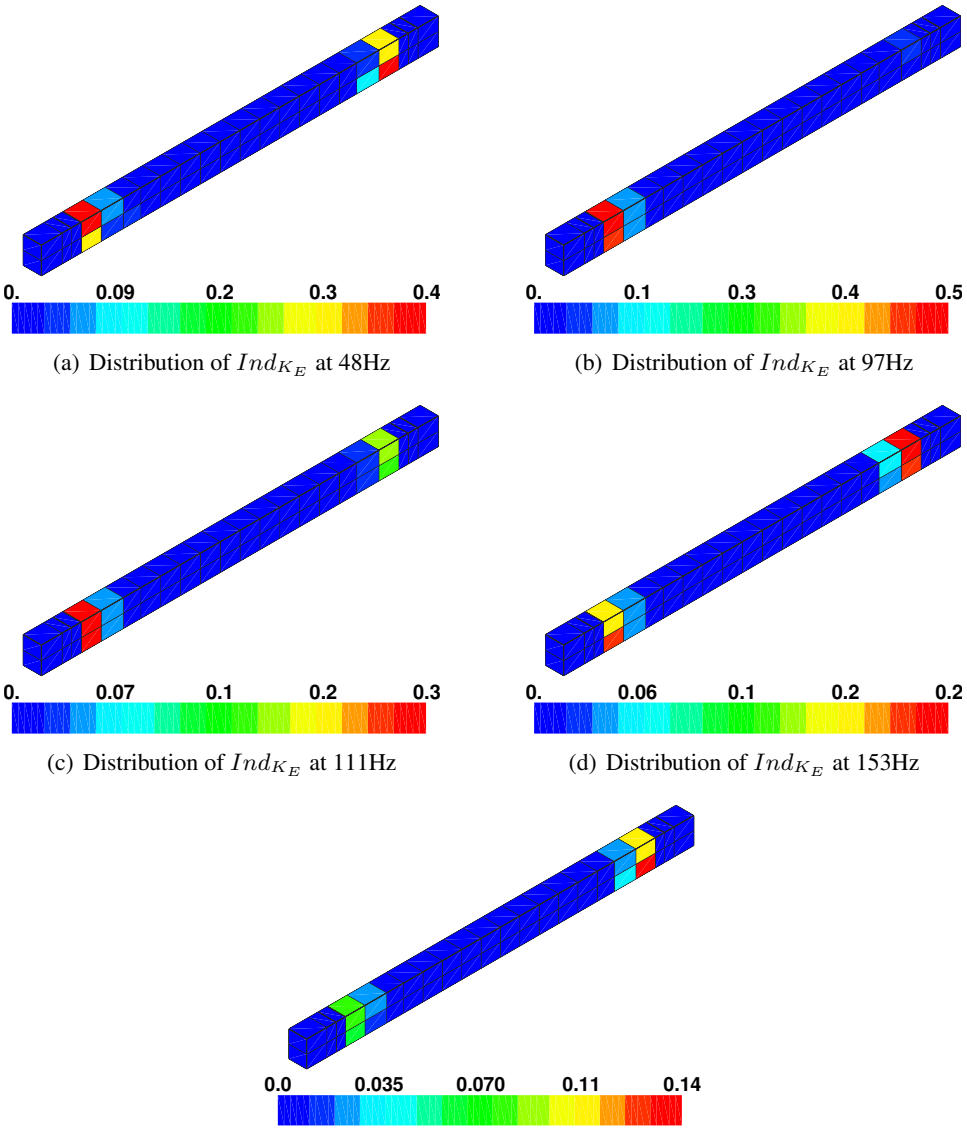

(a) Distribution of Ind_{K_E} at 48Hz

(b) Distribution of Ind_{K_E} at 97Hz

(c) Distribution of Ind_{K_E} at 111Hz

(d) Distribution of Ind_{K_E} at 153Hz

(e) Distribution of Ind_{K_E} at 261Hz

Figure 7.7: *Preliminary ECR analysis for a perfect double-clamped concrete beam FE model. Distribution of $IndK$ estimators over the structure at peak error frequencies.*

master-slave rigid condition as shown in Figure 7.8. The new nodes (N139 and N140 in the subsequent mesh) will adopt free vertical (z) and rotational (Rx) DOFs. Thus, the new FE model can be written:

$$\begin{bmatrix} Z_{ii} & Z_{ib} \\ Z_{bi} & Z_{bb} + \hat{Z} \end{bmatrix} \begin{Bmatrix} q_i \\ q_b \end{Bmatrix} = \begin{Bmatrix} F_i \\ \mathbf{0} \end{Bmatrix} \tag{7.1}$$

where $\hat{Z}$ represents the boundary impedance to be identified. In this study, it takes the form:

$$\hat{Z} = \begin{bmatrix} z^z_{139}(\omega) & 0 & 0 & 0 \\ 0 & z^{Rx}_{139}(\omega) & 0 & 0 \\ 0 & 0 & z^z_{140}(\omega) & 0 \\ 0 & 0 & 0 & z^{Rx}_{140}(\omega) \end{bmatrix} \tag{7.2}$$

where $z^z_i(\omega)$ and $z^{Rx}_i(\omega)$ are respectively the vertical (z) and rotational (Rx) impedance functions of boundary DOF i.

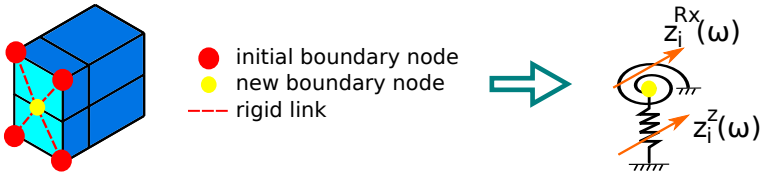

Figure 7.8: *Illustration of initially clamped DOFs condensation into a single DOF containing vertical (z) and rotational (Rx) motion. This model is adopted at each of both clampings.*

When applying the before-mentioned condensation and inversion equations (4.13) and (4.14) for boundary DOFs, the impedances shown in Figure 7.9 are obtained. One of the first remarks is that the order of magnitude is comparable to that of the structure's stiffness, clearly indicating that the perfect-clamping assumption was highly erroneous. Non negligible displacements at boundary DOFs must therefore be expected. Moreover, one can easily point out that impedances are non-symmetric for nodes N139 and N140 either for vertical DOFs (z) or rotational DOFs (Rx) what clearly confirms that the 4 boundary DOF'S must be considered as independent. For this reason, and considering that a parametric representation with a subspace identification method would require a high parametric order to capture the essential phenomena, the identified boundary impedances are introduced without further modification in the FE model (7.1).

Hence, a new model response with boundary coupling is obtained. Figure 7.10 illustrates the new FRF at the unobserved sensor location S8 and compares it to the real structure's response. As it can be seen, the simulation matches the measured data very well. Moreover, results are of similar quality regardless of the sensor location. One could rapidly conclude that this FE model with identified boundary impedances adequately represents the behavior of the real structure.

However, to confirm the good agreement between response and measurements, a new global ECR spectrum is calculated in order to evaluate the quality of the new model. It is presented in Figure 7.11 and compared to the initial error spectrum.

The new model with boundary impedances drastically improves the quality of the initial double-clamped one, in particular in the frequency range $[100Hz - 350Hz]$ achieving relative model errors lower than 5%. However the model quality, as measured by the ECR, deteriorates in the low-frequency range. Indeed, the $\xi^2_{r\omega}$ indicator, although significantly lower than for the initial model, still remains at

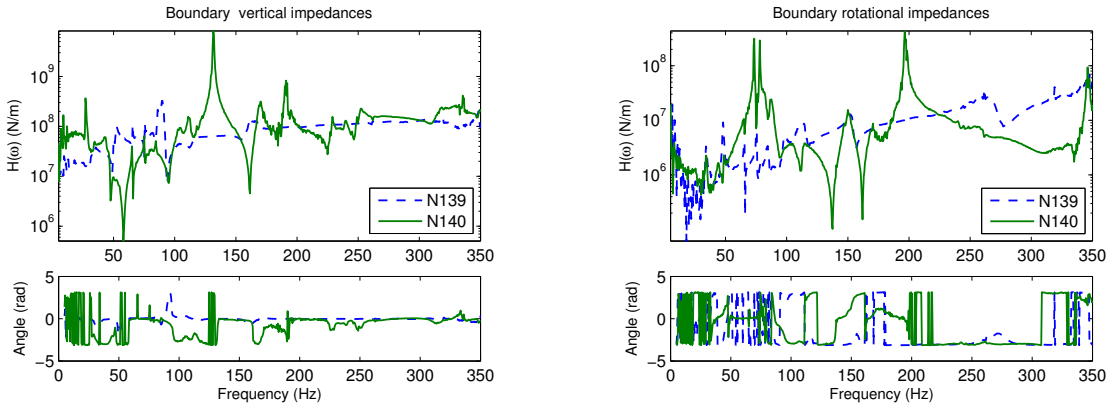

(a) Vertical (Dz) impedances.

(b) Rotational (DRx) impedances

Figure 7.9: *Identified boundary impedances of the concrete beam setup.*

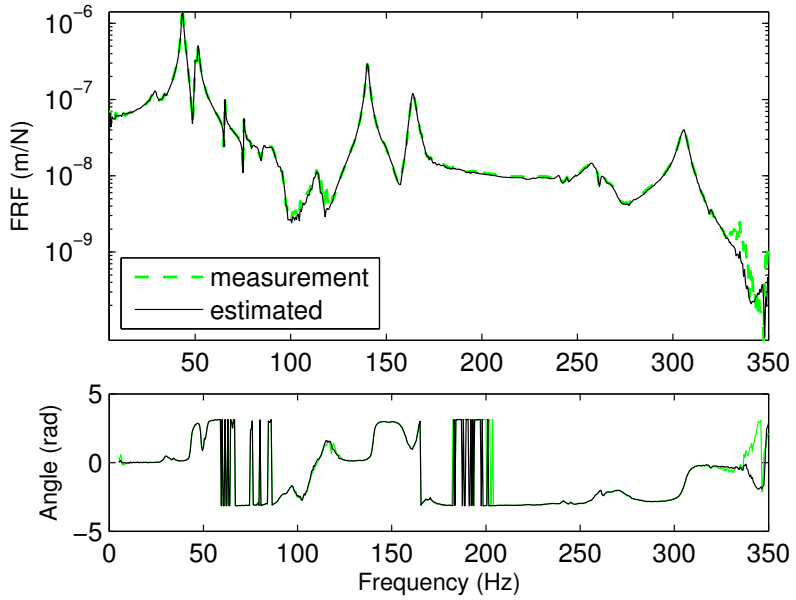

Figure 7.10: *FRF's comparison between measured and FEM with identified boundary impedances at sensor S8 location (unobserved).*

unacceptable levels (achieving a relative error of over 100% for very low frequencies). An analysis of the error spatial distribution for this frequency range reveals that model errors still remain concentrated in boundary regions as shown in Figure 7.12.

At this point, two different efforts have been realized in order to improve the model quality at low frequencies and are presented next. The first approach consists of adopting a new formulation for impedance identification in a specific way to minimize the ECR functionals. The second, seeks to identify model

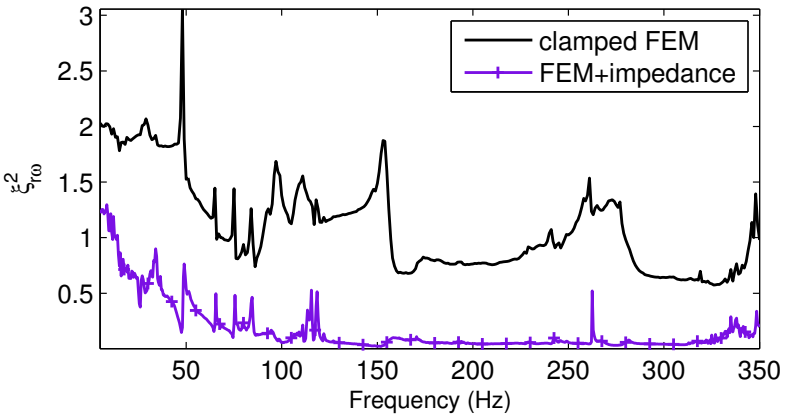

Figure 7.11: *Comparison of ECR spectrum between a perfect clamping FEM and an identified boundary impedance FEM.*

material parameters in an effort to minimize the ECR spectrum.

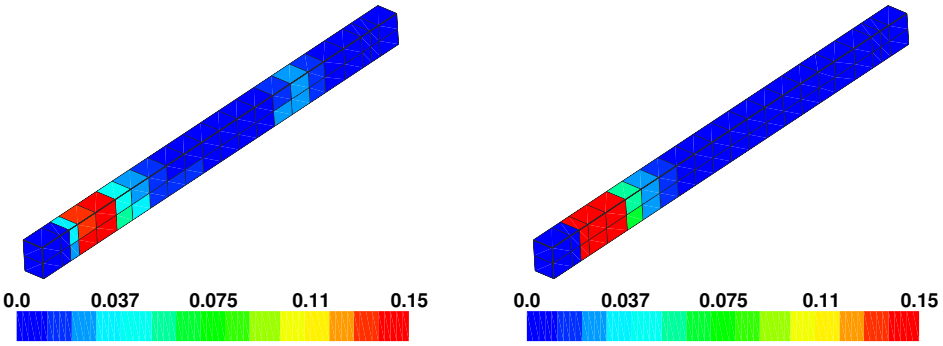

(a) Distribution of Ind_{K_E} at 92.5Hz

(b) Distribution of Ind_{K_E} at 151Hz

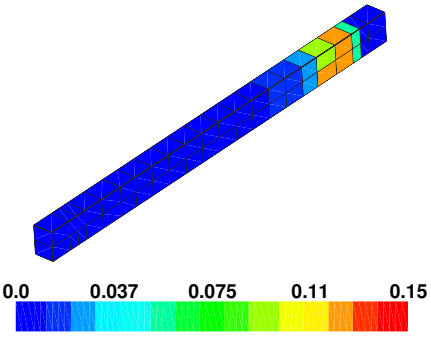

(c) Distribution of Ind_{K_E} at 240.5Hz

Figure 7.12: *ECR analysis for the reinforced concrete beam FE model with boundary impedances. Distribution of $IndK$ estimators over the structure at relevant peak error frequencies.*

7.2.1 A new approach to identify boundary conditions based in ECR functionals

To introduce the new approach used to identify unknown boundary impedances, equations (4.10) to (4.14) have been reviewed in a ECR framework. The key idea consists of finding boundary displacements and efforts that minimize the ECR cost function rather than the least square error between model response and measurements.

To do so, the procedure of condensation and inversion is now built upon the linear equations used to obtain the triple of admissible fields $\mathcal{T}_\omega = (\hat{u}, \hat{v}, \hat{w})$. Recall that to obtain $\mathcal{T}_\omega$ the system (B.11) of linear equations of the form $Ax = b$ needs to be solved where $x = \{(\hat{u} - \hat{v}) \quad (\hat{u} - \hat{w}) \quad \hat{u}\}^T$ is the sought vector of admissible fields (the reader may refer to Appendix B for further details). Here, system (B.11) is used instead of the equilibrium equation (4.9) to perform the condensation and inversion approach.

For this, a partition of the vector x of unknown DOFs into internal DOFs $x_i \in \mathbb{C}^{3\times n_i}$ and boundary DOFs $x_b \in \mathbb{C}^{3\times n_b}$ leads to:

$$\begin{bmatrix} A_{ii} & A_{ib} \\ A_{bi} & A_{bb} \end{bmatrix} \begin{Bmatrix} x_i \\ x_b \end{Bmatrix} = \begin{Bmatrix} b_i \\ b_b \end{Bmatrix} \tag{7.3}$$

Notice that in this transformation the boundary vectors x_b and b_b become:

$$\begin{aligned} x_b =& \{(\hat{u} - \hat{v})_b^T \quad (\hat{u} - \hat{w})_b^T \quad \hat{u}_b^T\}^T \quad ; \\ b_b =& \{\mathbf{0}_{n_b}^T \quad \mathbf{0}_{n_b}^T \quad -F_b^T\}^T \end{aligned} \tag{7.4}$$

where $\mathbf{0}_{n_b}$ represents a vector of zeros of length n_b. Hence, from the first row of equations in (7.3) one can write:

$$x_i = A_{ii}^{-1}(b_i - A_{ib}x_b) \tag{7.5}$$

and similarly to equation (4.12) the sought vector of boundary admissible fields solves the minimization problem:

$$\hat{x}_b = \underset{x_b}{\text{Argmin}} \quad \|\tilde{z} - \Upsilon x_i\|_W^2 = \|\tilde{z} - \Upsilon A_{ii}^{-1}(b_i - A_{ib}x_b)\|_W^2 \tag{7.6}$$

where $\tilde{z}$ and Υ and W represent a new vector of measurements and, respectively, the subsequent projection operator and space norm. Those quantities are specifically defined in order to minimize the ECR cost function (1.26). For this, we define:

$$\tilde{z} = \{\mathbf{0}_{n_i}^T \quad \mathbf{0}_{n_i}^T \quad \tilde{u}^T\}^T \tag{7.7}$$

as a new target vector that represents the fact that we aim to approach physical measurements $\tilde{u}$ for the kinematically admissible field $\tilde{u}_i$ and a discrepancy of dynamically admissible fields ($(\hat{u} - \hat{v})_i$ and $(\hat{u} - \hat{w})_i$) as close to zero as possible. The associated projection operator becomes:

$$\Upsilon = \begin{bmatrix} \mathbf{I}_{2\times n_i} & \mathbf{0} \\ \mathbf{0} & \Pi \end{bmatrix} \tag{7.8}$$

where Π is the initial observation operator. Finally, the new metric corresponding to the ECR functional is given by:

$$W = \begin{bmatrix} \frac{\gamma}{2}[K + T\omega^2 C] & \mathbf{0} & \mathbf{0} \\ \mathbf{0} & \frac{1-\gamma}{2}\omega^2[M] & \mathbf{0} \\ \mathbf{0} & \mathbf{0} & \frac{r}{1-r}[G_R] \end{bmatrix} \tag{7.9}$$

The sought boundary admissible fields $\hat{x}_b$ are obtained using a pseudo-inverse approach similarly to equation (4.13) by applying:

$$\begin{aligned} \hat{x}_b &= A^+(\Upsilon A_{ii}^{-1} b_i - \tilde{z}) \\ A^+ &= ([\Upsilon A_{ii}^{-1} A_{ib}]^T W [\Upsilon A_{ii}^{-1} A_{ib}])^{-1} [\Upsilon A_{ii}^{-1} A_{ib}]^T W \end{aligned} \tag{7.10}$$

and finally the unknown term b_b is obtained by:

$$b_b = A_{bi}[A_{ii}^{-1}(A_i - A_{ib}\hat{x}_b)] + A_{bb}\hat{x}_b \tag{7.11}$$

The impedance identification is therefore obtained from the last n_b rows of $\hat{x}_b$ and b_b corresponding to the kinematically admissible nodal displacements and the corresponding generalized nodal forces at boundary DOFs respectively.

This approach has been applied to the problem of boundary impedance identification of the reinforced concrete beam. The identified impedances are very close to the ones presented in Figure 7.9, although not identical. The introduction of such impedances slightly modifies the global error spectrum presented in Figure 7.13. The new $\xi^2_{r\omega}$ error spectrum presents, as expected, lower values than the ones obtained with the least squares based boundary impedances. However, in this study, differences are slight, indicating only marginal improvement of the model quality, in particular for lower frequencies, which was the first aim of this investigation.

Model parameter identification

In an effort to improve this results, updating the global structural model parameters using the ECR-UKF approach is now attempted. Let θ denote the vector of unknown parameters (Poisson's ratio, Young's modulus and mass density):

$$\theta = \{\nu \quad \mathrm{E} \quad \rho\}^T \tag{7.12}$$

Its introduction into a state-space formulation of the form (3.13) with an ECR cost function defined in the whole frequency range ($[5 - 350]$Hz) is used to perform the the parameter identification process with the ECR-UKF approach. Notice that, although not directly introduced in the parameter vector θ, the boundary unknowns $\hat{x}_b$ and b_b are also updated at each iteration step as the identification goes on. The results of the identification process are presented in Figure 7.14.

After the identification process, the following new model parameters are considered:

$$\hat{\nu} = 0.99\nu \quad ; \quad \hat{\mathrm{E}} = 0.81\mathrm{E} \quad ; \quad \hat{\rho} = 1.201\rho \tag{7.13}$$

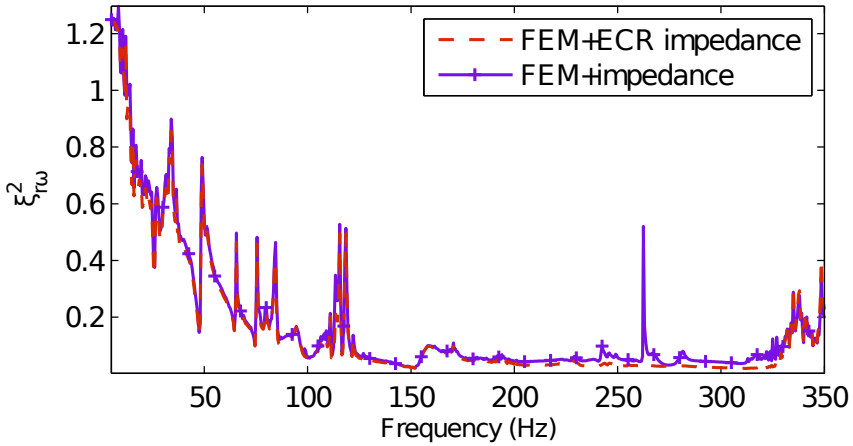

Figure 7.13: *Comparison of ECR spectrum between FEMs with Least Square based and ECR-based boundary impedances.*

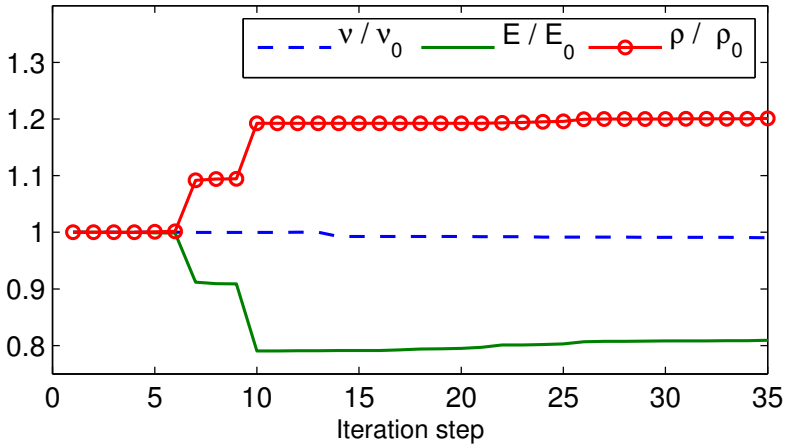

Figure 7.14: *Material parameter updating with the ECR-UKF approach.*

Introducing these new material parameters and identifying new ECR-based impedances leads to the error spectrum presented in Figure 7.15. As observed, results are improved since the relative errors are even lower but, once again, not enough to substantially decrease errors at low frequencies.

It is interesting to observe, however, how the ECR based boundary impedance identification differs from the initial least-squares approach: the obtained response, although giving better results in terms $\xi^2_{r\omega}$, does not necessarily fit the measured data better, in particular with respect to the model eigenfrequencies. Nevertheless, updating model parameters with the ECR-UKF approach introduces further improvement from the point of view of both amplitudes and eigenfrequencies (cf. Figure 7.16).

Analyzing again the ECR distribution of model errors, it has been found that errors are still concen-

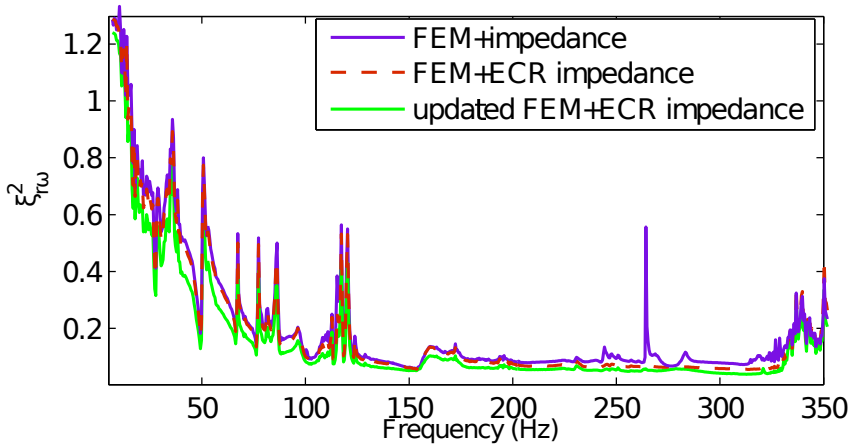

Figure 7.15: *Comparison of ECR spectrum between FEMs with L2-based and ECR-based boundary impedances.*

trated in the boundaries in the same fashion as obtained in Figure 7.12 (which are not explicitly shown since they are totally comparable to those of Figure 7.12).

This suggests the existence of remaining boundary errors in the modeling. Hence, in an effort to reduce them, the full DOFs associated to the boundary nodes are released and treated as independent (instead of being condensated into 4 DOF as defined in Figure 7.8), leading to a 16 new impedances to be identified.

Performing the ECR-based boundary impedance identification and ECR-UKF-based model parameter updating on this enriched model leads to the result shown in Figure 7.17. As observed, model errors are drastically reduced leading to an excellent model quality since relative error drops beneath 10^{-6}.

A possible explanation for this error reduction lies in the fact that the beam presents significant boundary displacements in y direction, which were omitted in the initial 4-DOF assumption illustrated in Figure 7.8. This horizontal motion certainly results from the fact that, under experimental conditions, the external load was not perfectly vertical.

This new model is considered as a reference with the new boundary impedances assumed to fully represent the structure's environment.

7.3 Study of the evolving structural damage

As already said, the reference beam was subjected to increasing levels of quasi-static loads ($F_{\text{stat}} = [10, 20, 30]$kN) producing controlled structural damage at its mid-span as illustrated in Figure 7.18.

The goal here was to investigate the ability of the ECR-UKF approach to first localize structural damage and identify its magnitude. Unfortunately, the studies carried out for this purpose do not allow one to capture these model changes as initially desired. As a matter of fact, either because the FE model is

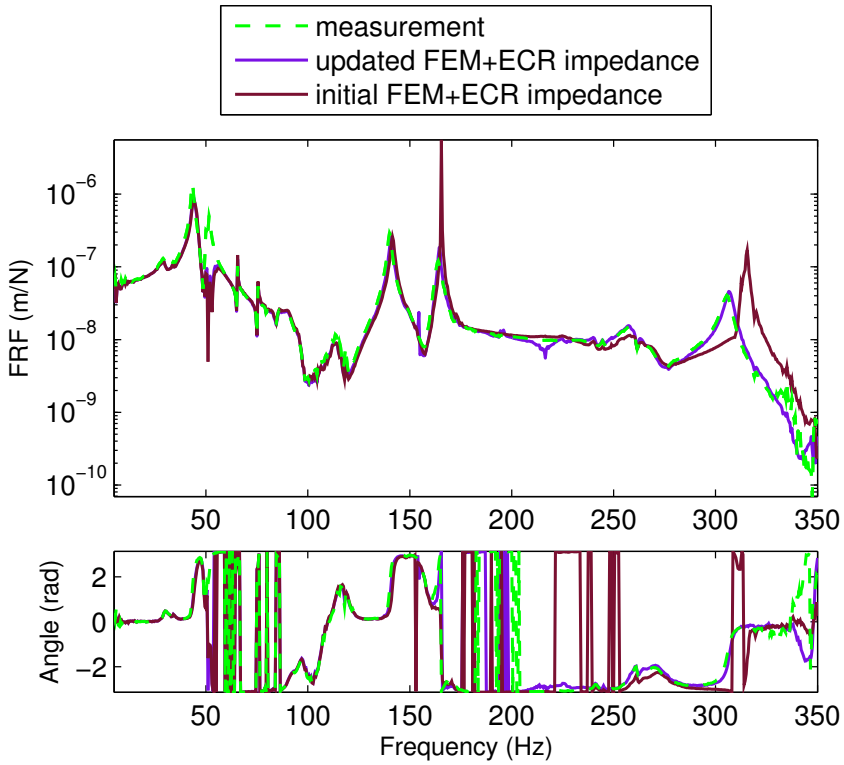

Figure 7.16: *FRF's comparison between measured and FE models (initial and updated) with ECR based boundary impedances at sensor S8 location (unobserved).*

not adapted to the intensity of the damage or because the coupling with boundaries introduces nonlinear effects that mask the damage effect, it has not been possible to spatially detect the presence of damage in the beam's mid-span through $\xi^2_{E\omega}$. However, the global ECR indicator $\xi^2_{r\omega}$ reveals an impoverishment of the model quality as damage increases. In Figure 7.19 the ECR spectrum of the undamaged structure and the most damaged stage ($F_{stat} = 30$kN) are compared.

One can observe a general offset of the relative ECR indicator suggesting a global model's quality deterioration. In addition, peak error frequencies ($[92Hz, 156Hz, 292Hz]$) seem to correspond to those where the beam's mid-span stiffness is most excited (beam flexion modes). In Figure 7.20 we compare the increment of ECR spectrum (denoted as $\Delta\xi^2_{r\omega} = (\xi^2_{r\omega}|_{\text{damaged}} - \xi^2_{r\omega}|_{\text{ref}})$) with respect to the undamaged reference one. One can see how the increment is always positive (indicating a model's degradation) and generally higher as damage increases.

Hence, the global ECR indicator $\xi^2_{r\omega}$ seems to capture the presence of structural damage. However, the passage from a global information ($\xi^2_{r\omega}$) to the local analysis of the error ($\xi^2_{Er\omega}$) when analyzing the

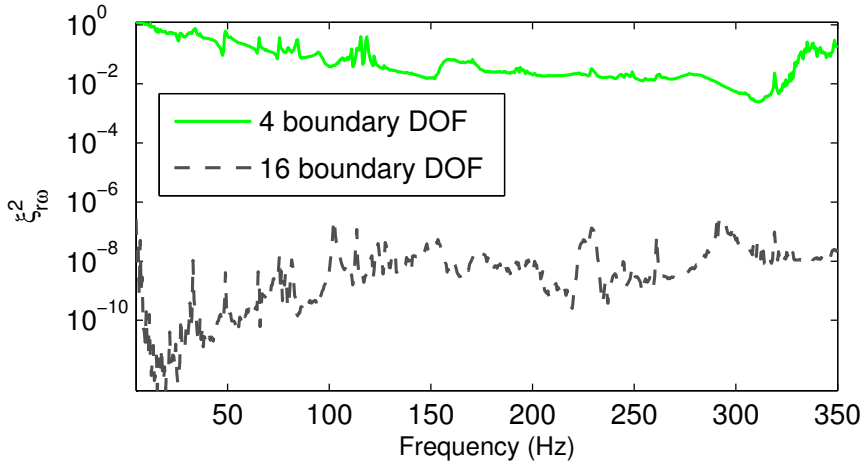

Figure 7.17: *Comparison of ECR spectrum for a model with 4 boundary DOFs and the new 16 DOFs boundary model.*

Figure 7.18: *Introduction of a quasi-static load producing structural damage (cracks) at the beam's mid-span.*

error spatial distribution is not able to reveal any structural change in the beam's mid-span. Again, errors seem to be concentrated in the boundaries probably masking the sought damage.

7.4 Conclusions

In this application example the ECR-UKF approach has been tested with real measurements obtained from an experimental campaign. A first study consisting of identifying strong boundary coupling with the surrounding test bench has been satisfactorily carried out. As a matter of fact, a preliminary ECR

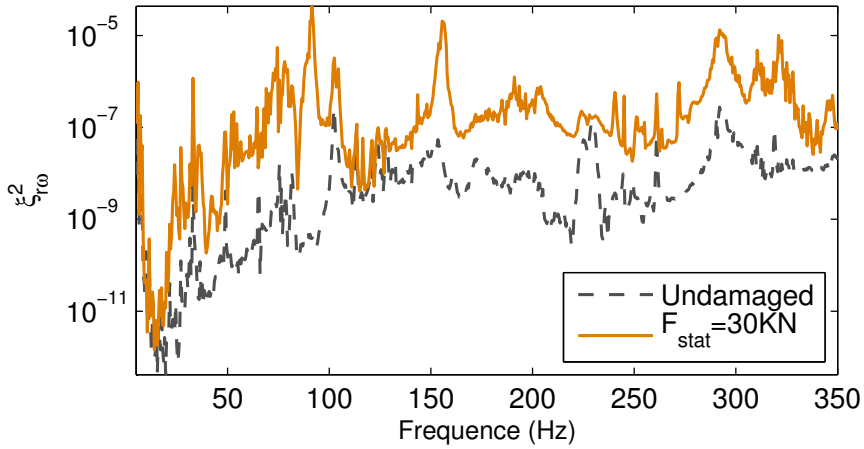

Figure 7.19: *Comparison of the ECR spectrum for the reference and the most damaged speciment using identical boundary impedance functions.*

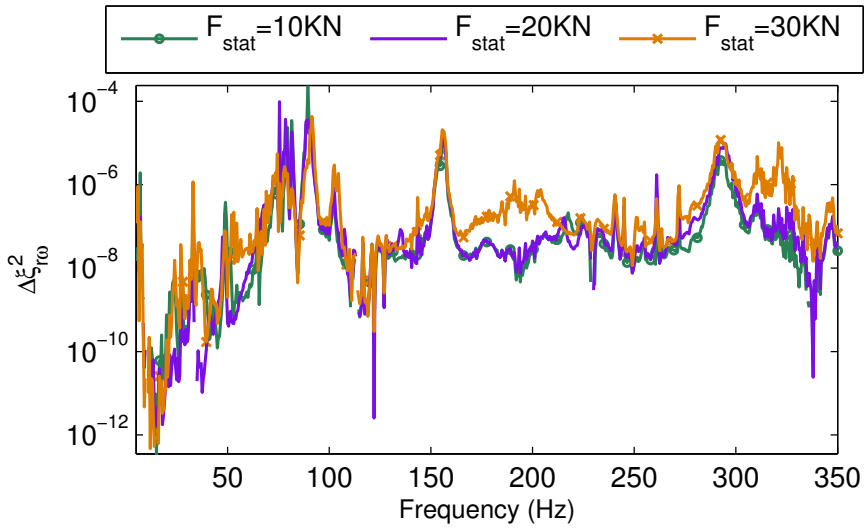

Figure 7.20: *Comparison of increment of ECR spectrum $\Delta\xi^2_{r\omega}$ for different levels of structural damage.*

analysis has shown its robustness to localize the presence of model errors in the boundary definition. A classical approach to identify boundary impedances clearly improved the model quality although results still needed an improvement at low frequencies. In this context, two different techniques have been applied to improve the results:

1. A new approach to identify boundary impedances based in the ECR equations improving the model quality compared to the classical least squares approach.

2. A model parameter identification based on the ECR-UKF approach to obtain the a best set of Poisson's ration, Young's modulus and mass density.

Both techniques have effectively shown an enhancement of the model quality with regard to the ECR criterion although, once again, not significant in the low frequency range. At the end, it has been crucial to reconsider the boundary motion assumptions to definitely obtain an acceptable result. Hence, the adequacy of the proposed techniques to tackle the widely known problem of boundary misspecification has been fulfilled.

As an example of structural modification identification, a further study to apprehend the ability of the ECR-UKF to localize and identify the presence of structural damage has been carried out. Unluckily, and despite the efforts, the investigations do not allow the ECR to spatially detect model changes as initially wished. Nevertheless, the global ECR analysis correctly indicates an impoverishment of the model quality apparently related to the presence of structural damage. However, the passage from the global analysis to the local search of model bias is not able to reveal the information sought. This might probably be explained either by the fact that the sensitivity of the FE model with respect to the damage intensity is too small or either because of the presence of nonlinear effects in boundaries that mask the damage effect impede in clearly localizing them in space. Unfortunately, this unforeseen difficulty does not allow one to go further in the application of the ECR-UKF technique in this case, and particularly the use of the UKF to track the presence and evolution of structural flaws.

Conclusion

Conclusions and future research

This work aimed at improving the solution of identification problems in structural dynamics within the industrial context of EDF's Research & Development (R&D) needs. In particular, three main objectives were pursued: identify FE model inaccuracies, take into account the case of evolutionary mechanical properties and guarantee the applicability of the proposed methods for industrial purposes.

To do so, a general strategy combining the Error in Constitutive Relation (ECR) and the Unscented Kalman filter (UKF) has been developed. This ECR-UKF approach allows to take advantage of the individual interesting features of each technique. While the ECR's ability to spatially localize erroneously modeled regions was used to improve the *a priori* knowledge of model errors, the UKF solved an ECR-based parameter identification problem for evolving parameters. Moreover, the choice of both the ECR and the UKF approaches was motivated for their compatibility within the numerical environment of the public FE software *Code_Aster* developed at EDF R&D.

The central part of this work subsequently studied the adequacy of the ECR-UKF approach to address problems of industrial relevance, with particular focus on structural damage assessment and mis-modeled boundary conditions identification.

The former has been investigated through several configurations such as a high-DOF cooling tower model subjected to wind excitation, a power plant auxiliaries building excited by seismic loadings or a beam-shaped structure embedding boundary condition mis-modeling. In all the examples, the use of the ECR information, from the global point of view to the local element-wise information, has been comprehensively studied. In particular, the case of the SMART benchmark has been used to evaluate its sensitivity with respect to the sensor distribution and the flaw location, size and intensity. Broadly speaking, ECR-based indicators showed a good ability to locate structural flaws and represent a reliable tool to study model errors. In particular cases, though, some difficulties appeared. Indeed, when studying complex structures, loadings may not conveniently excite structural defects and incomplete localization of model errors might be expected. Working with a larger frequency range, however, generally improved the quality of the results. In other cases, as reported in chapter 7, the global ECR indicator showed an increasing model error consistent with the damage progression, but the spatial localization of cracks remained unfeasible, probably because cracks were a local phenomena compared to the spatial distribution of experimental sensors and the chosen FE discretization.

Notwithstanding, the use of the ECR conveniently facilitated the construction of reduced-size parameter vectors for model-updating purposes, reducing the computational cost of the UKF.

In this work, the UKF presented the advantage of its ease of implementation and proved an excellent ability to track model changes. Importantly, in the current proposed ECR-UKF approach, the ECR functionals introduced as observation functions are formulated in the frequency-domain, requiring time-frequency equivalences. This represents a limitation of this approach since only sufficiently slow changes can be captured whereas a time-domain formulation of the ECR would have been a more natural formulation of the ECR-UKF approach. However, solving the ECR equations in the time-domain is still a computationally challenging task, the existing methods being inappropriate for industrial purposes. As

a future work, a coupled use of ECR and UKF in a time-domain formulation will be an interesting area of research when seeking a joint state and parameter estimation for systems with fast structural changes or when using nonlinear FE models.

Although the ECR-UKF in the frequency-domain addressed the problem of parameter identification only, a study of field reconstruction was also conducted in an effort to propose a system state estimation within the framework of this approach. The kinematically admissible field obtained from the ECR minimization problem was found to provide an appropriate solution to this problem. In a future work, this technique can be used in the construction of dynamical models in a mixed formulation, i.e. where the experimental data is completed with a projection basis built from an ECR field reconstruction approach.

On the other hand, the problem of boundary mis-modeling was investigated using not only purely numerical examples based on synthetic data, but also with one application to an experimental campaign. This kind of modeling error was generally correctly detected by the ECR but the question of how to model boundary impedances stand. An existing condensation technique was used to obtain preliminary impedance functions whose parameters can be obtained by means of the UKF. However, in the case of complex impedance functions, a subspace parametrization technique may lead to identify a large number of coefficients, and the use of non-parametric functions is recommended. Thus, the identification of preliminary impedances has been improved with a modified formulation of the condensation technique based on ECR functionals. In the application of a concrete beam with strong boundary interaction, the initial FE model enriched with the identified impedances gave particularly accurate prediction of the global dynamic behavior with respect to measurements, which encourages to use this approach in future work, for example, when applying a sub-structure formulation in a system where one or more of its sub-structures are poorly known.

Additionally, a specific time-domain approach based on a dual KF-UKF completed the work of boundary mis-modeling. Although it did not directly combine the use of ECR, this approach is of particular interest when dealing with the presence of nonlinear boundary behavior. In a future work, it will be interesting to apply this approach for large-DOF complex structures to (for example) problems of soil-structure interaction.

Aside from the study of the above-mentioned phenomena, the ECR-UKF algorithm has been enriched with additional features, so as to widen its applicability to other problems. For instance, the introduction of algebraic constraints in the identified parameter vector and the design of covariance matrices was considered. Indeed, when using Kalman filtering and in particular the UKF, both issues may strongly influence the stability and the quality of the solutions. In that sense, the study of these additional features is considered as a relevant information for a future use of the proposed ECR-UKF method.

To conclude, the ECR-UKF algorithm has been implemented within the environment of the FE software *Code_Aster* aiming an integration into a future distribution of this open-source computational platform. Routines were developed in Python language. In a future work, the implementation of ECR and UKF in a lower-level language of *Code_Aster* (Fortran) will increase their numerical performances.

Appendices

Appendix A

Stochastic interpolation: the BLUE formalism

The main purpose of data assimilation techniques is to obtain an enriched system state estimation $X^a \in \mathbb{C}^n$ by means of an *a priori* background knowledge $X^b \in \mathbb{C}^n$ combined with a set of observations $y \in \mathbb{C}^m$. In most of the cases, while the *a priori* X^b information is provided by a mathematical model, observations are the result of a measurement campaign. Both quantities are thus related to the true state $X^t \in \mathbb{C}^n$ by the following representation:

$$\left\{ \begin{array}{l} X^t = X^b + \mathbf{e}^b \\ y = H(X^t) + \mathbf{e}^o \end{array} \right. \tag{A.1}$$

where $H(\cdot)$ is the so-called observation operator embedding functions such as transformation, projection and/or interpolation needed to express relationships between state and observation spaces. In addition, $\mathbf{e}^b$ and $\mathbf{e}^o$ represent the *a priori* state error and the observation error, respectively. These stochastic quantities are assumed to verify the following properties:

$$\left\{ \begin{array}{l} \mathbb{E}[\mathbf{e}^b] = 0 \\ \mathbb{E}[\mathbf{e}^b(\mathbf{e}^b)^T] = P^b \end{array} \right. ; \qquad \left\{ \begin{array}{l} \mathbb{E}[\mathbf{e}^o] = 0 \\ \mathbb{E}[\mathbf{e}^o(\mathbf{e}^o)^T] = R \end{array} \right. \tag{A.2}$$

where P^b and R are the so-called background and observation error covariance matrices, and $\mathbb{E}$ denotes the expectation operator.

Within the framework of a linear observation model H, the solution for optimal stochastic interpolation is given by the BLUE (Best Linear Unbiased Estimator) formalism, whereby is sought as a linear combination of both the background knowledge X^b and the measurements y:

$$X^a = LX^b + Ky \tag{A.3}$$

where the matrices $L \in \mathrm{M}(\mathbb{C})_{n,n}$ and $K \in \mathrm{M}(\mathbb{C})_{n,m}$ are to be defined. To do so, the moments of the estimation error $\mathbf{e}^a := X^a - X^t$ will be studied.

Moreover, when considering a stochastic model, it seems natural to seek an unbiased state estimation, which can be expressed by:

$$\mathbb{E}[\mathbf{e}^a] = 0 \tag{A.4}$$

Besides, one can write:

$$\begin{aligned} \mathbf{e}^a &= X^a - X^t \\ &= L(X^b - X^t + X^t) + K(HX^t + \mathbf{e}^o) - X^t \\ &= L\mathbf{e}^b + K\mathbf{e}^o + (L + KH - I)X^t \end{aligned} \tag{A.5}$$

Taking expectations from this expression and imposing condition (A.4) leads to:

$$\mathbb{E}[\mathbf{e}^a] = (L + KH - I)\mathbb{E}[X^t] = 0 \quad \Rightarrow \quad L = I - KH \tag{A.6}$$

Finally, one can obtain the sought state X^a by:

$$X^a = X^b + K(y - HX^b) \tag{A.7}$$

Equation (A.7) is the most used form of the BLUE, where K is generally referred to as the gain matrix and $(y - HX^b)$ is called the innovation vector. On the other hand, when using (A.7) to perform linear stochastic interpolation, the covariance of the estimation error takes the form:

$$\begin{aligned} P^a &:= \mathbb{E}[\mathbf{e}^a \mathbf{e}^{aT}] \\ &= LP^bL^T + KRK^T \\ &= (I - KH)P^b(I - KH)^T + KRK^T \end{aligned} \tag{A.8}$$

In order to obtain an optimal state estimation, the gain matrix K is defined so as to minimize the estimation error, more specifically the value of Trace(P^a).

A straightforward variation derivation yields the optimal gain matrix, given by:

$$K = P^bH^T(R + HP^bH^T)^{-1} \tag{A.9}$$

and the optimal covariance matrix for the estimation error, given by:

$$P^a = (I - KH)P^b \tag{A.10}$$

The BLUE technique has been widely used in the domain of geosciences as a satisfactory data assimilation method for spatial interpolation. Moreover, the BLUE is actually the theoretical background of the variational formalisms 3D-Var and 4D-Var [11] used e.g. in weather forecasting. One can consider the BLUE as a particular case of kriging [78, 5] in a linear framework. Moreover, the BLUE is also related to the Kalman filter algorithm since a BLUE estimation is performed at each data assimilation step.

Appendix B

Minimization of the ECR functional and first order derivatives in a FE framework.

The FE formulation of the frequency-domain equation of motion given by (1.16) leads to the classical matrix equation:

$$[-\omega^2[M] + j\omega[C] + [K]]\{q\} = \{F\} \tag{B.1}$$

where $\{q\}$ is the vector of nodal displacement, $\{F\}$ the vector of nodal loadings and $[M], [C]$ and $[K]$ are the so-called mass, damping and stiffness matrices respectively and $\omega = 2\pi f$ (with f the prescribed frequency). Recall from chapter 1 that in the adopted ECR formulation, the following assumptions are made:

- $\partial_0\Omega = \emptyset$
- Prescribed loading $\bar{f}$ over $\partial_f\Omega$ is considered as a reliable information and directly embedded in $\{F\}$.
- A set of unreliable displacement data $\tilde{u}$ is available over $\partial_{fu}\Omega$.
- Displacement data $\bar{u}$ are restricted to the boundary $\partial_{u\backslash f}\Omega = \partial_u\Omega - \partial_{fu}\Omega$ and considered as a reliable information. This reliable kinematic information is generally enforced in the construction of model matrices by either introducing Lagrange multipliers or by considering matrices with active DOFs only, which is the solution adopted in this work. Thus, DOF corresponding to $\partial_{u\backslash f}\Omega$ are eliminated from all FE matrices. Therefore, the action of non-zero prescribed displacements is embedded in $\{F\}$.

In this framework, the Error in Constitutive Relation problem seeks at obtaining a triple of admissible fields $u \in \mathcal{U}(\Pi, \bar{u})$ and $(v, w) \in \mathcal{D}(\{F\}, \bar{u})$, defined in (1.26), that minimize the functional:

$$\begin{aligned} e^2(\{u\},\{v\},\{w\}) =& \frac{\gamma}{2}\{u-v\}^*[K + T\omega^2 C]\{u-v\} + \frac{1-\gamma}{2}\{u-w\}^*\omega^2[M]\{u-w\} \\ &+ \frac{r}{1-r}\{\Pi u - \tilde{u}\}^*[G_R]\{\Pi u - \tilde{u}\} \end{aligned} \tag{B.2}$$

where Π is the projection operator onto the measured DOFs, $[G_R]$ a positive-definite weighting matrix, γ and r are positive scalar weights and $\tilde{u}$ a set of unreliable measurements.

To fulfill the dynamic admissibility condition defined by $\mathcal{D}(\{F\}, \bar{u})$ the following constraint has to be taken into account:

$$[K + i\omega C]\{v\} - \omega^2[M]\{w\} = \{F\} \tag{B.3}$$

In order to solve this constrained optimization problem, a Lagrangian functional is introduced:

$$E(\{u\}, \{v\}, \{w\}, \{\lambda\}) = e^2(\{u\}, \{v\}, \{w\}) + \{\lambda\}^T([K + i\omega C]\{v\} - \omega^2[M]\{w\} - \{F\}) \tag{B.4}$$

where $\{\lambda\}$ is a vector of Lagrange multipliers.

The optimal value of $\{u, v, w, \lambda\}$ satisfies the stationarity condition:

$$\delta E = 0 \quad \forall \{\delta u, \delta v, \delta w, \delta\lambda\} \in \mathcal{U} \times \mathcal{D} \times \mathbb{U} \tag{B.5}$$

which expressed in explicit form and using the symmetry property of $[M]$, $[C]$ and $[K]$, leads to the following system of equations:

$$\begin{cases} \dfrac{\partial E}{\partial u} = \frac{\gamma}{2}[K + T\omega^2 C]\{u - v\} + \dfrac{1-\gamma}{2}\omega^2[M]\{u - w\} + \frac{r}{1-r}\Pi^T[G_r]\{\Pi u - \tilde{u}\} = 0 \\ \dfrac{\partial E}{\partial v} = \frac{-\gamma}{2}[K + T\omega^2 C]\{u - v\} + \{\lambda\}^T[K + i\omega C] = 0 \\ \dfrac{\partial E}{\partial w} = -\dfrac{1-\gamma}{2}\omega^2[M]\{u - w\} - \{\lambda\}^T\omega^2[M] = 0 \\ \dfrac{\partial E}{\partial \lambda^T} = [K + i\omega C]\{v\} - \omega^2[M]\{w\} - \{F\} = 0 \end{cases} \tag{B.6}$$

The third equation of (B.6) allows us to write:

$$\{\lambda\} = -\frac{1-\gamma}{2}\{u - w\} \tag{B.7}$$

consequently transforming the second equation in (B.6):

$$\frac{\gamma}{2}[K + T\omega^2 C]\{u - v\} + \frac{1-\gamma}{2}[K + i\omega C]\{u - w\} = 0 \tag{B.8}$$

Finally, the last equation can be rewritten depending on $\{u - v\}$, $\{u - w\}$ and $\{u\}$ as:

$$[K + i\omega C]\{u - v\} - \omega^2[M]\{u - w\} + [-[K] - i\omega[C] + \omega^2[M]]\{u\} = -\{F\} \tag{B.9}$$

Hence, the error fields $\{u - v\}$, $\{u - w\}$ et $\{u\}$ that verify (B.5) can be obtained by solving the system of linear equations:

$$\begin{bmatrix} \frac{\gamma}{2}[K+T\omega^2 C] & \frac{1-\gamma}{2}\omega^2[M] & \frac{r}{1-r}\Pi^T[G_r]\Pi \\ \frac{\gamma}{2}[K+T\omega^2 C] & \frac{1-\gamma}{2}[K+i\omega C] & 0 \\ (K+i\omega C) & -\omega^2[M] & [-[K]-i\omega[C]+\omega^2[M]] \end{bmatrix} \begin{Bmatrix} \{u-v\} \\ \{u-w\} \\ \{u\} \end{Bmatrix} = \begin{Bmatrix} \frac{r}{1-r}\Pi^T[G_r]\tilde{u} \\ 0 \\ -\{F\} \end{Bmatrix} \tag{B.10}$$

which, for the sake of clarity, will be expressed in the reduced form:

$$[\mathbf{A}]\{x\} = \{b\} \tag{B.11}$$

First order derivatives of the ECR functional

In this work, model matrices $[M(\theta)], [C(\theta)], [K(\theta)]$ are parametrized with set of model parameters θ. An optimal set of parameters $\hat{\theta}$ is sought from multi-frequency experimental data by minimizing the following functional:

$$\xi^2_{Tr}(\{\hat{u}\},\{\hat{v}\},\{\hat{w}\},\theta) = \int_{\omega_{min}}^{\omega_{max}} \eta(\omega) \left(\sum_{E\in\Omega} \frac{e^2_{E\omega}(\{\hat{u}\},\{\hat{v}\},\{\hat{w}\},\theta)}{D^2_\omega(\{\hat{u}\},\theta)} \right) \mathrm{d}\omega \tag{B.12}$$

where $D^2_\omega(\{\hat{u}\},\theta)$ represents the reference structural energy which in our case is obtained by:

$$D^2_\omega(\{\hat{u}\},\theta) = \frac{\gamma}{2}\{\hat{u}\}^*[K(\theta)+T\omega^2 C(\theta)]\{\hat{u}\} + \frac{1-\gamma}{2}\{\hat{u}\}^*\omega^2[M(\theta)]\{\hat{u}\} \tag{B.13}$$

In most cases studied in this work the Unscented Kalman filter (UKF) is used to solve the minimization problem. The UKF does not require the evaluation of the Jacobian of ξ^2_{Tr}. In contrast, the Extended Kalman filter (EKF), which was also needed for some of the examples, requires Jacobian evaluation. Thus, the following first order derivatives have to be evaluated for the EKF-based minimization of (B.12):

$$\frac{\partial}{\partial\theta_i}\left(\frac{e^2_\omega(\{\hat{u}\},\{\hat{v}\},\{\hat{w}\},\theta)}{D^2_\omega(\{\hat{u}\},\theta)} \right) = \frac{\frac{\partial e^2_\omega}{\partial\theta_i}\cdot D^2_\omega - e^2_\omega \cdot \frac{\partial D^2_\omega}{\partial\theta_i}}{(D^2_\omega)^2} \tag{B.14}$$

While the quantities e^2_ω and D^2_ω are directly available after solving equation (B.11), the parameter sensitivities $\frac{\partial e^2_\omega}{\partial\theta_i}$ and $\frac{\partial D^2_\omega}{\partial\theta_i}$ require additional derivation, resulting in expressions:

$$\begin{aligned} \frac{\partial e^2_\omega(\{u\},\{v\},\{w\},\theta)}{\partial\theta_i} =& \gamma\{u-v\}^T[K+T\omega^2 C]\frac{\partial\{u-v\}}{\partial\theta_i} \\ &+ \frac{\gamma}{2}\{u-v\}^T\frac{\partial[K+T\omega^2 C]}{\partial\theta_i}\{u-v\} \\ &+ (1-\gamma)\{u-w\}^T\omega^2[M]\frac{\partial\{u-w\}}{\partial\theta_i} \\ &+ \frac{1-\gamma}{2}\{u-w\}^T\omega^2\frac{\partial[M]}{\partial\theta_i}\{u-w\} \\ &+ \frac{2r}{1-r}\{\Pi u-\tilde{u}\}^T[G_R]\Pi\frac{\partial\{u\}}{\partial\theta_i} \end{aligned} \tag{B.15}$$

and:

$$\begin{aligned}\frac{\partial D^2_\omega(\{\hat{u}\},\theta)}{\partial\theta_i} =& \{u\}^T[\gamma(K+T\omega^2C)+(1-\gamma)\omega^2M]\frac{\partial\{u\}}{\partial\theta_i} \\ &+ \{u\}^T\frac{\partial[\frac{\gamma}{2}(K+T\omega^2C)+\frac{1-\gamma}{2}\omega^2M]}{\partial\theta_i}\{u\}\end{aligned} \tag{B.16}$$

In the above equations, the terms $\frac{\partial[K+T\omega^2C]}{\partial\theta_i}$ and $\frac{\partial\omega^2[M]}{\partial\theta_i}$ are the well known sensitivity terms of model matrices, generally provided by built-in operators in FE software. However, the partial derivatives terms $\frac{\partial\{u-v\}}{\partial\theta_i}$, $\frac{\partial\{u-w\}}{\partial\theta_i}$ and $\frac{\partial\{u\}}{\partial\theta_i}$ are computed by solving for these quantities the first-order sensitivity equations obtained by differentiating equations (B.11) with respect to θ_i.

Appendix C

The Unscented Kalman filter

To overcome the underlying assumptions and flaws inherent to the Extended Kalman filter (EKF), an alternative algorithm, referred to as the Unscented Kalman filter (UKF), was first proposed by Julier et al. [50, 51]. The basic difference between the EKF and the UKF lies in the manner in which Gaussian random variables are represented for the purpose of propagating them through nonlinear system equations. In the EKF, state distribution is approximated by a Gaussian random variable which is then propagated analytically through the first-order linearization of the nonlinear system equations. The UKF addresses this problem by using a deterministic sampling approach based on the mathematical Unscented transformation. The state distribution is then, as with the EKF, approximated by a Gaussian random variable, but is now sampled at a minimal set of carefully chosen sample points. These sample points completely capture the true mean and covariance of the Gaussian random variable, and when propagated though the nonlinear functions, yield exact evaluations of the posterior mean and covariance (while the EKF achieves first-order accuracy only). The reader may refer to [50, 52] for more information on UKF performance in predicting mean and covariance of a random variable that undergoes a nonlinear transformation. An illustration of the Unscented transformation is shown in Figure C.1.

To introduce the UKF, we begin by explaining the Unscented transformation. Consider propagating a random variable $\mathbf{x} \in \mathbb{R}^n$ with mean $\bar{\mathbf{x}}$ and covariance $\mathbf{P}_{\mathbf{x}}$. The minimal sampling points set used by the UKF, known as sigma points, is defined by:

$$\begin{aligned} \mathcal{X}_0 &= \bar{\mathbf{x}} \\ \mathcal{X}_i &= \bar{\mathbf{x}} + (\sqrt{(n+\lambda)\mathbf{P}_{\mathbf{x}}})_i \quad i = 1, \cdots, n, \\ \mathcal{X}_i &= \bar{\mathbf{x}} - (\sqrt{(n+\lambda)\mathbf{P}_{\mathbf{x}}})_i \quad i = n+1, \cdots, 2n \end{aligned} \tag{C.1}$$

where $(\sqrt{A})_i$ denotes the *i*th column of the matrix square root of A (e.g. lower-triangular Cholesky factor). The dispersion of the sigma points is controlled by the scalar λ defined by:

$$\lambda = \alpha^2(n + \kappa) - n \tag{C.2}$$

where n is the dimension of the state variable and α and κ are scaling factors. Parameter α is generally used to control the dispersion of sigma points around $\bar{\mathbf{x}}$ and is usually set to a small positive value

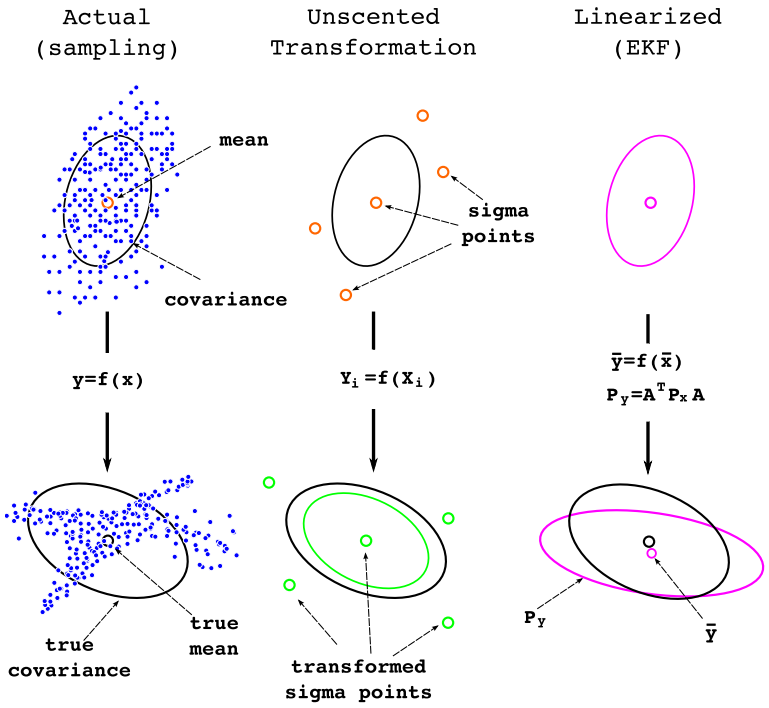

Figure C.1: *Illustrative comparison between the Unscented and linearization methods for nonlinear stochastic transformations.*

$1 \leq \alpha \leq 10^{-4}$. On the other hand, the scalar κ is a secondary scaling factor which is generally set to $3 - n$. The reader may refer to [49, 52] for further details on the choices of α and κ.

The Unscented transformation approaches the posterior statistics of a random variable $\mathbf{y}$ undergoing a nonlinear transformation $\mathbf{y} = f(\mathbf{x})$ in the following fashion:

$$\begin{aligned} \bar{\mathbf{y}} &\approx \sum_{i=0}^{2n} W_i^m \mathcal{Y}_i \\ \mathbf{P_y} &\approx \sum_{i=0}^{2n} W_i^c (\mathcal{Y}_i - \bar{\mathbf{y}})(\mathcal{Y}_i - \bar{\mathbf{y}})^T \end{aligned} \tag{C.3}$$

where W_i^m and W_i^c are the Unscented weighting factors defined by:

$$\begin{aligned} W_0^m &= \frac{\lambda}{n+\lambda} \\ W_0^c &= \frac{\lambda}{n+\lambda} + 1 - \alpha^2 + \beta \\ W_i^m &= W_i^c = \frac{1}{2(n+\lambda)}, \quad i = 1, \cdots, 2n. \end{aligned} \tag{C.4}$$

where β is a scalar used to introduce prior knowledge of the distribution of $\mathbf{x}$ (for Gaussian distributions $\beta = 2$ is optimal). Hence, the UKF is a straightforward extension of the Unscented transformation applied to the recursive equations of Kalman filtering, which is detailed in chapter 2 in Figure 2.7.

Appendix D

Implementation within Code_Aster FE software

The ECR and UKF algorithms, and their proposed combination, have been implemented within the framework of the public FE software *Code_Aster*. *Code_Aster* is an open-source code developed by EDF for a wide range of mechanical analyses and is available for download at http://www.code-aster.org.

In the present work, the use of ECR and UKF algorithms required further developments which were not available as built-in commands in *Code_Aster*. Thus, additional commands have been implemented in Python language aiming to use as many *Code_Aster* operators as possible, in an effort to be integrated in a future public release.

The reader will find in this appendix the sequence of main commands used to solve the ECR and UKF with *Code_Aster* in a work-flow fashion. The idea is not necessarily to give full details of the numerical developments but rather to bring a general overview and guidelines for a future user.

For this, the Python "Numpy" package is generally used as the fundamental tool to manipulate mathematical concepts such as matrices and arrays and perform complex operations like Cholesky decomposition or matrix inversions. However, the "Scipy" package is used in some cases to manipulate high DOFs models since the use of sparse matrices is then mandatory.

Solving the ECR equations (B.11) is the main numerical issue of this approach since it demands to start within the *Code_Aster* environment (basically to build up FE model operators), convert model information into Python concepts in order to solve the ECR problem, and go back to *Code_Aster* to evaluate the spatial distribution of error fields. The command flow is illustrated in Figure D.1 where only main demonstrative commands are shown.

It is important to highlight that, in an effort to decrease the computational cost in the Python code written in the course of this work, different routines have been implemented to use sparse or dense matrices (EXTR_MATR_SPARSE), as well as adapted functions to solve the ECR problem for undamped models (ECR_SOLVE).

On the other hand, one of the main difficulties when solving the ECR problem (B.11) using *Code_Aster*

consists in computing the elementary indicators Ind_{K_E} and Ind_{M_E} of equations (3.7) and (3.8) from error fields $\{\hat{u}-\hat{v}\}$ and $\{\hat{u}-\hat{v}\}$. As a matter of fact, these error fields, obtained in a Python data structure, must be introduced into a proper *Code_Aster* data structure to further compute element contributions to kinetic and potential energies. This operation can be done using a *Code_Aster* data structure of type *dyna_harmo* or *harmo_gene*, obtained from a *DYNA_LINE_HARM* calculation. To overcome this issue, artificial external loads are computed of the form:

$$\begin{aligned} \{F\}^{uv} &= [-\omega^2[M] + j\omega[C] + [K]]\{\hat{u}-\hat{v}\} \\ \{F\}^{uw} &= [-\omega^2[M] + j\omega[C] + [K]]\{\hat{u}-\hat{w}\} \end{aligned} \tag{D.1}$$

Hence, the artificial loads $\{F\}^{uv}$ and $\{F\}^{uw}$ are introduced in an auxiliary *DYNA_LINE_HARM* calculation that will produce the sought error fields with the needed data structure to perform elementary calculations. This particular way to overcome this point is temporary and may change when implementing the final public version, in a more efficient approach.

When it comes to boundary and kinematic model constraints, it is important to point out that when extracting model matrices from a *Code_Aster* data structure to a Python structure, the user can choose between two approaches: matrices with eliminated DOFs and matrices containing double Lagrange multipliers. While both can be used in the routine that solves the ECR problem, it has to be said that models containing kinematic constraints between DOFs (e.g. master-slave constraints, etc.) may fail in the ECR solver since matrix A defined in equation (B.11) is singular. This case has not been addressed in the present work and the user should have to pay special attention in this circumstances.

Finally, when dealing with high DOFs models, high cost computation has been encountered to perform the integral over frequencies defined in (1.28) when computing ξ^2_{Tr}. To this aim, the "CREA_CHAMP" operator with the key "ASSE" is used presenting numerical issues when using a high number of frequencies (in practice, we have encountered problems when adding more than 23 frequencies for a model with 6240 DOF). Thus, a particular specific approach has been adopted to overcome with this issue. The solution consists in evaluating ξ^2_{Er} only at peak error frequencies. Thus, the spatial error distributions at surrounding frequencies are supposed to have the same spatial distribution with only a difference of magnitude. This is a temporary way to overcome this problem and in a future work, a more robust development of the "CREA_CHAMP" operator will be proposed.

When it comes to the implementation of the UKF algorithm, all the needed computations are performed in Python language inside a *Code_Aster* framework. One of the advantages of the UKF algorithm is its ease of implementation. Indeed, since the nonlinear system functions are called as black-box operators (in our case the ECR work-flow described in Figure D.1), the additional steps are simply matrix manipulations. Thus, the specific UKF commands are shown in Figure D.2.

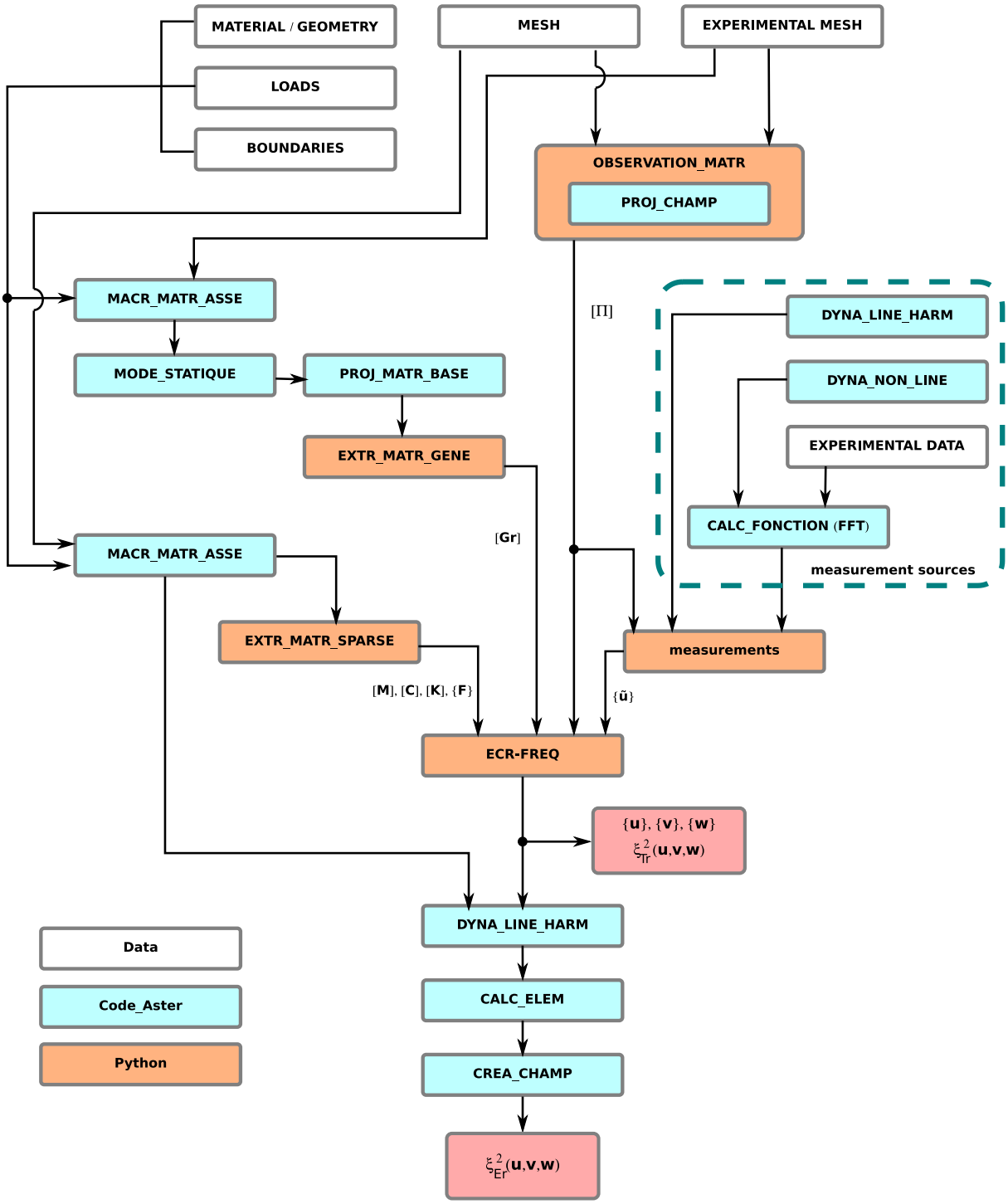

Figure D.1: *Numerical routines work-flow for solving the ECR problem within the Code_Aster FE software.*

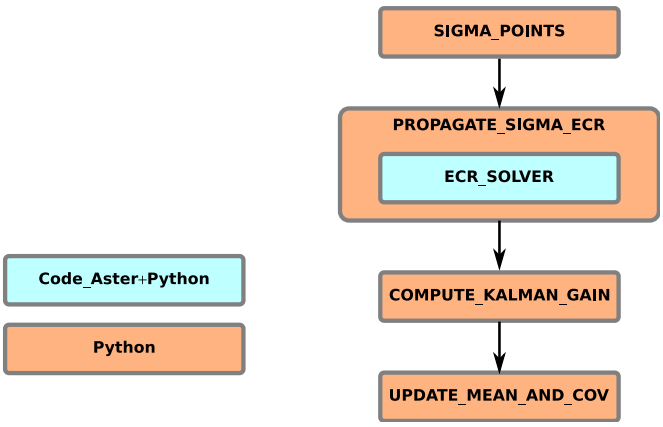

Figure D.2: *Implementation of the ECR-UKF algorithm for parameter identification.*

Appendix E

Application of the ECR to the SMART benchmark

This chapter is a verbatim reproduction of the two main chapters of Maïlys Pache undergraduate internship's final report concerning the application of the ECR methods to the SMART benchmark model.

E.1 Localisation de défauts sur le modèle SMART

L'objectif à long terme du stage est de tester la robustesse de la localisation de défauts de modélisation d'une structure existante, la maquette SMART, pour laquelle on dispose de mesures expérimentales. Afin de se donner les moyens d'interpréter les résultats de cette étude, nous avons procédé par étapes de difficulté croissante qui nous ont permis de mieux connaître la sensibilité de l'indicateur d'erreur aux différents types de défauts de modèle, et de développer des scripts et une méthodologie de calcul adaptés à nos besoins.

Dans ce premier chapitre consacré à la maquette SMART, nous n'utilisons donc pas les mesures expérimentales du benchmark qui sont exploitées dans la suite du stage. Comme dans le chapitre précédent, les mesures permettant d'évaluer l'erreur commise par le modèle sont générées par un calcul harmonique sur un modèle endommagé à l'aide de l'opérateur *Code_Aster* `DYNA_LINE_HARM`.

Les défauts à localiser sont de nouveau constitués par un affaiblissement du module d'Young sur une partie des éléments de la structure. Introduire une perte de raideur est en effet un bon moyen de modéliser de l'endommagement au niveau macroscopique.

Le modèle est soumis au chargement sismique horizontal bi-axial appliqué à la maquette SMART dans le cadre du benchmark. On utilise pour cela l'opérateur `CALC_CHAR_SEISME` de *Code_Aster* qui impose à la structure la sollicitation sismique associée aux accélérogrammes de l'expérience.

Le problème d'ERC est traité dans le domaine des fréquences. L'utilisation de cette sollicitation temporelle nécessite donc une transformée de Fourier des signaux d'efforts. Les deux directions de sollicitation sont schématisées en figure E.2.

E.1.1 Introduction : le modèle SMART

Le modèle éléments finis représentant la maquette SMART a été créé par le SEPTEN et est représenté en figure E.1. Il est constitué de 6240 degrés de liberté et d'éléments de type poutre et coques (modélisations `POU_D_EM`, `POU_D_EM` et `DKTG` de *Code_Aster*).

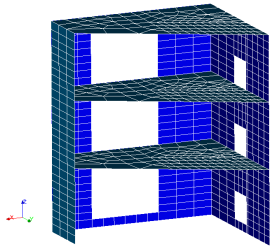

Figure E.1: *Modèle SMART.*

La maquette a été soumise à une série d'accélérogrammes horizontaux de niveaux croissant (0.05g à 1g) par l'intermédiaire de la table AZALEE, table vibrante appartenant au CEA SACLAY. Plusieurs configurations d'essais ont été exploitées par le département AMA pour estimer le comportement de la structure avant et après endommagement : maquette boulonnée sur la table vibrante, maquette posée sur le massif de construction ou encore suspendue par un plafonnier de déplacement. Au cours du stage, les calculs ont principalement été réalisés en considérant la maquette encastrée à sa base. La raison principale est que la première version de l'opérateur python `EXTR_MATR` développé en sparse ne fonctionnait pas pour les conditions limites correspondant à la configuration de la table vibrante (éléments discrets pour les ressorts, reliés entre eux par des liaisons solides). Des rapports d'essais réalisés dans le cadre du benchmark sont disponibles pour plus de précisions.

E.1.2 Localisation spatiale pour une fréquence unique

Comme expliqué précédemment, le calcul d'ERC mène à différentes qualités de localisation en fonction de la fréquence d'étude sélectionnée. La première démarche adoptée au cours de ce stage consiste à effectuer un premier calcul d'erreur globale du modèle sur une certaine bande de fréquence en vue de déterminer la fréquence maximisant le spectre d'erreur. On calcule ensuite le champ d'erreur par éléments à cette fréquence, pour laquelle les défauts du modèle sont à priori plus faciles à identifier.

Tracé du spectre et mise en évidence de fréquences d'intérêt

Un premier spectre d'erreur est présenté en figure E.3, correspondant à un affaiblissement de 20% de module d'Young sur un plancher du modèle SMART, comme illustré par la figure E.2.

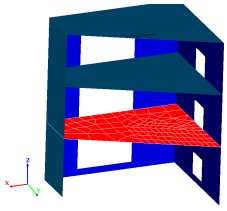

Figure E.2: *Défaut étudié. La sollicitation sismique s'exerce dans les direction X et Y.*

Les pics et creux du spectre peuvent être interprétés en traÃ§ant les réponses harmoniques de la structure aux fréquences correspondantes. On constate en observant la figure E.4 et le spectre que :

- A 38.1 Hz (E.4(a)), la déformée harmonique sollicite le défaut, pourtant l'erreur de modèle n'est pas décelée. La configuration de capteurs utilisée est représentée dans le paragraphe suivant en figure E.5(b) et fournit une explication à cette observation. La plupart des capteurs ne sont pas déplacés lors du mouvement de

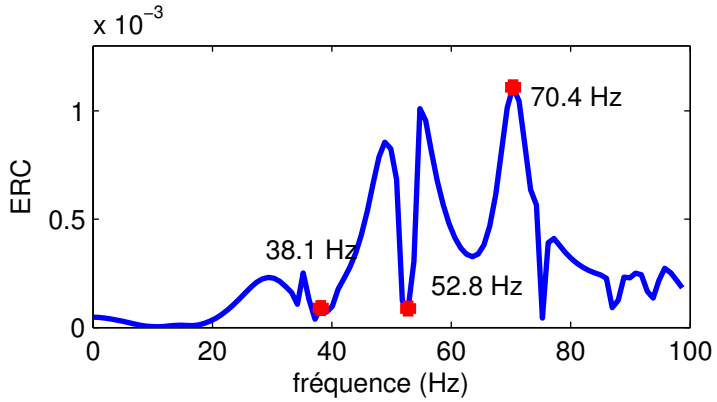

Figure E.3: *Spectre d'erreur globale pour un défaut de 20% de module d'Young sur le plancher 1 de la structure et fréquences particulières.*

la structure : en particulier les capteurs présents sur les coins des planchers. Le comportement *global* du modèle, tel qu'il est observé par les capteurs, est donc plutôt conforme au cas sans défaut.

- A 52.8 Hz (E.4(b)), l'ERC est également presque nulle car la déformée harmonique associée ne sollicite pas le défaut qui ne modifie donc pas le comportement de la structure.
- A 70.4 Hz (E.4(c)), cette fois, le défaut est bien sollicité par la déformée harmonique. Le comportement de la structure est donc modifié par sa présence. De plus, l'ensemble des capteurs sont déplacés lors du mouvement, ce qui leur permet de bien détecter cette modification.

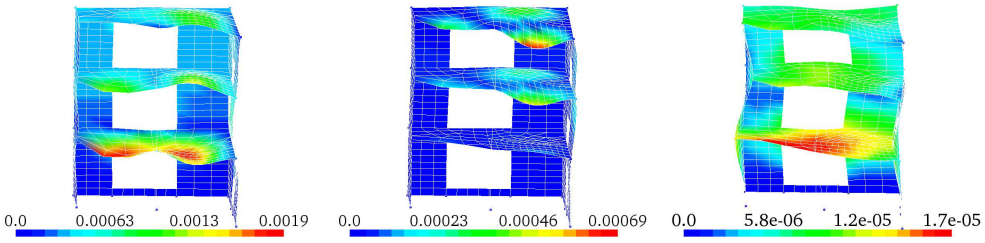

(a) 38.1 Hz (b) 52.8 Hz (c) 70.4 Hz

Figure E.4: *Déformées modales calculées pour les fréquences d'intérêt du spectre.*

On retrouve donc les constats effectués dans le chapitre précédent : le positionnement du défaut et des capteurs par rapport à la déformée harmonique est capital pour déceler le défaut.

Résultats de localisation

Emplacements des capteurs et premiers résultats

Afin de s'ajuster à la situation où les mesures proviennent de résultats d'essais, on utilise les capteurs implémentés sur la maquette SMART. Deux configurations utilisées au cours du benchmark sont représentées en figure E.5.

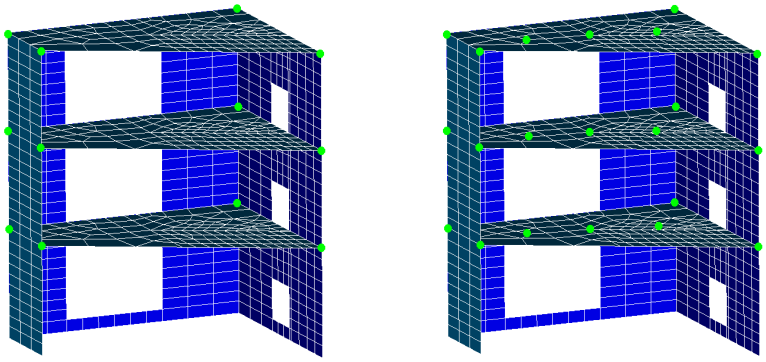

(a) Première configuration : 36 capteurs positionnés sur 12 noeuds.

(b) Seconde configuration : 63 capteurs positionnés sur 21 noeuds.

Figure E.5: *Configurations de capteurs utilisées. Pour chaque noeud en vert, les déplacements dans les directions X,Y,Z sont mesurés.*

Une première localisation d'un défaut de 20% de module d'Young sur une partie de la structure (illustrée en figure E.6) est réalisée pour ces deux configurations.

Les champs élémentaires représentés en figure E.7, tracés pour la fréquence du spectre maximisant l'erreur, correspondent à une bonne localisation du défaut, bien qu'on remarque des erreurs parasites autour de la fenêtre accolée à celui-ci.

L'ajout de capteurs sur les planchers de la maquette améliore dans une faible mesure le résultat : il n'est pas forcément nécessaire pour des défauts localisés sur les voiles (murs) de la structure. Il s'avère en revanche plus utile pour compléter le champ d'erreur lorsque l'on tente de déceler des défauts sur les planchers. Dans la suite, on utilisera la configuration à 63 capteurs.

Les spectres d'erreur (figure E.8) sont également quasiment identiques. Dans le cas où 63 déplacements sont observés, l'erreur est légèrement plus importante, on décèle en effet mieux le défaut.

La configuration où tous les déplacements des noeuds du maillage sont observés a également été testée et le résultat est représenté en figure E.9. On vérifie que la localisation est dans ce cas excellente – quoique encore incomplète – puisqu'on dispose de la quasi-totalité des informations sur le comportement réel de la structure (seules les rotations ne sont pas observées).

Localisation de différentes tailles de défaut

On presente ici d'autres résultats de localisation pour des défauts de taille différente afin de donner un aperÃ§u de la qualité de localisation obtenue par la méthode, pour la fréquence maximisant le spectre d'erreur.

La figure E.10 illustre la localisation d'un défaut d'assez grande taille. Le résultat est correct mais incomplet. De manière générale, il peut être assez difficile de visualiser un grand défaut à une fréquence donnée. En effet, lorsque la zone à localiser est importante, l'ensemble du défaut n'influe pas toujours sur le comportement de la structure.

Par ailleurs, retrouver un défaut de petite taille n'est pas toujours aisé non plus comme l'illustre la figure E.11 : la localisation est cohérente mais diffuse : il faudrait probablement monter à des fréquences très élevées, ce qui dans la pratique est difficilement réalisable, pour trouver un mode propre qui sollicite ce défaut de manière assez précise.

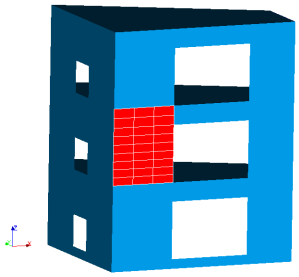

Figure E.6: *Défaut étudié.*

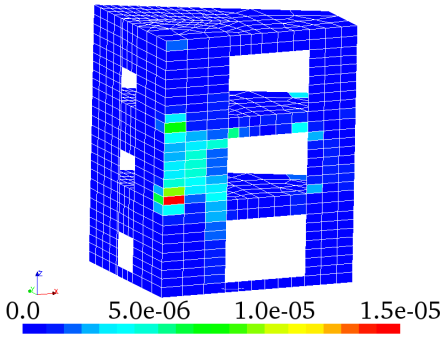

(a) Champ d'erreur par éléments pour 36 capteurs.

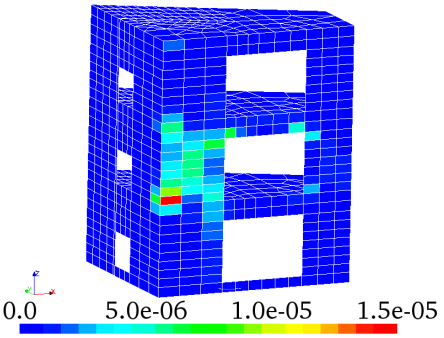

(b) Champ d'erreur par éléments pour 63 capteurs.

Figure E.7: *Résultats de localisation du défaut pour les deux configurations de capteurs (calcul réalisé à la fréquence maximisant l'erreur sur le spectre).*

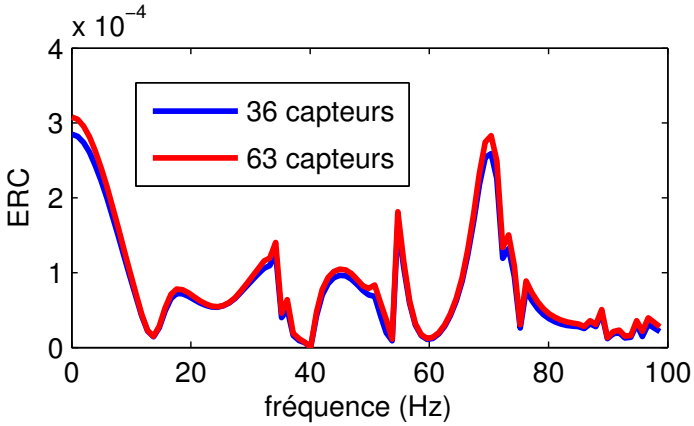

Figure E.8: *Spectres d'erreur correspondant aux deux configurations de capteurs.*

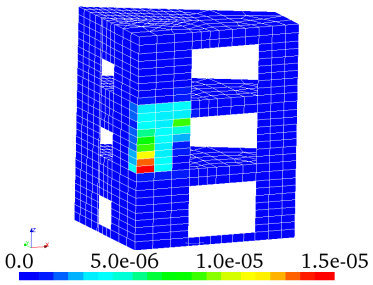

Figure E.9: *Champ d'erreur par éléments lorsque tous les déplacements sont observés.*

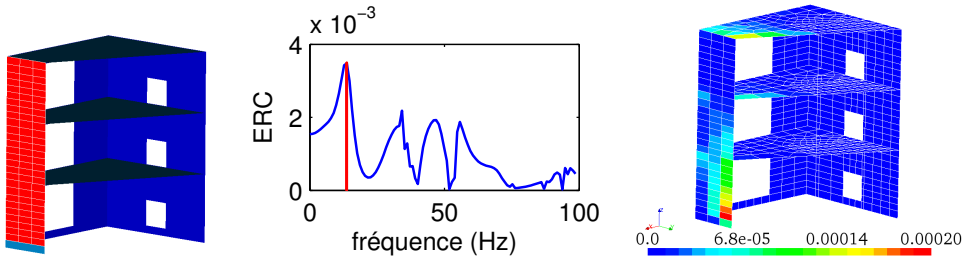

(a) Zone en défaut. (b) Spectre d'erreur. (c) Champ d'erreur.

Figure E.10: *Localisation d'un défaut de 20% de module d'Young sur un voile entier. La fréquence de localisation est mise en évidence en rouge.*

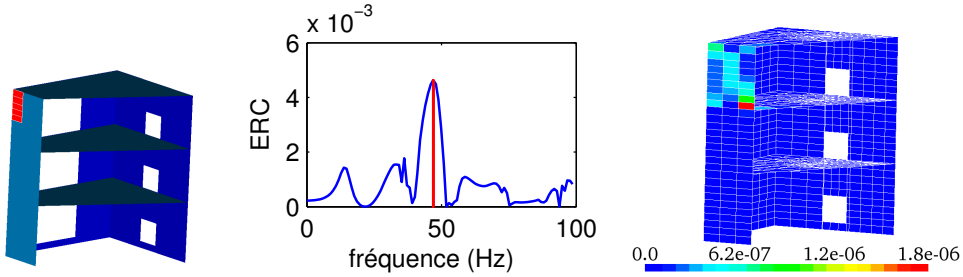

(a) Zone en défaut. (b) Spectre d'erreur. (c) Champ d'erreur.

Figure E.11: *Localisation d'un défaut de 20% de module d'Young sur 5 éléments du voile. La fréquence de localisation est mise en évidence en rouge.*

Influence de la répartition fréquentielle de l'erreur

La qualité de localisation à une fréquence donnée est également reliée à la répartition de l'erreur sur le spectre.

L'exemple précédent peut-être comparé à un défaut de taille égale mais placé différement sur la structure (voir figure E.12(a)).

Malgré la similarité des défauts, la qualité de localisation est assez diffuse dans un cas, et excellente dans le second, comme illustré sur les figures E.11(c) et E.12(c) respectivement. En observant les spectres associés à ces cas, on constate que l'erreur est également répartie de manière diffuse sur le spectre de la figure E.11(b), alors

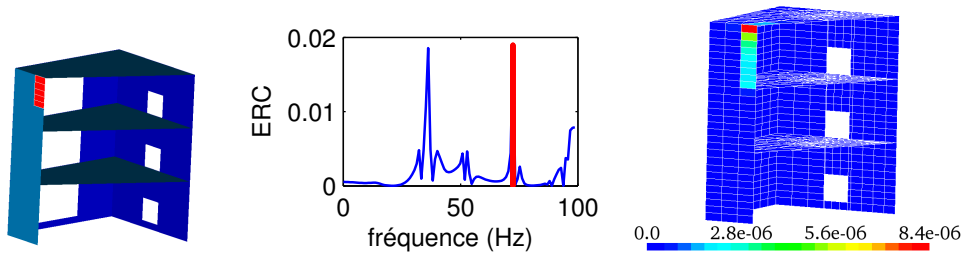

(a) Zone en défaut. (b) Spectre d'erreur. (c) Champ d'erreur.

Figure E.12: *Localisation d'un défaut de 20% de module d'Young sur 5 éléments du voile. La fréquence de localisation est mise en évidence en rouge.*

qu'en figure E.12(b) le spectre présente des pics importants où se concentre l'erreur. La localisation en ces pics est ainsi plus précise car les défauts y sont mieux décelés.

On déduit de ces observations que **la répartition de l'erreur sur le spectre est corrélée à la répartition spatiale du champ d'erreur**.

E.1.3 Amélioration de la méthode : localisation de défauts sur une bande de fréquences

Au vu de ces observations, il paraît cohérent de prendre en compte plusieurs fréquences pour localiser en défaut, en sommant les champs élementaires d'erreur calculés à ces fréquences avec une pondération, comme explicité en équation E.1.

$$e_E^2 = \int_{\omega_{min}}^{\omega_{max}} e_{\omega E}^2 \, \eta(\omega) \, d\omega \qquad ; \qquad \int_{\omega_{min}}^{\omega_{max}} \eta(\omega) \, d\omega = 1 \tag{E.1}$$

En pratique, cette somme est discrétisée : les deux sous-sections suivantes présentent deux méthodes de sélection des fréquences et de sommation proposées et étudiées pendant le stage.

Sélection de fréquences avec un pas de temps régulier

L'option la plus simple est de calculer le champ d'erreur par éléments à toutes les fréquences d'une certaine bande, et de pondérer la somme par le nombre de fréquences prises en compte. Cependant et malgré l'optimisation des scripts, nos capacités de calcul (les parties conversion des champs admissibles python en concepts *Aster* et calcul du champ élémentaire par *Code_Aster* étant notamment assez lourdes) limitent le nombre de fréquence utilisées à 22.

Nous avons donc dans un premier temps sélectionné 22 fréquences du spectre tracé de 0 à 100 Hz, prises avec un pas de temps régulier. Par exemple, la figure E.13(b) met en évidence les fréquences choisies pour la localisation du défaut de grande taille étudié en sous-section E.1.2 : on utilise 22 fréquences comprises entre 2 et 68 Hz prises avec un pas de temps de 3 Hz. L'équation E.1 devient :

$$e_E^2 \; = \; \sum_{i=1}^{22} e_{\omega_i E}^2 \;\; \eta(\omega_i) \qquad ; \qquad \eta(\omega_i) = \frac{1}{22} \tag{E.2}$$

En observant la figure E.13(c) et en la comparant au précédent résultat en figure E.10(c), on s'aperÃ§oit que la localisation est bien complétée et s'améliore de manière significative.

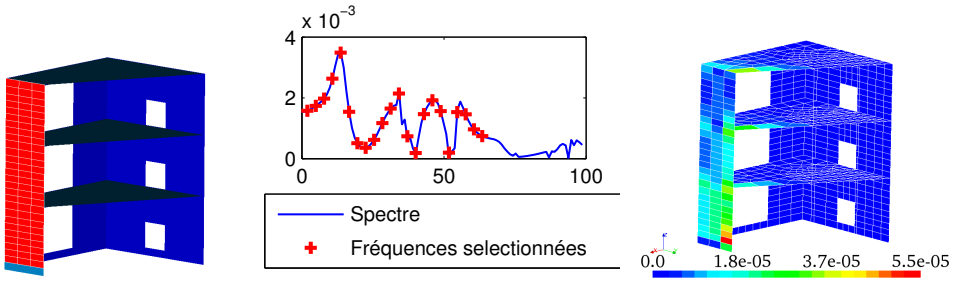

(a) Zone en défaut. (b) Spectre d'erreur et fréquences prises en compte. (c) Champ d'erreur sommé.

Figure E.13: *Localisation d'un défaut de 20% de module d'Young sur un voile entier en utilisant 22 fréquences prises avec un pas de temps régulier de 3 Hz.*

Extrapolation de la localisation sur des fréquences d'intérêt

Les temps de calculs et la mémoire utilisés pour obtenir le résultat précédent sont toutefois assez importants, ce qui nous a poussé à étudier une seconde méthode de sommation utilisant le spectre de manière plus efficace.

Cette méthode repose sur une hypothèse, dont nous allons démontrer la validité sur un exemple dans le paragraphe suivant : **à un pic d'erreur sur le spectre correspond une topologie spatiale de l'erreur**. Ainsi, on considère que toutes les fréquences d'un même pic conduisent au même champ d'erreur par éléments, à un facteur près. Pour déterminer ce facteur, on suppose que le rapport entre les erreurs globales de deux fréquences est égal au rapport entre les champs d'erreurs élémentaires de ces deux fréquences (équation E.5).

Le champ d'erreur total peut alors être approché par une combinaison linéaire d'un nombre limité de champs d'erreur. Ceux-ci sont calculés pour les fréquences constituant des maximaux locaux (pics) du spectre, fréquences particulièrement efficaces à déceler les défauts.

On rappelle la formule permettant de calculer le champ d'erreur total pour une somme discrétisée de N fréquences :

$$e_E^2 = \frac{1}{N} \sum_{j=1}^{N} e_{\omega_j E}^2 \tag{E.3}$$

Pour un spectre d'erreur constitué de N_{pics} pics d'erreur, on distribue les N fréquences au sein de ces N_{pics} qui correspondent chacun à une topologie de l'erreur, comme illustré en figure E.14 :

$$e_E^2 = \frac{1}{N} \sum_{i=1}^{N_{pics}} \sum_{j=1}^{N_i} e_{\omega_j E}^2 \tag{E.4}$$

Où N_i est le nombre de fréquences comprises dans le $i^{\text{ème}}$ pic.

Selon l'hypothèse considérée, pour une pulsation ω_j appartenant au pic i, le champ d'erreur élémentaire est approché par :

$$e_{\omega_j E}^2 \simeq e_{\omega_i E}^2 \frac{e_{\omega_j}^2}{e_{\omega_i}^2} \tag{E.5}$$

Où $e_{\omega_j}^2$ et $e_{\omega_i}^2$ désignent l'erreur globale calculée aux pulsations ω_j et ω_i.

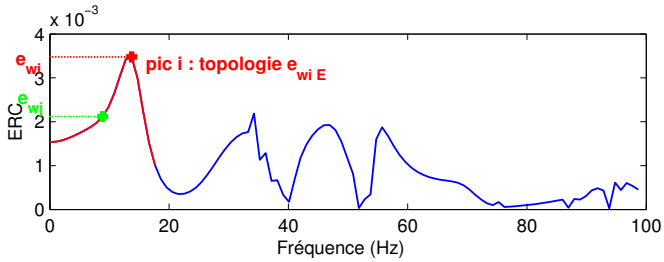

Figure E.14: *Exemple de pic d'erreur auquel on associe une topologie caractéristique. Le $i^{ème}$ pic est atteint pour la pulsation ω_i et mène au champ d'erreur élémentaire $e^2_{\omega_i E}$. La pulsation ω_j sera associée au même champ élémentaire à un facteur près.*

La somme se réécrit donc :

$$e^2_E = \frac{1}{N}\sum_{i=1}^{N_{pics}}\sum_{j=1}^{N_i} e^2_{\omega_i E}\,\frac{e^2_{\omega_j}}{e^2_{\omega_i}} = \frac{1}{N}\sum_{i=1}^{N_{pics}} e^2_{\omega_i E}\sum_{j=1}^{N_i}\frac{e^2_{\omega_j}}{e^2_{\omega_i}} \tag{E.6}$$

Ce qui permet de limiter le nombre de champs d'erreur élémentaires calculés au nombre de pics N_{pics}.

Validité de l'approximation

Le but ici est de vérifier qu'à un pic d'erreur dans le spectre est associé un champ d'erreur élémentaire caractéristique. Nous reprenons l'exemple précédent et calculons pour quelques fréquences sélectionnées sur quatre pics et représentées en figure E.15 les champs d'erreur élémentaires.

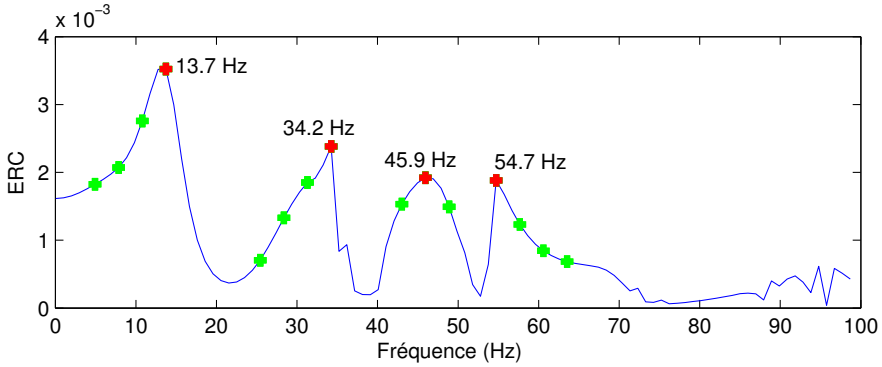

Figure E.15: *Défaut étudié et spectre d'erreur. En rouge les fréquences qu'on envisage de prendre en compte dans le calcul. En vert celles pour lesquelles on vérifie l'approximation.*

Les figures E.16 à E.19 présentent les champs obtenus pour les quatre pics. La fréquence pour laquelle le champ d'erreur sera pris en compte dans le calcul de la somme est mise en évidence en gras. On retrouve bien une forme de localisation propre à chaque pic, dont l'intensité diminue avec l'erreur globale calculée sur le spectre ci-dessus.

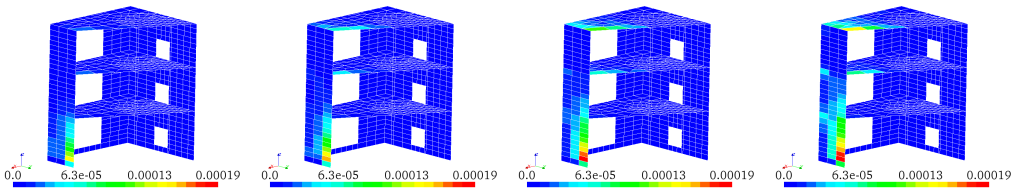

(a) 4.9 Hz (b) 7.9 Hz (c) 10.8 Hz (d) **13.7 Hz**

Figure E.16: *Champs d'erreur pour les fréquences du premier pic.*

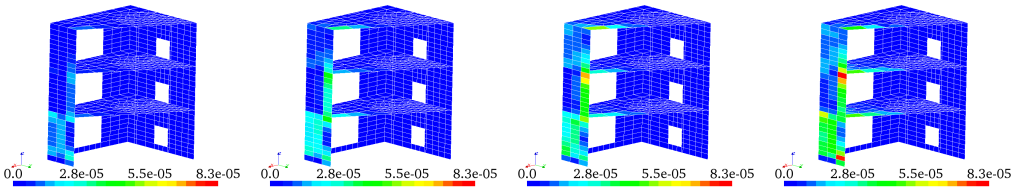

(a) 25.4 Hz (b) 28.4 Hz (c) 31.3 Hz (d) **34.2 Hz**

Figure E.17: *Champs d'erreur pour les fréquences du deuxième pic.*

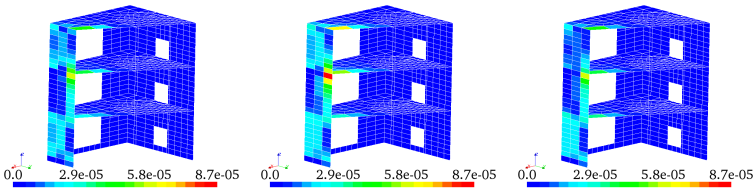

(a) 43.0 Hz (b) **45.9 Hz** (c) 48.9 Hz

Figure E.18: *Champs d'erreur pour les fréquences du troisième pic.*

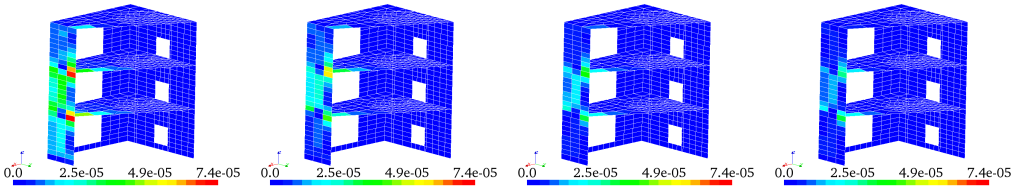

(a) **54.7 Hz** (b) 57.7 Hz (c) 60.6 Hz (d) 63.5 Hz

Figure E.19: *Champs d'erreur pour les fréquences du quatrième pic.*

Comparaison des deux méthodes de sommation

Nous reprenons maintenant cet exemple en calculant le champ d'erreur sommé par les deux méthodes explicitées au-dessus. Le calcul pour la seconde méthode s'est fait à l'aide d'un algorithme développé au cours du stage permettant de fragmenter le spectre en différents pics. Sur cet exemple, quatre pics ont été pris en compte. Le résultat de localisation est donc une somme pondérée de quatre champs d'erreur, au lieu de vingt-deux pour la première méthode. On représente en figure E.20 le champ d'erreur pour la fréquence maximisant le spectre, puis les champs d'erreur sommés avec les deux méthodes.

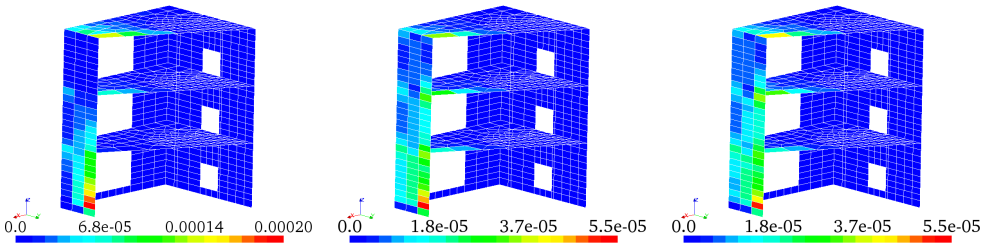

(a) Champ d'erreur pour la fréquence maximisant le spectre (27.4 Hz).

(b) Champ d'erreur sommé sur 22 fréquences prises avec un pas de temps régulier.

(c) Champ d'erreur sommé en utilisant 4 fréquences de pics et des facteurs de pondération calculés sur le spectre.

Figure E.20: *Comparaison entre les différentes méthodes de localisation.*

On constate en observant ces résultats d'une part que la sommation a permis d'améliorer un premier résultat incomplet, et d'autre part que les deux méthodes de sommation conduisent à des résultats très similaires, la seconde méthode ne diminuant pas la qualité de localisation, ce qui nous conforte dans l'idée qu'à un pic correspond un type de localisation. La seconde méthode de sommation pourra donc être utilisée pour économiser des ressources CPU.

Dans la suite du rapport, on tracera à chaque fois un champ d'erreur sommé sur le spectre.

E.1.4 Études de sensibilité

Cette section rassemble plusieurs études menées au cours du stage pour mieux connaître le comportement de l'indicateur d'ERC et ses possibilités.

Influence de l'intensité du défaut

La plupart des cas présentés jusqu'à maintenant visaient à localiser un défaut de 20% de module d'Young introduit sur une partie de la structure. En pratique, on peut être amené à recaler un modèle qui présente un défaut moins intense, ou au contraire à localiser des fissures qui affaiblissent une partie de la structure bien plus considérablement.

Nous illustrons ici l'influence de l'intensité du défaut de module d'Young sur la localisation de ce défaut dans le cas où une partie d'un voile représentée en figure E.21. Le champ d'erreur est tracé en figure E.22 pour des taux d'affaiblissements de 10, 50 et 90 %.

On constate sur cet exemple que contrairement à une idée naturelle, ce défaut est décelé de manière plus complète (l'erreur maximale reste bien sûr moindre, les tracés n'étant pas à la même échelle) par l'ERC lorsque son intensité est très faible. D'autres cas ont été étudiés et conduisent à une localisation de qualité égale quelque soit le niveau d'intensité du défaut. Ces résultats ne permettent donc pas de conclure quant à un comportement

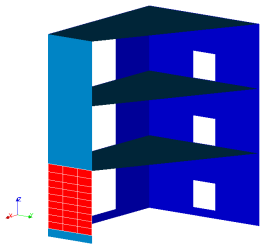

Figure E.21: *Défaut étudié.*

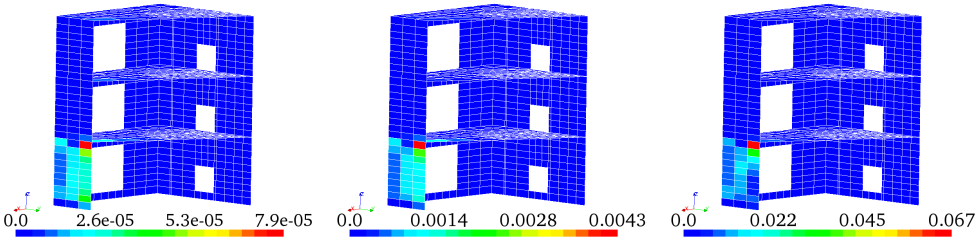

(a) Affaiblissement de 10 %. (b) Affaiblissement de 50 %. (c) Affaiblissement de 90 %.

Figure E.22: *Comparaison des champs d'erreur pour plusieurs intensités d'affaiblissement du module d'Young.*

particulier de l'ERC vis à vis de l'intensité des défauts implémentés sur SMART. On peut en revanche retenir que la méthode de localisation reste performante dans les cas d'intensités extrêmes.

Influence du paramètre *r*

Le paramètre r est un paramètre de pondération entre les deux parties de la fonctionnelle d'Erreur en Relation de Comportement qu'on rappelle ci-dessous.

$$\begin{aligned} e^2_\omega(\{U\},\{V\},\{W\}) &= \frac{\gamma}{2}\{U-V\}^T[\mathbf{K}+T\omega^2\mathbf{C}]\{U-V\} \\ &+ \frac{1-\gamma}{2}\{U-W\}^T[\omega^2\mathbf{M}]\{U-W\} \\ &+ \frac{r}{1-r}\{\Pi U-\tilde{U}\}^T[\mathbf{G}_r]\{\Pi U-\tilde{U}\} \end{aligned} \tag{E.7}$$

La première partie, composée des deux premiers termes de l'équation E.7, quantifie l'erreur en relation de comportement elle-même. Lorsque la valeur donnée à r est petite, ce terme est prépondérant dans la fonctionnelle à minimiser, ce qui suppose qu'on accorde une bonne confiance au respect de cette relation par notre modèle. La seconde partie de la fonctionnelle est constituée du troisième terme, évaluant l'écart du champ U aux mesures. Si on donne une valeur importante au paramètre r, on accorde plutôt une grande confiance aux mesures. Ce paramètre joue en fait le rôle de paramètre de régularisation de Tikhonov, concept expliqué en [14].

On évalue ici l'influence de ce paramètre en testant la localisation d'un défaut de 20% de module d'Young sur une partie de la structure représentée en figure E.23 pour r prenant les valeurs 0.1, 0.5 et 0.9. Les résultats sont présentés en figure E.24.

On constate que l'augmentation de r semble augmenter la concentration de l'erreur sur le défaut. Pour r=0.1, l'erreur déborde largement de la zone en défaut, jusque sur les planchers, pourtant dépourvus de défaut. Il faut

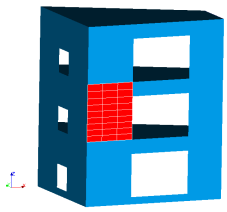

Figure E.23: *Défaut étudié.*

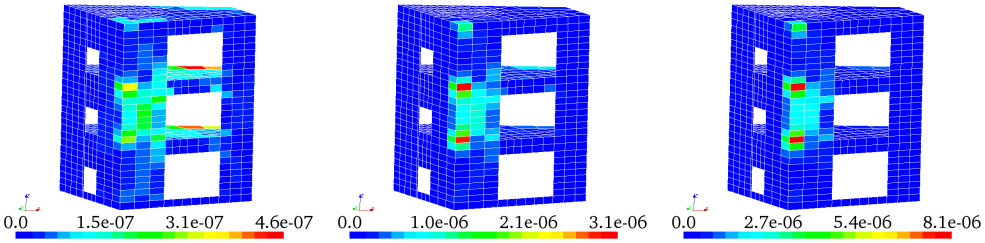

(a) r = 0.1 (b) r = 0.5 (c) r = 0.9

Figure E.24: *Comparaison des champs d'erreur pour plusieurs valeurs du paramètre r.*

noter que dans notre cas, les mesures sont numériques et donc parfaites. Toute l'erreur du modèle réside dans la matrice de raideur, et donc dans la vérification des relations de comportement. Par conséquent il paraît plus approprié de choisir une grande valeur de r, ce qui semble expliquer nos résultats.

Influence de la géométrie du modèle : cas défavorables

Jusqu'à maintenant, les exemples étudiés concernaient des défauts introduits sur les voiles (murs) de la structure. Cette sous-section illustre en particulier le cas de défauts implémentés sur les planchers en vue d'évaluer l'influence de la géométrie des zones en défaut sur la qualité de localisation.

La première figure (E.25) présente des résultats de localisation de défauts de 20 % de module d'Young sur des zones de différentes tailles du plancher. On remarque que dans les deux premiers cas la localisation est assez incomplète ou diffuse, et que le plancher présente des zones où la localisation semble difficile, tandis qu'à d'autres endroits elle paraît facilitée, comme dans le dernier cas.

Pour illustrer l'existence de telles zones, on tente de localiser un défaut entièrement compris dans une zone "d'ombre" en figure E.26. La qualité de localisation est cette fois particulièrement faible : le champ d'erreur est à la fois diffus et incomplet.

Nous avons également pu remarquer en sous-section E.1.2 que la proximité du défaut à une fenêtre peut amener la localisation à se diffuser autour de celle-ci. C'est ce que l'on constate particulièrement sur l'exemple suivant (figure E.27), où le défaut est d'une taille raisonnable mais le champ d'erreur associé est particulièrement diffus.

Ces deux exemples, qui sont les plus pénalisants trouvés sur la maquette SMART, indiquent que la qualité de la méthode peut s'altérer en particulier lorsque la géométrie de la structure est complexe, de toute évidence par l'intermédiaire du comportement harmonique des zones entâchées de défaut. L'interprétation des champs d'erreur peut dans ces cas être trompeuse. Toutefois, on note que ces résultats ne sont pas dépourvus de cohérence et

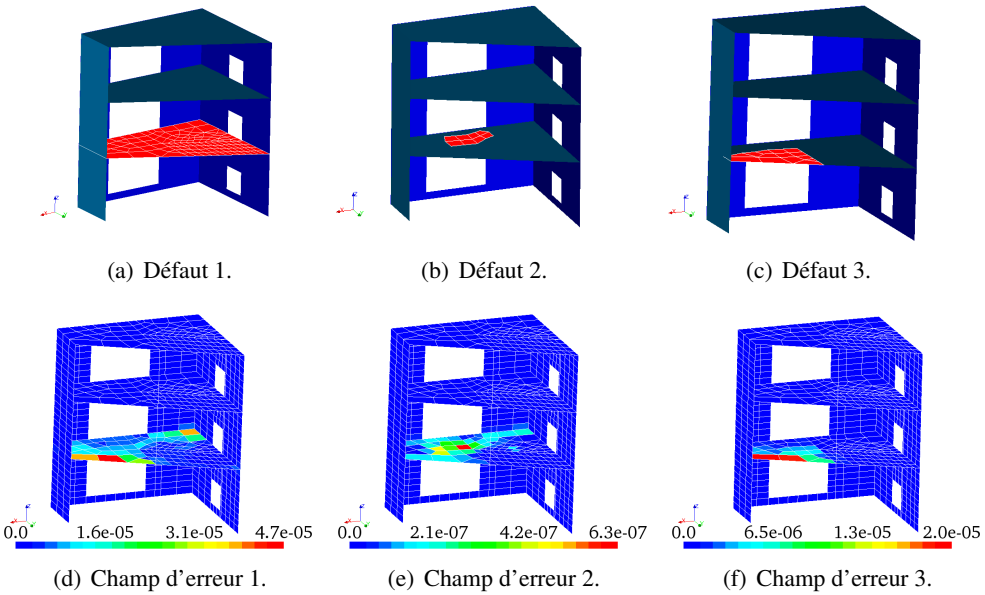

(a) Défaut 1. (b) Défaut 2. (c) Défaut 3.

(d) Champ d'erreur 1. (e) Champ d'erreur 2. (f) Champ d'erreur 3.

Figure E.25: *Résultats de localisation pour des défauts situés sur les planchers du modèle.*

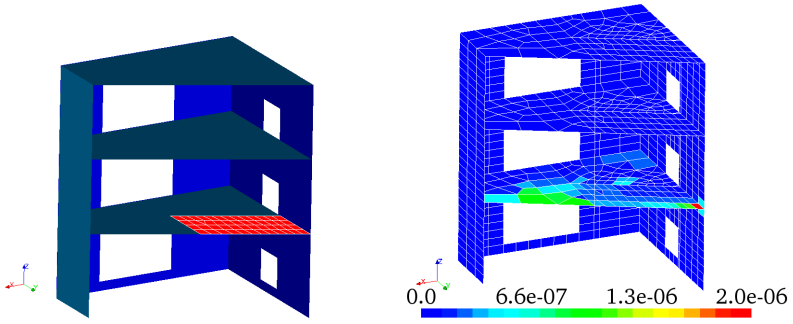

(a) Défaut. (b) Champ d'erreur.

Figure E.26: *Exemple d'un défaut dans une zone où la localisation est difficile.*

constituent un repérage, même grossier, du défaut.

Localisation de plusieurs défauts à une fréquence donnée

Lorsque l'on s'intéresse à l'écart entre un modèle et la structure qu'il est supposé représenter, on peut s'attendre à détecter plusieurs défauts, d'intensité et de taille différentes, inégalement répartis dans l'espace. Cette sous-section vise à tester la localisation de différentes zones entâchées d'erreur et éloignées les unes des autres afin de déterminer d'une part si une double localisation est possible, et d'autre part si des localisation parasites apparaîssent à des endroits "sains".

Le cas où une partie d'un voile et une partie d'un plancher subissent un défaut de raideur de 20% est étudié.

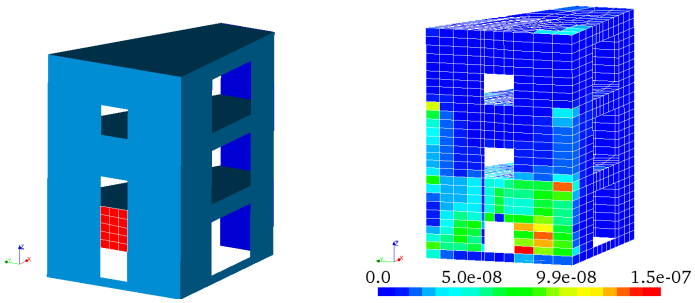

(a) Défaut. (b) Champ d'erreur.

Figure E.27: *Exemple d'un défaut à proximité de fenêtres.*

La figure E.28 présente le spectre d'erreur pour chacun des défauts puis celui pour les deux défauts.

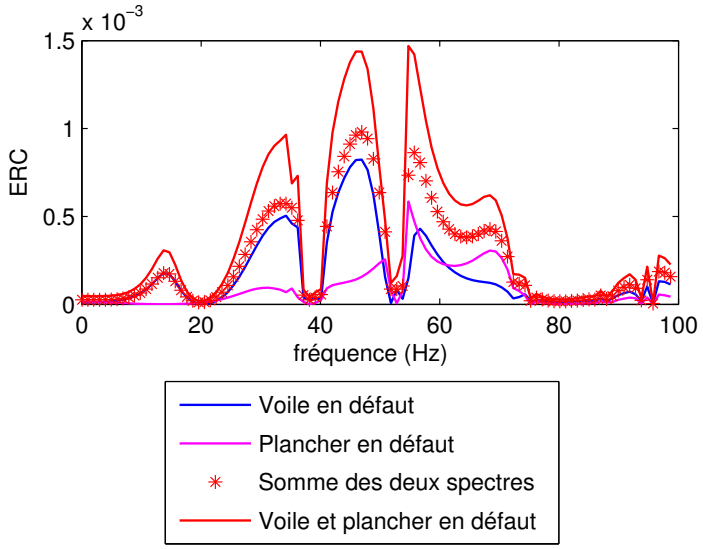

Figure E.28: *Spectres correspondant aux calculs d'ERC sur chaque défaut puis sur les deux défauts à la fois. En étoiles rouges la somme des spectres bleu et magenta.*

On compare la localisation individuelle de chaque défaut (figures E.29 et E.30) à la localisation des deux défauts (figure E.31).

On peut considérer en faisant une assez bonne approximation que les champs d'erreur s'additionnent, ce qui nous permet de conclure sur cet exemple qu'il semble possible de localiser plusieurs défauts à la fois sur une structure sans subir de défauts parasites.

E.1.5 Conclusion du chapitre

La première partie des études réalisée sur le modèle SMART avait pour objectifs d'une part d'évaluer les performances de l'identification basée sur l'ERC dans le cas où les mesures sont générées par un calcul sur un modèle

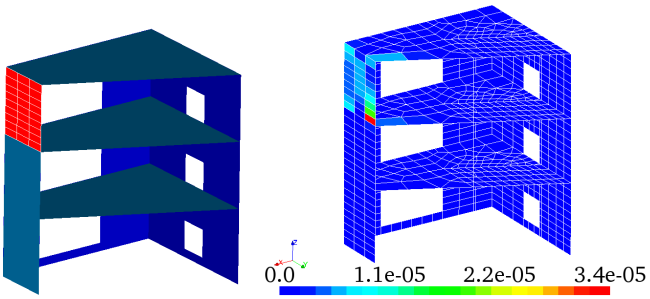

(a) Défaut. (b) Champ d'erreur.

Figure E.29: *Localisation d'un défaut situé sur un voile.*

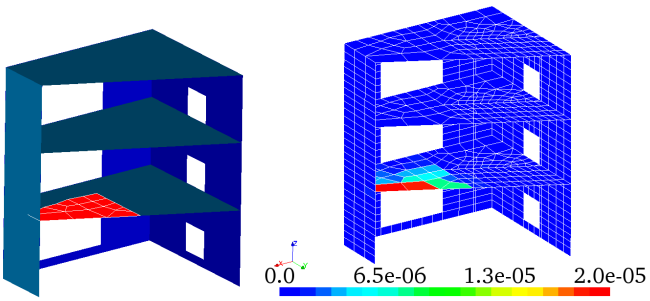

(a) Défaut. (b) Champ d'erreur.

Figure E.30: *Localisation d'un défaut situé sur le plancher du bas.*

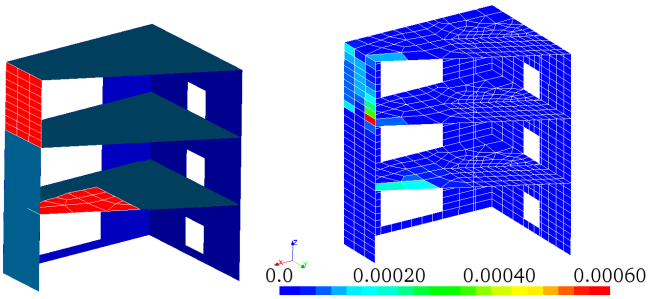

(a) Défaut. (b) Champ d'erreur.

Figure E.31: *Localisation des deux défauts.*

présentant un défaut de raideur, et d'autre part de commencer à développer une méthodologie de calcul adaptée à la résolution du problème sur SMART de manière efficace.

L'interprétation du spectre d'erreur a été le levier principal permettant d'atteindre ce deuxième objectif. Deux conditions ont été identifiées pour caractériser une fréquence donnant lieu à une bonne localisation du défaut : la déformée associée doit solliciter le défaut et une bonne partie des capteurs. Ce résultat pouvait être anticipé. Le choix d'une fréquence d'étude s'est ainsi porté sur celles qui maximisent l'Erreur en Relation de Comportement, indice témoignant du fait que le défaut est bien décelé.

Nous avons pu identifier une corrélation entre la répartition spatiale de l'erreur et sa répartition spectrale : lorsque l'erreur est concentrée sur une fréquence donnée, le calcul d'ERC amène à un champ d'erreur également concentré sur le défaut. A contrario, une erreur largement diffusée sur une bande de fréquence amènera à priori à un champ d'erreur diffus.

Il a rapidement été envisagé de considérer le calcul d'ERC sur une bande de fréquences plutôt que sur une fréquence unique, afin d'enrichir le résultat. Les résultats étant bons mais la méthode impliquant des temps de calculs assez élevés, une méthode de calcul du champ total a été développée en se basant sur une hypothèse vérifiée au cours du stage. On peut la formuler comme suit : à un pic d'erreur sur le spectre correspond une topologie caractéristique de l'erreur. Cette constatation s'explique par l'intermédiaire du comportement modal d'une structure, qui se déforme d'une manière caractéristique entre deux fréquences données, avec un pic de déformation atteint pour la fréquence propre.

Ce chapitre présente un bon aperÃ§u de la qualité des résultats obtenus pour localiser un défaut de raideur sur un modèle numérique. Dans l'ensemble, les résultats sont prometteurs, quoique des cas défavorables aient été identifiés. La capacité de localiser plusieurs défauts sans subir d'erreurs parasites a notamment été démontrée. La sensibilité de l'indicateur à différentes intensités de défauts ainsi qu'au paramètre r caractérisant la confiance aux mesures ont également été évalués ici.

Ces études constituent un bon socle de connaissances permettant d'aborder le chapitre suivant, visant à localiser des défauts d'endommagement sur un modèle numérique.

E.2 Localisation de non-linéarités sur le modèle SMART

La seconde partie de l'étude sur la maquette SMART exploite, là encore, des mesures "numériques" provenant d'un calcul sur un modèle éléments finis de SMART. Le but est à présent de localiser de l'endommagement non-linéaire et non plus des défauts de raideur.

Pour cela, on fait suivre au modèle éléments finis un calcul non-linéaire à l'aide de l'opérateur `DYNA_NON_LINE` de *Code_Aster*, en le soumettant aux sollicitations sismiques subies par la maquette SMART. Les non-linéarités apparaissant lors du calcul jouent à présent le rôle du défaut à localiser et les déplacements de la maquette aux points de capteurs sont prélevés pour constituer les mesures.

A la différence du chapitre précédent où un calcul harmonique générait des mesures dépendantes de la fréquence, les mesures sont à présent temporelles. En vue de les utiliser dans le cadre du problème d'ERC, qu'on traite dans le domaine des fréquences, une transformation de Fourier est nécessaire. Dans une première partie de l'étude, celle-ci est réalisée sur l'ensemble du signal temporel (voir figure E.32). On fenêtre ensuite le signal en plusieurs parties afin de suivre l'évolution temporelle de l'endommagement.

E.2.1 Étude de l'endommagement à localiser

La structure obéit à une loi de comportement en béton armé définie dans *Code_Aster* pour les structures minces (plaques et coques), nommée `GLRC_DM`. Cette loi de comportement intègre les phénomènes non linéaires tels que l'endommagement en s'appuyant sur des contraintes (sollicitations de flexion et membranaires) et déformations

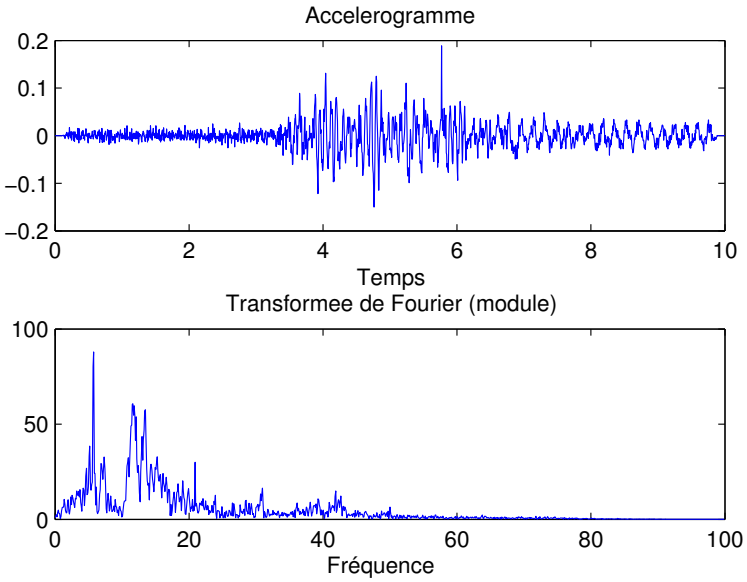

Figure E.32: *Accélérogramme et transformée de Fourier du signal complet.*

généralisées. Des variables internes d'endommagement mesurant l'affaiblissement relatif de raideur de la dalle en béton armé en traction, en compression et en flexion sont disponibles en postraitement. Une valeur nulle des variables représente un comportement linéaire et une valeur de 1 un endommagement maximum. On peut se référer à ce sujet à la documentation de *Code_Aster* correspondante.

Un calcul non-linéaire de 10 secondes est effectué sur le modèle. Celui-ci commence à s'endommager (son comportement devient non-linéaire) au bout de 4 secondes et atteint à la fin du calcul un état d'endommagement présenté en figure E.33. L'évolution temporelle des variables d'endommagement en traction et en flexion de l'élément le plus touché du modèle est également représenté en figure E.34. La variable d'endommagement en compression reste nulle au cours du calcul, ce qui s'explique par meilleure résistance en compression du béton armé.

E.2.2 Difficultés rencontrées

Les premiers résultats de localisation d'endommagement obtenus ont montré que l'utilisation de mesures temporelles était délicate. En effet, elle nécessite de calculer la transformée de Fourier discrète des mesures pour les convertir en mesures fréquentielles, ce qui revient à effectuer un certain nombre d'approximations, qui génèrent des erreurs.

Lors d'une première approche, les transformées de Fourier ont été réalisées sur le signal brut. Le calcul d'ERC a alors été effectué en considérant l'ensemble des 10 secondes puis en ne s'intéressant qu'à des fenêtres glissantes de 2.5 secondes, afin de suivre l'évolution temporelle de l'endommagement. Les résultats obtenus se sont avérés erronés : pour certaines fenêtres — notamment en considérant l'ensemble du signal — l'endommagement semblait correctement localisé (figures E.35(b) et E.35(g)), mais pour d'autres le résultat de localisation ne correspondait pas à l'emplacement du défaut (figures E.35(f) et E.35(h)). De plus, les champs d'erreurs obtenus pour les premiers instants du signal, lorsque la structure n'est pas encore endommagé, présentaient une intensité parfois plus importante que ceux correspondant à un état de la structure très endommagée, comme illustré en figure E.35(d). Ce dernier constat a conduit à remettre en cause les localisations obtenues qui semblaient correctes.

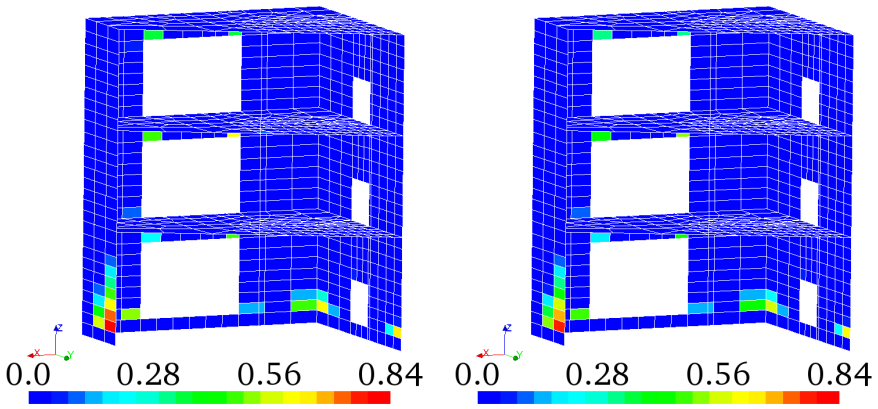

(a) Variable d'endommagement en traction. (b) Variable d'endommagement en flexion.

Figure E.33: *Champs d'endommagement à la fin du calcul.*

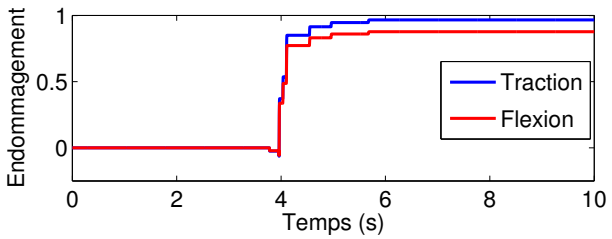

Figure E.34: *Évolution des variables d'endommagement de traction et de flexion d'un élément au cours du calcul non-linéaire, pour l'élément le plus endommagé.*

Afin de limiter au maximum les erreurs dues à la transformation de Fourier, les méthodes de calculs ont été corrigées afin de respecter un certain nombre de critères :

- Le résultat de la DFT effectuée par *Code_Aster* n'est plus interpolé sur une liste de fréquences d'intérêt. Celles-ci sont désormais prises dans les fréquences pour lesquelles la DFT est effectivement calculée.
- On vérifie qu'on ne prend en compte le résultat de la transformée de Fourier discrète (DFT) que pour des fréquences inférieures à la moitié de la fréquence d'échantillonnage. Au delà, le spectre subit un repliement, d'après le théorème de traitement du signal de Shannon-Nyquist.
- La discrétisation temporelle de l'accélérogramme doit être égale à celle des mesures obtenues par le calcul transitoire. Dans le cas contraire, leurs DFT ne sont pas comparables en intensité car ne comprennent pas le même nombre de points.
- Les accélérogrammes sont corrigés pour être de moyenne nulle. On utilise pour cela le mot-clef `CORR_ACCE` de l'opérateur `CALC_FONCTION` de *Code_Aster* qui supprime la dérive d'un signal.
- Un fenêtrage du signal a été envisagé, en utilisant par exemple des fenêtres de Hanning découpant le spectre en plusieurs parties sur lesquelles la DFT est calculée puis moyennée (de manière analogue au calcul fait par l'opérateur `CALC_SPEC`). Cependant, les accélérogrammes utilisés sont des signaux aléatoires. La fenêtre rectangulaire (soit aucun fenêtrage) est en fait la plus adaptée dans ce cas.

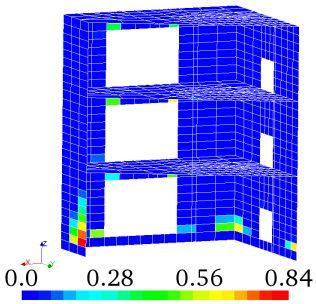

(a) Endommagement à la fin du calcul.

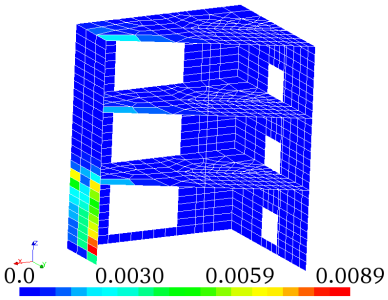

(b) Champ d'erreur pour l'ensemble du signal.

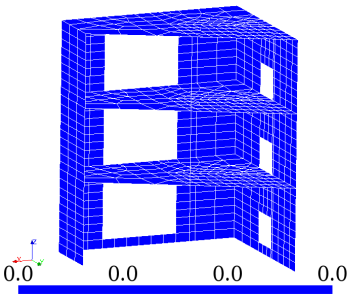

(c) Endommagement avant 4 s.

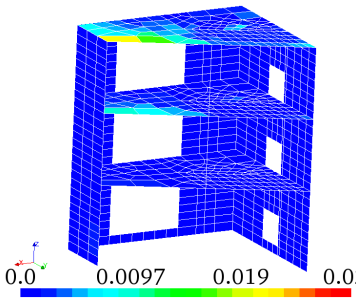

(d) Champ d'erreur pour la fenêtre 3 (de 1 à 3.5 s).

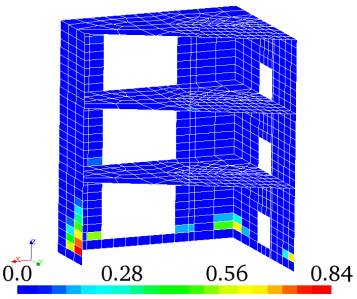

(e) Endommagement après 5.5 s

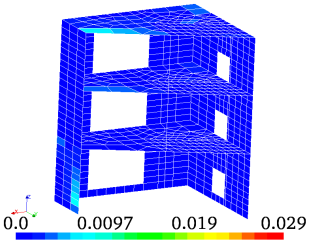

(f) Champ d'erreur pour la fenêtre 8 (de 3.5 à 6 s).

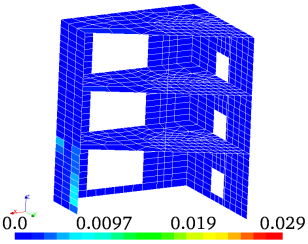

(g) Champ d'erreur pour la fenêtre 10 (de 4.5 à 7 s).

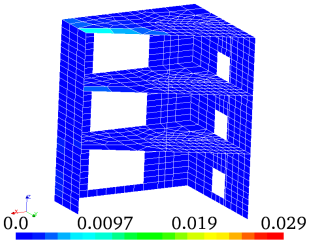

(h) Champ d'erreur pour la fenêtre 14 (de 6.5 à 9 s).

Figure E.35: *Premiers résultats de localisation d'endommagement.*

Cependant, ces précautions ne suffisent pas à améliorer le résultat d'ERC. Le problème provient bien de l'approximation faite en effectuant les DFT, mais les erreurs commises sont amplifiées par la normalisation de l'erreur globale par une énergie de référence : on rappelle la définition de l'erreur relative retenue jusqu'à présent en équation E.8 :

$$e_{\omega r}^2 = \frac{e_\omega^2}{\frac{\gamma}{2}\{\hat{U}\}^T[\mathbf{K}+T\omega^2\mathbf{C}]\{\hat{U}\}+\frac{1-\gamma}{2}\{\hat{U}\}^T[\omega^2\mathbf{M}]\{\hat{U}\}} \tag{E.8}$$

L'énergie de référence est calculée à chaque fréquence et dépend du champ $\hat{U}$. Cette méthode permet d'obtenir un bon indicateur d'erreur la plupart du temps. Cependant, dans notre cas, le contenu des accélérogrammes est très faible pour certaines fréquences, ce qui conduit à un champ $\hat{U}$ infinitésimal. On obtient ainsi à ces fréquences une erreur globale presque nulle et une erreur relative qui explose. La figure E.36 illustre ce phénomène.

On définit ainsi une nouvelle énergie de référence qui ne dépend pas de la fréquence, en sommant l'ensemble des énergies de référence calculées sur le spectre, comme présenté en équation E.9.

$$e_{\omega r}^2 = \frac{e_\omega^2}{\int_\omega(\frac{\gamma}{2}\{\hat{U}\}^T[\mathbf{K}+T\omega^2\mathbf{C}]\{\hat{U}\}+\frac{1-\gamma}{2}\{\hat{U}\}^T[\omega^2\mathbf{M}]\{\hat{U}\})d\omega} \tag{E.9}$$

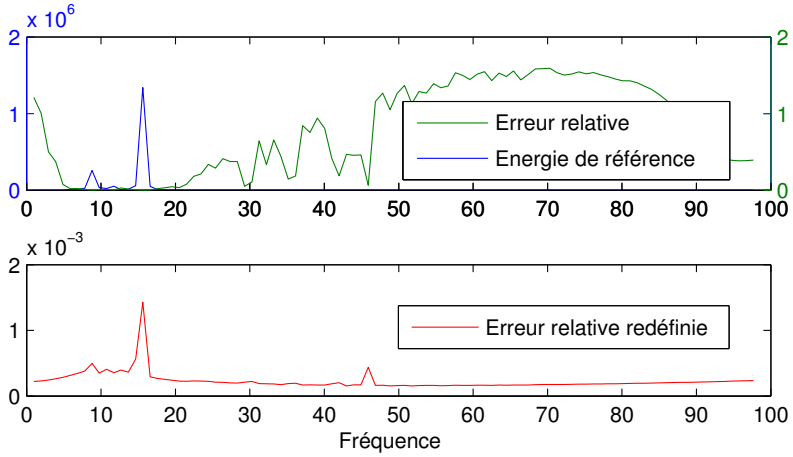

Figure E.36: *Tracé du spectre d'erreur relative pour deux approches. En haut, l'énergie de référence dépend de la fréquence et amplifie l'erreur pour les hautes et basses fréquences qui ne sont pas sollicitées (voir la DFT de l'accélérogramme en figure E.32). En bas, on résout ce problème en intégrant l'énergie de référence sur le spectre pour calculer l'erreur relative.*

E.2.3 Localisation des non-linéarités sur l'ensemble du signal

En figure E.37 est illustré le champ d'erreur correspondant au calcul d'Erreur en Relation de Comportement. On observe une bonne identification de la partie la plus endommagée de la structure. Des erreurs parasites sont également décelées sur les planchers pourtant "sains", mais leur intensité est moindre. En revanche, d'autres éléments ayant subi un fort endommagement (plus de 50% pour certains) n'apparaissent pas sur le champ d'erreur, probablement car les zones endommagées sont trop petites.

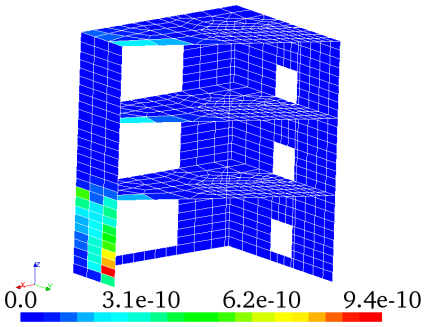

Figure E.37: *Résultat de localisation de l'endommagement.*

E.2.4 Localisation des non-linéarités par fenêtrage du signal

Les accélérogrammes et les mesures sont maintenant découpés avant d'être de nouveau utilisés dans le calcul d'ERC. On espère ainsi pouvoir suivre l'évolution de l'endommagement dans le temps. On utilise 16 fenêtres de 2.5 secondes glissant avec un pas de temps de 0.5 secondes.

L'endommagement de la structure n'évolue qu'entre 4 et 5.5 secondes. On regroupe donc au sein d'une même figure les fenêtres correspondant à la localisation d'un niveau d'endommagement donné. Les figures E.38 à E.40 permettent de visualiser pour chaque fenêtre :

- La partie de l'accélérogramme correspondant à la fenêtre utilisée (ou aux fenêtres utilisées, lorsque celles-ci sont regroupées) ;
- L'endommagement de la structure à localiser, pris au dernier pas de temps de la fenêtre considérée ;
- Le résultat de champ d'erreur par éléments pour cette fenêtre.

Les calculs d'ERC permettent effectivement d'observer l'évolution temporelle de l'endommagement. L'erreur relative est tracée pour différentes fenêtres caractéristiques en figure E.41. Cette figure montre à quel point l'erreur augmente en intensité au cours du temps, ce qui témoigne de l'apparition des non-linéarités au cours du calcul. Celles-ci ne sont détectées qu'à partir de la fenêtre 7 et augmente brièvement en intensité dans les fenêtres suivantes, comme l'illustrent les figures E.38 à E.40. D'après la figure E.34, l'endommagement réel apparaît au bout de quatre secondes pour atteindre très rapidement sa valeur maximale et n'évoluer plus ensuite. On constate cependant que le champ d'erreur ne reste pas constant : il est particulièrement intense en fenêtre 10. Cette fenêtre correspond à des instants où l'accélération imposée est très importante. Dans les fenêtres suivantes, la sollicitation s'atténue comme illustré en figure E.40(a). Ceci explique le fait qu'on détecte mieux l'endommagement à la fenêtre 10 qu'aux suivantes : la structure est beaucoup plus sollicitée.

Enfin, les éléments endommagés auparavant non détectés dans le champ d'erreur peuvent à présent être observées pour les fenêtres 10 et 13.

E.2.5 Conclusion du chapitre

Le but de cette seconde étape sur la maquette SMART était d'exploiter des mesures générées par un calcul transitoire non-linéaire pour traiter le problème d'ERC. Le défaut à localiser était constitué par des non-linéarités apparaissant lors du calcul et éloignant le modèle générateur des mesures du modèle de référence.

Un premier résultat utilise les déplacements (numériquement) mesurés sur SMART lors d'un calcul de 10 secondes, le modèle étant soumis à un chargement sismique horizontal bi-axial. Le champ d'erreur calculé permet une bonne estimation de l'endroit le plus endommagé de la structure.

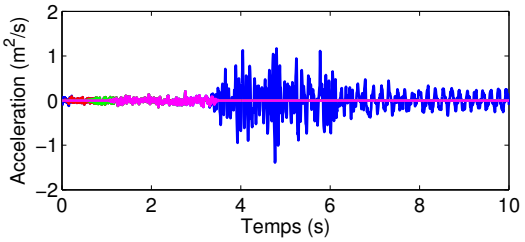

(a) Fenêtrages 1 à 3.

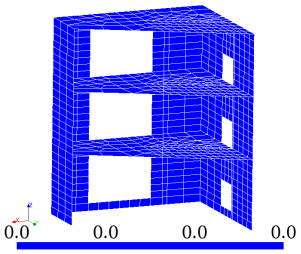

(b) Endommagement avant 4 s

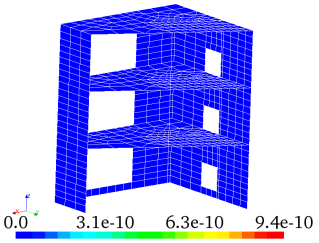

(c) Champ d'erreur pour la fenêtre 1 (de 0 à 2.5 s).

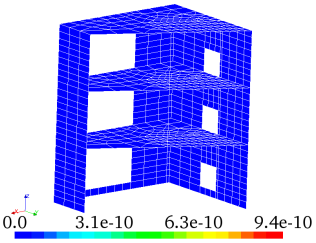

(d) Champ d'erreur pour la fenêtre 2 (de 0.5 à 3 s).

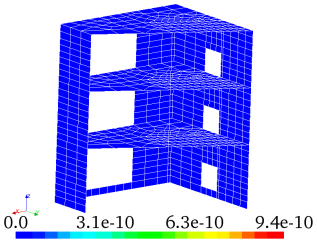

(e) Champ d'erreur pour la fenêtre 3 (de 1 à 3.5 s).

Figure E.38: *Résultats des fenêtres 1 à 3, correspondant à la localisation de l'endommagement illustré en figure E.38(b).*

Dans un second temps, les mesures et accélérogrammes ont été découpés en plusieurs fenêtres successives. Cette nouvelle étude permet d'approcher l'évolution temporelle de l'endommagement grâce à l'ERC. On obtient de plus une localisation plus complète de l'endommagement subi par la structure.

E.3 Conclusion et perspectives

La méthode d'identification basée sur l'Erreur en Relation de Comportement a été testée sur un cas particulier supposé représentatif du type d'études menées à l'échelle industrielle à EDF, la maquette SMART.

Le rapprochement de l'objectif s'est fait de manière progressive, en commençant par introduire des défauts de raideur dont on contrôle toutes les caractéristiques (taille, emplacement, intensité), puis en intégrant des défauts d'endommagement, plus proches de ceux qu'on peut être amené à rencontrer dans un cadre industriel, avant d'exploiter les mesures expérimentales, entâchées de bruit, en vue de localiser des défauts dont on ne connaît rien à l'avance. La dernière partie reste encore à faire à l'heure actuelle.

Les résultats de localisation de défauts obtenus jusqu'à présent sur ce modèle ont permis de tirer un certain nombre de conclusions quant à l'efficacité d'une part, et d'autre part quant à l'utilisation de la méthode d'ERC.

On peut retenir pour le premier point les résultats de sensibilité à des paramètres tels que le nombre et la position des capteurs créant les mesures, ou encore l'emplacement, la taille et l'intensité du (ou des) défaut(s), résultats provenant principalement d'études complètement numériques, les mesures étant générées par un calcul. Les conclusions tirées de ce type d'étude permettent d'aborder des calculs basés sur des mesures expérimentales en toute connaissance de l'indicateur d'erreur et donc d'en interpréter les résultats plus facilement et plus justement. Il est envisagé de compléter ces résultats dans la suite du stage en développant un indicateur quantitatif de la sensibilité de l'ERC à une topologie de défaut, par l'intermédiaire du mot-clef `SENSIBILITE` de *Code_Aster*.

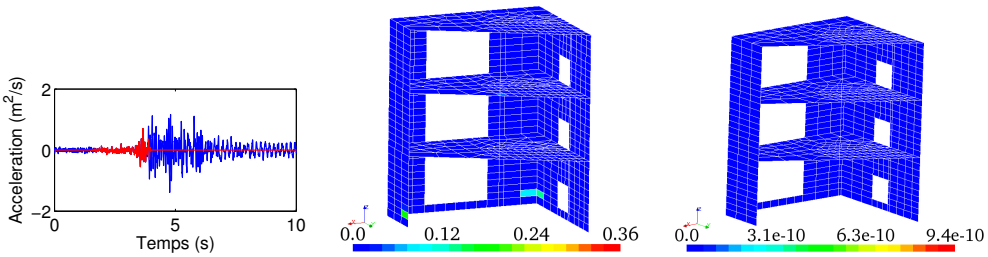

(a) Fenêtrage 4 : de 1.5 à 4s. (b) Endommagement à 4 s (c) Champ d'erreur.

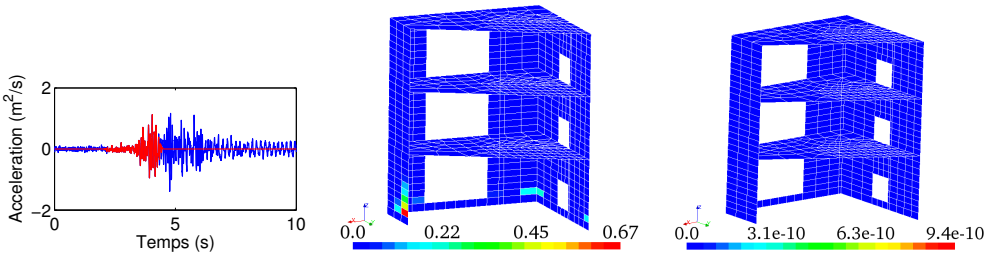

(d) Fenêtrage 5 : de 2 à 4.5s (e) Endommagement à 4.5 s (f) Champ d'erreur.

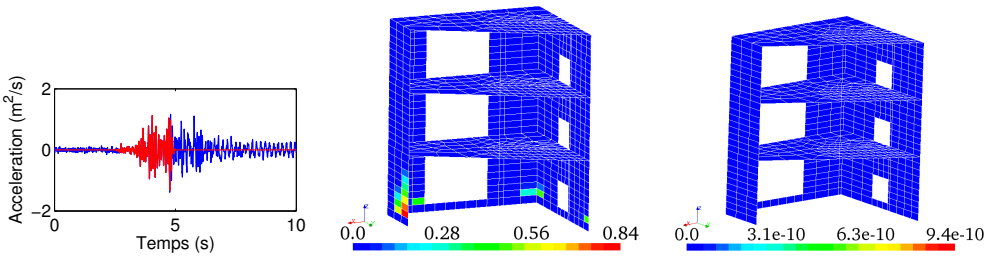

(g) Fenêtrage 6 : de 2.5 à 5s (h) Endommagement à 5 s (i) Champ d'erreur.

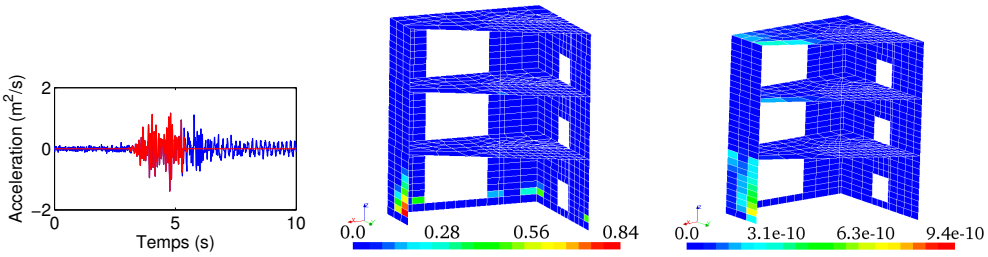

(j) Fenêtrage 7 : de 3 à 5.5s (k) Endommagement à 5.5 s (l) Champ d'erreur.

Figure E.39: *Résultats des fenêtres 4 à 7, correspondant à différents niveaux d'endommagement illustrés sur la colonne du milieu.*

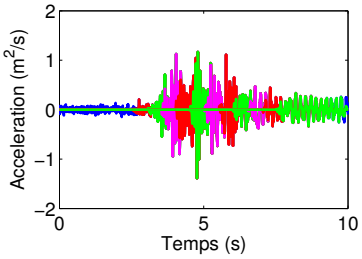

(a) Fenêtrages 8 à 16.

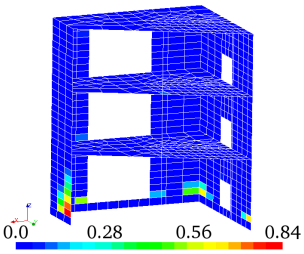

(b) Endommagement après 5.5 s

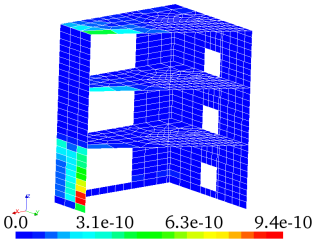

(c) Champ d'erreur pour la fenêtre 8 (de 3.5 à 6 s).

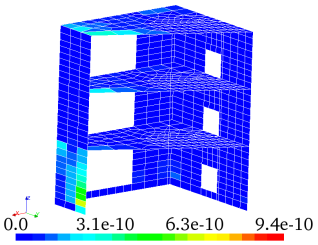

(d) Champ d'erreur pour la fenêtre 9 (de 4 à 6.5 s).

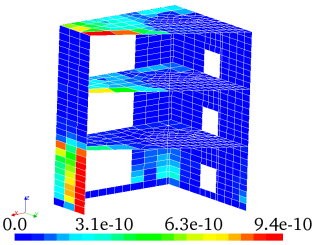

(e) Champ d'erreur pour la fenêtre 10 (de 4.5 à 7 s).

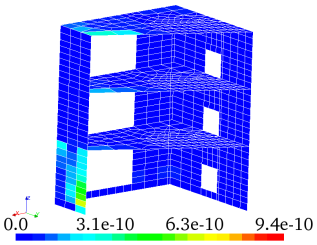

(f) Champ d'erreur pour la fenêtre 11 (de 5 à 7.5 s).

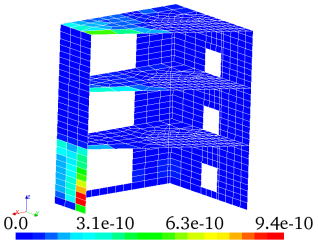

(g) Champ d'erreur pour la fenêtre 12 (de 5.5 à 8 s).

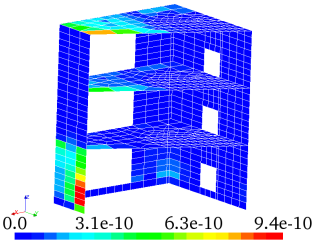

(h) Champ d'erreur pour la fenêtre 13 (de 6 à 8.5 s).

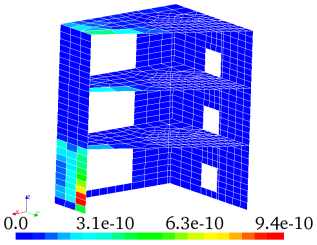

(i) Champ d'erreur pour la fenêtre 14 (de 6.5 à 9 s).

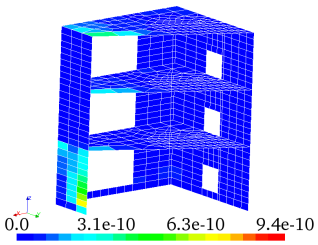

(j) Champ d'erreur pour la fenêtre 15 (de 7 à 9.5 s).

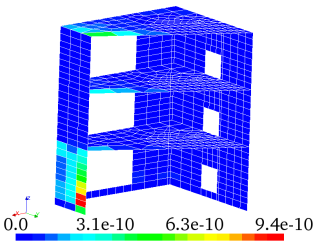

(k) Champ d'erreur pour la fenêtre 16 (de 7.5 à 10 s).

Figure E.40: *Résultats des fenêtres 8 à 16, correspondant à la localisation de l'endommagement illustré en figure E.40(b).*

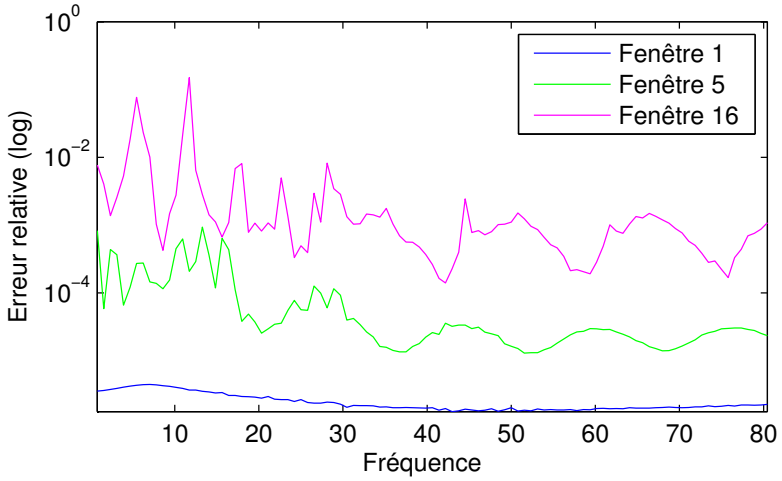

Figure E.41: *Spectre d'erreur pour différentes fenêtres.*

Le spectre d'erreur a été interprété comme un bon indicateur de la qualité de localisation à une fréquence donnée. Il a également été identifié comme un élément sur lequel s'appuyer pour choisir une méthode de localisation, caractérisée par le nombre de fréquences prises en compte, le choix de ces fréquences, et la manière de sommer les champs d'erreur associés. Des méthodologies de calcul se différenciant les unes des autres par ces caractéristiques ainsi que par la gestion de la mémoire et le degré d'utilisation conjointe de *Code_Aster* et du langage python ont ainsi été testées et appreciées pour choisir une méthodologie efficace et cohérente, dépendante du besoin de l'utilisateur.

Le développement de cette méthodologie et des scripts pythons associés aura permis d'élaguer le travail nécessaire à une éventuelle intégration des méthodes d'identification basées sur l'ERC dans *Code_Aster*, par le biais de macro-commandes ou d'opérateurs adaptés, intégration dont la pertinence pourra être évaluée à la lumière de ce stage. Une première intégration de l'ERC pour traiter des problèmes de grande taille aura dans tous les cas été réalisée ici, menant à des résultats encourageants.

Des mesures générées par un calcul transitoire non-linéaire ont dans un deuxième temps été exploitées pour localiser de l'endommagement. Cette étude a mis en évidence le fait qu'une utilisation de mesures temporelles dans l'ERC était délicate et nécessitait la prise d'un certain nombre de précautions. Les calculs ont finalement aboutis à des résultats encourageants et laissent penser que l'ERC permet non seulement de localiser des zones ayant subi un comportement non-linéaire au cours d'un calcul, mais également de suivre dans le temps l'apparition de l'endommagement sur la structure.

La dernière étape, utilisant les mesures expérimentales sur la maquette SMART pour évaluer l'écart au modèle éléments finis, n'aura malheureusement pas pu être abordée au cours de ce stage, qui fournit cependant une bonne connaissance des techniques d'utilisation de l'ERC nécessaire à sa réalisation. Le pas à franchir est néanmoins important car il implique de passer d'une situation où le modèle générant les mesures est parfaitement connu à un cas où les mesures sont issues d'essais, donc qui non seulement peuvent être entâchées de bruit, mais qui de plus représentent une structure réelle, ce qui l'écarte intrinsèquement du modèle éléments finis.

Bibliography

[1] H. AHMADIAN, J. METTERSHEAD, AND M. FRISWELL, *Boundary condition identification using characteristic equations*, J. Sound Vibr., 247(5) (2001), pp. 755–763.

[2] O. ALLIX, P. FEISSEL, AND P. THEVENET, *A delay damage mesomodel of laminates under dynamic loading: basic aspects and identification issues*, Comput. Struct., 81 (2003), pp. 1177–1192.

[3] S. ANDRIEUX, A. BEN ABDA, AND H. D. BUI, *Sur l'identification de fissures planes via le concept d'écart à la réciprocité en élasticité*, Comptes rendus de l'Académie des Sciences, 324 (1997), pp. 1431–1438.

[4] J. ARGAUD, *Synthèse sur les méthodes d'identification, de recalage et d'assimilation de données*. Note interne EDF: H-I23-2008-04019-FR, janvier 2009.

[5] J. P. ARGAUD, B. BOURIQUET, P. ERHARD, S. MASSART, A. PONCOT, AND S. RICCI, *Représentation des erreurs en assimilation de données et matrices de variance-covariance*. Note interne EDF: I23-2009-00571-FR-0.6, 2009.

[6] M. ARNST, *Inversion of probabilistic models of structures using measured transfer functions*, PhD thesis, École Centrale Paris, 2007.

[7] M. S. ARULAMPALAM, S. MASKELL, N. GORDON, AND T. CLAPP, *A tutorial on particle filters for online nonlinear/non-gaussian bayesian tracking*, IEEE Transactions on Signal Processing, 50 (2002), pp. 174–188.

[8] D. AUROUX AND J. BLUM, *Back and forth nudging algorithm for data assimilation problems*, Comptes Rendus de l'Académie des sciences, 340 (2005), pp. 873–878.

[9] E. BALMÈS, *Review and evaluation of shape expansion methods*. IMAC XVIII, 2000.

[10] J. BEN ABDALLAH, *Inversion Gaussienne appliquée à la correction paramétrique de modèles structuraux*, PhD thesis, Ecole Polytechnique, 1995.

[11] M. BOCQUET, *Introduction aux principes et méthodes de l'assimilation de données en géophysique*. Notes de cours de l'ENSTA, 2005.

[12] G. BOLZON, R. FEDELE, AND G. MAIER, *Parameter identification of a cohesive crack model by kalman filter*, Comp. Meth. Appl. Mech. Eng., 191 (2002), pp. 2847–2871.

[13] M. BONNET, *Problèmes inverses.* Cours de DEA DSSC. Ecole Centrale Paris, 2004.

[14] M. BONNET AND A. CONSTANTINESCU, *Inverse problems in elasticity*, Inverse Problems, 21 (2005), pp. R1–R50.

[15] M. BOUTAYEB AND D. AUBRY, *A strong tracking extended kalman observer for nonlinear discrete-time systems*, IEEE Transactions on Automatic Control, 42(2) (1997), pp. 581–586.

[16] H. D. BUI, *Introduction aux problèmes inverses en mécanique des matériaux*, Eyrolles, 1993.

[17] J. CARPENTER, P. CLIFFORD, AND P. FEARNHEAD, *Improved particle filters for nonlinear problems*, IEE proceedings. Radar, Sonar Navigation, 147 (1999), pp. 1–7.

[18] E. CHATZI, *Development and Application of Parametric System Identification Algorithms for Structural Health Monitoring*, PhD thesis, Columbia University, 2010.

[19] A. CHOUAKI, *Une méthode de recalage des modèles dynamiques de structures avec amortissement*, PhD thesis, Ecole Normale Supérieure de Cachan, 1998.

[20] A. CONSTANTINESCU, *Sur l'identification des modules élastiques.*, PhD thesis, École Polytechnique, 1994.

[21] A. CORIGLIANO, A. GHISI, AND S. MARIANI, *Impact induced composite delamination: State and parameter identification via unscented kalman filter*, Comp. Meth. Appl. Mech. Eng., 194 (2005), pp. 5242–5272.

[22] A. CORIGLIANO AND S. MARIANI, *Parameter identification in explicit structural dynamics: performance of the extended kalman filter*, Comp. Meth. Appl. Mech. Eng., 193 (2004), pp. 3807–3835.

[23] A. CORIGLIANO, S. MARIANI, AND B. ORSATI, *Identification of gurson tvergaard material model parameters via kalman filtering technique*, International Journal of Fracture, 104 (2000), pp. 349–373.

[24] D.CLOUTEAU, *Stochastic computational mechanics*. Cours de DEA DSSC. Ecole Centrale Paris, 2004.

[25] D. DEGRAUWE, G. DE ROECK, AND G. LOMBAERT, *Uncertainty quantification in the damage assessment of a cable-stayed bridge by means of fuzzy numbers*, Computers and Structures, 87 (2009), pp. 1077–1084.

[26] A. DERAEMAEKER, *Sur la maîtrise des modèles en dynamique des structures à partir de résultats d'essais*, PhD thesis, Ecole Normale Supérieure de Cachan, 2001.

[27] A. DERAEMAEKER, P. LADEVÈZE, AND P. H. LECONTE, *Reduced bases for model updating in structural dynamics based on constitutive relation error*, Comp. Meth. Appl. Mech. Eng., 191 (2002), pp. 2427–2444.

[28] G. DESROZIERS, L. BERRE, B. CHAPNIK, AND P. POLI, *Diagnosis of observation and background and analysis-error statistics in observation space*, Quarterly Journal of the Royal Meteorological Society, 131 (2005), pp. 3385–3396.

[29] G. DESROZIERS AND S. IVANOV, *Diagnosis and adaptive tuning of observation-error parameters in a variational assimilation*, Quarterly Journal of the Royal Meteorological Society, 127 (2001), pp. 1433–1452.

[30] S. DOEBLING, C. FARRAR, M. PRIME, AND D. SHEVITZ, *Damage identification and health monitoring of structural and mechanical systems from changes in their vibration characteristics: a literature review*, tech. rep., LA-13070-MS, Los Alamos National Laboratory, Los Alamos, New Mexico, USA, 1996.

[31] M. EHRENDORFER, T. PALMER, AND F. BOUTIER, *Analysis and forecast error covariances in exact kalman filter.*, Research Activities in Atmospheric and Oceanic Modeling, 31 (2001), pp. 1.17–1.18.

[32] M. EHRENDORFER AND J. J. TRIBBIA, *Optimal prediction of forecast error covariances through singular vectors*, Journal of the Atmospheric Sciences, 54 (1997), pp. 286–313.

[33] G. EVENSEN, *Sequential data assimilation with a nonlinear quasi-geostrophic model using monte carlo methods to forecast error statistics.*, Journal of Geophysical Research, 99(C5) (1994), pp. 10143–10162.

[34] ——, *The ensemble kalman filter: theoretical formulation and practical implementation*, Ocean Dynamics, 53 (2003), pp. 343–367.

[35] C. FARRAR AND S. DOEBLING, *An overview of modal-based damage identification methods*, in Proceedings of DAMAS conference, Sheffield, UK, June 1997.

[36] P. FEISSEL, *Vers une stratégie d'identification en dynamique rapide pour des données incertaines*, PhD thesis, Ecole Normale Supérieure de Cachan, 2003.

[37] P. FEISSEL AND O. ALLIX, *Modified constitutive relation error identification strategy for transient dynamics with corrupted data: The elastic case.*, Comp. Meth. Appl. Mech. Eng., 196 (2006), pp. 1968–1983.

[38] S. FRIKHA, G. COFFIGNAL, AND J. L. TROLLE, *Boundary condition identification using condensation and inversion. application to operating piping network*, J. Sound Vibr., 233(3) (2000), pp. 495–514.

[39] S. FRIKHA, M. GAUDIN, AND G. COFFIGNAL, *Boundary condition error for parametric updating of in-operation systems. application to piping systems*, J. Sound Vibr., 241(3) (2001), pp. 373–399.

[40] M. GREWAL AND A. ANDREWS, *Kalman Filtering : Theory and practice using Matlab*, John Wiley & Sons Inc., 2001.

[41] G.WELCH AND G. BISHOP, *An introduction to the kalman filter.*, tech. rep., UNC-Chapel Hill, 2006.

[42] K. HADJ-SASSI, *Une stratégie d'identification conjointe des paramètres et de l'état de structures à comportements non-linéaires. Assimilation de données et erreur en loi de comportement*, PhD thesis, École Polytechnique, 2007.

[43] B. HALPHEN AND Q. S. NGUYEN, *Sur les matériaux standards généralisés*, Journal de Mécanique, 14 (1975), pp. 39–63.

[44] P. HARGRAVE, *A tutorial introduction to kalman filtering and kalman filters: Introduction, applications and future developments.*, tech. rep., IEEE Colloquium and STC Technol. Ltd., 1989.

[45] S. HAYKIN, *Kalman Filtering and Neural Networks*, John Wiley & Sons Inc., 2001.

[46] S. HAYWARD, *Mathematics in signal processing IV*, Oxford University Press, 1998, ch. Constrained Kalman filter for least-squares estimation of time-varying beamforming weights, pp. 113–125.

[47] M. HOSHIYA, K. ISHII, AND S. NAGATA, *Structural identification by extended kalman filter*, Journal of Engineering Mechanics, 110 (1984), pp. 1757–1770.

[48] M. HOSHIYA AND A. SUTOH, *Kalman filter finite element method in identification*, Journal of Engineering Mechanics, 119 (1993), pp. 197–210.

[49] S. JULIER, *The scaled unscented transformation*, in Proceedings of the American Control Conference, 2002, pp. 4555–4559.

[50] S. J. JULIER AND J. K. UHLMANN, *A general method for approximating nonlinear transformations of probability distributions*, tech. rep., Department of Engineering Science and University of Oxford,, 1996.

[51] ——, *A new extension of the kalman filter to nonlinear systems.*, in Proceedings of AeroSense: The 11th Int. Symposium on Aerospace/Defense Sensing and Simulation and Controls and Orlando and 1997., 1997.

[52] ——, *Unscented filtering and nonlinear estimation*, Proceedings of the IEEE, 92 (2004), pp. 401–402.

[53] R. KALMAN, *A new approach to linear filtering and prediction problems*, Transactions of the ASME, Ser. D, Journal of Basic Engineering, 82 (1960), pp. 34–45.

[54] R. KANDEPU, B. FOSS, AND L. IMSLAND, *Applying the unscented kalman filter for nonlinear state estimation*, Journal of Process Control, 18 (2008), pp. 753–768.

[55] P. LADEVÈZE, *Comparaison des modèles des milieux continus*, PhD thesis, Université Pierre-et-Marie-Curie, 1975.

[56] ——, *Recalage de modélisations des structures complexes*, Tech. Rep. 33.11.01.4, Aérospatiale, Les Mureaux, 1983.

[57] P. LADEVÈZE AND N. MOËS, *A new a posteriori error estimation for nonlinear time-dependent finite element analysis*, Comp. Meth. Appl. Mech. Eng., 157 (1997), pp. 45–68.

[58] P. LADEVÈZE AND M. REYNIER, *A localization method of stiffness errors for the adjustment of FE models*, ASME publishers, 1989, ch. FE Modeling and Analysis, pp. 355–361.

[59] P. LADEVÈZE, M. REYNIER, AND N. MAIA, *Error on the constitutive relation in dynamics: Theory and application for model updating*, Inverse Problems in Engineering Mechanics I, 1994, ch. I, pp. 251–256.

[60] P. LADEVÈZE AND J. WAEYTENS, *Model verification in dynamics through strict upper error bounds*, Comp. Meth. Appl. Mech. Eng., 198 (2009), pp. 1775–1784.

[61] X. LIU, P. ESCAMILLA-AMBROSIO, AND N. LIEVEN, *Extended kalman filtering for the detection of damage in linear mechanical structures*, J. Sound Vibr., 325 (2009), pp. 1023–1046.

[62] L. LJUNG AND T. SÖDERSTRÖM, *Theory and Practice of Recursive Identification*, MIT Press, 1983.

[63] J. MAECK, M. ABDELWAHAB, B.PEETERS, G. DEROECK, J. DEVISSCHER, W. DEWILDE, J. NDAMBI, AND J. VANTOMME, *Damage identification in reinforced concrete structures by dynamic stiffness determination*, Engineering tructures, 22 (2000), pp. 1339–1349.

[64] B. A. MILLER AND S. A. HOWARD, *Identifying bearing rotordynamic coefficients using an extended kalman filter*, tech. rep., NASA/TM-215298, 2008.

[65] K. MOSEGAARD AND A. TARANTOLA, *Probabilistic Approach to Inverse Problems.*, International Handbook of Earthquake & Engineering Seismology, 2002, ch. Part A, pp. 237–265.

[66] L. NERGER, S. DANILOV, G. KIVMAN, W. HILLER, AND J. SCHRÖTER, *Data assimilation with the ensemble kalman filter and the seik filter applied to a finite element model of the north atlantic*, Journal of Marine Systems, 65 (2007), pp. 288–298.

[67] H. NGUYEN, O.ALLIX, AND P.FEISSEL, *A robust identification strategy for rate-dependent models in dynamics*, Inverse Problems, 24 (2008), pp. 1–24.

[68] M. NODET, *Modélisation mathématique et assimilation de données lagrangiennes pour l'océanographie*, PhD thesis, Université de Nice Sophia Antipolis, 2005.

[69] D. PARRISH AND J. DERBER, *The national meteorological center's spectral statistical interpolation analysis system*, Monthly Weather Review, 120 (1992), pp. 1747–1763.

[70] F. PLED, L. CHAMOIN, AND P. LADEVÈZE, *On the techniques for constructing admissible stress fields in model verification: Performances on engineering examples*, International Journal for Numerical Methods in Engineering, 88 (2011), pp. 409–441.

[71] J. PORRIL, *Optimal combination and constraints for geometrical sensor data*, International Journal of Robotics Research, 7 (1988), pp. 66–77.

[72] R. PROVASI, G. ZANETTA, AND A. VANIA, *The extended kalman filter in the frequency domain for the identification of mechanical structures excited by sinusoidal multiple inputs*, Mechanical Systems and Signal Processing, 14(3) (2000), pp. 327–341.

[73] E. REYNDERS, A. TEUGHELS, AND G. D. ROECK, *Finite element model updating and structural damage identification using omax data*, Mechanical Systems and Signal Processing, 24 (2010), pp. 1306–1323.

[74] J. RHIM AND S. LEE, *A neural network approach for damage detection and identification of structures*, Computational Mechanics, 16 (1995), pp. 437–443.

[75] I. B. RODES, *A tutorial introduction to estimation and filtering*, IEEE Transaction on Automatic Control, 16 (1971), pp. 688–706.

[76] D. SIMON, *Training fuzzy systems with the extended kalman filter*, Fuzzy Sets and Systems, 132 (2002), pp. 189–199.

[77] ——, *Optimal State Estimation. Kalman, H_∞ and nonlinear approaches*, John Wiley & Sons Inc., 2006.

[78] M. L. STEIN, *Interpolation of spatial data: some theory for kriging*, Springer, 1990.

[79] R. STENGEL, *Optimal Control and Estimation*, Dover Publications and Inc, 1986.

[80] A. TARANTOLA, *Inverse problem theory*, SIAM, 2005.

[81] A. TARANTOLA AND B. VALETTE, *Generalized nonlinear inverse problems solved using the least squares criterion.*, Reviews of Geophysics and Space Physics, 20 (1982), pp. 219–232.

[82] B. TEIXEIRA, L. TÔRRES, L. AGUIRRE, AND D. BERNSTEIN, *On unscented kalman filtering with state interval constraints*, Journal of Process Control, 20 (2010), pp. 45–57.

[83] A. TEUGHELS AND G. D. ROECK, *Structural damage identification of the highway bridge z24 by fe model updating*, J. Sound Vibr., 278 (2004), pp. 589–610.

[84] A. TIKHONOV AND V.Y.ARSENIN, *Solutions of ill-posed problems.*, Winston Wiley & Sons, 1977.

[85] R. TIPIREDDY, H. A. NASRELLAH, AND C. S. MANOHAR, *A kalman filter based strategy for linear structural system identification based on multiple static and dynamic test data*, Probabilistic Engineering Mechanics, 24 (2009), pp. 60–74.

[86] P. VACHHANI AND S. NARASIMHAN, *Robust and reliable estimation via unscented recursive nonlinear dynamic data reconciliation*, Journal of Process Control, 16 (2006), pp. 1075–1086.

[87] M. M. A. WAHAB, G. D. ROECK, AND B. PEETERS, *Parametrisation of damage in reinforced concrete structures using model updating*, J. Sound Vibr., 228(4) (1999), pp. 717–730.

[88] W. WEN AND H. DURRANT-WHYTE, *Model-based multi-sensor data fusion*, in IEEE International Conference on Robotics and Automation, 1992, pp. 1720–1726.

[89] N. WIENER, *Extrapolation, interpolation, and smoothing of stationary time series.*, Wiley, 1949.

[90] K. XIONG, H. ZHANG, AND C. CHAN, *Performance evaluation of ukf-based nonlinear filtering*, Automatica, 42 (2006), pp. 261–270.

[91] E. ZHANG, *Étude de problèmes inverses en dynamique des structures par inférence bayésienne (Recalage de modèle et reconstruction des efforts)*, PhD thesis, Université Techologique de Compiègne, 2010.